

First row transition metal compounds for the oxygen evolution reaction

3d-Übergangsmetallverbindungen für die Sauerstoffentwicklungsreaktion
zur Erlangung des akademischen Grades Doktor-Ingenieur (Dr.-Ing.)

Dissertation von Jona Schuch geboren in Lindenfels

First Reviewer: Prof. Dr. Wolfram Jaegermann

Second Reviewer: Prof. Dr. Wolfgang Ensinger

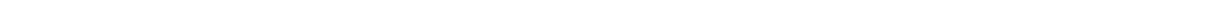
TU Darmstadt, FB 11 – Material- und Geowissenschaften

Darmstadt 2021



TECHNISCHE
UNIVERSITÄT
DARMSTADT





First row transition metal compounds for the oxygen evolution reaction

3d-Übergangsmetallverbindungen für die Sauerstoffentwicklungsreaktion

Vom Fachbereich Material- und Geowissenschaften

der Technischen Universität Darmstadt

im Fachgebiet Oberflächenforschung

zur Erlangung des akademischen Grades eines

Doktor-Ingenieurs (Dr.-Ing)

Dissertation

vorgelegt von

M.Sc. Jona Schuch

Tag der Einreichung: 13.10.2021

Tag der Prüfung: 07.12.2021

Erster Gutachter: Prof. Dr. Wolfram Jaegermann

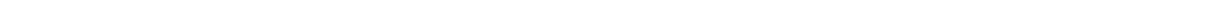
Zweiter Gutachter: Prof. Dr. Wolfgang Ensinger

Jahr der Veröffentlichung der Dissertation auf TUpriints: 2022

URN: [urn:nbn:de:tuda-tuprints-202879](https://nbn-resolving.org/urn:nbn:de:tuda-tuprints-202879)

Veröffentlicht unter CC BY-SA 4.0 International

<https://creativecommons.org/licenses/>



Erklärung zur Dissertation

Hiermit versichere ich, die vorliegende Dissertation ohne Hilfe Dritter nur mit den angegebenen Quellen und Hilfsmitteln angefertigt zu haben. Alle Stellen, die aus Quellen entnommen wurden, sind als solche kenntlich gemacht. Diese Arbeit hat in gleicher oder ähnlicher Form noch keiner Prüfungsbehörde vorgelegen.

Ort und Datum:

Unterschrift:

(Jona Schuch)

Abstract

The aim of this work was to find alternative catalyst systems for the oxygen evolution reaction (OER) in alkaline solutions. The state-of-the-art catalyst systems consist mainly of expensive and rare noble metal catalysts, like platinum, iridium, or ruthenium compounds. First-row transition metal compounds were identified to be promising alternatives for noble metal catalyst systems.

For this purpose, in the first part of this work, manganese-based oxides (MnO_x) were investigated. Firstly, the manganese-based oxides were synthesized as thin films by a plasma-enhanced chemical vapor deposition process onto titanium substrates. By varying the deposition process parameters, different MnO_x phases were produced and subsequently characterized. Afterwards, the determined process parameters were used to successfully deposit the MnO_x catalysts onto several other substrate materials. It was shown that the catalytic activity of the manganese oxides for the OER is influenced by the oxidation state of the manganese and, in addition, by the contact between the catalyst and the used substrate material. In particular a strong reduction of the catalytic activity was found for the deposition onto titanium substrates, which was attributed to the formation of a native oxide layer on the titanium surface, inhibiting a low resistive charge carrier transfer.

In the second part of this work, powdered nano-structured cobalt boride compounds were analyzed as a starting material to investigate their applicability for the alkaline OER. In a second step, a ternary compound was formed by the incorporation of iron ($\text{Co}_{1-x}\text{Fe}_x$)₂B and nickel ($\text{Co}_{1-x}\text{Ni}_x$)₂B (with $0 \leq x \leq 0.5$) into the dicobalt boride system. The transition metal borides were synthesized by a low-temperature solution synthesis with a subsequent calcination step. For the electrochemical investigation, the binary and ternary compounds were embedded into NafionTM containing ink and drop coated on polished glassy carbon substrates. It was shown that the transition metal borides oxidize under OER reaction conditions forming metal oxide/hydroxide or rather oxyhydroxide species. The activity of the dicobalt borides (Co_2B) was improved by an incorporation of up to 50wt% of iron or up to 20wt% of nickel. Especially the incorporation of up to 30wt% of iron showed a positive impact on the onset potential of the OER. Finally, the stability of the best performing catalysts was confirmed over an extended time period.

Kurzzusammenfassung

Ziel dieser Arbeit war es, alternative Katalysatorsysteme für die alkalische Sauerstoffentwicklungsreaktion zu finden. Die heutigen anwendungsrelevanten Systeme bestehen hauptsächlich aus seltenen und teuren Edelmetallkatalysatoren, wie Platin, Iridium oder Ruthenium Verbindungen. Als erfolgversprechende alternative Katalysatorsysteme wurden Übergangsmetallverbindungen der ersten Reihe des Periodensystems identifiziert.

Im ersten Teil dieser Arbeit wurden hierfür Mangan-basierte Oxide (MnO_x) untersucht. Diese wurden, im ersten Schritt, mittels plasmaunterstützter chemischer Gasphasenabscheidung auf Titan Substraten als dünne Schichten aufgetragen. Durch die Variation der Prozessparameter konnten unterschiedliche MnO_x Phasen hergestellt und charakterisiert werden. Die gefundenen Parameter konnten anschließend erfolgreich für die Deponierung auf anderen Substratmaterialien angewendet werden. Es zeigte sich, dass nicht nur die Oxidationsstufe des Mangans die katalytische Aktivität des Manganoxids für die Sauerstoffentwicklungsreaktion beeinflusst, sondern, dass auch dem Kontakt zwischen Substrat- und Katalysatormaterial eine entscheidende Rolle zukommt. Ein besonders negativer Effekt auf die katalytische Aktivität wurde bei der Verwendung von Titanfolie als Substratmaterial gefunden, da dieses eine schlecht leitende native Oxidschicht an der Oberfläche bildet, die einen niederohmigen Ladungstransfer verhindert.

Im zweiten Teil dieser Arbeit wurden nanostrukturierte pulverförmige Kobalt-Borid Verbindungen als Startmaterial analysiert und auf ihre Wirksamkeit für die alkalische Sauerstoffentwicklungsreaktion getestet. In einem zweiten Schritt wurde durch die Zugabe von Eisen ($(\text{Co}_{1-x}\text{Fe}_x)_2\text{B}$) bzw. Nickel ($(\text{Co}_{1-x}\text{Ni}_x)_2\text{B}$) (mit $0 \leq x \leq 0.5$) in die Kobalt-Borid Verbindungen ein ternäres System gebildet. Die Übergangsmetall-Boride wurden über eine Flüssigphasensynthese bei niedrigen Temperaturen hergestellt und anschließend kalziniert. Für die elektrochemischen Untersuchung wurden die binären und ternären Katalysatoren in eine NafionTM-haltige Tinte eingebettet und auf polierte Glaskohlenstoff Substrate deponiert. Es zeigte sich, dass die Übergangsmetall-Boride während des Betriebs als Sauerstoffentwicklungskatalysatoren an der Oberfläche oxidieren und Metall-Oxid/Hydroxid bzw. Metall-Oxyhydroxid Verbindungen bilden. Die katalytische Aktivität konnte jeweils durch die Zugabe von bis zu 50wt% Eisen bzw. bis zu 20wt% Nickel verbessert werden. Besonders auffällig war die deutliche Reduzierung des Startpotentials der Sauerstoffentwicklungsreaktion mit einer Zugabe von bis zu 30wt% Eisen. Abschließend konnte zudem die Stabilität der besten Mischsysteme über eine längere Zeitspanne bestätigt werden.

Publications and Contributions

This work was conducted from December 2015 till September 2021 in the surface science group of Prof. Dr. Wolfram Jaegermann in the department of material science at the Technical University of Darmstadt. Parts of this work were already published or presented on conferences.

First author* publications:

- ❖ **J. Schuch***, S. Klemenz*, P. Schuldt, A.-M. Zieschang, S. Dolique, P. Connor, B. Kaiser, U. I. Kramm, B. Albert and W. Jaegermann, “Efficient Oxygen Evolution Electrocatalyst by Incorporation of Nickel into Nanoscale Dicobalt Boride“, ChemCatChem, 2021. DOI: 10.1002/cctc.202002030
- ❖ S. Klemenz*, **J. Schuch***, S. Hawel, A.-M. Zieschang, B. Kaiser, W. Jaegermann and B. Albert, “Highly Efficient Oxygen Evolution Electrocatalyst by Incorporation of Iron into Nanoscale Cobalt Borides“, ChemSusChem, 2018. DOI: 10.1002/cssc.201801547

Corporate publications of the BMBF project:

- ❖ P. Connor*, **J. Schuch**, B. Kaiser and W. Jaegermann, “The Determination of Electrochemical Active Surface Area and Specific Capacity Revisited for the System MnO_x as an Oxygen Evolution Catalyst”, Zeitschrift für Physikalische Chemie, 2020. DOI: 10.1515/zpch-2019-1514
- ❖ C. Walter*, P. Menezes, M. Lerch, S. Orthmann, **J. Schuch**, P. Connor, B. Kaiser and M. Driess, “A Molecular Approach to Manganese Nitride Acting as a High Performance Electrocatalyst in the Oxygen Evolution Reaction”, Angewandte Chemie & Angewandte Chemie International Ed., 2017. DOI: 10.1002/anie.201710460

Further contributions to publications:

- ❖ G. Cherkashinin*, **J. Schuch**, B. Kaiser, L. Alff and W. Jaegermann, “High Voltage Electrodes for Li-Ion Batteries and Efficient Water Electrolysis: An Oxymoron?”, Journal of Physical Chemistry Letters, 2020. DOI: 10.1021/acs.jpcllett.0c00778
- ❖ A.-M. Zieschang*, J. D. Bocarsly, **J. Schuch**, C. V. Reichel, B. Kaiser, W. Jaegermann, R. Seshadri and B. Albert, “Magnetic and Electrocatalytic Properties of Nanoscale Cobalt Boride, Co_3B ”, Inorganic Chemistry, 2019. DOI: 10.1021/acs.inorgchem.9b02617
- ❖ Y. Feng*, Z. Yu, **J. Schuch**, S. Tai, L. Wiehl, C. Fasel, W. Jaegermann and R. Riedel, “Ternary Nowotny Phase $\text{Mo}_{3+2x}\text{Si}_3\text{C}_{0.6}$ Dispersed in a Porous SiC/C Matrix: A Novel Catalyst for Hydrogen Evolution Reaction”, Journal of the American Ceramic Society, 2019. DOI: 10.1111/jace.16731

- ❖ S. Tao*, F. Yang, **J. Schuch**, W. Jaegermann and B. Kaiser, “Electrodeposition of Nickel Composite Nanoparticles for Alkaline Hydrogen Evolution Reaction: Correlating Electrocatalytic Behavior and Chemical Composition Obtained by XPS”, ChemSusChem, 2017. DOI: 10.1002/cssc.201702138
- ❖ N. Weidler*, **J. Schuch**, F. Knaus, P. Stenner, S. Hoch, A. Maljusch, R. Schaefer, B. Kaiser and W. Jaegermann, XPS Investigation of PECVD Deposited NiO_x, NiO_x(OH)_y and Co-NiO_x(OH)_y: Influence of the Chemical Composition on the Catalytic Activity for the OER, The Journal of Physical Chemistry C, 2017. DOI: 10.1021/acs.jpcc.6b12652
- ❖ N. Weidler*, S. Paulus, **J. Schuch**, J. Klett, P. Stenner, S. Hoch, A. Maljusch, J. Brötz, C. Wittich, B. Kaiser and W. Jaegermann, CoO_x thin film deposited by CVD as efficient water oxidation catalyst: Change of oxidation state in XPS and its correlation to electrochemical activity, Physical Chemistry Chemical Physics, 2016. DOI: 10.1039/C5CP05691H

Conference contributions:

- ❖ **J. Schuch**, J. Doerfer, B. Kaiser, W. Jaegermann, “Manganese Oxides for the Oxygen Evolution Reaction”, Poster, 115th Annual Meeting of the German “Bunsen-Gesellschaft for Physical Chemistry e.V.”, 5th to 7th of May 2016, Rostock – Germany.
- ❖ **J. Schuch**, N. Weidler, F. Yang, B. Kaiser, W. Jaegermann, “Deposition of Manganese Oxides by CVD: First results”, Presentation, Mangan Conference, 13th and 14th of October 2016, Berlin – Germany.
- ❖ **J. Schuch**, P. Connor, “Deposition of Manganese Oxides by (PE)CVD and PVD”, Presentation, Mangan Status Meeting, 26th of April 2017, Mülheim an der Ruhr – Germany.
- ❖ **J. Schuch**, S. Hawel, P. Schuldt, B. Kaiser, W. Jaegermann, „Highly Efficient Oxygen Evolution Electrocatalyst by Incorporation of Iron or Nickel into Nanoscale Cobalt Borides“, Poster, 69th Annual Meeting of the International Society of Electrochemistry, 2th to 7th of September 2018, Bologna – Italy.
- ❖ **J. Schuch**, P. Connor, B. Kaiser, W. Jaegermann, “Tuning the catalytic performance of Mn_xO_y oxygen evolution catalysts by a variation of layer thickness and substrate material”, Poster, International Bunsen-Discussion-Meeting, April 1st to 5th 2019, Taormina – Italy.

Supervised student theses:

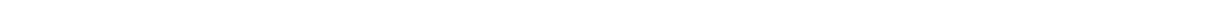
- ❖ **Stefan Hawel**, *Investigation of Cobalt Boride (Co₂B) as Catalyst for Electrochemical Water Splitting*, Master-Thesis, 2017.

-
- ❖ **Patrick Schuldt**, *Lithium-Ionen Batteriematerialien für die Sauerstoffentwicklungsreaktion*, Bachelor-Thesis, 2019.
 - ❖ **Bohan Xu**, *Nickel-Iron-Boride catalysts for the Oxygen Evolution Reaction*, Advanced Research Lab, 2020.
 - ❖ **Biffo Abdulkadir**, *A Review on Hydrogen Evolution Reaction Inhibiting Anode Electrode Materials for Vanadium Redox Flow Batteries*, Advanced Research Lab, 2021.
 - ❖ **Piyatep Ngernklay**, *The Electrochemical Tuning of $\text{LiCo}_{(1-x)}\text{Fe}_x\text{PO}_4$ by Electrochemical Delithiation and XPS Study*, Advanced Research Lab, 2021.

Table of contents

Erklärung zur Dissertation.....	V
Abstract.....	VI
Kurzzusammenfassung.....	VII
Publications and Contributions.....	VIII
Table of contents.....	XI
List of abbreviations.....	XIII
Symbols.....	XIII
1 Introduction.....	1
2 Fundamentals.....	7
2.1 Electrochemistry.....	7
2.1.1 Electrochemical double-layer.....	9
2.1.2 Transition state theory.....	10
2.2 Oxygen evolution reaction on ternary systems.....	14
2.2.1 The potential-determining step.....	14
2.2.2 Synergetic effects.....	16
2.3 Determination of the electrochemical surface area.....	18
2.4 Photoelectron spectroscopy.....	20
2.4.1 Quantitative analysis.....	24
2.4.2 Determination of the film thickness.....	24
3 Manganese oxide for the oxygen evolution reaction.....	27
3.1 Material perspective: Manganese oxides.....	27
3.1.1 Role of manganese oxide in the photosystem II.....	28
3.1.2 Classification of manganese oxide as an oxygen evolution reaction catalyst.....	29
3.1.3 XPS specifics of manganese oxides.....	31
3.2 Methodological background.....	33
3.2.1 Plasma enhanced chemical vapor deposition (PE-CVD).....	33
3.3 Experimental.....	36
3.3.1 Substrate Preparation.....	36
3.3.2 Setup of the PE-CVD reactor.....	37
3.3.3 CVD precursor analysis.....	39
3.3.4 Electrochemical measurement protocol.....	40
3.4 Manganese oxide for the oxygen evolution reaction.....	43
3.4.1 Limitations of the manganese oxide deposition by PE-CVD.....	43
3.4.2 Electrochemical characterization of manganese oxide thin films.....	47
3.4.3 Changes in oxidation state during the electrochemical investigation.....	51
3.5 Manganese oxide deposition: Effect of the support.....	54
3.5.1 XPS characterization of manganese oxides on different support materials.....	54
3.5.2 Electrochemical characterization of manganese oxide thin films.....	55
3.5.3 Changes in oxidation state during the electrochemical investigation.....	60
3.6 Conclusions.....	62
4 Transition metal borides for the oxygen evolution reaction.....	65
4.1 State of the art.....	65

4.1.1	Crystal structure.....	65
4.1.2	Water electrolysis.....	66
4.1.3	Electrochemical redox behavior.....	68
4.1.4	Specifics to X-Ray photoelectron spectroscopy.....	75
4.2	Experimental	80
4.2.1	Synthesis route of the transition metal borides	80
4.2.2	Choice of substrate material	81
4.2.3	Substrate preparation.....	81
4.2.4	Catalyst ink preparation and drop coating	82
4.2.5	Electrochemical protocol	83
4.2.6	Preliminary XPS analysis of Nafion™.....	84
4.2.7	Electron microscopy	86
4.2.8	Atomic absorption spectrometry.....	86
4.3	Dicobalt boride (Co ₂ B) and tricoalt boride (Co ₃ B)	87
4.3.1	Surface analysis with XPS.....	87
4.3.2	Electrochemical investigation	91
4.4	Incorporation of iron into dicobalt boride (Co _{1-x} Fe _x) ₂ B	96
4.4.1	Surface analysis of the catalyst powders	96
4.4.2	Electrochemical investigation	102
4.4.3	XPS – oxidation state changes during operating conditions.....	106
4.4.4	Conclusion of the proposed mechanism.....	109
4.5	Incorporation of nickel into dicobalt boride (Co _{1-x} Ni _x) ₂ B.....	112
4.5.1	Surface analysis of the catalyst powders	112
4.5.2	Electrochemical investigation	118
4.5.3	XPS – oxidation state changes during operation	124
4.5.4	Conclusion of the proposed mechanism.....	131
5	Conclusions and Perspectives.....	133
	List of references	CXXXVII
	Appendix.....	CLIII
	Danksagung	CLXX



1 Introduction

The transition from nuclear and fossil fuel to renewable energy and the protection of the world's climate are predominant topics of the last two decades. As decided in the Paris contract, most of the world's community has agreed on holding the global warming temperature below a threshold value of 2 °C as defined from the start of the industrial era.^[1] Today, the annual global energy demand of the world population is roughly thirty times higher compared to the end of the 19th century.^[2] A further increase is expectably caused not only by improved living standards but also by the rapid technological development. This progress is linked to a growing demand for energy per person and in combination with an increase in the world population (cf. **Figure 1.0.1a**), as a consequence, the energy demand will rise further (cf. **Figure 1.0.1b**).^{[3], [4]}

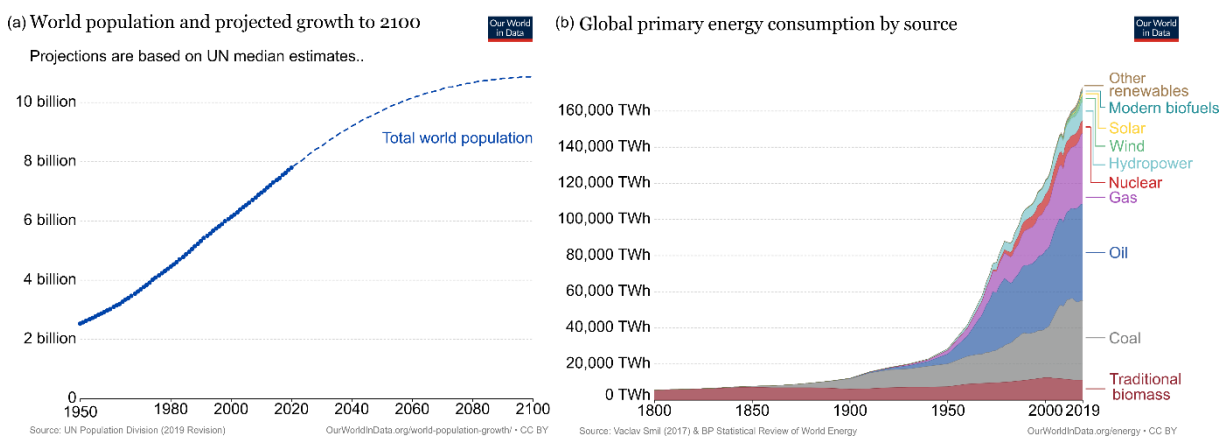


Figure 1.0.1: (a) Development of the world's population and projected growth to the year 2100.^[3] (b) The global primary energy consumption by different energy sources until 2019.^[4]

Most of the world's current energy harvesting is still based on fossil fuels, *e.g.* coal, oil, and gas, which are not indefinitely available and will all be consumed not later than 2100.^{[5]–[7]} This unpromising perspective and the associated unceasing exhaust of greenhouse gas forces the global community to take action. At present, the replacement of fossil fuels by renewable energy sources is not only a recommended action but must become reality soon. To accomplish this objective, the energy produced by renewable sources must supersede the existing infrastructure of energy supplied by fossil fuels and additionally, has to keep pace with the everlasting rise of energy demand of the world.^{[8], [9]} Consequently, a variety of different renewable energy sources have to be accessed to accomplish the requirement set by the global community to exit from nuclear and fossil-fuel energy.

One attribute that most renewable energy sources have in common is their unsteady energy supply, meaning that *e.g.*, solar and wind power fluctuate during the day-night cycle, but also vary between the seasons and are dependent on the location of the power plant. It is illusory to

assume that the world's power consumption can be adjusted accordingly. However, there are different solutions to ensure a steady and permanent energy supply for everyone independent of the location and the time of day. One solution can be the launch of backup power plants that need to be able to perform rapid run-up and shut-down cycles to compensate for the off-time of the renewable energy system, which also means that almost twice the needed power capacity needs to be installed and serviced.^{[8], [9]} Alternatively, with a suitable energy storage solution the installation of additional power plants can be prevented. This energy storage solution requires a buildup of large amounts of renewable energy sources so that their overproduction during run-time can be stored to bridge any power shortages from their discontinuity. Some of these bridging solutions are already in use but do not yet feature the necessary storage capacities. So far, they are mostly used to stabilize the grid.^{[8]–[10]} To be able to provide a stable power supply system, most often a storage solution for at least two weeks is assumed, but according to the annual production of renewable energy systems, even a storage solution across the seasons should be implemented.^[11] So far, only pumped water storage and power-to-gas applications are promising solutions for large-scale energy storage capacities over longer periods (cf. **Figure 1.0.2**).^{[9], [10], [12]} Pumped storages have the disadvantage that they require certain geographical conditions to be able to use the potential energy differences to store energy. Additionally, large areas of the landscape have to be occupied to build such storage systems.^[10] Whereas, the tanks for the storage of power-to-gas applications could be placed subterraneously, leading to a low footprint.^[10]

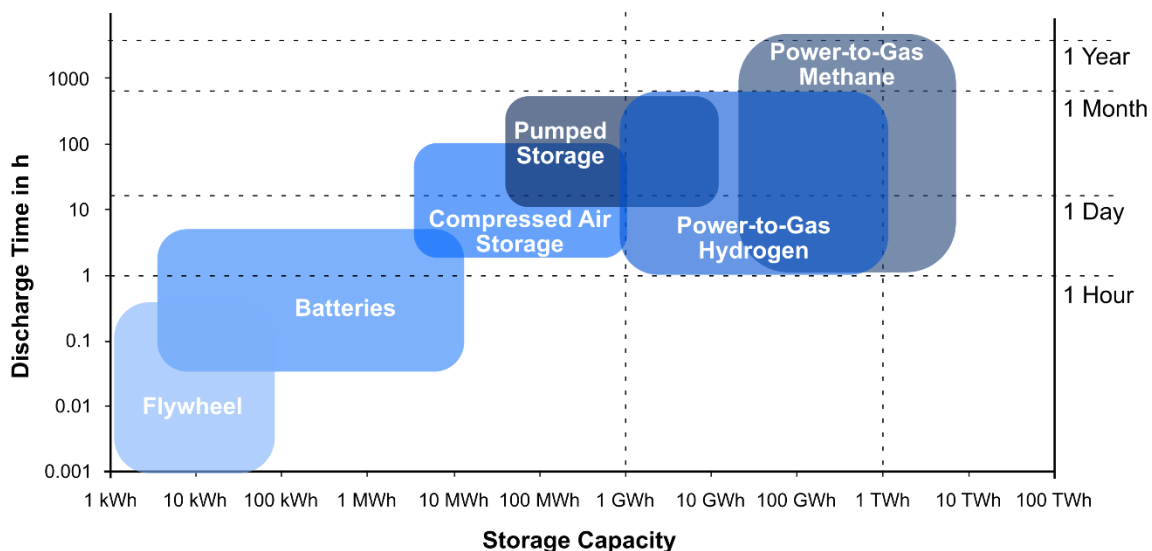
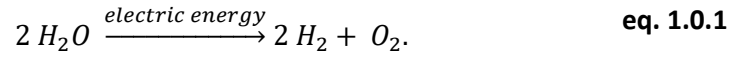
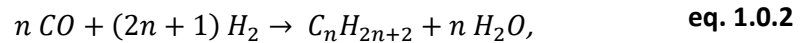


Figure 1.0.2: Comparison of different energy storage solutions in terms of storage capacity and discharge time. Adapted and modified from ^{[12], [13]}.

Power-to-gas applications are chemical energy storage systems. The basic principle is to transform a chemical reactant with an energetically uphill reaction into a fuel.^[14] Consequently, the reaction requires energy from renewable energy sources to drive the reaction. Once needed, the reverse reaction can be initiated, releasing part of the previously stored energy, which can be inserted into the grid. The straightforward reaction for a power-to-gas application would be the electrolysis of water into hydrogen and oxygen, according to



During the charging process with renewable energy, hydrogen and oxygen are produced inside an electrolyzer. The produced hydrogen is compressed and can be stored in salt caverns or special tanks.^[10] If the renewable energy production stagnates the hydrogen can be used to drive combustion turbines or fuel cells to generate electricity, which then is supplied into the grid. Alternatively, the hydrogen can be used as a reactant in the Fischer-Tropsch reaction, according to



in order to produce hydrocarbons, which offer higher energy densities.^[15] Wherever energy densities are insignificant, hydrogen possesses advantages in comparison to hydrocarbons. It exhibits lower transformation losses and the direct conversion to electrical power via fuel cells is possible.^{[10], [14]} Also, the combustion of hydrogen is a clean process, which neither produces greenhouse gases nor hazardous compounds and only leads to the formation of water as the end product. Nowadays, the electrolysis of water can be processed by three technologically practicable methods: the alkaline (AE) the proton exchange membrane (PEM – acidic), and the high-temperature electrolysis (HTE).^{[8]–[10], [14]} For each of these systems the life cycle and the efficiency have to be optimized separately, as well as the development of new cost-efficient and abundant catalyst materials. Consequently, fundamental research is necessary to detect new materials and investigate their applicability for the electrochemical water splitting reaction. Generally, two electrodes are needed to split water into hydrogen and oxygen. At the anode, the oxygen evolution reaction (OER) takes place whereas hydrogen is produced at the cathode. To ensure an efficient overall water splitting reaction, both reaction sides have to be optimized for specific environmental conditions.

The following thesis is focused on the preparation, investigation, and optimization of suitable catalyst materials for the anodic reaction side (OER) in alkaline media. So far, the most common catalysts used for the OER in acidic electrolytes are noble metal catalysts consisting of IrO_x, RuO_x, and PtO_x. These materials are rarely available in the earth's crust (*cf.* **Figure 1.0.3**) and, consequently, are regarded as critical resources with high costs.^[16] The utilization of alkaline electrolytes for the water splitting process enables other possible transition metals and their compounds to be used as catalyst materials. In this context, mainly the first-row transition

metals *e.g.*, cobalt, iron, nickel, and manganese, and their respective compounds are materials of interest. These materials can be found in higher concentrations in the earth's crust (*cf.* **Figure 1.0.3**) and are stable in alkaline electrolytes.^{[17]–[19]}

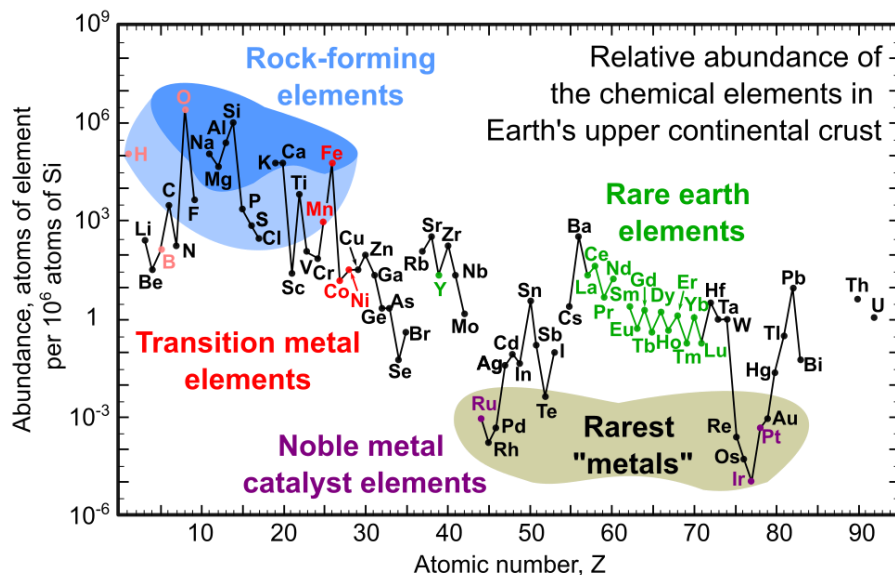
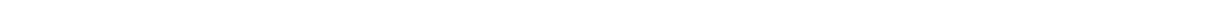


Figure 1.0.3: Abundance (atomic fraction) of the chemical elements in Earth's upper continental crust as a function of atomic numbers Z . Many of the elements are classified as rock-forming elements in blue, rarest metals in beige, and rare earth elements in green. Additionally, the noble metal catalyst elements are shown in purple and the transition metal elements which are used in this work to replace rarest metals are marked in red. Further elements used in this work are marked in light red. Adapted and modified from ^[20].

For quite some time now, manganese-based oxides have been in the scope of environmental research fields since manganese is known to be a working OER catalyst in the world of plants. In the photosystem II (PS II), manganese clusters ($\text{Mn}_4\text{O}_5\text{Ca}$) function as oxygen-evolving centers and reduce water in four consecutive steps by using the power of the sun.^{[21]–[25]} Accordingly, one objective of the OER research is to better understand the oxygen-evolving process of plants and to develop manganese-based catalysts for the OER.^[26] In the first part of this work (*cf.* **Section 3**), different manganese oxides are investigated for their applicability as thin-film electrocatalysts for the OER. The focus of the project is the activity and stability of manganese oxide in alkaline electrolytes. Simultaneously, general aspects of electrochemical water splitting are investigated concerning the significance of the interface between the substrate and the catalytic overlayer on the efficiency of the manganese oxide.

Alongside the comprehension of already known catalyst systems, the detection of new up-and-coming catalysts is crucial to explore materials that offer a perfect balance between performance, stability, and cost. Consequently, more and more different material families, like sulfides,^{[27], [28]} carbides,^[29] nitrides,^{[29]–[31]} phosphides,^{[27], [29]} and borides of transition

metals^{[29], [32]} are investigated as catalysts for the OER and the hydrogen evolution reaction (HER). In the second part of this work (*cf.* **Section 4**), powdered transition metal (M) borides (M_2B and M_3B) with cobalt, nickel, and iron are investigated for their applicability for the OER and HER. Accordingly, dicobalt boride (Co_2B) is used as the starting material and is mixed with iron and nickel to form the ternary compounds $(Co_{1-x}Fe_x)_2B$ and $(Co_{1-x}Ni_x)_2B$ with $0 \leq x \leq 0.5$. This work focuses on the electrochemical properties of these materials and their changes under operation conditions.



2 Fundamentals

In the first part of this chapter, an introduction to the basic concepts of electrochemistry (*cf.* **Section 2.1**) and electrochemical (EC) catalysis (*cf.* **Section 2.2** and **Section 2.3**) is given. The second part deals with the underlying principles of photoelectron spectroscopy methods (*cf.* **Section 2.4**), technical insights into the used measurement system at the DAISY-FUN (*Darmstädter Integriertes System für fundamentale Untersuchungen*).

2.1 Electrochemistry

Electrochemistry describes the correlation of a chemical redox reaction with the flow of an electrical current. Two fundamental electrochemical processes can be discriminated:

- (1) Electrolysis: The chemical reaction is driven by an applied external potential (*e.g.* water splitting)
- (2) Galvanic element: A chemical reaction of two suitable materials generates a usable external electrical current (*e.g.* battery)

In equilibrium, EC reactions are reversible including a transfer of a certain amount n of electrons ($n \cdot e^-$) between a redox couple (Red/Ox). Thus, they can be separated into two half-reactions:

The cathodic reduction reaction



and the anodic oxidation reaction



In an EC cell, the investigation of a single half-cell reaction can be achieved by a three-electrode setup (*cf.* **Figure 2.1.1**). In a three-electrode setup, the current is measured between the counter electrode (CE) and the working electrode (WE), while the potential is measured between the working electrode (WE) and the reference electrode (RE). REs are based on specific redox systems with constant concentrations of the active redox couple, which possess stable and well-known potentials, and are easy to handle. A summary of common REs and their related potentials is given in **Table 2.1.1**. The oxidation of an EC redox reaction takes place at the anode and the reduction at the cathode. Each half-cell of a redox couple exhibits a characteristic potential, the redox potential E_{redox} . It is defined in a thermodynamic state of equilibrium, meaning that the forward and backward reaction takes place at the same rate. A tabulated form of common redox couples and their related equilibrium potentials (E_{redox}^0) is known as the EC series, which

is only valid for standard conditions (temperature $T = 298.15$ K, pressure $p = 1$ atm, and effective concentrations of 1 M L^{-1} of each aqueous species) and is related to a specific potential scale defined by the standard hydrogen electrode¹ (SHE).

PECC-2 Zahner cell

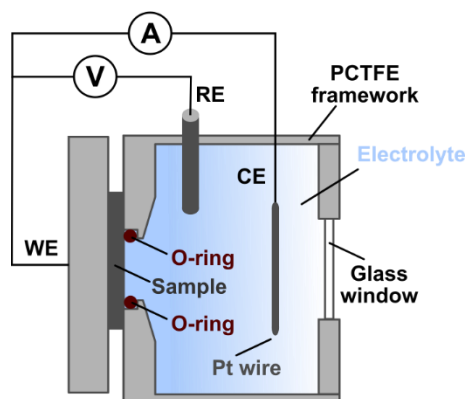


Figure 2.1.1: Schematic representation of a three-electrode setup on the basis of a PECC-2 Zahner cell (Zahner Elektrik GmbH & Co. KG). The current flow is measured between the counter electrode (CE – Platinum wire) and the working electrode (WE – sample). The potential is measured between the WE and the reference electrode (RE – mercury/mercury oxide).

Table 2.1.1: Common reference electrodes and their potential relation to each other. The given electrode potentials are valid for standard conditions with a temperature T of 298.15 K, a pressure p of 1 atm, and effective concentrations of 1 M L^{-1} of each aqueous species.

Reference electrodes		Electrode potential relations to each other	
Standard hydrogen electrode	(SHE)	$E_{\text{SHE}} = 0 \text{ V}$	activity of H^+ is 1 M
Normal hydrogen electrode	(NHE)	$E_{\text{SHE}} \approx E_{\text{NHE}}$	concentration of H^+ is 1 M
Mercury oxide (1 M NaOH)	(Hg/HgO)	$E_{\text{SHE}} = E_{\text{Hg/HgO}}$	+ 0.140 V
Silver chloride (3 M KCl)	(Ag/AgCl)	$E_{\text{SHE}} = E_{\text{Ag/AgCl}}$	+ 0.210 V
Reversible hydrogen electrode	(RHE)	$E_{\text{SHE}} = E_{\text{RHE}}$	+ 0.059 V · pH

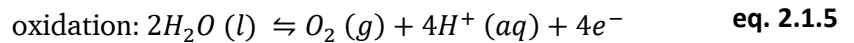
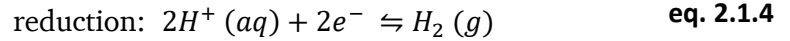
The SHE potential of the $2\text{H}^+(\text{aq.}) + 2e^- \rightleftharpoons \text{H}_2$ reaction has been defined to be equal 0.0 V. The deviation from standard conditions of these equilibrium redox potentials for simple reactions can be calculated by the Nernst equation

¹ The reference electrode SHE consists of a platinised platinum sheet immersed in an aqueous solution of unit activity of H^+ in contact with hydrogen gas ($p=1 \text{ atm}$)^[33]

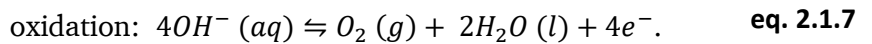
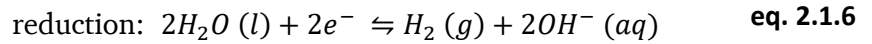
$$E_{Redox} = E^0_{redox} + \frac{RT}{zF} \cdot \ln\left(\frac{a_{Ox}}{a_{Red}}\right), \quad \text{eq. 2.1.3}$$

in which E^0_{redox} is the redox potential under standard conditions, T is the temperature, z is the number of electrons transferred in the reaction, R is the gas constant, F is the Faraday constant, and a_{Ox} and a_{Red} are the activities of the oxidized and reduced species, respectively.

In the water-splitting reaction, two redox couples must be considered, the H_2/H^+ and H_2O/O_2 . For these redox couples in acidic aqueous electrolyte, the half-reactions are



and in alkaline aqueous electrolyte



Thermodynamically, the half-cell reactions of **Equation 2.1.4** to **Equation 2.1.7** take place at specific potentials related to the H_2/H^+ redox potential of the SHE:

$$E^0_{redox} (H^+ / H_2) \equiv 0.00 \text{ V (activity} = 1; \text{ pH} = 0)$$

$$E^0_{redox} (H_2O / O_2) = 1.23 \text{ V (activity} = 1; \text{ pH} = 0)$$

$$E^0_{redox} (H_2O / H_2) = -0.83 \text{ V (activity} = 1; \text{ pH} = 14)$$

$$E^0_{redox} (OH^- / O_2) = 0.40 \text{ V (activity} = 1; \text{ pH} = 14)$$

The minimum applied potential needed for the water-splitting reaction is defined by the potential difference of the two occurring half cells according to

$$\begin{aligned} \Delta E_{Redox} &= E^0_{redox} (H_2O / O_2) - E^0_{redox} (H^+ / H_2) \\ &= 1.23 \text{ V.} \end{aligned} \quad \text{eq. 2.1.8}$$

2.1.1 Electrochemical double-layer

When a metal electrode is brought into contact with an electrolyte an EC double-layer is formed at the interface between the solid electrode and the liquid electrolyte. The simplest model of the EC double-layer is the compact double-layer, in which a layer of either positive or negative charged solvated ions forms a compact layer on top of the oppositely charged electrode. The so-called Helmholtz-layer acts as a capacitor with a plate distance of half of the diameter of the solvated ions.^[33] After the Helmholtz model of the double-layer, Gouy and Chapman were the first to consider that the ions in the electrolyte are affected by thermal motion and, thus, should

form a diffuse double-layer instead of a compact one. However, both of these models are not sufficient to describe the underlying physical processes on its own.^[34] Stern brought the two models together, pointing out that both ideas combined lead to the best description of the EC double-layer. Stern stated that the position of the Helmholtz plane will alter with the type of ion attached to the electrode surface. In **Figure 2.1.2** the combined model is shown schematically. Stern stated that some ions can be partially de-solvated and hold close to the surface by van-der-Waals-forces, whereas others remain within a distance to the surface, due to their solvation shells. These two types of ions define the inner- and outer Helmholtz plane. Behind the outer Helmholtz plane, the diffuse double-layer is formed by an excess of ions of the opposite charge of the electrode.^[33]

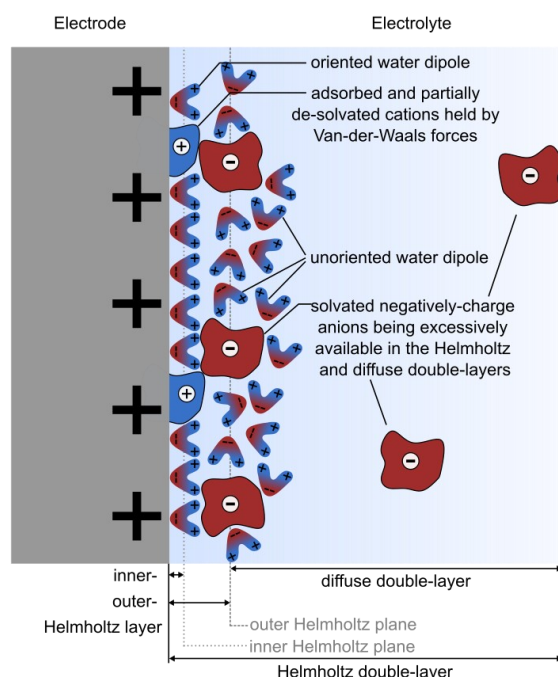


Figure 2.1.2: Schematic representation of the electrochemical double-layer formation between a positively charged electrode and an electrolyte. The water dipoles of the electrolyte are oriented near the electrode/electrolyte interface forming together with partially de-solvated cations the inner Helmholtz plane, while the excessively available solvated negatively charged anions form with unoriented water dipoles the outer Helmholtz plane. Behind the two planes, excessively available solvated anions are distributed along the diffuse double-layer. Adapted and modified from ^[33].

2.1.2 Transition state theory

Consider a chemical reaction of the form $A + B \rightleftharpoons \text{products}$. In the theory of the activated complex, the reaction between the educts A and B is displayed as crossing through an activated complex (AB^*) which represents the equilibrium between the forward and backward reaction. The reaction rate constant k of the forward (k_f) or backward (k_b) reaction shows an Arrhenius dependency (cf. **Figure 2.1.3a**) of

$$k_{f/b} = k_{f/b}^0 \exp\left(-\frac{\Delta G_{f/b}^{*0}}{RT}\right), \quad \text{eq. 2.1.9}$$

in which T is the temperature, R is the gas constant, k^0 is the probability factor, and ΔG^{*0} the Gibbs free energy activation barrier height. Indices f and b distinguish the forward and backward reaction, respectively. Correspondingly, the total reaction rate

$$v = c_A c_B k_{f/b} = c_A c_B k_{f/b}^0 \exp\left(-\frac{\Delta G_{f/b}^{*0}}{RT}\right) \quad \text{eq. 2.1.10}$$

depends on $k_{f/b}$ and the concentrations of the educts c_A and c_B . In an EC reaction, the theory of the activated complex can be considered for the transfer of electrons from a metal electrode across the Helmholtz double-layer (where the activated complex is formed) to a redox species inside the electrolyte solution (cf. **Figure 2.1.3a**). The potential difference between the metal electrode ($\varphi_{Me^0,eq}$) and the electrolyte (φ_L) without an applied potential is given by

$$\Delta\varphi_{eq.} = \varphi_{Me^0,eq} - \varphi_L. \quad \text{eq. 2.1.11}$$

If an external potential η is applied to the electrode, the Gibbs free energy change ΔG of that electrode is correlated with

$$\Delta G = -z \cdot F \cdot \eta, \quad \text{eq. 2.1.12}$$

where F is the Faraday constant and z gives the number of moles of electrons. Thus, if an external potential η is applied to the electrode (cf. **Figure 2.1.3b**) according to

$$\eta = \varphi_{Me^1} - \varphi_{Me^0,eq}, \quad \text{eq. 2.1.13}$$

the potential energy of the electrons at the electrode $G(\varphi_{Me^0,eq})$ is affected by the applied potential change with

$$\Delta G(\varphi_{Me^1}) = G(\varphi_{Me^0,eq}) + z \cdot F \cdot \eta. \quad \text{eq. 2.1.14}$$

In contrast to that, the potential energy of the redox species ($G_{Me^{2+}^0}$) in the electrolyte will not be influenced by an external potential since the redox species are not adsorbed on the electrode surface. The barrier heights for the formation of the activated complex for the forward ΔG_f^{*1} and backward ΔG_b^{*1} reaction with an externally applied potential vary with the linear potential change across the Helmholtz double-layer² (cf. **Figure 2.1.3b**). Thus, they depend on the position inside the Helmholtz double-layer at which the activated complex is formed. This position can adopt values between zero and unity and is defined as the charge transfer coefficient³ α .

² The linear potential decrease is considered for the simplest case of the Helmholtz double-layer model inside the compact layer.

³ In literature, the charge transfer coefficient is either defined as α (starting the distance from the electrode) or as β (starting the distance from the electrolyte), with $\alpha = (1-\beta)$.^{[33][34]}

Thus, the potential energy needed for the formation of the activated complex of the forward reaction can be determined with

$$\Delta\varphi = \Delta\varphi_{eq.} + \eta \quad \text{eq. 2.1.15}$$

to

$$\Delta G_f^{*1} = \Delta G_f^{*0} - \alpha \cdot z \cdot F \cdot \Delta\varphi \quad \text{eq. 2.1.16}$$

and for the backward reaction to

$$\Delta G_b^{*1} = \Delta G_b^{*0} + (1 - \alpha) \cdot z \cdot F \cdot \Delta\varphi. \quad \text{eq. 2.1.17}$$

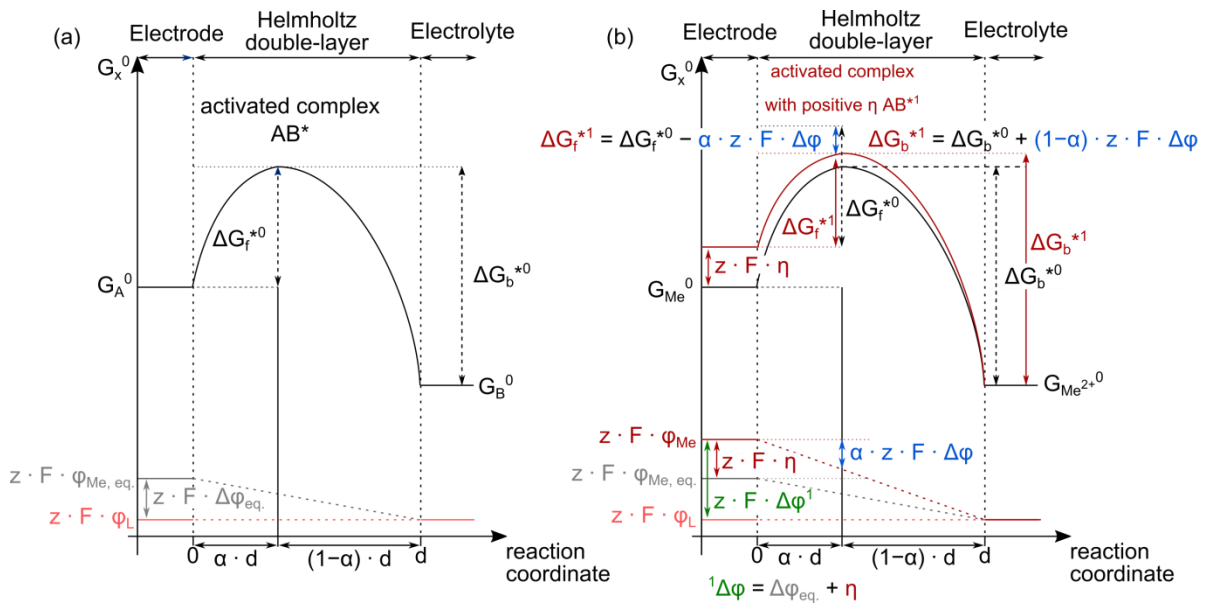


Figure 2.1.3: Schematic pictures of the activated complex theory in combination with the Helmholtz double-layer. The x-axis shows the reaction coordinate and the y-axis the Gibbs free energy G_x^0 . **(a)** General illustration of a metal electrode (G_A^0) in contact with an electrolyte (G_B^0) with the required energies ΔG_f^{*0} and ΔG_b^{*0} to form the activated complex AB^* from the forward and backward reaction, respectively. The forward reaction is favored without an applied bias since $\Delta G_f^{*0} < \Delta G_b^{*0}$. The potential difference between the electrode ($\varphi_{Me,eq.}$) and the electrolyte (φ_L) decreases across the Helmholtz double-layer linearly according to the simple Helmholtz double-layer model.^[33] **(b)** The energy for the formation of the active complex AB^{*1} changes with an applied negative overpotential η from ΔG_f^{*0} and ΔG_b^{*0} to ΔG_f^{*1} and ΔG_b^{*1} according to the depicted equations. The barrier height for the forward reaction gets reduced by the applied overpotential η and the value of the charge transfer coefficient α . From the evaluated dependencies, the Butler-Volmer equation can be derived.

Equation 2.1.15, **Equation 2.1.16**, and **Equation 2.1.10** can be used to determine the overall reaction rate, which can be given with the current density of the forward (or anodic)

$$j^+(\varphi) = -z \cdot F \cdot c_A k_f^0 \exp\left(-\frac{\Delta G_f^{*1}}{RT}\right) \quad \text{eq. 2.1.18}$$

and backward (or cathodic)

$$j^-(\varphi) = -z \cdot F \cdot c_A k_b^0 \exp\left(-\frac{\Delta G_b^{*1}}{RT}\right) \quad \text{eq. 2.1.19}$$

reaction. These anodic and cathodic values describe two partial current densities of different algebraic signs at each potential φ . If the actual electrode potential φ is given by $\varphi = \varphi_r + \eta$, in which η is the overpotential and φ_r is the rest potential at which

$$j^+(\varphi_r) = +j_0 \text{ and } -j^-(\varphi_r) = -j_0 \quad \text{eq. 2.1.20}$$

is valid, then **Equation 2.1.15** and **Equation 2.1.16** change to

$$j^+(\eta) = j_0 \cdot \exp\left(\frac{\alpha \cdot z \cdot F \cdot \eta}{RT}\right) \quad \text{eq. 2.1.21}$$

$$j^-(\eta) = -j_0 \cdot \exp\left(-\frac{(1-\alpha) \cdot z \cdot F \cdot \eta}{RT}\right), \quad \text{eq. 2.1.22}$$

with j_0 being the exchange current density. The anodic and cathodic current densities can be combined with the total net current $j(\eta)$ forming the Butler-Volmer equation:

$$j(\eta) = j^- + j^+ = j_0 \left[\exp\left(\frac{\alpha \cdot z \cdot F \cdot \eta}{RT}\right) - \exp\left(-\frac{(1-\alpha) \cdot z \cdot F \cdot \eta}{RT}\right) \right]. \quad \text{eq. 2.1.23}$$

For large enough anodic or cathodic overpotential (typically $\eta > 100$ mV), one of the exponential terms becomes dominant and the other one can be neglected, forming the anodic (*cf.* **Equation 2.1.21**) and the cathodic current part (*cf.* **Equation 2.1.22**) of the Butler-Volmer equation. If these equations are brought into the form of $\eta = a + b \ln(j)$, the Tafel equations for the anodic and cathodic regime are obtained:

$$\text{anodic: } \eta = -\frac{RT}{\alpha \cdot z \cdot F} \ln(j_0) + \frac{RT}{\alpha \cdot z \cdot F} \ln(j^+) \quad \text{eq. 2.1.24}$$

$$\text{cathodic: } \eta = \frac{RT}{(1-\alpha) \cdot z \cdot F} \ln(j_0) - \frac{RT}{(1-\alpha) \cdot z \cdot F} \ln(j^-). \quad \text{eq. 2.1.25}$$

The Tafel equation is often used to experimentally determine the exchange current density j_0 and the Tafel slope of metal electrodes. It must be kept in mind that the Butler-Volmer equation is only a model approach, which is valid for one-electron transfer processes only. Additionally, this model is neither considering tunneling of electrons through energetic barriers nor electronic states of intermediate adsorbates, which are formed during each of the half-cell reactions of the water-splitting process.^[33]

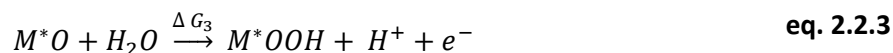
2.2 Oxygen evolution reaction on ternary systems

The overall water splitting reaction is defined by the combination of the two half-cell reactions given in **Equation 2.1.4** to **Equation 2.1.7** for an acidic and an alkaline environment. Whereas for the HER a two-electron transfer and one intermediate reaction step are needed, the OER requires a four-electron transfer and three intermediate reaction steps to form the gaseous product, leading to a larger overpotential for the reaction.

Developing effective catalysts to support the bond-making or bond-breaking reactions which occur at the interface between electrode and electrolyte, is a decisive criterion for improving the efficiency of the OER.^[35] Since 2007, density functional theory-based (DFT) simulations of the electronic structure of catalyst surfaces have yielded insights into the reaction pathway of the OER and have identified new OER descriptors which indicate material properties that an ideal catalyst for the OER should provide.^{[36]–[38]} These properties could be achieved by structural modifications or by a combination of certain elements to ensure improved catalytic activity of the compound.^[37] The DFT approach allows an investigation of surface properties during OER which cannot be easily addressed by experimental methods, due to the short lifetime of intermediates and harsh reaction conditions at the interface between catalyst and electrolyte.^[39]

2.2.1 The potential-determining step

Extensive computational research targeting the OER has been done by Rossmeisl and Norskov *et al.* in the past. Their research led to the development of an effective DFT method to model the thermochemistry of EC reactions. For the application to the OER, they considered the following associative reaction mechanism for most metal surfaces (M^*) with adsorbed intermediate:^[36]



This reaction mechanism was developed for acidic conditions. However, the thermodynamic considerations are independent of pH as the free energies deduced from the above equations vary in the same way with pH.^[40] The Gibbs free energies of adsorption ΔG_i (*cf.* **Equation 2.2.5**) for each individual reaction step ΔG_{MOH} , ΔG_{MO} , and ΔG_{MOOH} are calculated by the difference in the adsorption energies of the two intermediates (*IM*) at a certain potential ($q \cdot V$):^[39]

$$\Delta G_i = \Delta G_{IM2} - \Delta G_{IM1} - q \cdot V. \quad \text{eq. 2.2.5}$$

Thus, each individual reaction step of the OER can be calculated for a certain material by using the difference in the adsorption energies of the two intermediates. By calculating each reaction step for a certain catalyst, a diagram can be constructed that displays information about the rate determining step.

The Gibbs free energy of reaction pathways plotted versus the reaction coordinate for an ideal and a virtual real catalyst with different overpotentials are depicted in a so-called free energy diagram in **Figure 2.2.1**.^[41]

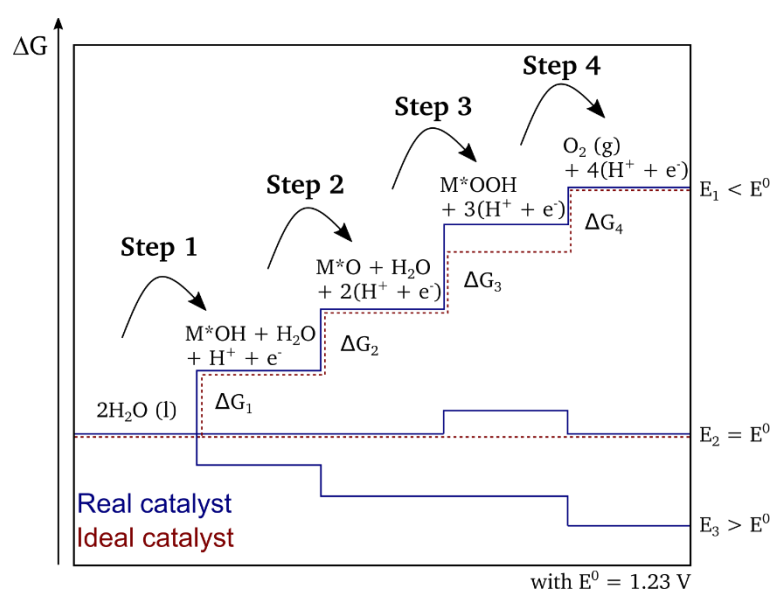


Figure 2.2.1: Schematic energy diagram for the associative reaction pathway showing the Gibbs free energy of the reactive species and the intermediates of the OER versus the reaction coordinate for three different overpotentials E_1 , E_2 , and E_3 in relation to $E^0 = 1.23$ V). The dotted red lines illustrate the energetic transitions of an ideal catalyst (with $\Delta G_1 = \Delta G_2 = \Delta G_3 = \Delta G_4$), while the solid blue lines indicate the energetics of a real catalyst (with $\Delta G_3 > \Delta G_1 = \Delta G_2 > \Delta G_4$) at the overpotentials E_1 , E_2 , and E_3 . Due to equivalent energy steps of the ideal catalyst, the OER can proceed at a lower overpotential (at $E_2 = E^0$) than the real catalyst. The real catalyst requires higher potentials (E_3) to drive the OER, due to the rate-limiting step of the M^*OOH intermediate. Adapted and modified from ^[41].

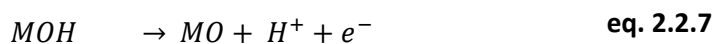
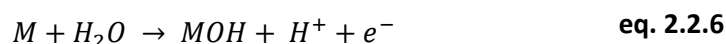
The energetic transitions for the real catalyst are given with $\Delta G_3 > \Delta G_1 = \Delta G_2 > \Delta G_4$. All steps are thermodynamically unfavorable at a potential below the reversible potential ($E^0 = 1.23$ V vs. RHE) so that $E_1 - E^0 = \eta < 0$. With increasing potential ($E_2 - E^0 = \eta = 0$) the free energies of the individual steps become thermodynamically favorable. However, due to different ΔG_i values, also different potentials are required to make the reaction thermodynamically favorable. Therefore, the formation of the M^*OOH intermediate (step 3) is defined as the potential-determining step for the real catalyst. In contrast to this, an ideal catalyst shows four similar energy steps ($\Delta G_1 = \Delta G_2 = \Delta G_3 = \Delta G_4$) and, thus, all steps are already thermodynamically

favorable at the potential E_2 , leading to an overall lower overpotential.^{[37], [39], [41]} The approach by Rossmeisl and Norskov accounts for the thermochemistry of the individual reaction steps with the approximation, that each of these steps is thermodynamically favorable for the OER to proceed. If this is not the case, additional energy barriers must be considered. The highest of those barriers indicates the rate-determining step.^[39] According to the scaling relation expressed by Rossmeisl *et al.*^[39], the sum of energies which is required to form the intermediates $M\text{-}^*\text{O}$ and $M\text{-}^*\text{OOH}$ remains approximately the same.^{[37], [39], [42]} Hence, if the energy barrier forming the intermediate $M\text{-}^*\text{O}$ is low, the energy barrier to form the $M\text{-}^*\text{OOH}$ intermediate must correspondingly be higher and vice versa.^[37] While the mechanisms of single metal catalysts are well described by the scaling relations of adsorbed $^*\text{OH}$ and $^*\text{OOH}$,^{[36], [43]} the reaction mechanism and the synergetic effect of bimetallic systems are still in the focus of current research.

2.2.2 Synergetic effects

Multi-component catalyst systems are one promising research path to find new suitable catalyst systems for the OER and simultaneously improve the catalytic performance of state-of-the-art OER catalysts. With regard to the thermochemical model of Rossmeisl and Norskov^{[36], [43]} (cf. **Section 2.2.1**), a surface composition of two or more different metals may be advantageous. The first metal may be ideal to form the $M\text{-}^*\text{O}$ intermediate while the second metal may be ideal to form the $M\text{-}^*\text{OOH}$ intermediate and, thus, sidestep the scaling relation for single metal materials. This concept could give an idea why mixtures of different metals can be beneficial for the catalytic activity of mixed-metal compounds. While several combinations of two metals for the purpose of improving the OER performance have been tested,^{[44], [45], [54], [46]–[53]} two examples shall be highlighted:

One relevant example for this work is formulated in the publications of Gorlin *et al.*^[55], El-Deab *et al.*^[56], and Mohammad *et al.*^[57], who found that manganese-based oxides show increased OER activity in the presence of gold. Another relevant mixed-metal system was calculated by Busch *et al.*^[58] for the reaction paths of Co and Fe, and the reaction path of the combination of CoFe. A binuclear reaction path (dissociative) was assumed, which is a similar reaction mechanism as the “Bockris electrochemical oxide path” (direct oxygen recombination) with the corresponding reactions:^{[39], [59], [60]}



In **Figure 2.2.2** the calculated stepwise dehydrogenation process for the Co, Fe, and CoFe catalyst are illustrated concerning the two primary steps in this mechanism, namely the oxidation of two M-*OH hydroxyl groups forming two M=*O oxo groups and the following μ -peroxo bond formation.^[58]

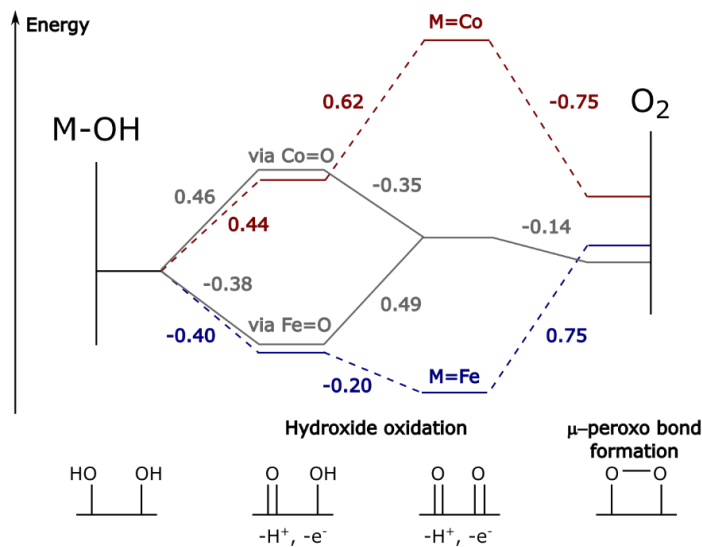


Figure 2.2.2: The reaction energetics for hydroxide oxidation ($2 \text{ M-OH} \rightarrow 2 \text{ M=O}$) and μ -peroxo bridge formation at the homo-binuclear iron (blue dashed) and Co (red dashed) sites and the hetero-binuclear FeCo (grey solid lines) sites, illustrating the stepwise dehydrogenation process. The energy values show exothermic and endothermic reactions and are given in eV. Adapted and modified from^[58].

Busch *et al.*^[58] showed that the choice of the transition metal is crucial for the enhancement in OER performance. Two classes of transition metals were identified: The M-O moieties in the Co phase (also Mn and Ni) have radical character, therefore their formation is endothermic. Secondly, the M=O bonds for the Fe phase (also Cr, V) are stable and the subsequent O-O formation is strongly endothermic. Both reaction pathways need higher overpotentials for the different reaction steps. Due to the mixing of the materials, first Fe=O and Co=O can be formed and the reactivity of the Co=O counteracts the inertness of the Fe=O that the formation of the di-hydroxo species is only slightly endothermic, while the subsequent μ -peroxo bond shows slightly exothermic behavior.^{[39], [58]} Additionally, the cobalt-iron oxide system was investigated by Burke *et al.*^[47], who showed experimentally that a certain amount of incorporated iron can increase the intrinsic OER activity of the CoOOH catalyst. In contrast to the theory of Busch *et al.*^[58], they attributed the increase in activity to a strong electronic interaction between the cobalt and the iron, since an anodic shift in the $\text{Co}^{2+/3+}$ redox couple has been detected.^[47] An analog shift has been found by Trotochaud *et al.*^[45] for the nickel-iron system. Again, the OER activity of the catalyst with incorporated iron has been increased compared to the single-metal NiOOH. In both cases, the redox wave shifts anodically, which implies that the iron hinders the cobalt and nickel centers to oxidize from a 2+ to a 3+ oxidation state.^{[45], [47]}

2.3 Determination of the electrochemical surface area

A precise determination of the electrochemical surface area (ECSA) of a catalytic system is neither a standardized procedure nor a straightforward method.^[61] The three most common ways to normalize the electrocatalytic activity of a catalyst system are presented in **Figure 2.3.1a** on the basis of a catalyst surface:^[35]

- (1) geometric activity given in $\text{mA cm}^{-2}_{\text{geom}}$ is defined by the current normalized to the geometric area of the electrode,
- (2) specific activity given in $\text{mA cm}^{-2}_{\text{catalyst}}$ is defined by the current per unit real surface area of the electrocatalyst, and
- (3) mass activity given in $\text{mA mg}^{-1}_{\text{catalyst}}$ is defined by the current per unit loading mass of the electrocatalyst.

The geometric normalization of a catalytic system is an easy way to normalize the activity of a catalyst. But the fact that not only the foremost atomic surface layer of the catalyst contributes to the catalytic activity, makes the normalization to a geometric area imprecise. The same is true for a specific surface area measured, for instance with an atomic force microscope.^[61] Consequently, the approach of the normalization onto a given loading mass of a catalyst seems the best approach. However, this method neither accounts for deeper regions inside the bulk of the catalyst nor for the bulk of larger sized nanoparticles, which do not contribute to the catalytic activity.^[61] One way to determine the specific activity of a catalytic system via an electrochemical approach is the determination of the ECSA by the differential capacitance approach.^{[33], [34], [62], [63]} This approach is based on the model of the EC double-layer which develops if an electrode is immersed into an electrolyte solution (*cf.* **Section 2.1**). This EC double-layer can be physically treated as a capacitor.^{[33], [34], [64], [65]} If a potential is applied onto the EC system, different types of reactions can occur at the surface of the electrode, including conversion reactions (*e.g.* oxidation or reduction of the electrode surface), corrosion reactions (*e.g.* dissolution of the catalyst), and catalytic reactions (*e.g.* HER or OER). These reactions occur by a transfer of electrons across the electrode/electrolyte interface, and thus, across the EC double-layer, which will change during these reactions. In a potential range at which no reactions occur, the ECSA can be determined. In **Figure 2.3.1b** a typical cyclic voltammogram (CV) of a nickel-containing electrode is shown. The potential areas at which redox reactions or catalytic reactions occur are marked in red, meaning that it is not possible to determine the ECSA there. The potential window suitable for the determination is marked in green. At this point, a constant current flow due to the charging and discharging of the EC double-layer can be measured.

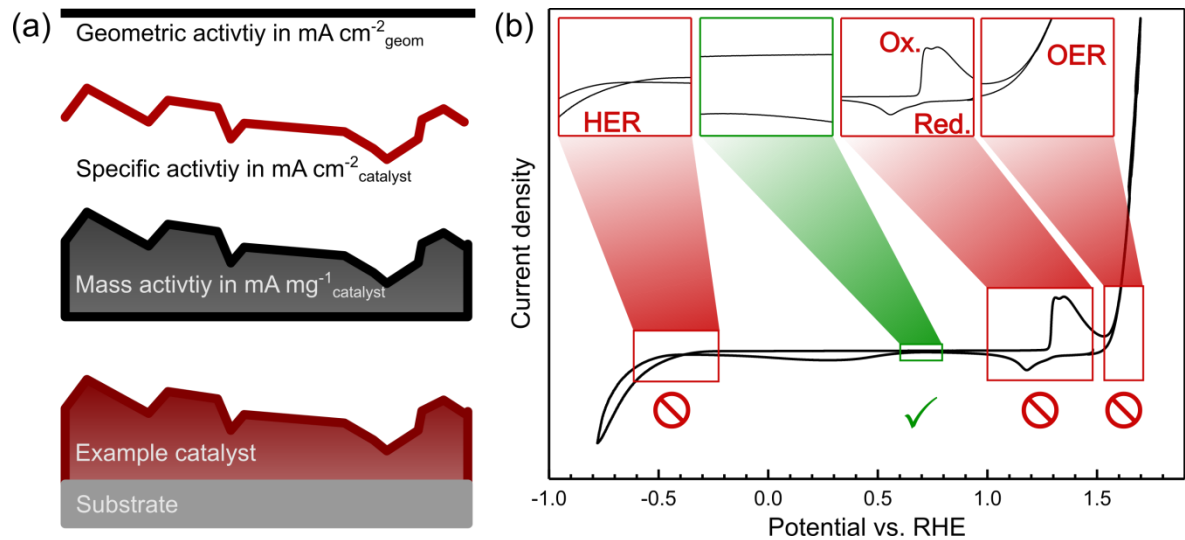


Figure 2.3.1: (a) Schematic representation of the different ways to normalize the activity of a catalytic system. Adapted and modified from [35]. (b) Representation of how to select a potential window for the determination of the electrochemical surface area (ECSA) by the fast sweep scan approach. A potential at which no chemical reaction occurs or rather the current density of the cyclic voltammogram (CV) curve shows symmetric values around 0 mA cm⁻² (cf. green area) must be chosen to determine the ECSA.

The differential double-layer capacitance C_{DS} can be described by

$$C_{DS} = \frac{dQ}{d\phi} \quad \text{eq. 2.3.1}$$

$$i = \frac{dQ(\phi)}{dt} \quad \text{eq. 2.3.2}$$

in which the current i depends on the charge Q at a potential ϕ over time t . If both equations are combined the differential double-layer capacitance C_{DS} can be determined by

$$i = C_{DS} \frac{d\phi}{dt}. \quad \text{eq. 2.3.3}$$

Consequently, the value of C_{DS} can be derived using a set of CVs with different scan rates. The set of resulting currents for the different scan rates at one specific potential of these CVs plotted against the scan rates results in a linear dependence of the two quantities. The slope of the linear regression is the C_{DS} . If the C_{DS} is normalized to the specific capacitance value C_s , which is valid for 1 cm² of the investigated material, the ECSA can be calculated to

$$ECSA = \frac{C_{DS}}{C_s}. \quad \text{eq. 2.3.4}$$

For the specific capacitance C_s , reference values of ideally flat surfaces of a comparable material are required.^[63] For example, McCrory *et al.*^[19] summarized some specific capacitance values of metal oxides to range between 22 and 130 $\mu\text{F cm}^{-2}$.

2.4 Photoelectron spectroscopy

Photoelectron spectroscopy (PES) is a feasible tool to directly investigate the electronic properties of surface-near regions of materials (< 10 nm).^[66] There are different PES methods⁴, which all have in common, that electrons from a sample are excited by photon irradiation. The illumination of the sample with photons of defined energy larger than the ionization energy causes the electrons to leave the sample with a remaining characteristic kinetic energy. This kinetic energy is used to analyze the chemical composition, oxidation states, and electronic structure of the sample.^[67] In this work, X-ray photoelectron spectroscopy (XPS) with a monochromatic Al K_{α} X-ray source (XR 50, SPECS Surface Nano Analysis GmbH) with a photon energy of 1486.74 eV was used as the illumination source. The XPS analyzer system is calibrated to the emission lines of copper, gold, and silver and it exhibits a measurement precision of ± 50 meV.

A schematic image of an XPS analysis setup is shown in **Figure 2.4.1**. The excited electrons pass through an electron lens system into a hemispherical analyzer (PHOIBOS 150, SPECS Surface Nano Analysis GmbH), in which they are retarded by a fixed analyzer transmission function and resolved by their kinetic energy. The electrons are detected with a set of channel electron multipliers. The ultra-high vacuum (UHV) conditions are used to reduce the inelastic scattering of the electrons and to avoid impurities and adsorbates.^[68]

The working principle of the XPS is based on the outer photoelectric effect. If a solid surface is irradiated with photons of energy $h\nu$, electrons can be excited and emitted from the sample when the photon energy is higher than the work function the electrons have to overcome to leave the sample.^[68] The emitted electrons possess then a kinetic energy E_{kin} , which correlates with the binding energy E_{bin} of the electron in its initial state, which can be calculated from

$$h\nu = E_{kin} + E_{bin}. \quad \text{eq. 2.4.1}$$

Elements can be identified due to their unique set of core level energies. The notation of such a core level line is given by the element, the main quantum number n , and the orbital angular momentum quantum number⁵ l , for example Ni $2p_{3/2}$ (cf. **Figure 2.4.2**).

⁴ X-ray photoelectron spectroscopy (XPS), Ultraviolet photoelectron spectroscopy (UPS), angle-resolved photo-emission spectroscopy (ARPES), and two-photon photoelectron (2PPE) spectroscopy.

⁵ The orbital angular momentum quantum number l is described by the letters s , p , d , and f for $l=0$, $l=1$, $l=2$, and $l=3$.

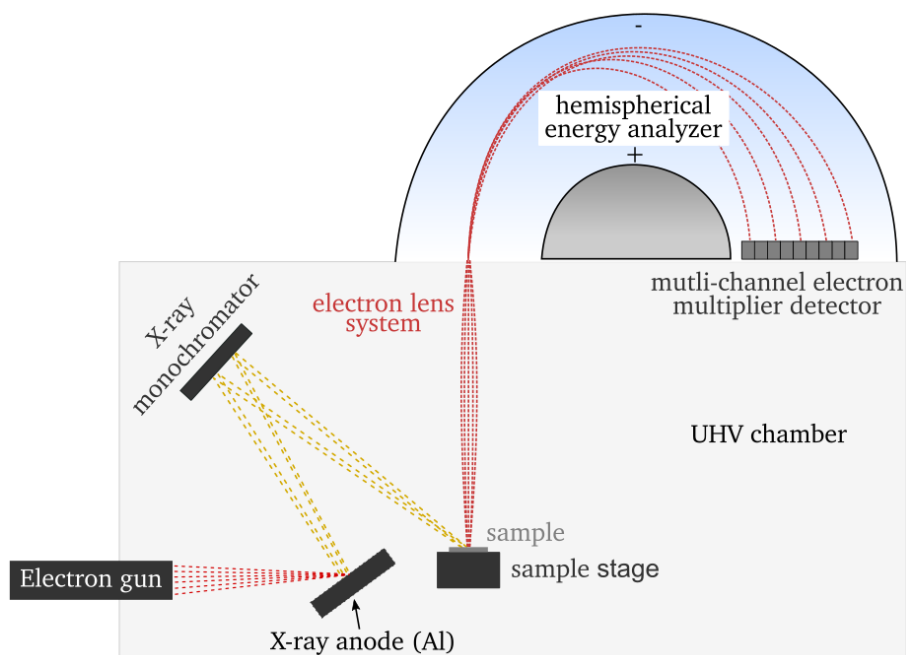


Figure 2.4.1: Schematic drawing of the XPS setup. From the X-ray anode (aluminum), the photons move through a monochromator before they reach the sample, releasing or emitting electrons out of surface-near regions. The electrons are focused by an electron lens system before they get energy-resolved in the hemispherical analyzer and detected by a multi-channel electron multiplier.

Photoelectrons, which experience an energy loss by inelastic collisions, contribute to the background signal of the XP spectrum.^{[68], [69]} A typical XP survey spectrum of a sputtered nickel foil with the corresponding electron processes is shown in **Figure 2.4.2**. The emission of core-level electrons is one of the main processes measured by XPS. The measured kinetic energies of those electrons carry information about the element and the nearest surrounding of the atom, which is defined by the bond type and bonding partners of the atom. Consequently, the electron density around the atom changes, which is reflected in the chemical shift of the core level lines.^{[66], [68]} A suitable example for the chemical shift in XPS is the C 1s photoemission line for polymeric functional groups. The E_{Bin} of the carbon components increases as the number of oxygen atoms bonded to carbon increases with $\text{C-C} < \text{C-O} < \text{C=O} < \text{O-C=O} < \text{O-(C=O)O-}$ since oxygen is more electronegative than carbon.^[70]

Auger electrons are another element specific emission measurable by XPS. Auger electrons originate from indirect excitation by a three-step process and their energetic positions are independent from the X-ray source.^{[66], [68]} Due to direct photon irradiation an electron is excited from an atomic shell (*i.e.* emission of core-level electron), leaving a vacancy behind. Another electron from a higher energy level falls into the vacancy, releasing the energy difference of the two energy levels. This energy can either be released as a photon or it can be transferred to another electron, the Auger electron. The notation for the Auger line is given by the element and the letters of the three corresponding energy levels.

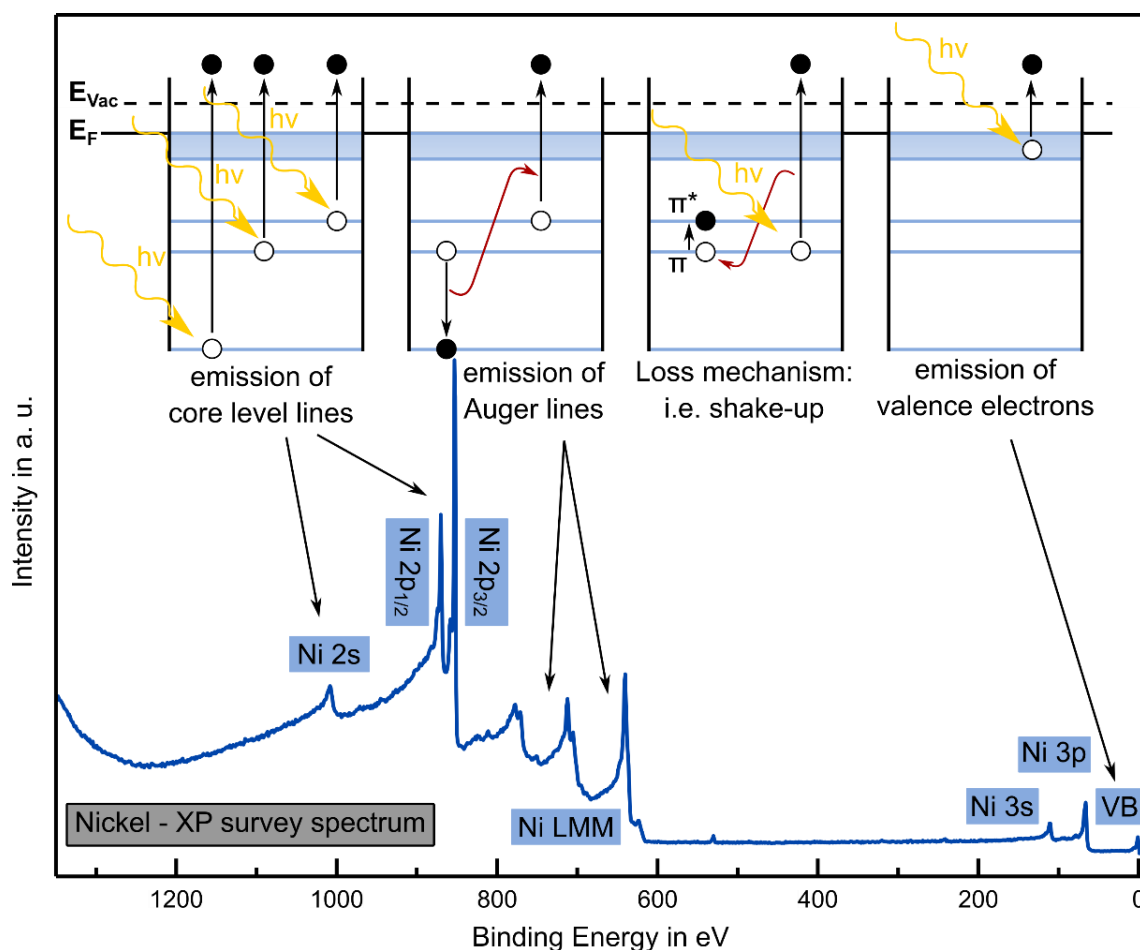


Figure 2.4.2: XP survey spectrum of a sputtered nickel foil with schematic images of the different electron excitation mechanisms due to photon irradiation and the origin of the characteristic emission lines as well as possible loss lines. The development of these signals is described in the text.

If the vacancy is located in the K -level and the electron falls down from the L -level and gives the energy to an Auger electron at the L -level, the Auger transition will be named KLL .^{[66], [68], [69]} Additionally, emissions from valence electrons can be detected, which reflect in first approximation the density of states in the valence band of the material.^[68] Besides these three main emission species, there are additional effects which can either lead to other emission lines or to changes in the above mentioned main emission species. One of these effects is the spin-orbit coupling (*cf.* **Figure 2.4.3**) which can occur for an orbital angular momentum of $l \geq 1$. The spin-orbit coupling results from a parallel or an antiparallel spin ($\pm \vec{s}$) of a core level electron to the orbital angular momentum ($\pm \vec{l}$). The total orbital angular momentum j is described by

$$j = |\vec{l} \pm \vec{s}|. \quad \text{eq. 2.4.2}$$

The difference in the total orbital angular momentum leads to an energy difference in the emission lines and, thus, to a splitting of the core levels. The spin-orbit coupling for the p , d , and f orbital is depicted in **Figure 2.4.3** with the respective area ratios of the emission lines. The intensities of the lines are given by their multiplicity ($I \propto 2j+1$).

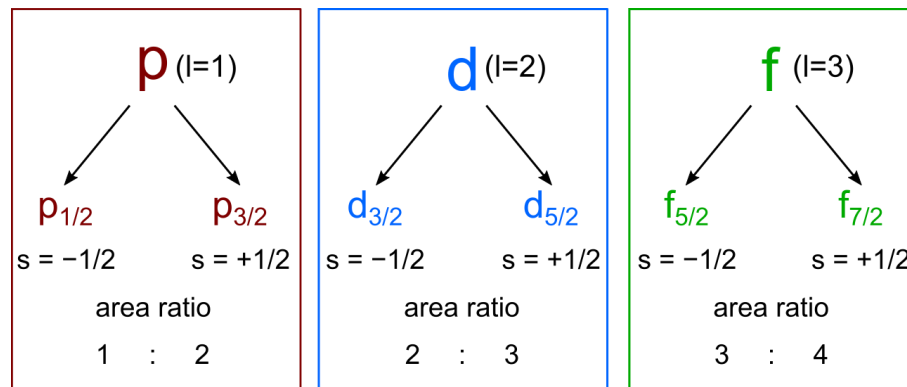


Figure 2.4.3: Spin-orbit coupling for the p , d , and f orbitals with the corresponding notation of the core levels and the related area ratios. The difference in the total orbital angular momentum leads to an energy difference in the emission lines and, thus, to a splitting of the core levels.

The complete notation of the spin-orbit coupled Ni 2p emission line is given by the Ni $2p_{3/2}$ and Ni $2p_{1/2}$ signal and is shown in **Figure 2.4.2**. Further emission lines can be generated by so-called shake-up (*cf.* **Figure 2.4.2**) and shake-off processes. Already excited photoelectrons transfer some of their kinetic energy to valence electrons inside the material. If the receiving electron gains enough energy to leave the sample, the process is called shake-off. If the receiving electron stays inside the material, the process is called shake-up. Both incidences lead to an intensity loss in the main core emission line and, simultaneously, to an additional emission line at lower kinetic energies or rather higher binding energies. The shake-up emission is a satellite line and can give information about the chemical bonding of the atom since a discrete kinetic energy loss occurs. This discrete energy loss is defined by the transition of a valence electron from an occupied to a higher unoccupied level (*e.g.* π to π^*). This effect is often observed for transition metals due to the partly unoccupied 3d band. In contrast to the shake-up process, the energy loss of the shake-off emission is undefined and contributes to the background of the spectrum.^{[67]–[69]}

Additionally, the final state effect can further change the core level lines of certain elements (*e.g.* cobalt). It is based on the relaxation of the excited electron, which can lead to a change in the charge carrier distribution inducing a variation of the core level lines. A prominent example is the oxidation states visible for the Co 2p photoemission line: Co^0 (778.2 eV) < Co^{3+} (779.6 eV) < Co^{2+} (780.5 eV).^{[66]–[68]}

2.4.1 Quantitative analysis

Besides the qualitative analysis of a compound, quantitative information of the composition of the surface can be collected with XPS. The elemental ratios can be estimated with the intensities of the respective core level emission lines, which are determined from the integrated intensities of the emission lines.^[71] The lower integration limit is given by the background. Additionally, the intensities measured for each element are influenced by spectrometer and material relevant factors, which are summarized in the relative sensitivity factors (RSF).^[72] These values are determined by the spectrometer manufacturer (*cf.* **Table 2.4.1**). The quotient of the intensity and the RSF value yields the relative concentrations of the different elements in the sample.^[71]

Table 2.4.1: Relative sensitivity factors (RSFs) of the relevant elemental photoemission lines for the performed quantitative analysis, given by the CasaXPS software.^[71]

	Mn 2p	Fe 2p	Co 2p	Ni 2p	S 2p	B 1s	C 1s	O 1s	F 1s
RSF	13.91	16.42	19.16	22.18	1.68	0.49	1.00	2.93	4.43

2.4.2 Determination of the film thickness

XPS enables the measurement of the layer thickness by the modification of the Lambert-Beer law, which describes the damping of light while passing through a medium.^[73] This can be transferred to electrons that pass through a thin layer. The layer thickness can be determined with the intensity of the substrate material line before and after the deposition of the thin layer. The layer thickness d_L of the thin film is calculated with

$$d_L = \lambda \cdot \ln\left(\frac{I_0}{I_L}\right) \cos(\beta), \quad \text{eq. 2.4.3}$$

in which λ is the inelastic mean free path length of the electrons (IMFP), β the incident angle of the electrons through the layer, I_0 the intensity of the substrate emission line, and I_L the intensity of the substrate emission line with a deposited layer of the thickness d_L . In the applied XPS system the incident angle β of the electrons is 0° , which leads to multiplication with unity. The IMFP depends on the energy of the electron and the penetrated material. In 1979, Seah and Dench^[74] provided a review on IMFP values and examined an underlying formula of the fitted data, leading to IMFP values λ_A for electrons with a kinetic energy E_{kin} according to

$$\lambda_A(E_{kin}) = \frac{143}{E_{kin}^2} + 0.054 \cdot E_{kin}^{1/2}. \quad \text{eq. 2.4.4}$$

The IMFP values for the relevant photoemission lines and substrates are given in **Table 2.4.2** and were calculated by the NIST⁶ standard reference database with the Gries-method⁷ using the expected density of the phase und the corresponding photoemission line of the substrate.^{[75], [76]}

Table 2.4.2: Inelastic mean free path length λ values of the C 1s, Au 4d, Ti 2p, and Fe 2p emission for the determination of the layer thickness of manganese oxide with the Gries-method.^[76]

	E_{Bin}	$\lambda \text{ MnO}$	$\lambda \text{ Mn}_2\text{O}_3$
C 1s	285 eV	7.8 Å	8.9 Å
Au 4d	335 eV	8.6 Å	9.9 Å
Ti 2p	458 eV	10.6 Å	12.1 Å
Fe 2p	710 eV	14.5 Å	16.5 Å

⁶ National institute of standards and technology of the U.S. Department of Commerce.

⁷ A method for the calculation of the inelastic mean free path (IMFP) for any known sample composition without detailed information about the physical properties of the sample (*e.g.* band gap).

Part A

Plasma enhanced chemical vapor deposition of manganese oxide thin films for the OER

3 Manganese oxide for the oxygen evolution reaction

The first part of the experiments presented in this work is motivated by the PS II, which is the light-driven oxygen evolution part of the overall photosynthesis system used by nature.

In this study, manganese oxide thin films were deposited via a plasma-enhanced chemical vapor deposition (PE-CVD) reactor (*cf.* **Section 3.3.2**) onto titanium (Ti) substrates to identify the potential manganese oxide phases and to clarify the limitations of the used deposition process (*cf.* **Section 3.4**). Subsequently, the selected process parameters were used to deposit manganese oxides thin films onto four other substrates: glass-like carbon (GC), highly oriented pyrolytic graphite (HOPG), stainless-steel (SS), and indium doped tin oxide (ITO) with a sputtered gold overlayer (*cf.* **Section 3.5**).

Additionally, the EC performance towards the OER of the manganese oxide thin film catalysts is monitored, as well as the changes happening during this EC investigation on the surface of the catalysts. These changes are monitored with XPS in each of these sections.

3.1 Material perspective: Manganese oxides

Manganese is one of the most abundant elements in the earth's crust and can be found in many different minerals. Manganese has been found in oxidation states between 3- to 7+ among which the oxidation states 2+, 3+, and 4+ are the most common. More than 30 unique minerals have been discovered consisting of manganese oxide and/or hydroxides.^{[77]–[79]} Different types of manganese oxides can form several structure types, which are mostly based on an MnO₆ octahedral building block.^{[78], [80]} The MnO₆ octahedral structure (*cf.* **Figure 3.1.1**) contains O²⁻ ions, which are octahedrally coordinated around the central Mnⁿ⁺ ions and can be arranged due to edge- and/or corner-sharing.^{[78], [80]} In general, two types of structures can be discriminated: ① a tunnel or chain structure and ② a layer structure. Both structures can contain water, protons, and/or electrolyte cations. The chain structure is formed by corner-sharing of the MnO₆ octahedrons, while the tunnel structure originates through a combination of single or multiple chains of the MnO₆ octahedrons.^{[78], [80]} The layer structure results from stacking layers of the MnO₆ octahedrons. Moreover, a mixture of different manganese oxide phases can lead to the incorporation of one phase into another, resulting in new structures. These highly variable structure types make the manganese oxides, on the one hand, to a suitable candidate for many different applications and research fields, but, on the other hand, to a complex and challenging research subject.^{[78], [80]}

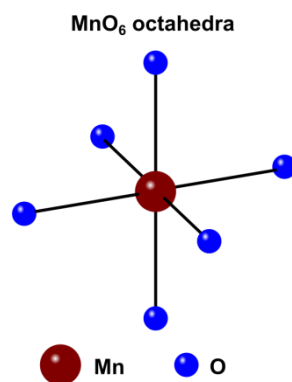


Figure 3.1.1: Schematic illustration of the MnO₆ octahedral structure building block.^[80] The MnO₆ octahedral structure consists of O²⁻ ions, which are octahedrally coordinated to the Mnⁿ⁺ ions in the center. The overall structure of most manganese oxides is based on this MnO₆ building block, which can be arranged by edge- and/or corner-sharing to form different structure types.

3.1.1 Role of manganese oxide in the photosystem II

The choice of manganese oxides for the OER originates in the biochemistry of plants. In nature, plants can split water into oxygen and hydrogen by using the energy of the sun. The overall process is called photosynthesis, while oxygen is produced at Mn₄O₅Ca-clusters in the PS II. The stepwise oxidation of water at the Mn₄O₅Ca-cluster is performed with four subsequent intermediate steps (S₀ - S₄), illustrated schematically in **Figure 3.1.2**.^{[23]–[25]} During each intermediate step, a photon is adsorbed in a chlorophyll P680. The charge is transferred by the redox-active tyrosine (Y_Z) amino acid to the Mn₄O₅Ca-cluster. Each of these charge transfer steps leads to the transition of one Mn³⁺ to Mn⁴⁺. The Mn₄O₅Ca-clusters in the second to last stage (S₃) feature four Mn⁴⁺ ions before in the last step oxygen is released and the initial state (S₀) of the oxidation process is restored.

The commonly used four-step OER mechanism of the manganese cluster is also called Kok-cycle. Several potential mechanisms for the Kok-cycle are discussed.^{[21], [23]–[25], [81]–[83]} It is worth mentioning that the calculated overpotential values required to evolve oxygen with the Mn₄O₅Ca-clusters in the PS II are far lower compared to the measured values for noble metal catalysts.^[26] The overpotential losses to drive a current density of 12 mA cm⁻² are estimated to be only 60 mV at neutral pH,^[26] which is a surprisingly low value. For both systems, the evolution of oxygen is achieved by four electron transfer steps at the surface of a catalyst. However, the two systems vary in terms of the amount of involved atomic sites in the OER. The model of Rossmisl *et al.*^{[36], [43]} considers that the evolution of oxygen takes place at a single atomic site, while in the PS II a manganese complex with several manganese atoms and surrounding amino acids are involved.^{[23]–[25]} This particular environment could be beneficial for the OER, by varying the entropy of the system due to self-organization.^{[26], [84]–[86]}

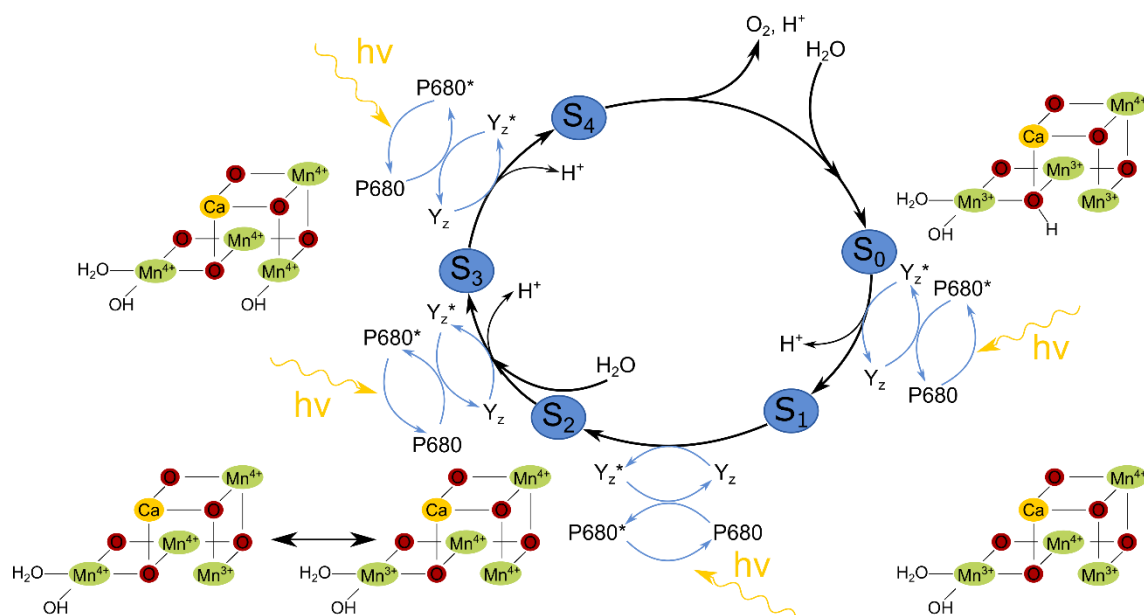


Figure 3.1.2: The stepwise oxygen evolution reaction (OER) at the $\text{Mn}_4\text{O}_5\text{Ca}$ -cluster of the photosystem II. During each step, a photon is adsorbed in the chlorophyll P680. The charge is transferred by a tyrosine (Y_z) amino acid to the $\text{Mn}_4\text{O}_5\text{Ca}$ -cluster. In each of these charge transfer steps a transition of one Mn^{3+} to Mn^{4+} occurs. After the $\text{Mn}_4\text{O}_5\text{Ca}$ -cluster exhibits four Mn^{4+} ions in step S_3 oxygen is evolved and the initial state (S_0) of the oxidation process is restored. The picture is a combined representation of the Kok-cycle from Najafpour *et al.*^{[23], [24]} and Lubitz *et al.*^[25].

3.1.2 Classification of manganese oxide as an oxygen evolution reaction catalyst

Since the early 1970s, the interest in transition metal catalysts for EC water splitting reaction has increased. The cheap alternative to conventional noble metal catalyst system raised attention, especially for an industrial application.^[87]

Morita *et al.*^{[88]–[90]} and Naumann *et al.*^[91] systematically characterized manganese oxides as a catalyst for the OER. In 1986, Matsumoto and Sato^[92] summarized the progress in transition metal oxides for the OER. They concluded that IrO_2 exhibits the lowest overpotential to run a current density of 10 mA cm^{-2} in alkaline media ($\eta_{10}=0.28 \text{ V}$), followed by nickel- ($\eta_{10}=0.30 \text{ V}$), and cobalt-based ($\eta_{10}=0.35 \text{ V}$ to 0.40 V) transition metal oxides. In their ranking, manganese- ($\eta_{10}=0.40 \text{ V}$ to 0.47 V) and iron-based ($\eta_{10}=0.45 \text{ V}$ to 0.78 V) transition metal oxides showed lower activity towards the OER. In an acidic electrolyte, RuO_2 showed the lowest overpotential to run a current density of 10 mA cm^{-2} ($\eta_{10}=0.23 \text{ V}$ to 0.30 V).^[92] Matsumoto and Sato^[92] suggested, that the chemical composition of a catalyst is not solely responsible for its catalytic activity, but is influenced by certain factors, *e.g.* the electrical conductivity, the structure of the surface, and the bonding properties between the metal and the oxide. Furthermore, the junction between the catalyst and the support plays a key role in tailoring the optimum activity of a catalyst.

A key advantage of manganese oxide compounds compared to other transition metals is its stability for the OER across a broad pH range.^{[93], [94]} Various studies of water oxidation with manganese oxides catalysts in acidic,^{[88]–[90], [94]–[98]} neutral,^{[93], [94], [99]} and alkaline electrolyte^{[55], [89], [90], [93], [94], [100]–[104]} have been performed. The Pourbaix diagram of the manganese water system (*cf.* **Figure 3.1.3**) shows that the OER predominantly takes place in the $\text{Mn}^{+\text{IV}}\text{O}_2$ region.^[105]

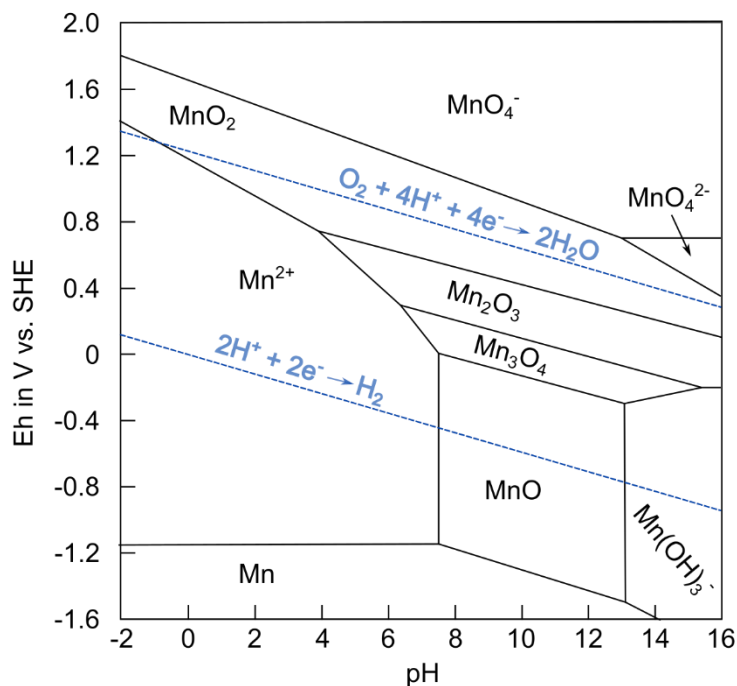


Figure 3.1.3: Pourbaix diagram of the manganese water system at 25 °C adapted and modified from ^[105]. The half-cell reactions of the HER and OER are illustrated with dashed lines.

Apart from a thermodynamic perspective, it is generally agreed that, as a catalyst for the OER, manganese oxide forms mainly a $\text{Mn}_2\text{O}_3/\text{MnO}_2$ active phase, which corresponds to an oxidation state between Mn^{3+} and Mn^{4+} .^{[87], [90], [93], [100], [106]} These active manganese oxidation states are equal to the one involved in the PS II (*cf.* **Section 3.1.1**). In the process, tunnel and layer structures built up from $[\text{MnO}_6]$ -octahedrons are of particular interest since these structures showed higher catalytic activity compared to 3-dimensional stacked manganese oxide structures in neutral electrolyte.^{[107], [108]} Motivated by the $\text{Mn}_4\text{O}_5\text{Ca}$ cluster of the PS II, the incorporation of calcium and other alkali and earth alkali metals into the $[\text{MnO}_6]$ -tunnel structures were investigated.^{[99], [107], [109]–[111]} From nature, incorporation of alkali and earth alkali metals into manganese oxides are known.^[108] Kosasang *et al.*^[112] synthesized manganese oxides with different incorporated alkali and earth alkali metals and investigated their performance for the OER and the oxygen reduction reaction (ORR) in alkaline media. They found that the incorporation of

lithium into MnO_x showed the lowest overpotential for the OER, followed by sodium, potassium, rubidium, and cesium. In neutral electrolyte, the highest activity for the OER was reached by incorporation of calcium into birnessite, followed by strontium, potassium, and magnesium.^[109] A positive influence by incorporation of cations in tunnel- and layer-coordinated manganese complexes was found.^{[107], [113]} It was suggested, that the incorporation of cations can have a beneficial effect on the formation of MnO_2 during the water oxidation.^{[107], [109]–[111]}

3.1.3 XPS specifics of manganese oxides

Manganese exhibits a variety of unique oxides phases, which can show oxidation states of Mn^{+2} , Mn^{3+} , and Mn^{+4} . Interpretation of the XPS results is challenging due to mixtures of more than one manganese oxide phase inside a single compound. Additionally, the Mn $2p_{3/2}$ photoemission line exhibits a fine structure, which was first described theoretically by Gupta and Sen^{[114], [115]}. This data was used by Nesbitt *et al.*^[116] and Biesinger *et al.*^[117] for their experimental XPS data. It was shown that each manganese oxidation state exhibits five to six different Mn $2p_{3/2}$ emission sub-lines, which originate from electrostatic, spin-orbit, and crystal field interactions. These interactions lead to a multiplet splitting in the $2p_{3/2}$ photoemission line of transition metals and make a general assignment of the peak positions a challenging task.

However, certain unique characteristics for the different manganese oxide phases can be identified. The shake-up satellite splitting in the Mn $2p_{1/2}$ photoemission line shows such a characteristic. Oku *et al.*^{[118], [119]} found that for transition metals the difference between the emission line and the shake-up signal decreases with an increasing occupation of the d-orbital (d3 for MnO_2 , d4 for Mn_2O_3 , and d5 for MnO). Gorlin *et al.*^[120] reported the difference between the shake-up and the Mn $2p_{1/2}$ photoemission line as 6.0 eV, 10.0 eV, and 11.8 eV for MnO , Mn_2O_3 , and MnO_2 , respectively. The second clear differentiating factor is the multiplet splitting of the Mn 3s photoemission line. Fadley *et al.*^[121] stated that it originates from two final states due to an exchange interaction between electrons in the material. The reported energetic difference values for the Mn 3s multiplet splitting of the MnO , the Mn_2O_3 , and the MnO_2 are 5.9 ± 0.1 eV, 5.3 ± 0.2 eV, and 4.7 ± 0.2 eV, respectively.^{[79], [118]–[120], [122]–[125]} A summary of the important peak positions, satellites, and satellite energy differences are presented in **Table 3.1.1**. Exemplary Mn 2p (*cf.* **Figure A 1a, b**) and Mn 3s (*cf.* **Figure A 1c**) XP detail spectra of different manganese oxide phases from literature are shown in the appendix.^{[117], [120]} In addition to the peak characteristics, the compound or compound mixture can always be described by the stoichiometry of manganese and oxygen through the Mn 2p and O 1s photoemission line, combined with the respective RSF values (*cf.* **Section 2.4** and **Table 2.4.1**).

Table 3.1.1: XPS summary of different relevant manganese phases with oxidation states, peak positions of Mn 2p, Mn 3s, and O 1s photoemission lines and their differences in satellite structure. ^{[79], [118]–[120], [122]–[126]}

Manganese Phase	Oxidation State	Binding energy in eV					
		Mn 2p _{3/2} & 2p _{1/2}	satellite	energy difference	Mn 3s	energy difference	O 1s
Mn	0	638.4±0.1	x	-	82.6±0.1	-	-
		649.6±0.1	x	-	-	-	-
MnO	+2	641.2±0.5	✓	5.2±0.3	89.0±0.3	5.9±0.1	529.9±0.3
		652.8±0.5	✓	5.9±0.2	83.1±0.3		
Mn ₂ O ₃	+3	641.6±0.3	x	-	88.9±0.2	5.3±0.2	529.9±0.3
		653.4±0.4	✓	10.0±0.0	83.1±0.3		
MnO ₂	+4	642.0±0.2	x	11.5±0.3	89.1±0.3	4.7±0.2	529.4±0.3
		653.7±0.2	✓	11.5±0.3	84.4±0.3		

3.2 Methodological background

3.2.1 Plasma enhanced chemical vapor deposition (PE-CVD)

The chemical vapor deposition (CVD) is the formation of a solid layer onto a substrate material by the reaction and/or the decomposition of a volatile gaseous chemical precursor. These chemical reactions occur on or in the vicinity of a normally heated substrate surface. With the so-called thermally activated (TA) CVD high deposition temperatures are needed to grow uniform high-quality layers with acceptable growth rates onto a substrate.^{[127], [128]} For sensible substrate materials, high deposition temperatures are problematic. Consequently, the thermal energy must be partially substituted by an alternative energy source like a laser or plasma.^[128] In this work, manganese oxide thin films have been deposited on different substrates from a dimanganese decacarbonyl ($\text{Mn}_2(\text{CO})_{10}$) precursor material using PE-CVD at substrate temperatures of only 150 °C (cf. **Section 3.4.1**). Since CVD is a “non-line-of-sight” technique also complex structures (e.g. rough surfaces or foams) can be coated with a uniform thickness of the desired material (cf. **Figure 3.2.1**).^[128] Thus, this deposition technique is suitable for a systematic study of thin layers on flat surfaces as well as advanced measurements for catalytic applications, involving the deposition onto high surface area substrates with porous structures.

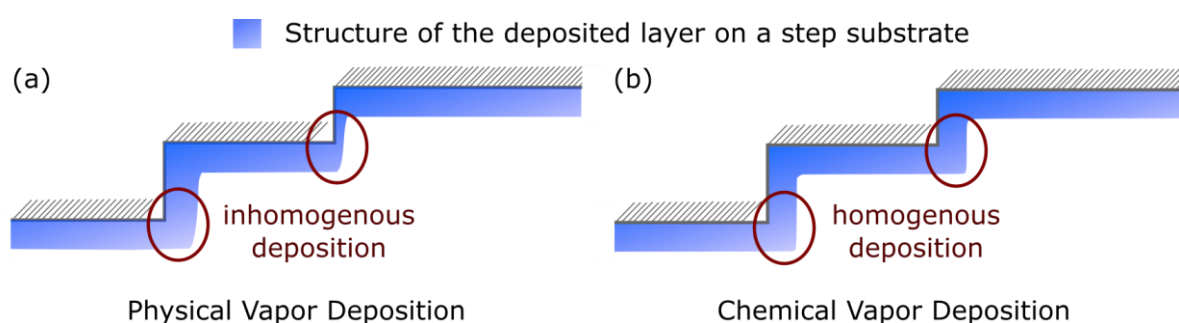
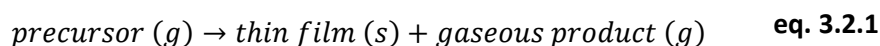


Figure 3.2.1: Comparison of the deposition structure onto a stepped surface by (a) physical and (b) chemical vapor deposition. Adapted and modified by ^[129].

In every CVD process, gaseous reactants (precursors) are admitted into a reactor (cf. **Figure 3.2.2**). The following chemical reaction



occurs near or directly on the heated substrate surface. The main gas flow of a reaction gas mixture passes over the substrate surface. A stagnant boundary layer forms in the vapor close to the surface of the substrate, in which the gas stream velocity, the concentration of the reactants, and the temperature are not equal to the quantities of the main gas stream.

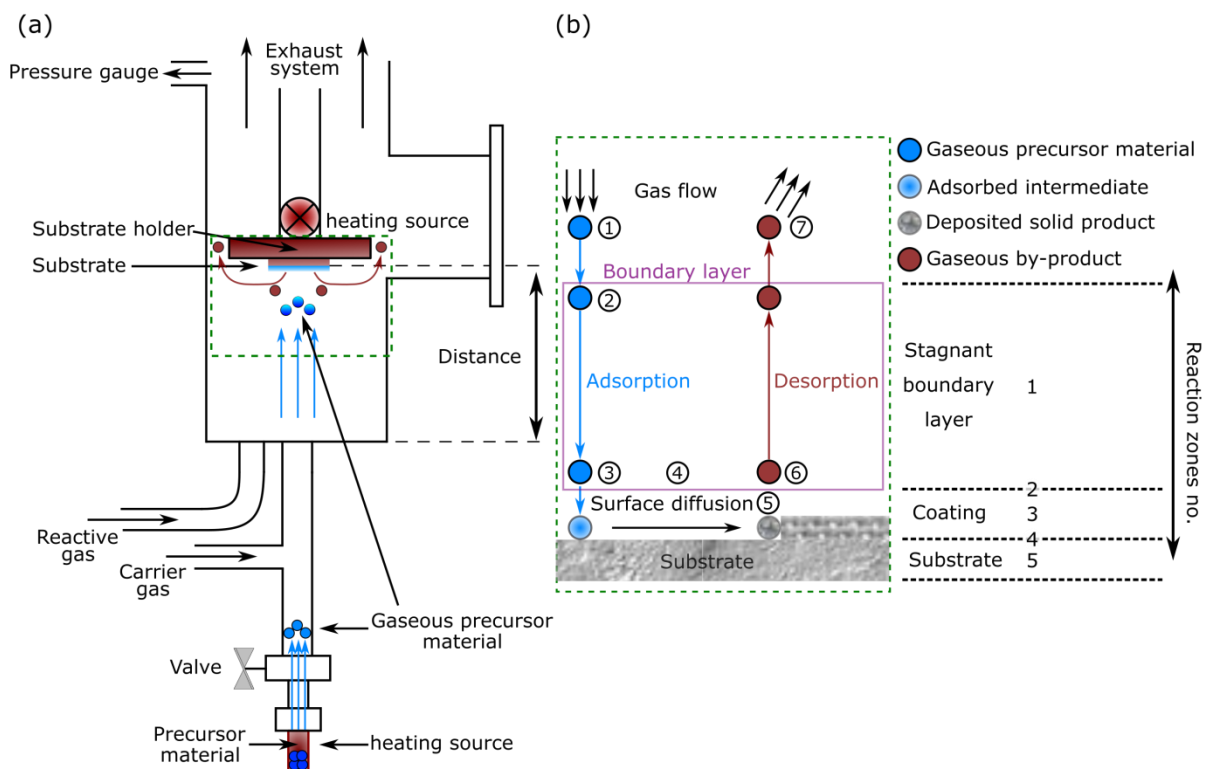


Figure 3.2.2: (a) Schematic picture of the chemical vapor deposition (CVD) reactor used in this work. (b) Schematic description of the diffusion processes during the CVD. ① The gaseous precursor material is transported across the boundary layer ② to the surface of the substrate, at which a surface reaction occurs ③. Afterward, the material can diffuse across the surface ④ and form a dense and uniform layer ⑤. Finally, the residuals are transported away from the surface ⑥ across the boundary layer to the exhaust ⑦. The formation of the stagnant boundary layer is marked, and on the right, the different CVD reaction zones are shown.^[128] More details to the reaction zones can be found in the text.

During the deposition process the gaseous precursor material (*cf.* **Figure 3.2.2b**) and gaseous products are transported across this boundary layer. Within the boundary layer, the reactants can adsorb and diffuse to the substrate, at which either surface reactions or nucleation occurs. If the reactive species cannot adsorb on the surface, it will leave the boundary layer without forming a film. If a reactive species is finally adsorbed on the surface of the substrate, the material can further diffuse along the surface forming a dense and uniform layer. The adsorption and desorption rates of the CVD process are typically controlled by the substrate temperature, the mass transport to the surface (*e.g.* gas flow velocity and precursor temperature), and the total pressure inside the reactor.^{[127]–[129]} Inside a CVD reactor, five reaction zones can be discriminated (*cf.* **Figure 3.2.2b**).^[128] In reaction zone 1, homogeneous chemical reactions can occur in the bulk gas within the boundary layer. This phenomenon is often reached at high temperatures, at which various intermediates can be formed in the gas phase. Due to these homogeneous reactions happening in zone 1, an increased portion of the precursor material does not reach the surface, leading to a decrease in deposition rate.^[128] Heterogeneous reactions occur in the phase boundary between vapor and coating (zone 2), at which the transport from

the boundary layer onto the substrate takes place. The side products of these heterogeneous chemical reactions are desorbed from the surface of the substrate and transferred back into the boundary layer. High temperatures in the CVD reactor and on the substrate can lead to various solid-state reactions (e.g. phase transformations or recrystallization) which take place in zones 3 to 5. In zone 4, surface diffusion occurs.^[128] In CVD, every process step (① to ⑥) can be the rate-limiting step. These steps can be summarized in either a mass transport limited process or a surface kinetics limited process. In the case of mass transport limitation, the diffusion of the gaseous reactants across the boundary layer is rate-determining, and the reaction occurring at the surface of the substrate proceeds fast. This limitation is typically observed at high temperatures and high pressures, leading to high deposition rates. Additionally, the deposited layer tends to form particles and shows low conformity. In the case of surface kinetic limitation, the transport of the gaseous reactants in the vapor phase is fast and the surface reactions are rate determining. With a surface kinetics-controlled process, layers with uniform thickness even on complex-shaped substrates can be achieved.^{[127]–[129]}

The integration of a plasma in the CVD process establishes additional chemical reaction pathways with lower activation energy. Thus, the deposition with PE-CVD can be conducted at considerably lower substrate temperatures compared to the TA CVD process.^{[127]–[129]}

In general, a gaseous plasma is defined as a quasi-neutral gas of charged particles containing atoms, molecules as well as electrons and cations.^[130] The chemical reactions inside a plasma are based on two basic events. First, a chemically active species is formed by inelastic collisions of precursor molecules with energetic particles (mainly electrons) generated inside of the plasma. Second, energy is transferred to the surface of the substrate surface to facilitate surface processes such as particle migration and heterogeneous reaction kinetics. The plasma can be generated by a direct current (DC) or by a radio frequency (RF) source.^{[127], [130]} The RF discharge can be driven capacitively or inductively and leads to an acceleration of electrons in an oscillating field with amplitudes in a frequency range of 0.1 to 40 MHz.

3.3 Experimental

This section describes the applied preparation routes of the plasma-enhanced chemical vapor deposited manganese oxide catalysts and the subsequent analysis steps. First, the preparation of different substrates and the specification of the PE-CVD reactor setup are introduced, followed by a summary of the used PE-CVD parameter range. The precursor temperature is derived from a subsequent thermogravimetric precursor material analysis (TGA). Finally, the EC measurement protocol is defined.

3.3.1 Substrate Preparation

The choice of substrate material influences the EC performance of a catalyst substantially. The interface between the substrate and the deposited catalyst can either favor or hinder the transfer of charge carriers (electrons and holes) throughout the material system. Additionally, a well-defined substrate is crucial in nearly all areas of surface science research and applications. In **Table 3.3.1** the substrate materials used as a basis for the deposition of manganese oxide with PE-CVD are summarized, including the cleaning procedure and additional processing steps.

The glassy carbon substrates were sanded and polished by hand. Each substrate was sanded with abrasive silicon carbide (SiC) grinding paper of European (P-grade) grit sizes of P400, P1000, P1500, P2000, and P2500 (Starcke GmbH & Co. KG) and then polished with two aluminum oxide suspensions with particle sizes of 1 and 0.05 μm (Buehler AG). The polished substrates were cleaned with acetone and isopropanol (Carl Roth, purity $\geq 99.8\%$) for 10 minutes and then dried in a nitrogen gas flow. For the stainless-steel substrates, a sample preparation system (Buehler Phoenix 4000) was used. Each substrate was sanded with abrasive SiC grinding paper (Struers) of P320, P1000, P2400, and P4000 grit sizes at a speed of 150 rpm for 10 to 20 minutes each. Subsequently, the samples were cleaned in an ultrasonic bath with distilled water for 5 minutes to remove residual material. The subsequent polishing steps were performed with diamond paste (DP-Paste M, Struers) with grain sizes of 6, 3, 1, and 0.25 μm with a single force sample operation of 15 to 20 N at 150 rpm for 4 minutes. After each step, the substrates were rinsed with distilled water. To remove the remaining diamond paste from the substrates, they were cleaned in acetone and isopropanol (Carl Roth, purity $\geq 99.8\%$) in an ultrasonic bath for ten minutes each.

The cleaning procedures were investigated by XPS analysis after the different cleaning stages and are documented in the appendix (*cf.* **Figure A 2** to **Figure A 6**)

Table 3.3.1: Summary of the different used substrates, their supplier, and the chosen preparation procedures for each of these substrate types.

Sub- strate	Composition	Supplier	Cleaning Procedure	Miscellaneous
Ti-sheet	Titanium 99.2% purity with TiO ₂ layer	Alfa Aesar	soap 10 min acetone 10 min isopropanol 10 min hydrochloric acid	-
ITO	Indium tin oxide	Alineason	soap 10 min acetone 10 min isopropanol	50 nm Au sputtered* ¹ overlayer
Stain- less- steel	X5CrNi18-10 <u>#1.4301</u>	-	soap 10 min acetone 10 min isopropanol	different grinding steps before cleaning
HOPG	Highly oriented pyrolytic graphite	K-TEK Nano-technology	scotch tape	-
GC	Glassy Carbon	HTW GmbH	10 min acetone 10 min isopropanol	grinding and polishing to mirror finish before cleaning

*¹ Direct current sputter process with a Quorum Q300TD sputter coater provided by the MA group (Prof. W. Ensinger, TUDa)

3.3.2 Setup of the PE-CVD reactor

The experimental setup of the PE-CVD system (*cf.* **Figure 3.3.1**) can be divided into three main construction parts: a vacuum unit, a reaction chamber, and the gas/precursor inlet system. The vacuum unit consists of a sealed manipulator feedthrough, which is connected to a small stainless-steel flange (Vacom, KF 50), a pressure gauge (Lesker, 275i Series), and a rotary pump (Pfeiffer Vacuum, ONF 25 M). The PE-CVD system lacks a turbopump and can only be evacuated to pressures at approximately 0.01 mbar. Therefore, the pressure gauge is only used at the beginning of the pump down and not during the deposition process, at which the maximum throughput of the pump is used. Carbon impurities (on the sample/substrate) have to be considered, since no ultra-high vacuum conditions were reached and the sample transport to the XPS analysis chamber was not an *in-vacuo* transport. The cold-wall reaction chamber, that contains a vertically oriented T-piece, is connected to vacuum unit at the top, as the lateral flange forms the load lock, and the bottom part is connected to the gas inlet system. A copper coil is

placed close to the reaction chamber for employing an inductive plasma in the CVD system. The copper coil is placed outside of the reaction chamber to avoid coating. Since the copper coil is not located inside the chamber – but closely outside of it – a shielding effect of the material of the reaction chamber must be considered. This shielding of the inductive plasma can be reduced by the application of a quartz glass T-piece (Aachener Quarzglas-Technologie Heinrich).

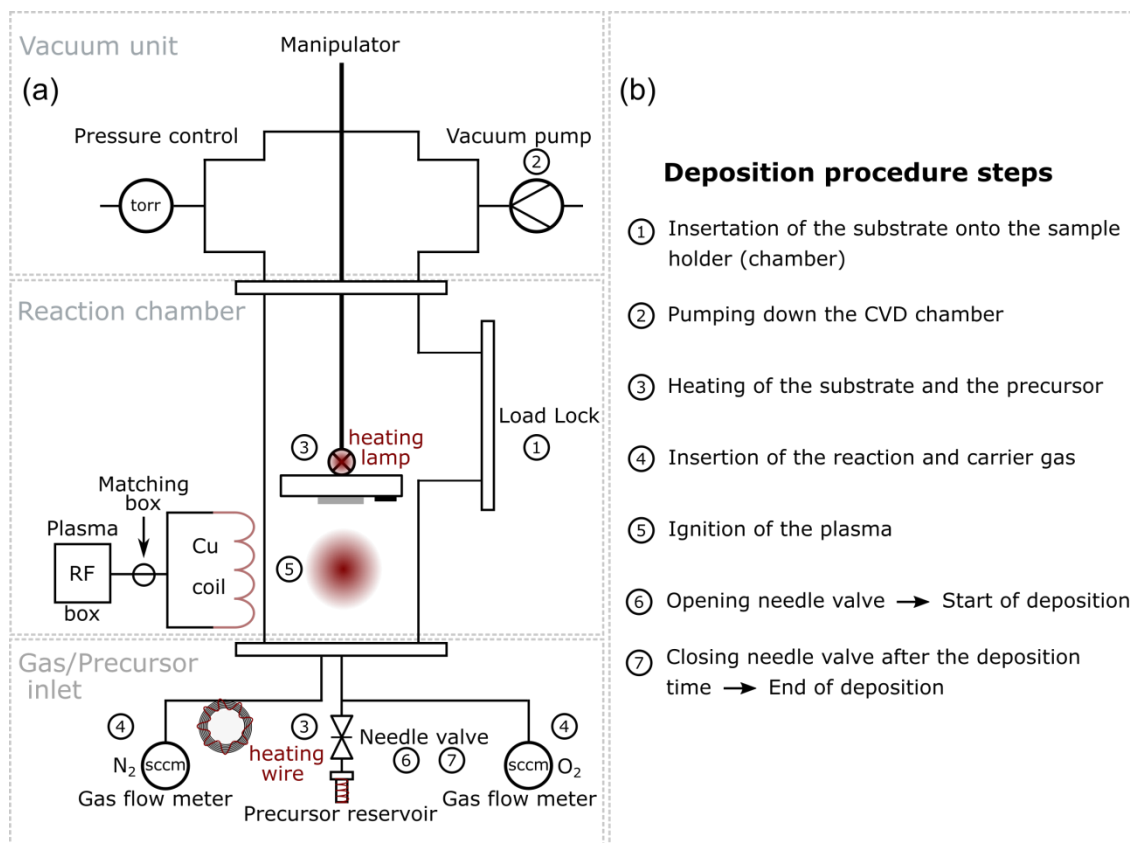


Figure 3.3.1: (a) Schematic picture of the used Plasma enhanced chemical vapor deposition (PE-CVD) reactor divided into the three main construction parts: vacuum unit, reaction chamber, and gas/precursor inlet system. The numbers in the picture illustrate the deposition sequence for the PE-CVD process further described in (b).

The high thermal loading stability in combination with its transparency allows the monitoring of the ignition and the burning of the plasma. The plasma power is supplied by a RF generator (PFG 300 RF, Hüttinger Elektronik GmbH & Co. KG), as the matching box (PFM 1500 A, Hüttinger Elektronik GmbH & Co. KG) provides a constant impedance between the generator and the matching box. The substrate holder is attached to the manipulator and the distance between the gas inlet and the sample can be adjusted. The best working distance was determined to be 12.5 cm, which was used throughout the manganese oxide depositions. The sample is heated by a halogen lamp (24 V/150 W) on the upper side and regulated by temperature control (Eurotherm, 2416). The sample is in direct contact with the heating unit and is equipped with an

Omicron sample holder at the bottom side. The precursor inlet system is mainly built from Swagelok fittings, which are connected to the glass T-piece by a workshop-made stainless-steel connector with three precursor lines. The precursor and the carrier gas lines are heated with heating wires (Horst GmbH, 020103 HS 2.0, 250 W). For the carrier gas, the tubing is coiled up and heated. The reactive gas is introduced by an additional inlet installed at the minimum distance to the precursor needle valve at the bottom of the reaction chamber. In all experiments, nitrogen was used as the carrier gas and oxygen or air was used as the reactive gas. The flow is regulated by float-type flowmeters (ABB, Series 6100). The largest possible size of the sample is 1x1 cm² and is limited by the omicron sample holder, which is used for the XPS analysis system in the DAISY-FUN.

Several steps must be considered before starting the deposition procedure. First, the substrate and the substrate holder are separately cleaned. A detailed description of the cleaning steps for the different substrate materials was presented above in **Section 3.3.1**. The sample is then placed onto the sample holder and fixed by M1.6 screws. Afterward, the deposition procedure is performed with the processing steps shown in **Figure 3.3.1b**.

Adaptable process parameters are ① precursor temperature T_{pre} , ② substrate temperature T_{sub} , ③ gas flow of nitrogen and/or oxygen, ④ plasma power P , ⑤ deposition time t , and the distance d between the sample stage and the precursor gas inlet (*cf.* **Table 3.4.1**). To reduce the number of possible deposition parameter variations P , d , and T_{pre} were kept constant for all samples. The determination of a suitable precursor temperature was determined by thermal analysis of the precursor material, shown in **Section 3.3.3**.

3.3.3 CVD precursor analysis

The evaporation temperature of the precursor material is one key parameter ensuring the success of the deposition process. Ideally, the precursor evaporates without decomposing. To identify these parameters for the precursor material thermogravimetric analysis (TGA) can be used. The TGA determines the mass loss as a function of temperature and were performed by Claudia Fasel (group of Prof. R. Riedel, TUDa).

In **Figure 3.3.2** the TGA measurement of the $(Mn_2(CO)_{10})$ precursor in nitrogen atmosphere is shown. The TGA indicates a simple one-step evaporation, leaving a residual mass of only 2%. The thermal decomposition of $Mn_2(CO)_{10}$ starts around 100 °C and the material is 98% decomposed at around 200 °C. Fillman and Tang^[131] found that the thermal decomposition is divided into two reactions: breaking of covalent bonds and CO-loss. To ensure an ideal deposition of manganese by PE-CVD, the precursor crucible was heated with a constant temperature of 85 °C throughout all samples.

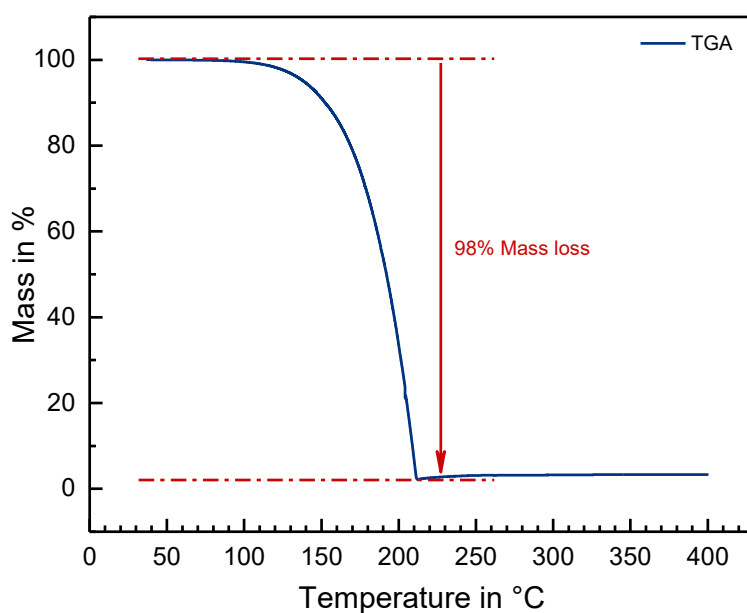


Figure 3.3.2: Thermogravimetric analysis (TGA) of $\text{Mn}_2(\text{CO})_{10}$ precursor material in a nitrogen atmosphere.

3.3.4 Electrochemical measurement protocol

The electrocatalytic performance tests were conducted using a GAMRY Interface 1000E potentiostat (C3 Prozess- und Analysetechnik GmbH) in a commercial Zahner cell (PECC-2, Zahner-Elektrik GmbH & Co. KG). All measurements were conducted using a three-electrode setup (*cf.* **Section 2.1**) with a mercury/mercury oxide reference electrode (Hg/HgO – C3 Prozess- und Analysetechnik GmbH) and a platinum wire as a counter electrode in an alkaline electrolyte (0.1 M and 1 M KOH – Carl Roth GmbH & Co. KG).

The PECC-2 Zahner cell (*cf.* **Figure 2.1.1**) consists of polychlorotrifluoroethylene (PTCFE) with a total volume of 7.2 mL. Samples can be investigated through a side opening, which can be perspective reduced by different sizes of O-rings. For a better comparison of the measured data, an EC protocol was established (*cf.* **Figure 3.3.4**).

In the first measurement of the electrochemical protocol, the open circuit potential (OCP) between the RE and the WE was obtained to ensure that both electrodes are electrically connected. Afterwards, the electrolyte resistance was determined using EC impedance spectroscopy (EIS) at the OCP. EIS uses a direct voltage which is combined with an alternating voltage. A resulting current is measured consisting of an alternating current (AC) and a direct current (DC) part. In a simple picture (*cf.* **Figure 3.3.3**), the EC cell can be described by an equivalent circuit called Randle-circuit, at which R_s defines the resistance of the setup and R_p and C represent the transfer resistance and the EC double-layer capacitance of the electrode to the electrolyte, respectively. R_s is mostly dominated by the resistance of the electrolyte. To determine this resistance a

frequency range between 100 Hz and 100 MHz is used. At low frequencies, C gets charged and discharged and acts as a blocking element, so that no current can flow. The measured impedance is the sum of R_s and R_p . At high frequencies, C discharges not completely and acts as a conductor with negligible resistance. Thus, the current flow is only defined by R_s , which can be determined in that way.

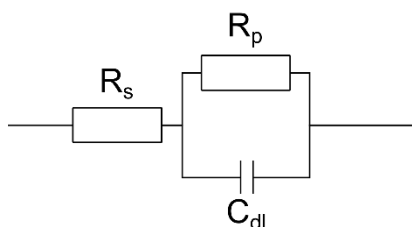


Figure 3.3.3: Simple equivalent Randle-circuit for the description of an electrochemical cell. The components R_s , R_p , and C_{dl} represent the setup, the transfer resistance, and the electrochemical double-layer capacitance, respectively.

Additional to the EIS measurements, the electrodes were investigated by CV. This was conducted to detect the reactions happening at the electrode at increasing and decreasing potentials. CVs in a suitable potential range can additionally be used to investigate the catalytic activity of an electrode.

1. Open circuit potential (OCP) measurement
2. Electrochemical impedance spectroscopy (EIS) measurement at the OCP at a frequency range from 100 Hz to 100 MHz
3. CV measurement from 1 V – 1.9 V vs. RHE for 3 cycles ($v = 50$ mV/s)
4. CV conditioning from 1 V – 1.5 V vs. RHE for 50 cycles ($v = 100$ mV/s)
5. CV measurement from 1 V – 1.9 V vs. RHE for 3 cycles ($v = 50$ mV/s)
6. CV measurement from 1 V – 1.9 V vs. RHE for 2 cycles ($v = 10$ mV/s)

Figure 3.3.4: Description of the electrochemical measurement protocol used for all deposited manganese oxide catalysts investigated in this work. The abbreviation CV stands for cyclic voltammogram, v defines the scan rate of the CV curve, and RHE describes the reversible hydrogen electrode.

For the EC protocol, specific potential ranges towards the OER were used (cf. **Figure 3.3.4**). Afterwards, the measured potential values of the CVs were all corrected by the electrolyte or rather the setup resistance $I_{measured} \cdot R_s$ obtained by the EIS measurement. Additionally, the measured potential was referred to the RHE scale according to (cf. **Table 2.1.1**)

$$E(RHE) = E_{measured} + 0.059 V \cdot pH + E_{Hg/HgO}^0(SHE) - I_{measured} \cdot R_s. \quad \text{eq. 3.3.1}$$

The protocol was extended for the most promising samples with a constant current or a constant potential measurement to investigate the stability of these catalysts over a longer time period. If not stated otherwise, all samples are corrected with the electrolyte resistance.

3.4 Manganese oxide for the oxygen evolution reaction

In this chapter, the characterization of the deposited manganese oxide films regarding their XPS characteristics, oxidation states, film thicknesses, and EC performances are presented.

3.4.1 Limitations of the manganese oxide deposition by PE-CVD

The deposition of manganese-based thin-film catalysts via PE-CVD, using oxygen as a reactive gas, can lead to different reaction products, namely MnO, Mn₂O₃, and MnO₂ (cf. **Section 3.1** and **Section 3.1.3**). To produce different manganese oxide phases, mainly the substrate temperature T_{Sub} and the oxygen content in the reactive gas flow were varied (cf. **Table 3.4.1**). The lowest possible T_{Sub} to deposit any manganese oxide on any substrate was experimentally determined to be 150 °C. Below $T_{Sub}=150$ °C, no deposition of manganese was achieved. The lowest nitrogen gas flow possible to ignite a plasma inside the reactor was 75 sccm, which corresponds to an oxygen content in the reactive gas of 62.5%. The thin films were deposited on freshly cleaned titanium substrates (cf. **Section 3.3.1**). The XP survey and detail spectra of the titanium substrates after different cleaning steps can be found in the appendix (cf. **Figure A 2**).

It needs to be mentioned, that the employed PE-CVD reactor (cf. **Section 3.3.2**) was not equipped with a turbopump and was not directly connected to the UHV analysis system of the DAISY-FUN. Therefore, the deposited thin films are *ex situ* samples and can contain impurities, like hydrocarbons.

Table 3.4.1: Summary of the possible deposition parameters with PE-CVD in combination with the used boundaries for each of these parameters. The precursor temperature (T_{Pre}), the plasma power, and the distance between the gas inlet and the sample were kept constant for all experiments.

Process Parameter	Temperature in °C		Time in min	Gas Flow in sccm		Plasma Power in W	Distance d in cm
	T_{Pre}	T_{Sub}		O ₂	N ₂		
Fixed	✓	✗	✗	✗	✗	✓	✓
Lowest	85	150	2	20	75	90	12
Highest	85	350	20	125	180	90	12

*1 The precursor temperature (T_{Pre}) was fixed to 85 °C due to subsequent analysis of the precursor material by thermogravimetric analysis (TGA) (cf. **Section 3.3.3**).

As described in **Section 3.1.3** the Mn 2p_{3/2} photoemission line exhibits a fine structure.^{[114]–[117]} The various signals for each oxidation state of manganese overlap and result in a challenging

assignment of the present manganese oxide phase. Thus, other characteristics that are considered unique (*cf.* **Section 3.1.3**) are used to identify the composition of the deposited thin films. In **Figure 3.4.1** the Mn 2p, O 1s, Mn 3s, and the valence band (VB) spectra of the manganese oxides deposited at the lowest ($T_{Sub}=150\text{ }^{\circ}\text{C}$) and the highest ($T_{Sub}=350\text{ }^{\circ}\text{C}$) applied substrate temperature are shown. For both samples, the substrate signal is only slightly visible, indicating a comparable layer thickness of approximately 5 nm (*cf.* **Figure A 7**). The deposition of both samples was conducted for 20 minutes with an oxygen and a nitrogen flow of 100 sccm. With an Mn 2p_{1/2} satellite energy difference of 10.0 eV and an Mn 3s multiplet splitting of 5.4 eV, the low-temperature phase exhibits characteristics of an Mn₂O₃ phase with an oxidation state of Mn^{+III} [79], [118], [133], [119], [120], [122]–[126], [132]

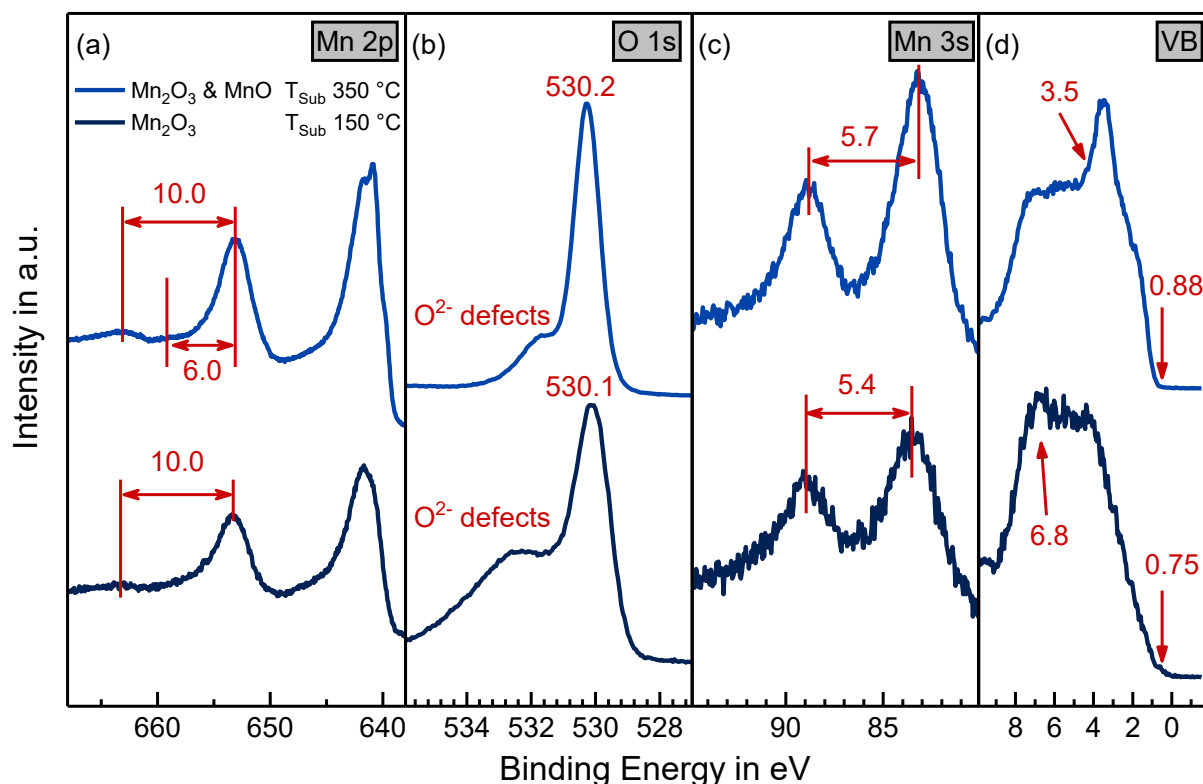


Figure 3.4.1: XP detail spectra of two manganese oxide samples deposited on titanium substrates at substrate temperatures (T_{Sub}) of 150 °C and 350 °C. For both samples, the deposition time was 20 min. In **(a)** the Mn 2p, **(b)** the O 1s, **(c)** the Mn 3s, and **(d)** the valence band (VB) detail spectra are shown with the respective characteristic peak energy differences marked (*cf.* **Section 3.1.3**).

In contrast, the high-temperature phase exhibits two Mn 2p_{1/2} satellite peaks at differences of 10.0 eV and 6.0 eV and a Mn 3s multiplet splitting of 5.7 eV. The energy difference of 10.0 eV can, again, be attributed to Mn₂O₃, while the 6.0 eV is characteristic for MnO. [120], [132], [133] The Mn 3s multiplet splitting of 5.7 eV fits neither for a pure Mn₂O₃ nor for a pure MnO phase. [118]–[120], [123], [125] Thus, the high-temperature phase consists presumably of a mixture of MnO and

Mn₂O₃. The O 1s photoemission lines of the Mn₂O₃ and the mixed-phase show intense peaks at 530.1 eV and 530.2 eV, respectively. Biesinger *et al.*^[117] reported values of 529.97 eV for MnO and 529.96 eV for Mn₂O₃, which are in good agreement with the obtained values. For the PE-CVD deposition process, additional defects (oxygen vacancies or oxygen interstitials) and precursor residual (hydrocarbons) have to be considered. The survey spectra and the C 1s detail spectra of the two presented samples can be found in the appendix (*cf.* **Figure A 7**). Both film impurities can be observed in the O 1s photoemission line at higher binding energies than the metal oxide signal and are expected to decrease with increasing T_{Sub} since the surface diffusion increases, leading to fewer defects. The precursor shows a higher rate of decomposition at higher temperatures. Thus, the signal of precursor residuals should decrease. An intense broad signal is observed for the low-temperature sample at a binding energy of approximately 531.8 eV with an additional tail at even higher binding energies. The O 1s peak structure decreases with increasing T_{Sub} and shifts to approximately 531.3 eV for the high-temperature sample. The tail of the peak structure is attributed to hydrocarbons,^[70] while the signals at 531.8 eV and 531.3 eV are attributed to oxygen lattice defects or even hydration during the *ex-vacuo* transport to the DAISY-FUN analysis chamber.^[117] Biesinger *et al.*^[117] reported values of 531.25 eV and 531.63 eV for the Mn₂O₃ and MnO phase, respectively, and attributed them to defective oxide, hydroxide, or hydration. The VB spectra show a VB onset of 0.75 eV and 0.88 eV for the low and the high-temperature phase, respectively. Additionally, a peak at approximately 3.5 eV is visible for the high-temperature phase and a small ridge at 6.8 eV for the low-temperature phase. The peak at 3.5 eV can be attributed to localized 3d states.^{[123], [132], [133]} Di Castro and Polzonetti^{[132], [133]} observed these 3d states only for MnO, while they obtained a decreasing peak with increasing oxidation of the MnO phase to Mn₂O₃. During the oxidation of MnO, they observed a peak increase of the O 2p valence band states at a binding energy of approximately 7.0 eV. Thus, the small ridge at 6.8 eV in the VB spectrum can be attributed to O 2p electrons.^{[123], [132], [133]} Consequently, the peak structure indicates the presence of MnO on the surface of the high-temperature sample.^{[132], [133]}

In addition to the peak analysis, the stoichiometric composition of the layer was determined with XPS using a Shirley background.^[134] To calculate the oxygen-to-manganese (O-to-Mn) ratio of the manganese oxide layer, the total area below the Mn 2p photoemission line and the metal oxide component of the O 1s signal combined with the element-specific RSF values (*cf.* **Table 2.4.1**) are used. In **Figure 3.4.2a** the calculated O-to-Mn ratios deposited at different T_{Sub} are shown. The manganese oxide phases deposited at $T_{Sub} < 250$ °C show an O-to-Mn ratio of approximately 1.50. At T_{Sub} between 250 °C and 260 °C, the ratio decreases from 1.50 to 1.33 and stays at 1.33 until the highest used T_{Sub} ($T_{Sub}=350$ °C). The same trend is obtained by plotting the Mn 3s multiplet splitting as a function of the T_{Sub} (*cf.* **Figure 3.4.2b**). Below a T_{Sub} of 250 °C, an Mn 3s multiplet splitting of approximately 5.3 eV is observed (O-to-Mn=1.50). At

T_{Sub} between 250 °C and 260 °C, the splitting increases from 5.3 eV to 5.6 eV and stays at approximately 5.6 eV until the highest used substrate temperature (O-to-Mn=1.33). The obtained O-to-Mn ratios and the Mn 3s multiplet splitting analysis confirm the results obtained from the peak analysis of the low- and high-temperature samples. Consequently, it can be stated that a Mn_2O_3 (O-to-Mn=1.5) phase is formed with $150\text{ °C} < T_{Sub} < 250\text{ °C}$, while a mixture of Mn_2O_3 (O-to-Mn=1.5) and MnO (O-to-Mn=1) is formed for $T_{Sub} > 260\text{ °C}$.

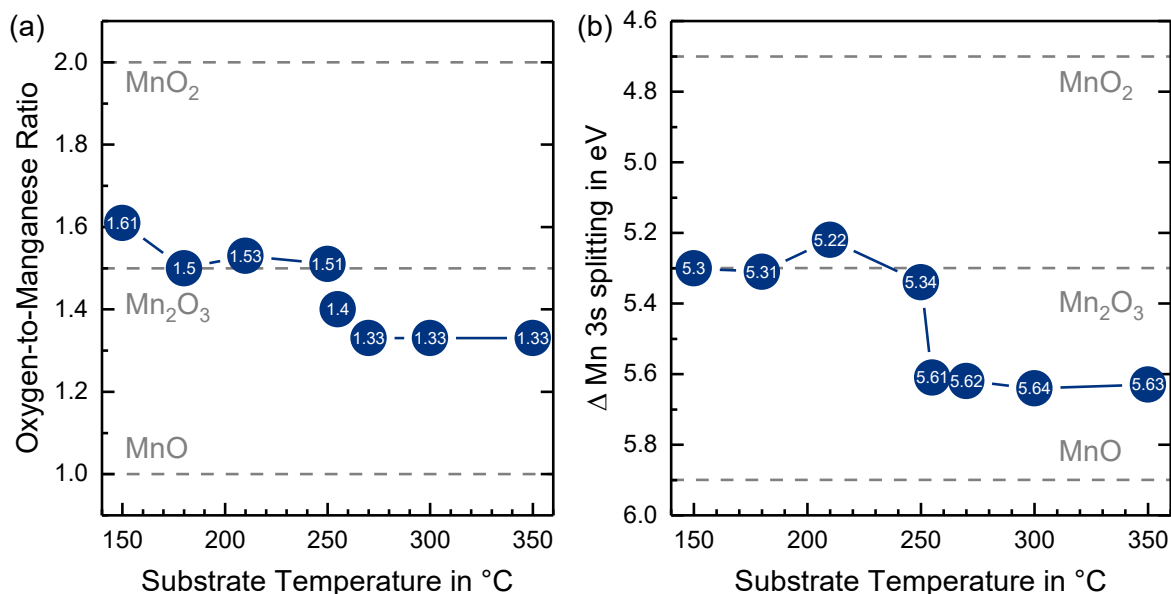


Figure 3.4.2: XPS analysis of the manganese oxide thin films deposited with PE-CVD at different substrate temperatures. The trend of the (a) oxygen-to-manganese (O-to-Mn) ratio and of the (b) Mn 3s splitting difference for the different substrate temperatures (T_{Sub}) are shown with marked stoichiometries and peak characteristics for MnO, Mn_2O_3 , and MnO_2 .

In addition to the variation of the T_{Sub} , a variation of the oxygen content of the reactive gas flow was investigated. In **Figure 3.4.3a** the Mn 3s multiplet splitting and in **Figure 3.4.3b** the Mn $2p_{1/2}$ to satellite energy difference are shown as a function of the oxygen content inside the reactive gas. The total gas flow was kept constant at 200 sccm and 300 °C was used as T_{Sub} . In contrast to the variation of the T_{Sub} , no change in the deposited manganese oxide phase can be observed by varying the oxygen content inside the reactive gas. The Mn 3s splitting exhibits values between 5.6 eV and 5.7 eV for all samples and varies only slightly in the range of the XPS measurement error (< 50 meV). The Mn $2p_{1/2}$ to satellite energy difference exhibits values between 10.2 eV and 10.3 eV and a smaller satellite signal at approximately 6.0 eV. The variation in binding energies is in the same range as observed for the Mn 3s multiplet splitting. Thus, all phases deposited at different oxygen content inside the reactive gas form a mixture of Mn_2O_3 and MnO, which was already observed for the samples deposited at $T_{Sub} > 250\text{ °C}$.

In conclusion, with PE-CVD only two different manganese oxide phases could be produced, one mainly pure Mn_2O_3 phase at low $T_{\text{Sub}} < 250\text{ }^\circ\text{C}$ and one mixed Mn_2O_3 & MnO phase at $T_{\text{Sub}} > 250\text{ }^\circ\text{C}$. The variation of the oxygen content inside the reactive gas showed no influence on the produced manganese oxide films.

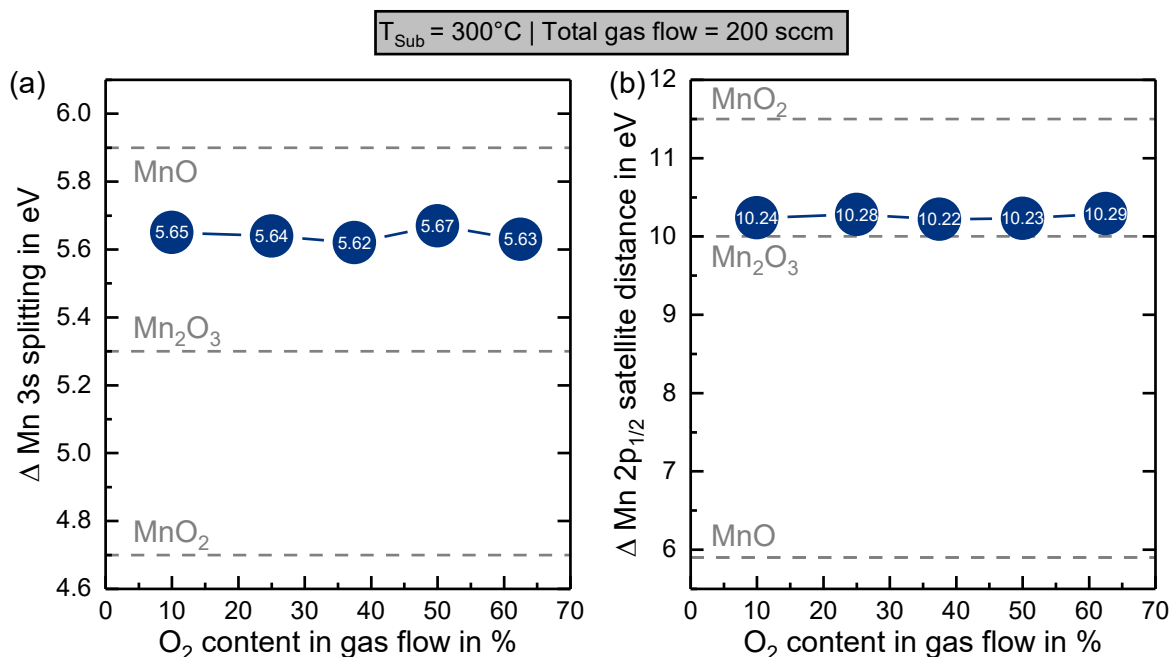


Figure 3.4.3: XPS analysis of the manganese oxide thin films deposited with PE-CVD at a substrate temperature of $300\text{ }^\circ\text{C}$ with varying oxygen content in the gas flow. The total gas flow was kept constant at 200 sccm. The trend in the (a) Mn 3s splitting energy difference and in the (b) Mn $2p_{1/2}$ to satellite energy difference for the different oxygen contents in the gas flow are shown with marked characteristics for MnO , Mn_2O_3 , and MnO_2 .

3.4.2 Electrochemical characterization of manganese oxide thin films

In this chapter, the EC performance of the previously described manganese oxide thin films deposited on titanium (*cf.* Section 3.4.1) is investigated. The EC investigation is conducted towards the OER using the introduced protocol (*cf.* Section 3.3.4). Based on the guidelines of the BMBF project (Mangan 03EK3552), a characterization of the produced thin films in 1 M KOH was demanded. However, several EC investigations of the deposited manganese oxide thin films showed poor stability in the electrolyte (*cf.* Figure A 8 and Figure A 9). The instability of manganese oxide in 1 M KOH ($\text{pH}=14$) for the OER is also visible in the Pourbaix diagram (*cf.* Figure 3.1.3) forming MnO_4^{2-} and at higher potentials MnO_4^- anions.^[105] To be able to investigate the manganese oxide with XPS after the EC investigation an electrolyte with a lower ionic concentration (0.1 M KOH with $\text{pH}=13$) is used for the subsequent experiments.

According to the EC measurement protocol (cf. **Section 3.3.4**), four subsequent CV measurements were conducted to investigate the manganese oxide catalysts. In **Figure 3.4.4a** the first recorded CVs before the conditioning step are shown for one Mn_2O_3 ($T_{\text{Sub}}=150^\circ\text{C}$) and one mixed Mn_2O_3 & MnO ($T_{\text{Sub}}=300^\circ\text{C}$) sample. In the inset of **Figure 3.4.4a**, the conditioning step for both samples is shown. The dashed line marks a current of 0 mA cm^{-2} to highlight deviations at which possible redox reactions occur. In **Figure 3.4.4b** the recorded CVs for the two samples are shown after the conditioning step. From the Pourbaix diagram of manganese with water (cf. **Figure 3.1.3**) a transition of Mn^{3+} to Mn^{4+} should be observable between a potential of 1.05 V to 1.10 V vs. RHE. A second transition from Mn^{4+} to MnO_4^- should occur approximately at 1.5 V vs. RHE but is not visible here.

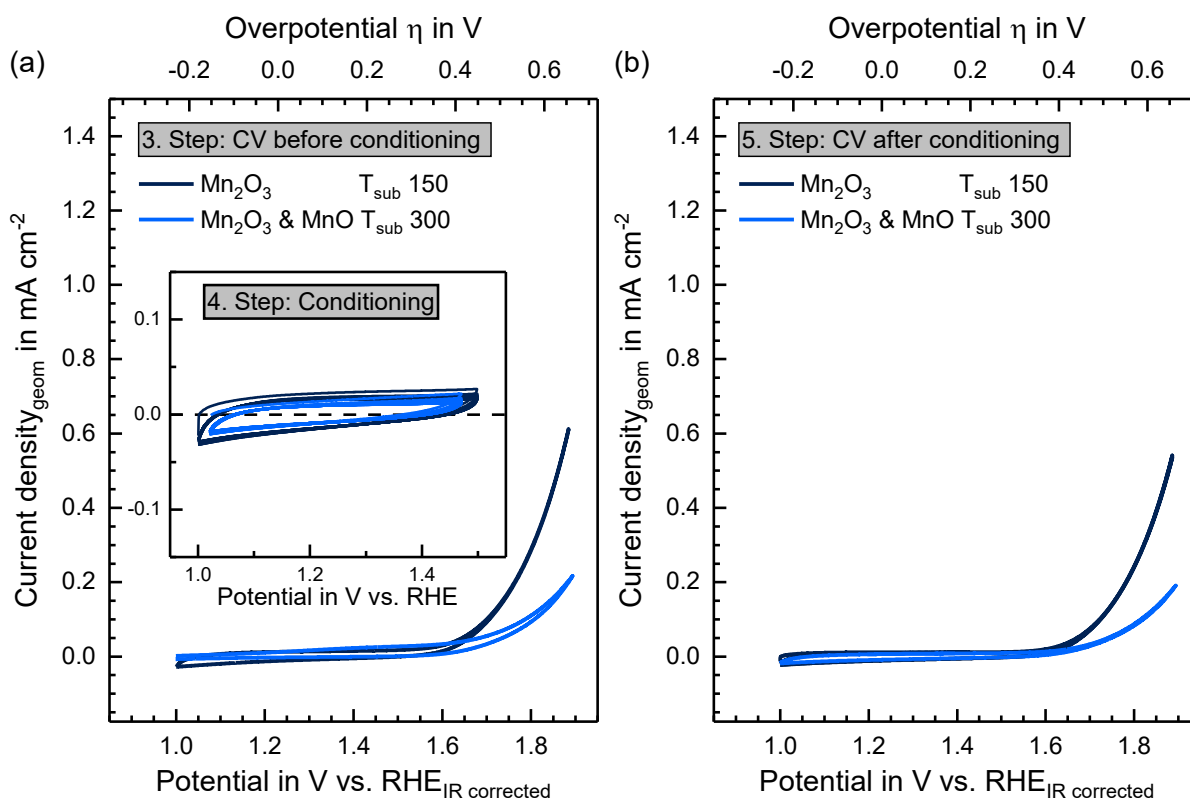


Figure 3.4.4: Cyclic voltammograms (CVs) of one Mn_2O_3 (dark blue – $T_{\text{Sub}}=150^\circ\text{C}$) and one Mn_2O_3 & MnO mixture (light blue – $T_{\text{Sub}}=300^\circ\text{C}$) sample in 0.1 M KOH for the OER. **(a)** Showing the CVs before the conditioning step with the subsequent conditioning step in the inset and **(b)** illustrating the CVs after the conditioning step. The CV curves are measured according to the electrochemical protocol with a scan rate of 50 mV s^{-1} from 1.0 V to 1.9 V vs. RHE and are iR compensated (cf. **Section 3.3.4**). The conditioning step was measured at a scan rate of 100 mV s^{-1} from 1.0 V to 1.5 V vs. RHE.

The first recorded CVs of the two samples show higher activity for the Mn_2O_3 sample with a maximum current density of 0.61 mA cm^{-2} , compared to 0.22 mA cm^{-2} for the mixed Mn_2O_3 & MnO sample in the measured potential range. The potential range of the conditioning step was chosen to include the reversible redox transition of Mn^{3+} to Mn^{4+} . Only the first cycle of the conditioning step shows a larger hysteresis than the following ones. After the conditioning step

slightly lower activities for both samples are measured in the potential range. The Mn_2O_3 sample exhibits a maximum current density of 0.54 mA cm^{-2} while the mixed Mn_2O_3 & MnO sample shows a maximum of 0.19 mA cm^{-2} . After the conditioning step, a decreased hysteresis is visible for both samples, which implies that during the conditioning step a transition occurred. However, compared to other transition metals, the observed redox waves are low and broad. This could be caused by a low electrical conductivity of manganese oxides, which could inhibit chemical transition at the surface of the catalyst. Since the CVs before and after the conditioning step show only minor changes, the conditioning step will not be discussed for the following systems. The comparison of the following catalytic systems will be presented based on the third CV measurement after the conditioning step (cf. **Figure 3.4.4b**). Since the conductivity of a catalytic system plays an important role in the EC performance, a thickness variation of the higher active Mn_2O_3 phase ($T_{\text{Sub}}=150 \text{ }^\circ\text{C}$) was conducted. The samples were deposited with equal deposition parameters for 2 min, 5 min, 10 min, and 20 min. From XPS analysis (cf. **Figure A 10**) the film thickness for each of the films was calculated using **Equation 2.4.3** (cf. **Section 2.4**). In **Figure 3.4.5a** the film thickness is plotted as a function of the deposition time. In **Figure 3.4.5b** the EC performance for the four different film thicknesses is shown.

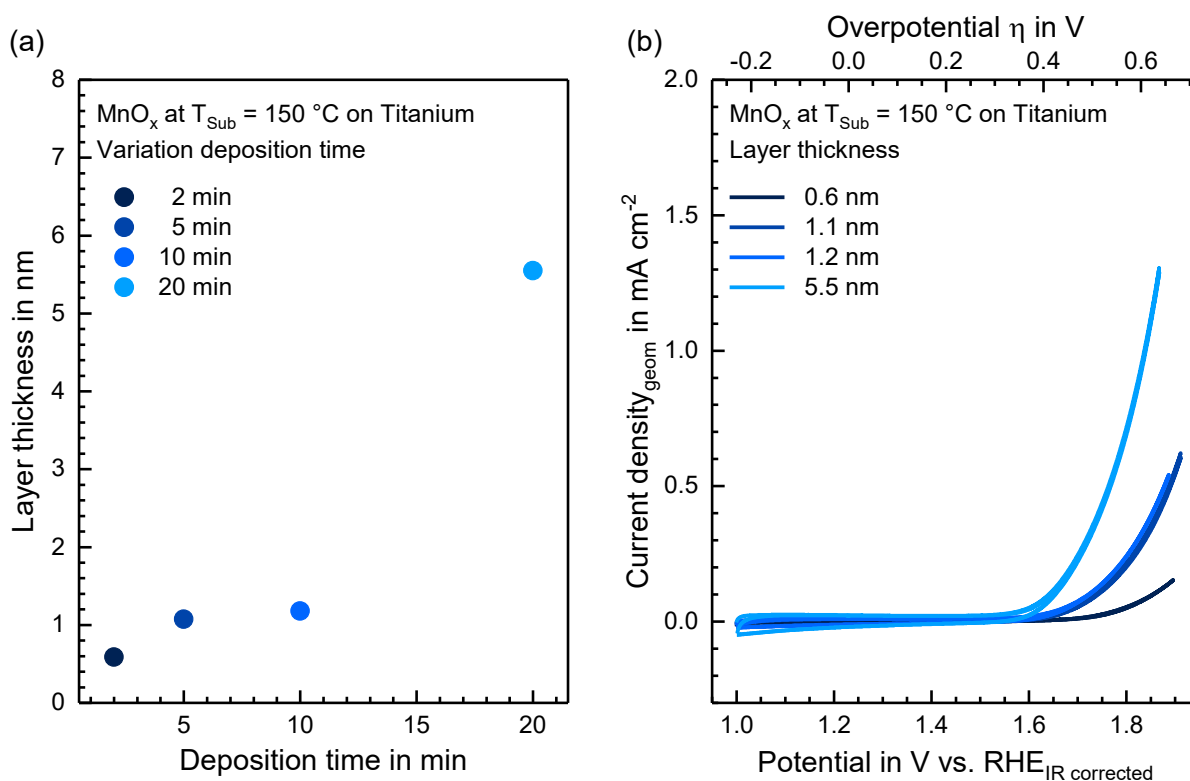


Figure 3.4.5: (a) Determination of the layer thickness of manganese oxides with XPS deposited on titanium for four different deposition times: 2 min, 5 min, 10 min, and 20 min. (b) Cyclic voltammograms (CVs) of the four different layer thicknesses on titanium in 0.1 M KOH for the OER. The CVs are measured according to the electrochemical protocol with a scan rate of 50 mV s^{-1} from 1.0 V to 1.9 V vs. RHE and are iR compensated (cf. **Section 3.3.4**).

Contrary to the expectation that a thicker manganese oxide film exhibits a higher electrical resistance and, thus, a lower EC activity, the EC performance increases with increasing film thickness. One explanation for the increase in EC performance with increasing film thickness could be the roughness of the titanium substrate. If only the valley parts of the titanium substrate are coated with manganese oxide a not completely compact and dense manganese oxide layer is formed, leading to a lower overall active manganese oxide area, which consequently shows a lower EC performance.

In summary, the manganese oxide phases show only minor activity towards the OER deposited onto titanium substrates. The Mn_2O_3 phase shows a higher performance than the mixed Mn_2O_3 & MnO phase. The activity of the Mn_2O_3 phase increases with increasing film thickness. The distinct redox transitions visible in the Pourbaix diagram for the manganese water system are challenging to identify at the proposed potentials.^[105] XPS analysis after the EC investigation can help to identify the changes happening on the surface of the catalysts.

3.4.3 Changes in oxidation state during the electrochemical investigation

After the EC investigation, the manganese oxide samples were again characterized by XPS to monitor possible changes during the EC testing. In **Figure 3.4.6** and **Figure 3.4.7** the Mn 2p, O 1s, Ti 2p, and Mn 3s detail spectra of the low-temperature sample ($T_{Sub}=150\text{ }^{\circ}\text{C}$ – Mn_2O_3) and the high-temperature sample ($T_{Sub}=300\text{ }^{\circ}\text{C}$ – Mn_2O_3 & MnO) before and after the EC testing are shown.

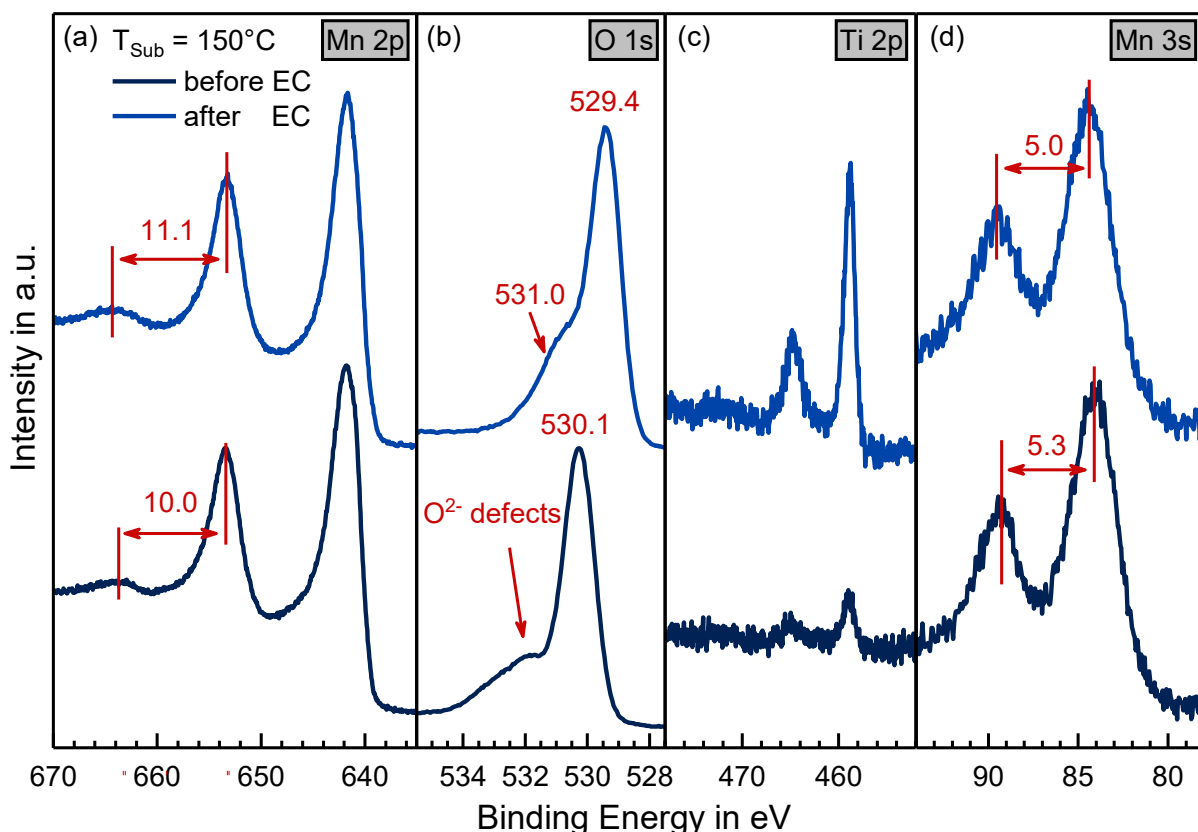


Figure 3.4.6: XP detail spectra of the low-temperature manganese oxide sample ($T_{Sub}=150\text{ }^{\circ}\text{C}$ – Mn_2O_3) sample deposited on a titanium substrate before (dark blue) and after electrochemical investigation (light blue). The deposition time was 20 min. In **(a)** the Mn 2p, **(b)** the O 1s, **(c)** the Ti 2p, and **(d)** the Mn 3s detail spectra are shown with the respective characteristic peak energy differences marked (*cf.* **Section 3.1.3**).

The Mn 2p photoemission lines measured after the EC investigation show an increase in the Mn 2p_{1/2} satellite energy difference for both samples. The energy difference changes from 10.0 eV to 11.1 eV for the low-temperature sample (*cf.* **Figure 3.4.6a**), while for the high-temperature sample, the satellite with a energy difference of 6.0 eV vanishes, and the second satellite signal shifts from 10.0 eV to 10.9 eV (*cf.* **Figure 3.4.7a**). These changes indicate an increase in the oxidation state for both samples.^{[118]–[120]} A Mn 2p_{1/2} satellite energy difference of approximately 11 eV is characteristic for a MnO_2 phase with an oxidation state of Mn^{4+} .^[120] The Mn 3s photoemission lines of the two samples after the EC investigation (*cf.* **Figure 3.4.6d** and

Figure 3.4.7d) still exhibit a multiplet splitting. The Mn 3s multiplet energy difference for the low-temperature sample decreases from 5.3 eV before the EC investigation to 5.0 eV after the EC testing. The same trend is visible for the high-temperature sample, which shows a change from 5.7 eV before the EC investigation to 5.1 eV after the EC testing. The Mn 3s multiplet distances of the samples after the EC investigation imply an oxidation state between Mn^{3+} and Mn^{4+} .^{[118]–[120], [123], [125]} From the O 1s photoemission line (cf. Figure 3.4.6b and Figure 3.4.7b), the manganese compound can be identified as a phase with mainly oxidic character.

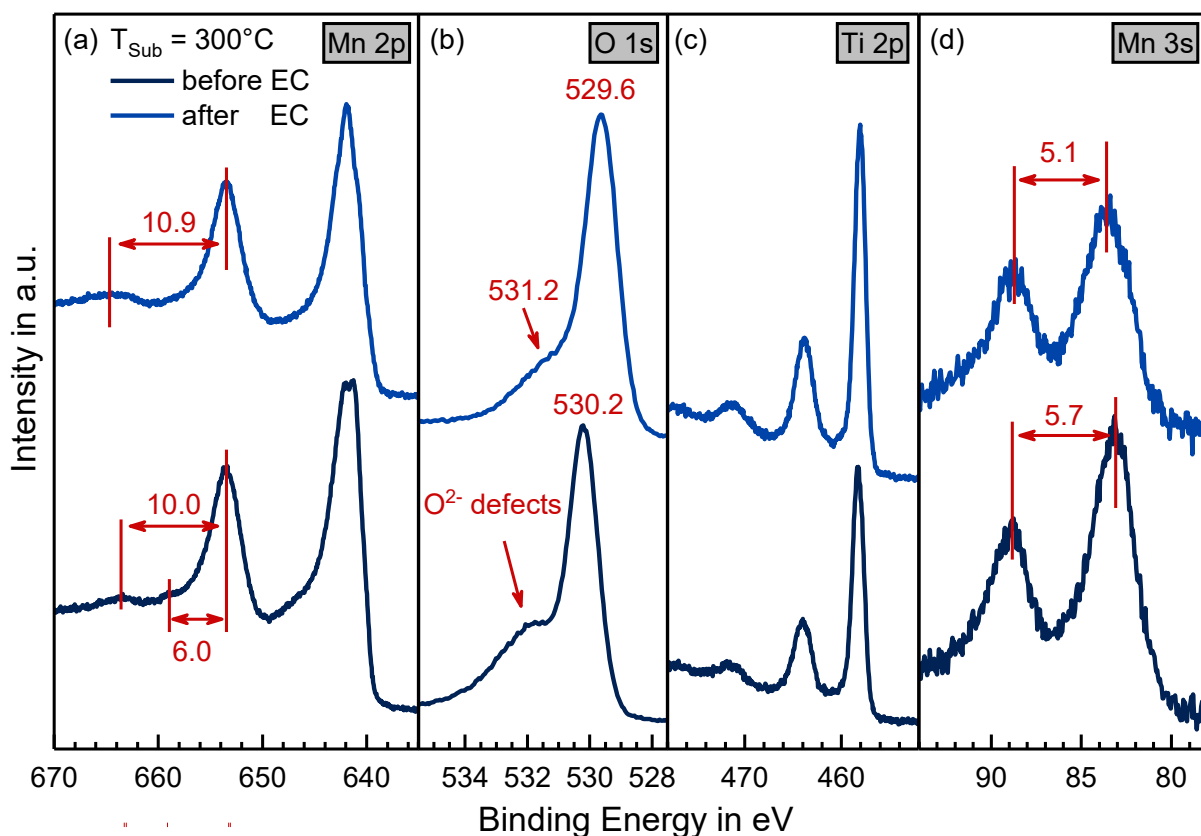


Figure 3.4.7: XP detail spectra of the high-temperature manganese oxide sample ($T_{\text{Sub}}=300\text{ }^{\circ}\text{C}$ – Mn_2O_3 & MnO) sample deposited on a titanium substrate before (dark blue) and after electrochemical investigation (light blue). The deposition time was 20 min. In (a) the Mn 2p, (b) the O 1s, (c) the Ti 2p, and (d) the Mn 3s detail spectra are shown with the respective characteristic peak energy differences marked (cf. Section 3.1.3).

The metal oxide signals shift for both samples after the EC testing to lower binding energies. The low-temperature sample exhibits a signal at 529.4 eV, while the high-temperature sample shows a signal at 529.6 eV. Biesinger *et al.*^[117] reported values of 529.54 eV and 529.51 eV for MnO_2 phases, which are in good agreement with the obtained values. For both samples, the photoemission line of the substrate (Ti 2p) shows an increase in intensity after the EC investigation. Consequently, the measured peak structure after the EC investigation indicates a transition of the manganese catalyst to an oxidation state of mainly Mn^{4+} . For both catalysts, the Mn^{4+} phase shows mostly oxidic character. The increased intensity of the substrate signal is

most likely caused by a partial dissolution of the manganese oxide catalyst inside the electrolyte during the EC testing.

3.5 Manganese oxide deposition: Effect of the support

In **Section 3.4** the limitations in the PE-CVD process on titanium substrates (*cf.* **Section 3.4.1**) were described and the EC investigations on these catalytic systems, including the subsequent change in composition, were presented. In the following, the obtained data of the deposition process are used to investigate different junctions to the manganese oxide catalysts by varying the support materials and probing the EC performance of the resulting catalyst-support systems.

3.5.1 XPS characterization of manganese oxides on different support materials

The requirements for the chosen substrate materials are dictated by the water electrolysis application of the manganese oxides, meaning that they have to exhibit good electrical conductivity, be inert in the chosen electrolyte for the used potentials, and should possess comparable roughness. The titanium foil (*cf.* **Figure A 2**) exhibits a native titanium dioxide layer (TiO_2), which is stable over the used potential range and exhibits no catalytic activity towards the OER in alkaline media.^{[135], [136]} Aside from that, two carbon-based substrates (GC and HOPG), one stainless-steel⁸ (SS), and one transparent conductive oxide (ITO) are chosen to serve as support materials. GC and HOPG have been widely used as an electrode material.^{[137]–[139]} GC is especially often used for spin- and drop coating applications since it can be polished to a mirror finish. GC and HOPG exhibit chemical stability and electrocatalytic inertness in alkaline media over a broad potential range.^{[137]–[139]} It was shown by Benck *et al.*,^[139] that ITO is chemical stable in alkaline media towards the OER. However, the deposition of manganese oxide onto ITO leads to a reduction of the ITO layer, causing a decrease in electrical conductivity. Consequently, the ITO was coated by sputtering with a 50 nm thick layer of gold (Au). The SS support was chosen to function as an industrial application approach. The austenitic SS is a cheap and chemically stable alternative to the other substrates. However, for purely scientific investigations the steel is unsuitable since the elemental composition of the sheets can vary and it contains materials that already show electrocatalytic activity towards the OER. The SS and the GC substrates were ground and polished as described in **Section 3.3.1**.

The XPS characteristics of the manganese oxide phases deposited for 20 min at substrate temperatures of 150 °C and 300 °C are summarized for the used substrates in **Table 3.5.1**. A majority of the samples exhibited the same phases, which were already found for the titanium foil support (*cf.* **Section 3.4.1**). The only exception was observed for the manganese oxide deposited at $T_{\text{Sub}}=150$ °C on GC, which showed an Mn 2p_{1/2} to satellite energy difference of

⁸ Stainless-steel X5CrNi18-10 – TK 1.430

approximately 11.6 eV and an Mn 3s multiplet splitting of approximately 4.9 eV. The Mn 2p_{1/2} to satellite energy difference is roughly 1.6 eV higher and the Mn 3s multiplet splitting is approximately 0.4 eV lower as for the other samples deposited at the same deposition parameters. The Mn 2p_{1/2} to satellite energy difference fits XPS characteristics observed for MnO₂ while the Mn 3s multiplet splitting corresponds to a manganese oxidation state between Mn³⁺ and Mn⁴⁺. [118]–[120], [123], [125]

Table 3.5.1: XPS characteristics of manganese oxide phases deposited for 20 min at substrate temperatures (T_{Sub}) of 150 °C and 300 °C on titanium foil (Ti – with native titanium oxide (TiO₂) layer), glass-like carbon (GC), highly oriented pyrolytic graphite (HOPG), glass with indium tin oxide (ITO) with 50 nm of sputtered gold (Au), and stainless-steel*¹ (SS). The subsequent preparation procedures of the substrates are given in **Section 3.3.1**.

Substrate	T_{Sub}	Δ Mn 2p _{1/2} to satellite energy difference	Δ Mn 3s multiplet splitting energy difference	O 1s
Ti/TiO ₂	150 °C	10.0 eV	5.3 eV	530.1 eV
Ti/TiO ₂	300 °C	6.0 eV; 10.0 eV	5.7 eV	530.2 eV
GC	150 °C	11.6 eV	4.9 eV	529.2 eV
GC	300 °C	6.0 eV; 10.1 eV	5.7 eV	530.0 eV
HOPG	150 °C	10.4 eV	5.3 eV	529.8 eV
HOPG	300 °C	5.8 eV; 10.2 eV	5.7 eV	529.8 eV
Glass/ITO/Au	150 °C	10.6 eV	– * ²	529.4 eV
SS* ¹	150 °C	10.4 eV	5.3 eV	529.5 eV
SS* ¹	300 °C	5.9 eV; 10.3 eV	5.7 eV	529.8 eV

*¹ polished stainless-steel (X5CrNi18-10 – TK 1.4301)

*² no evaluation possible due to an overlap of the Mn 3s signal with the Au 4f photoemission line

3.5.2 Electrochemical characterization of manganese oxide thin films

In this chapter, the EC performance of the characterized manganese oxide thin films on GC, HOPG, ITO/Au, and SS (*cf.* **Section 3.5.1**) is investigated. The EC investigation was conducted towards the OER in 0.1 M KOH using the protocol introduced in **Section 3.3.4**.

In **Figure 3.5.1** the CVs after the conditioning step of the samples deposited onto GC, HOPG, ITO/Au, and SS at T_{Sub} of 150 °C and 300 °C are shown. For a better comparison of the presented catalytic system, the boundary values of the x- and y-axis scales are equally stacked.

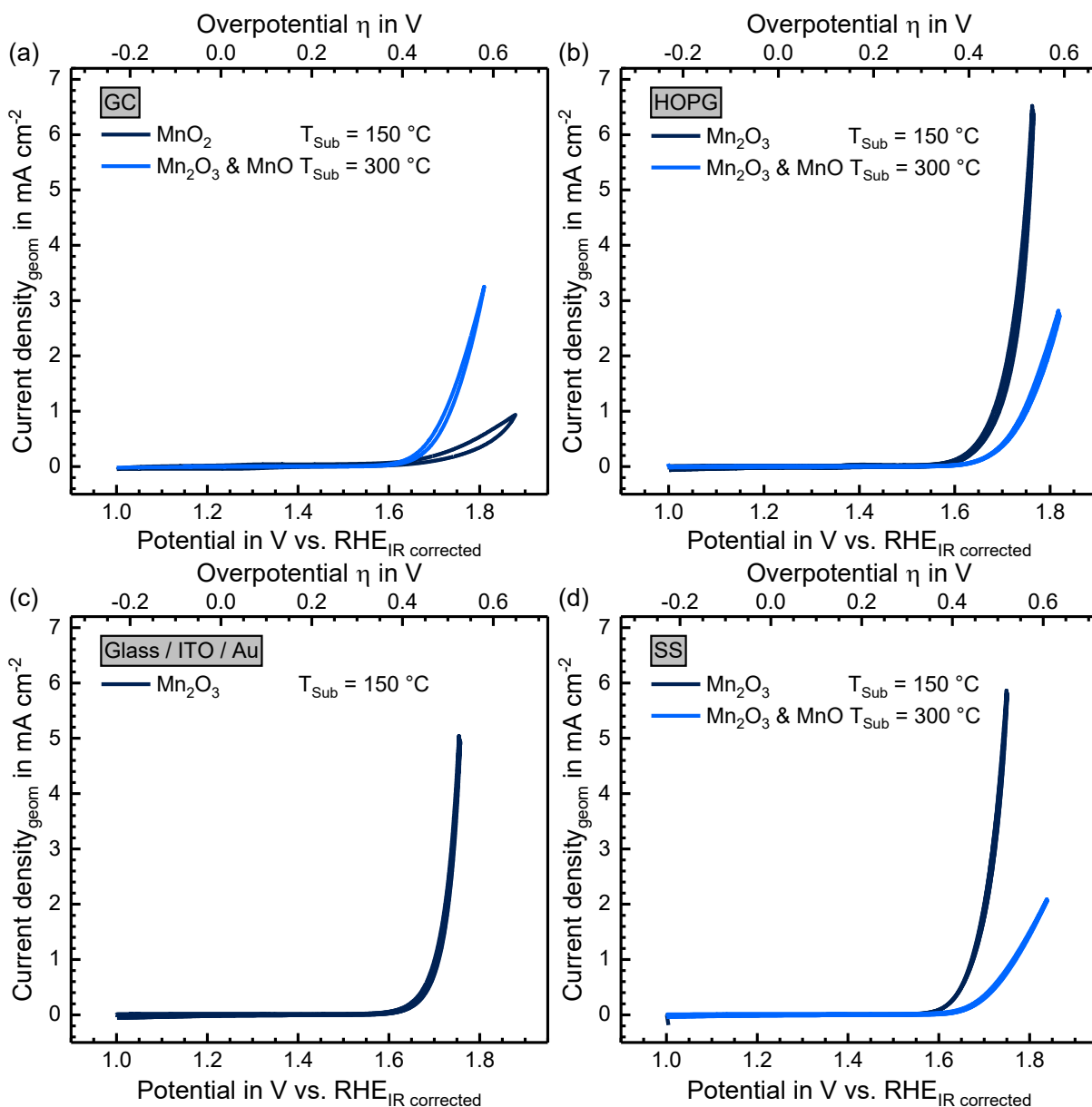


Figure 3.5.1: Cyclic voltammograms (CVs) of the Mn_2O_3 (dark blue – $T_{\text{Sub}}=150\text{ }^\circ\text{C}$) and the Mn_2O_3 & MnO mixture (light blue – $T_{\text{Sub}}=300\text{ }^\circ\text{C}$) samples towards the OER on (a) Glass-like carbon (GC), on (b) highly oriented pyrolytic graphite (HOPG), (c) indium tin oxide (ITO) with 50 nm of sputtered gold (Au), and (d) on stainless-steel (X5CrNi18-10 – TK 1.4301). The CVs are recorded after the conditioning step with a scan rate of 50 mVs^{-1} in 0.1 M KOH from 1.0 V to 1.9 V vs. RHE and are iR compensated (cf. Section 3.3.4). For a better comparison of the activity on the support materials, the boundary values of the x- and y-axis scales are equally stacked.

It is noticeable, that the low-temperature sample (dark blue) shows comparable activity on HOPG (cf. Figure 3.5.1b), ITO/Au (cf. Figure 3.5.1c), and SS (cf. Figure 3.5.1d). The maximum current densities (j_{max}) reached for these substrates in the applied potential range are 6.52 mA cm^{-2} (HOPG) > 5.86 mA cm^{-2} (SS) > 5.04 mA cm^{-2} (ITO/Au), which is a significantly higher activity as was reached for the manganese oxide deposited on titanium substrates ($j_{\text{max}}=0.61\text{ mA cm}^{-2}$). However, the low-temperature phase deposited onto GC exhibited after

the EC conditioning only a maximum current density of 0.94 mA cm⁻². In the appendix (cf. **Figure A 11**), the first five CV cycles of this sample are shown. It is observable that the electrocatalytic activity decreases significantly after the first ($j_{max}^{\#1}=7.87$ mA cm⁻²) and second CV cycle ($j_{max}^{\#2}=6.80$ mA cm⁻²). The lowest j_{max} was recorded after the fifth subsequent cycle ($j_{max}^{\#5}=0.94$ mA cm⁻²). From XPS analysis after the EC investigation, a complete detachment of the catalyst from the substrate was observed (cf. **Figure A 11**). Thus, the measured current density after five cycles is attributed to a blank GC substrate, which consequently explains the low activity or rather electrocatalytic inertness towards the OER.^{[137]–[139]}

The fact that the low-temperature phase detaches from the substrate, explains why the high-temperature sample on GC shows higher activity than the low-temperature sample. For all other tested support materials, the opposite trend is observable. On HOPG and SS the low-temperature sample shows superior catalytic activity compared to the high-temperature sample. For ITO/Au no high-temperature phase was investigated. Even on the titanium substrates, a higher catalytic activity was measured for the low-temperature phase (cf. **Figure 3.4.4**). The high-temperature phase shows the highest maximum current density deposited on GC ($j_{max}=3.23$ mA cm⁻²) followed by HOPG ($j_{max}=2.82$ mA cm⁻²), SS ($j_{max}=2.09$ mA cm⁻²) and Ti ($j_{max}=0.22$ mA cm⁻²). A summary of the measured EC characteristics is given in **Table 3.5.2**.

Table 3.5.2: Summary of the overpotentials (η_l) at a current density of 1 mA cm⁻² and the maximum reached current densities (j_{max}) in the measured potential range for the manganese oxides deposited at substrate temperatures (T_{Sub}) of 150 °C and 300 °C on several support materials. The overpotentials were determined with iR compensation (cf. **Section 3.3.4**).

Phase	Mn ₂ O ₃ ($T_{Sub}=150$ °C)		Mn ₂ O ₃ & MnO ($T_{Sub}=300$ °C)	
	η_l (mV) at $j=1$ mA cm ⁻²	j_{max} (mA cm ⁻²)	η_l (mV) at $j=1$ mA cm ⁻²	j_{max} (mA cm ⁻²)
Ti/TiO ₂	–	0.61	–	0.22
GC	–* ¹	0.94* ¹	490	3.23
HOPG	450	6.52	510	2.82
ITO/Au	470	5.04	–	–
SS	440	5.86	530	2.09

*¹ Manganese dioxide (MnO₂) was found on the GC support after the deposition at $T_{Sub}=150$ °C. After the first two CV cycles the layer was detached from the support (cf. **Figure A 11**).

As a reason for the superior catalytic performance of the low-temperature phase, the higher electrical conductivity of pure Mn₂O₃ compared to a Mn₂O₃ phase mixed with MnO was considered since MnO exhibits a far lower electrical conductivity compared to Mn₂O₃.^{[140], [141]} Another

possible explanation is that the transformation of the mixed Mn_2O_3 & MnO phase into the EC active MnO_2 could be hindered, and thus, a complete transformation into MnO_2 is not possible. This assumption will be further discussed in **Section 3.5.3**.

One explanation for the significant higher activity of both manganese oxide phases on HOPG, ITO/Au, and SS compared to Ti/ TiO_2 could be the native oxide layer on titanium, which has been part of the discussion by Morita *et al.*^{[89], [90]}. They investigated the effects of precious metal supports and precious metal interlayer (Ti/ MnO_x , Ti/ $\text{RuO}_x/\text{MnO}_x$, and Pt/ MnO_x) on the catalytic performance of manganese oxide catalysts, demonstrating that the overpotential at a current density of 10 mA cm^{-2} of the Ti/ MnO_x catalyst system gets reduced by 100 mV to 200 mV by a RuO_x interlayer.^[89] They attributed the low catalytic activity to a native oxide layer on the titanium and to the generation of a mixed phase of MnO_x and TiO_2 phase at the interface of the two materials. The titanium substrates used in this work exhibit a native titanium oxide layer. From the XPS analysis of the cleaning procedure, the layer thickness of the native oxide layer can be estimated to be below 10 nm since the metallic titanium signal in the Ti 2p photo-emission line is visible at a binding energy of 454.5 eV (*cf.* **Figure A 2**). However, the native oxide layer on top of titanium can reduce the overall conductivity of the catalyst support system. Similar results were found by Connor^[142], who investigated interfaces between sputter-deposited manganese oxides and different support materials electrochemically with impedance spectroscopy. The measurements showed that the Ti/ TiO_x supports exhibit an additional contribution to the impedance value, while the ITO/Au support system only exhibits the impedance value of the catalyst/electrolyte interface.^[142] Schmeißer *et al.*^[143] even reported that no ohmic properties are found at a metal contacted to an oxidic interlayer. At the contact, a double-layer potential is formed, which leads to an offset voltage at the interface.^[143]

In addition to the catalytic activity of a catalyst system, the stability plays a key role in the applicability of a catalytic material. The stability measurements were conducted for the most active catalyst phase ($T_{\text{Sub}}=150 \text{ }^\circ\text{C}$) deposited on the best working support materials (SS and HOPG) with chronoamperometry (CA) at a constant potential of 1.8 V vs. RHE for 2 h. In **Figure 3.5.2a** the CVs of the low-temperature phase deposited onto HOPG and SS are shown without iR correction. The reached current density is marked in red and projected to the CA measurement (*cf.* **Figure 3.5.2b**) as an expected reference value. In the CVs, both catalytic systems show with a reached current density of approximately $j_{\text{CV}}= 2.7 \text{ mA cm}^{-2}$ at 1.8 V vs. RHE comparable catalytic activity. During the CA measurement, however, two different trends for the catalytic systems are emerging. The current density of the manganese oxide catalyst deposited on HOPG decreases by approximately 0.7 mA cm^{-2} over the first 15 minutes until the current stabilizes and remains stable until the end of the measurement time at a current density of $j_{\text{end}}=2.1 \text{ mA cm}^{-2}$. The manganese oxide catalyst deposited on SS exhibits a linear increase in current density over the whole measurement time of about 0.8 mA cm^{-2} to a final current density

of $j_{end}=3.5 \text{ mA cm}^{-2}$. From an XPS analysis after the CA measurement, an increase in the Fe 2p photoemission line is visible for the catalyst deposited onto the SS substrate (*cf.* **Figure 3.5.3**), which is equivalent to a decrease in the layer thickness of the manganese oxide catalyst.

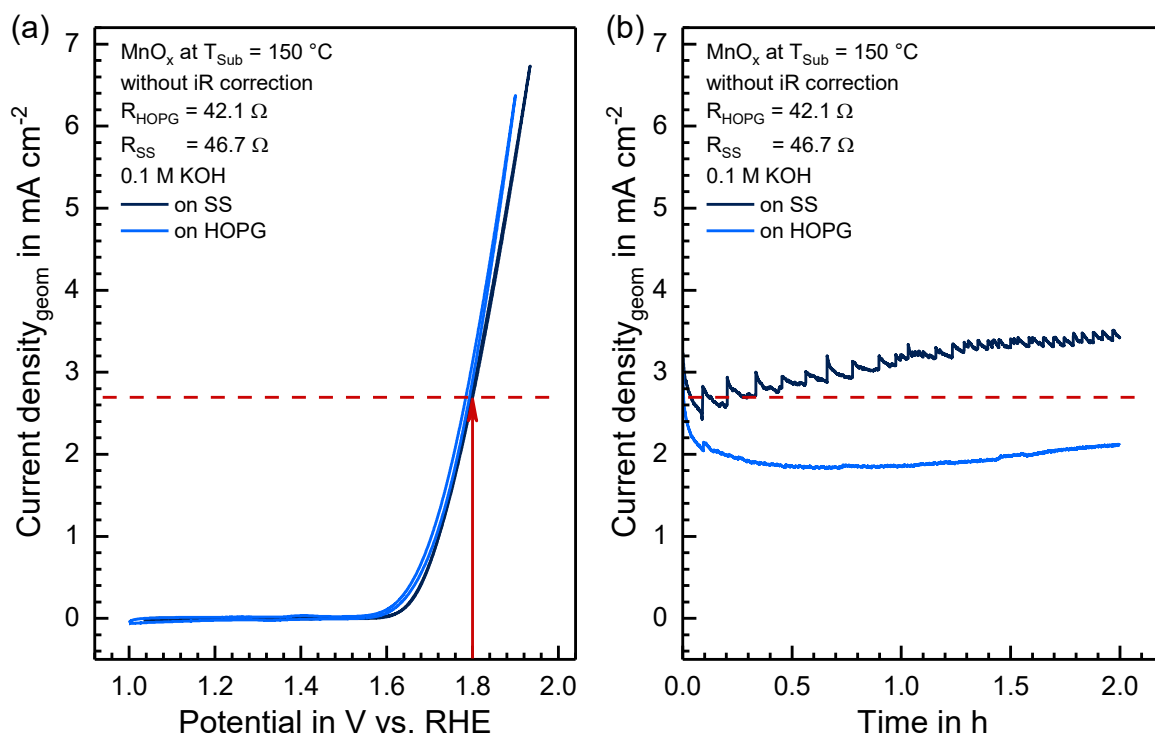


Figure 3.5.2: (a) Cyclic voltammograms (CVs – $v=50 \text{ mV s}^{-1}$) of the Mn_2O_3 ($T_{\text{Sub}}=150 \text{ }^\circ\text{C}$) phase on stainless-steel (SS) and highly oriented pyrolytic graphite (HOPG) in 0.1 M KOH without iR correction. The electrolyte resistance for the two samples (R_{SS} & R_{HOPG}) are determined with electrochemical impedance spectroscopy (EIS). (b) Chronoamperometry at a constant potential of 1.8 V vs. RHE of the same samples for 2 h. The red line illustrates the current density reached with the CV measurement. The emerging maxima and minima in the current density are due to oxygen evolution at the surface of the catalyst. The gas bubbles block parts of the catalyst’s surface until they reach a critical size and detach from the surface leading to an abrupt rise in current density.

Since the SS support material exhibits an intrinsic catalytic activity towards the OER, the increase in current density during the CA measurement is attributed to a partial contribution of the support material to the oxygen evolution. The XPS analysis after the CA measurement of the manganese oxide deposited on HOPG does not deliver a distinct result in terms of the layer thickness because the HOPG substrate consists of carbon and, thus, overlaps with the photoemission line of carbon impurities and hydrocarbons. The carbon impurity and hydrocarbon content on the surface increases during the *ex-vacuo* transport and during the EC investigation, falsifying the substrate signal.

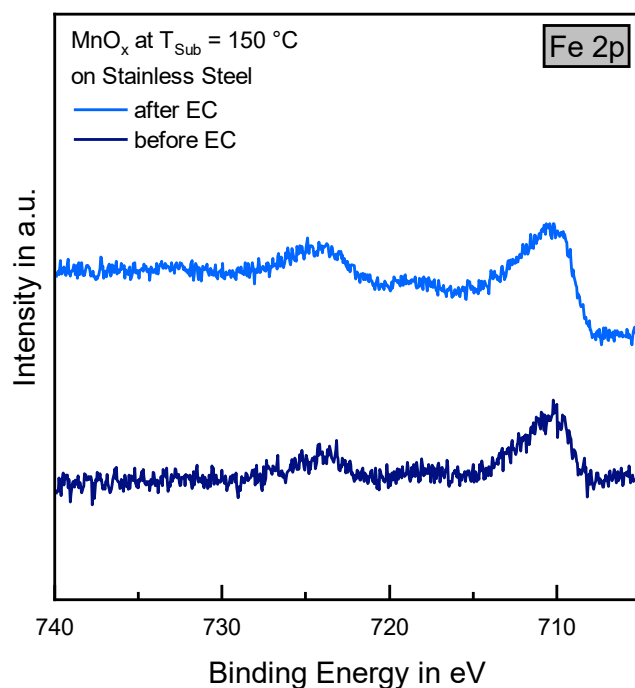


Figure 3.5.3: XP Fe 2p detail spectra of the low-temperature manganese oxide ($T_{Sub}=150\text{ °C} - \text{Mn}_2\text{O}_3$) sample deposited on a stainless-steel substrate before (dark blue) and after electrochemical stability test (light blue).

3.5.3 Changes in oxidation state during the electrochemical investigation

In addition to the XPS measurement after the stability testing, an XPS analysis after the standard EC investigation of all samples was conducted to monitor changes happening during the EC testing. The XPS characteristics of the manganese oxide phases (with $t_{dep}=20\text{ min}$) deposited at substrate temperatures of 150 °C and 300 °C before and after the EC investigation are summarized for the used substrates in **Table 3.5.3**. It is observable that all phases experience a change during the EC testing. This change can mainly be identified in the Mn $2p_{1/2}$ to satellite energy difference and in the Mn 3s multiplet splitting energy difference.^{[79], [118]–[120], [122]–[126]}

The evaluated binding energies of the characteristic photoemission line positions (*cf.* **Table 3.5.3**) indicate an oxidation state of manganese between Mn^{3+} and Mn^{4+} ,^{[79], [118]–[120], [122]–[126]} which is expected for manganese oxide OER catalysts in alkaline media.^{[87], [90], [93], [100], [106]} On titanium and stainless-steel support materials, the low-temperature samples exhibit a slightly higher Mn $2p_{1/2}$ to satellite energy difference and a slightly lower Mn 3s multiplet splitting energy difference after the EC testing compared to the high-temperature samples. Consequently, the manganese of the low-temperature phases possesses a higher oxidation state after the EC investigation than the manganese in the high-temperature phase.^{[118]–[120]} This observation fits the assumption that the high-temperature sample exhibits a hindrance towards the formation of the EC active MnO_2 phase during the EC testing and, thus, exhibits lower catalytic activity than the low-temperature phase.

Table 3.5.3: XPS characteristics of the electrochemical investigated manganese oxide phases (cf. Section 3.5.2) deposited at substrate temperatures (T_{Sub}) of 150 °C and 300 °C on titanium foil (Ti – with native titanium oxide (TiO₂) layer), glass-like carbon (GC), highly oriented pyrolytic graphite (HOPG), glass with indium tin oxide (ITO) with 50 nm of sputtered gold (Au), and stainless-steel*¹ (SS).

Substrate	T_{Sub}	Δ Mn 2p _{1/2} to satellite energy difference		Δ Mn 3s multiplet splitting energy difference		O 1s	
		before EC	after EC	before EC	after EC	before EC	after EC
Ti/TiO ₂	150 °C	10.0 eV	11.1 eV	5.3 eV	5.0 eV	530.1 eV	529.4 eV
Ti/TiO ₂	300 °C	6.0 eV 10.0 eV	- 10.9 eV	5.7 eV	5.1 eV	530.2 eV	529.6 eV
GC	150 °C	11.6 eV	–* ³	4.9 eV	–* ³	529.2 eV	–* ³
GC	300 °C	6.0 eV 10.1 eV	- 10.7 eV	5.7 eV	5.3 eV	530.0 eV	529.5 eV
HOPG	150 °C	10.4 eV	11.0 eV	5.3 eV	5.0 eV	529.8 eV	529.4 eV
HOPG	300 °C	6.8 eV 10.2 eV	- 10.9 eV	5.7 eV	5.0 eV	529.8 eV	529.4 eV
Glass/ITO/Au	150 °C	10.6 eV	11.1 eV	– * ²	–* ²	529.4 eV	529.3 eV
SS* ¹	150 °C	10.4 eV	11.0 eV	5.3 eV	5.0 eV	529.5 eV	529.3 eV
SS* ¹	300 °C	5.9 eV 10.3 eV	- 10.7 eV	5.7 eV	5.3 eV	529.8 eV	529.6 eV

*¹ polished stainless-steel (X5CrNi18-10 – TK 1.4301)

*² no evaluation possible due to an overlap of the Mn 3s signal with the Au 4f photoemission line

*³ no evaluation possible due to a detachment of the catalyst

3.6 Conclusions

In the first part of this work, thin manganese oxide films were successfully deposited via a PECVD process onto different substrates. To explore the possibilities and limits of the deposition technique the generated thin-film catalysts were investigated with XPS on titanium. Based on the variation of the substrate temperature, a pure Mn_2O_3 phase and a mixed $\text{Mn}_2\text{O}_3/\text{MnO}$ phase were synthesized. The pure Mn_2O_3 phase was produced at substrate temperatures above $150\text{ }^\circ\text{C}$ and below $250\text{ }^\circ\text{C}$, while the mixed $\text{Mn}_2\text{O}_3/\text{MnO}$ phase was formed at substrate temperatures above $250\text{ }^\circ\text{C}$. The variation of oxygen content inside the reactive gas showed no impact on the prepared manganese oxide phase composition.

While the manganese oxide thin film catalysts showed no stability in 1 M KOH towards the OER, maximum current densities of 0.54 mA cm^{-2} and 0.19 mA cm^{-2} were achieved at a potential of 1.9 V vs. RHE in 0.1 M KOH for the low-temperature and high-temperature phase, respectively. The low achieved current densities are attributed to a native titanium dioxide interlayer on top of the titanium substrate material, possessing only poor electrical conductivity.^[89]
[90]

Initially, the deposition of manganese oxide thin films onto silicon photoabsorber systems were planned. Due to the low current densities reached by the MnO_x catalyst system the application as a catalyst in a photoelectrochemical system can be advantageous compared to the usage as a standard catalyst in the dark, at which higher current densities are applied. But due to the poor stability of the MnO_x catalyst systems in 1 M KOH , this work package was not pursued further.

In a second step, the established manganese oxide phases were deposited onto substrates that do not form non-conductive native oxide layers, namely HOPG, GC, ITO/Au, and SS. As substrate temperatures $T_{\text{Sub}}=150\text{ }^\circ\text{C}$ for the pure Mn_2O_3 and $T_{\text{Sub}}=300\text{ }^\circ\text{C}$ for the mixed $\text{Mn}_2\text{O}_3/\text{MnO}$ phases were chosen, respectively. Equal compositions of the manganese oxide thin films were achieved for all substrate materials at the characteristic substrate temperatures. Only the low-temperature ($T_{\text{Sub}}=150\text{ }^\circ\text{C}$) phase deposited on GC showed XPS characteristics of MnO_2 instead of an Mn_2O_3 phase. However, the subsequent EC analysis of that catalyst in 0.1 M KOH led to a complete dissolution of the MnO_2 after five CV cycles. The pure Mn_2O_3 sample showed with an average maximum current density of $j_{\text{max}}^\theta=5.81\text{ mA cm}^{-2}$ a higher activity on all other tested substrates, compared to the average maximum current density of $j_{\text{max}}^\theta=2.71\text{ mA cm}^{-2}$ for the mixed $\text{Mn}_2\text{O}_3/\text{MnO}$ phases (cf. **Figure 3.6.1**). The increased activity of the pure Mn_2O_3 catalysts compared to the mixed $\text{Mn}_2\text{O}_3/\text{MnO}$ phases are, on the one hand, attributed to a better intrinsic conductivity of the thin films in the absence of MnO ,^{[140], [141]} and, on the other hand, a better transition capability of the Mn_2O_3 to the EC active $\text{Mn}_2\text{O}_3/\text{MnO}_2$ during the EC investigation.^{[87], [90], [93], [100], [106]}

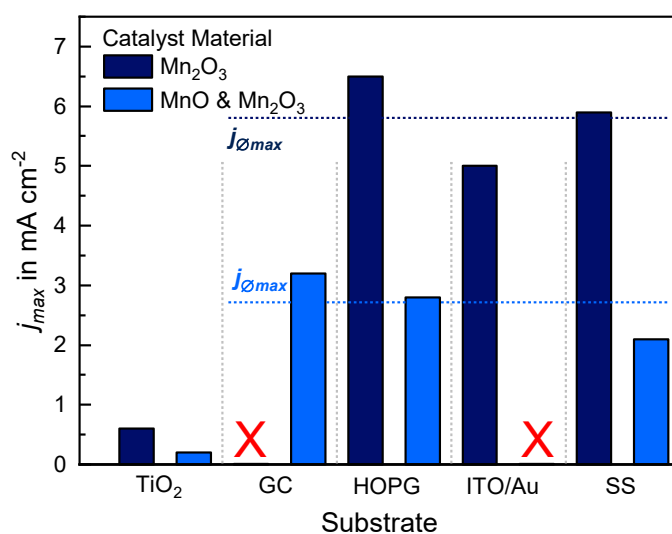


Figure 3.6.1: Summary of the current densities (j_{max}) reached at 1.9 V vs. RHE in 0.1 M KOH with the Mn₂O₃ and MnO & Mn₂O₃ catalysts on different substrate materials. The dotted lines indicate the average maximum current density ($j_{\phi_{max}}$) reached for the Mn₂O₃ (blue) and MnO/Mn₂O₃ (light blue) on substrate that do not form a non-conductive native oxide layer (GC, HOPG, ITO/Au, and SS).

Additionally, the catalysts with the highest achieved current densities (Mn₂O₃ on HOPG and Mn₂O₃ on SS) showed a stable behavior at a constant potential of 1.8 V vs. RHE in 0.1 M KOH for 2 hours.

PART B

Transition metal borides for the oxygen evolution reaction

4 Transition metal borides for the oxygen evolution reaction

The second part of this work is motivated by the search for new catalyst systems for the OER, consisting of non-noble metal cations and nonmetal anions. The transition metal borides were provided by the research group of Professor Barbara Albert (TU Darmstadt, department of chemistry, Eduard-Zintl-institute of inorganic and physical chemistry). Preliminary work for this study concerning the choice of substrate material and the investigation of the ideal ink composition for these structures was performed by M.Sc. Stefan Hawel (master's thesis). Additional EC investigations concerning primarily cobalt-nickel boride structures were performed by Patrick Schuldt (student assistant). The results presented in **Section 4.3** concerning tricobalt boride were published in the journal *Inorganic Chemistry*,^[144] the results presented in **Section 4.4** were published in the journal *ChemSusChem*,^[145] and the results presented in **Section 4.5** were published in the journal *ChemCatChem*.^[146]

In this study, dicobalt boride (Co_2B) is used as a starting material (*cf.* **Section 4.3**), since the cobalt system is a well-characterized system for water electrolysis and cobalt oxides were already characterized in terms of their activity towards the OER by Dr. Natascha Weidler.^{[135], [147]} The Co_3B is investigated as a second binary system (*cf.* **Section 4.3**). Additionally, to the binary Co_2B and Co_3B systems, the combination of Co_2B with other transition metals is investigated. Therefore, iron and nickel with different concentrations are incorporated into the Co_2B phase, forming $(\text{Co}_{1-x}\text{Fe}_x)_2\text{B}$ (*cf.* **Section 4.4**) and $(\text{Co}_{1-x}\text{Ni}_x)_2\text{B}$ (*cf.* **Section 4.5**) with $0 \leq x \leq 0.5$.

4.1 State of the art

Transition metal borides (TMBs) can offer a variety of different structures and properties, which lead to different potential application fields. Besides their high hardness, melting points, and thermal conductivity, they exhibit different functional properties like superconductivity, magnetic properties, and catalytic activities.^{[148]–[150]}

4.1.1 Crystal structure

The dimetal borides (M_2B – with $\text{M} = \text{Co}, \text{Fe}, \text{and Ni}$) crystallize in the Al_2Cu tetragonal structure (*cf.* **Figure 4.1.1a**), while the Co_3B crystallizes in the Fe_3C orthorhombic structure (*cf.* **Figure 4.1.1b**).^{[148], [149], [151], [152]} Both structures belong to the class of TMBs with isolated boron atoms. The Al_2Cu and Fe_3B structure for the synthesized $(\text{Co}_{1-x}\text{Fe}_x)_2\text{B}$ and $(\text{Co}_{1-x}\text{Ni}_x)_2\text{B}$ and the Co_3B catalysts was confirmed by X-ray diffraction (XRD) measurements (*cf.* **Figure A 12**, **Figure A 13**, and **Figure A 14**). With the incorporation of iron into the Co_2B , an increase in unit cell

volume was observed.^{[145], [153]} The change in the unit cell of the incorporation of nickel into Co_2B was not investigated.

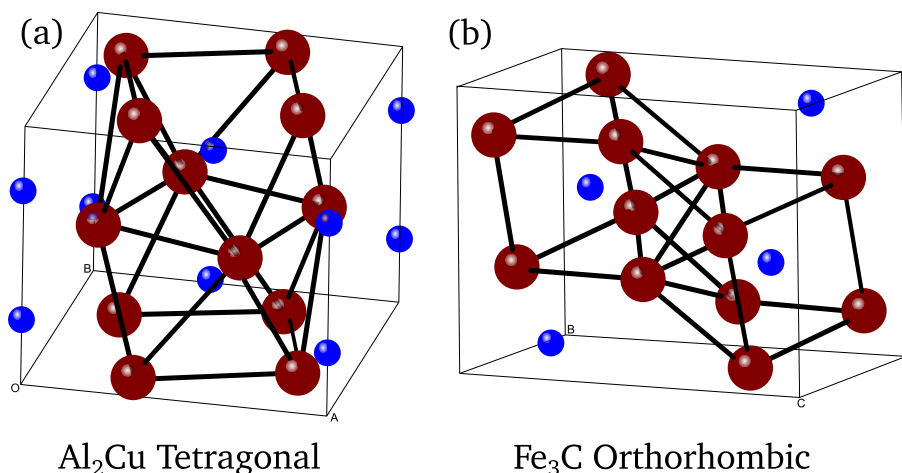


Figure 4.1.1: (a) Structure types for the di-metal (M_2B) and (b) tri-metal boride (M_3B) phases. The M_2B phases (with $\text{M} = \text{Co}, \text{Fe}, \text{Ni}$) crystallize in the Al_2Cu tetragonal structure, while M_3B (with $\text{M} = \text{Co}$) crystallizes in the Fe_3C orthorhombic structure.^{[148], [149], [154][155]} Boride atoms are illustrated in blue and metal atoms are shown in red. Adapted and modified from^[148].

4.1.2 Water electrolysis

The applicability of TMBs as electrocatalysts for the OER was already observed by Osaka *et al.*^{[156], [157]} as early as 1980. However, the research efforts of TMBs for water electrolysis remained static until recently, when the research and the funding for finding new catalyst materials for the water-splitting reaction have been intensified, due to rising costs in already established noble metal (Pt, Ru, Ir, etc.) catalyst systems.^{[18], [19], [39], [158]} The scope of finding new materials went from transition metal oxides to materials beyond the oxidic character. These materials were formed out of comparable transition metal cations, but with substitutional anions like nitrogen,^{[30], [31]} phosphor,^{[159]–[162]} or boron^{[163], [164]}.

In the last 5 years, a lot of studies with different TMBs have been conducted with respect to the water-splitting reaction. The binary cobalt,^{[165], [166]} nickel,^{[167], [168]} and iron boride^[169] systems were investigated by several groups for their HER and OER performance.

After the first investigation of Co_2B in alkaline media (0.1 M KOH) by Masa *et al.*,^[165] Ma *et al.*^[166] studied the differences in activity of Co_xB (with $x=1-3$) for the OER in alkaline media. They found that Co_2B is the most active of the three Co_xB phases for the OER in 1 M KOH and 0.1 M KOH. The overpotential values achieved at 10 mA cm^{-2} (η_{10}) by Co_2B on glass-like carbon (GC) in 0.1 M KOH ($\eta_{10}=371 \text{ mV}$) were comparable to the ones published by Masa *et al.*^[165] ($\eta_{10}=380 \text{ mV}$). In contrast to Co_xB , Ni_xB was at first only investigated towards the HER, showing

with overpotential values of $\eta_{20}=194$ mV (Ni_2B)^[167] and $\eta_{10}=135$ mV ($\text{Ni}_{2.7}\text{B}$)^[168] at current densities of 20 mA cm^{-2} and 10 mA cm^{-2} only moderate activity in 1 M KOH. The most active phase for the HER was identified by Li *et al.*^[169] to be FeB_2 . In 1 M KOH, the FeB_2 electrode reached remarkable low overpotentials for the HER ($\eta_{10}=61$ mV) and the OER ($\eta_{10}=296$ mV). The activity can be traced back to high surface areas measured by the Brunauer-Emmett-Teller method (BET). A summary of the relevant parameters of the previously mentioned publications is shown in **Table 4.1.1**.

Table 4.1.1: The different single metal boride – M_xB (M= Co, Ni, Fe) catalysts from Masa *et al.*^[165] Ma *et al.*^[166] Zhang *et al.*^[167] Zeng *et al.*^[168] and Li *et al.*^[169] investigated in alkaline electrolytes are summarized. The respective catalyst loadings, overpotentials for current densities of 10 mA cm^{-2} (η_{10}) or 20 mA cm^{-2} (η_{20}) for the OER and HER, and the used substrates are listed.

Catalyst	Substrate	Electrolyte	Loading in mg cm^{-2}	BET in $\text{m}^2 \text{ g}^{-1}$	Overpotential η in mV	
					HER	OER
Co_2B ^[165]	GC	0.1 M KOH	0.21	9.70	$\eta_{10}=328$	$\eta_{10}=380$
CoB ^[166]	GC	0.1 M KOH	0.20	-	-	$\eta_{10}=405$
Co_2B ^[166]	GC	0.1 M KOH	0.20	-	-	$\eta_{10}=371$
Co_3B ^[166]	GC	0.1 M KOH	0.20	-	-	$\eta_{10}=378$
Co_2B ^[166]	Carbon Paper	1 M KOH	0.20	-	$\eta_{10}=109$	$\eta_{10}=287$
Ni_2B ^[167]	GC	1 M KOH	1.00	-	$\eta_{20}=194$	-
$\text{Ni}_{2.7}\text{B}$ ^[167]	Cu	1 M KOH	1.40	-	$\eta_{10}=135$	-
FeB_2 ^[169]	GC	1 M KOH	0.20	51 – 65* ¹	$\eta_{10}=61$	$\eta_{10}=296$

*¹ Brunauer-Emmett-Teller (BET) measurements were performed before ($51 \text{ m}^2 \text{ g}^{-1}$) and after electrochemical (EC) investigation ($65 \text{ m}^2 \text{ g}^{-1}$).

Ma *et al.*^[166] attributes the improved catalytic performance of the TMBs compared to the transition metal oxides (TMOs) to the formation of a surface species (MOOH) during the EC investigation, while the metal boron (M_xB) bulk of the material stays intact. The M_xB bulk favors the overall activity of the catalyst by providing a higher electrical conductivity compared to a metal oxide phase.^{[165], [166]} Masa *et al.*^[165] further attributes the improved catalytic performance of the crystalline Co_2B catalyst to the boron itself. They assume that the boron induces strain into the crystal lattice, therefore, potentially reducing the energetic and kinetic barrier for the hydroxylation, meaning that the *OOH intermediate can be formed more easily.

In 2016, the first ternary boride system using nickel-cobalt boride has been investigated by Gupta *et al.*^[170] for its catalytic activity to the HER. In recent years, the research effort of these systems has been increased tremendously. Numerous investigations of mostly Co-Fe,^{[171]–[174]} Ni-Fe,^{[172], [175]} Co-Ni,^{[170], [172], [173], [176], [177]} and also Co-Fe-Ni borides^[173] have been published for catalyzing either the OER, the HER, or both. As substrates mainly inert substrates such as glass-like carbon, copper foil, or carbon sheets, but also substrates with intrinsic activity like nickel foams have been used at different pH values. A general way to compare different TMB systems is difficult to accomplish, due to several different synthesis routes, strongly differing micro- or nanostructures, different electrode assemblies (loading amount, substrate, ink composition, etc.), and largely differing EC surface areas. For interested readers, the first review article concerning TMBs for the EC water splitting reaction by Gupta *et al.*^[32] has just been published. The idea of the incorporation of a second transition metal inside of a known M₂B system is based on the multitude of publications mainly addressing multi-metal oxides for catalysis purposes.^{[45], [47]–[54]} It is known that a mixture of at least two 3d metals can enhance the overall catalytic performance of the metal oxide compounds.^{[45], [47], [49], [50], [52]} The enhanced catalytic performance is mostly attributed to synergetic effects between the metals involved. However, most of these processes are not well understood in detail. Models regarding synergetic effects are summarized in **Section 2.2.2**.

4.1.3 Electrochemical redox behavior

In this work, a defined EC protocol (*cf.* **Section 4.2.5**) was used for the transition metal borides in an alkaline electrolyte. The protocol was developed to stimulate specific electrochemically induced redox reactions of the catalyst in this environment. It is well known that starting materials tend to transform in aqueous electrolytes during the water oxidation reaction. These transformations can either lead to the development of a stable passivation layer or result in the formation of an unstable soluble phase. The “Atlas of electrochemical Equilibria in Aqueous Solutions”^[178] reports the potential-to-pH equilibrium diagrams in water for numerous elements. These potential-to-pH diagrams (Pourbaix diagrams) describe the thermodynamics of EC reactions of a material at a certain potential in a given environment. The following paragraphs discuss the EC redox behavior of relevant elements, *i.e.* cobalt, iron, and nickel in alkaline media.

Cobalt electrodes

In **Figure 4.1.2** the Pourbaix diagram of cobalt in water is shown. In comparison to the data published by Pourbaix^[178] in 1966, more recently produced data introduce only slight changes.^[179] Apart from minor changes regarding potential values for the formation of the different oxide and hydroxide phases, recent publications have replaced the $\text{Co}(\text{OH})_3$ phase with the CoOOH phase. In the used electrolyte ($\text{pH}=14$) cobalt transforms at around -0.7 V vs. NHE to $\text{Co}^{2+}(\text{OH})_2$ and is suggested to be stable until -0.2 V vs. NHE. After that, $\text{Co}(\text{OH})_2$ converts first to Co_3O_4 (mixed oxidation state of $\text{Co}^{2+}/\text{Co}^{3+}$) and then at a potential of 0.1 V vs. NHE to Co^{3+}OOH . At potentials around 0.9 V vs. NHE, it is suggested that CoOOH transforms further to Co^{4+} forming the CoO_2 phase.^[179] Already in 1971, Behl and Toni^[180] investigated the anodic oxidation of cobalt in KOH. They used a rotating ring disc electrode (RRDE) to investigate the oxidative nature of cobalt metal rods in KOH.

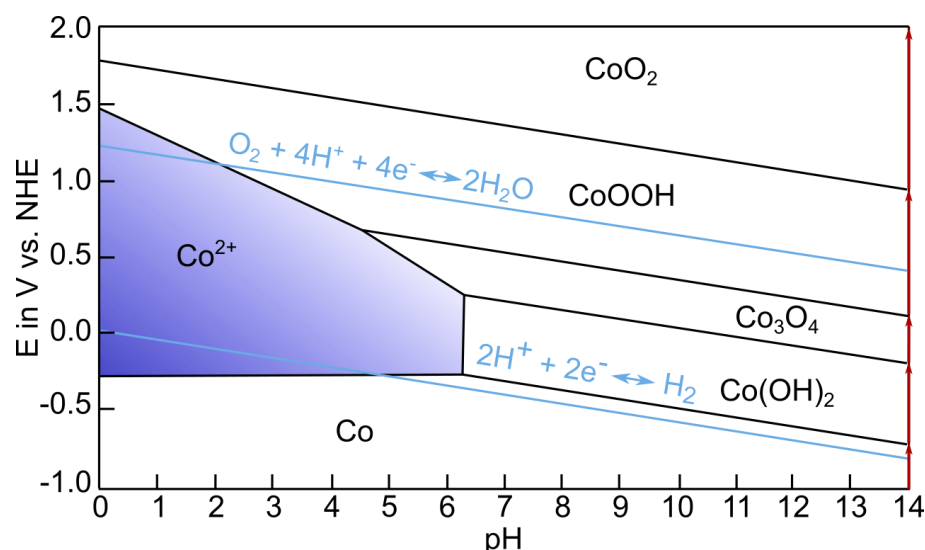


Figure 4.1.2: Pourbaix diagram of cobalt in water adapted and modified from ^[179]. The red arrows show the transition of the cobalt electrode at the used $\text{pH}=14$. In blue the unstable regime is marked.

In **Figure 4.1.3** the CV curve of cobalt in 1 M KOH in the range of -1.1 V to 0.7 V vs. Hg/HgO is shown. The corresponding reactions for the labeled oxidation peaks I-V in the CV are given in **equation 4.1.1** to **4.1.4**. Behl and Toni^[180] found that after the transition to $\text{Co}(\text{OH})_2$ (peak II) the phase becomes soluble until the formation of a few monolayer thin Co_3O_4 species at peak III. Subsequently, peak IV represents the oxidation from Co^{2+} to Co^{3+} forming CoOOH . Peak V is attributed to the oxidation of Co^{3+} to Co^{4+} in CoO_2 . In an article by Benson *et al.*^[181], the formation of $\text{Co}(\text{OH})_3$ was disproven and the formation of CoOOH was verified by XRD. The formation of CoO_2 has been a topic of discussion since the phase transformation from CoOOH to CoO_2 is reversible and therefore it is only detectable by in-operando measurement

techniques. Since the work of Hamdani *et al.*^[182] and Simpraga, it is agreed that close to the water oxidation reaction of cobalt the CoOOH transforms into CoO₂. Behl and Toni^[180] observed two reduction waves in the cyclic voltammetry curve of cobalt at a potential around 1.06 V vs. RHE and between 0.16 V and 0.36 V vs. RHE. The first wave (Peak VI) is attributed to a reduction of CoOOH to Co(OH)₂, while other more recent studies attribute a long and broad peak (cf. Figure 4.1.4 - peak VII) between -0.8 V and -0.4 V vs. Hg/HgO (roughly around 0.1 and 0.5 V vs. RHE) to the reduction of the Co³⁺ species to Co²⁺.^{[183]-[187]} In 2013, Doyle *et al.*^{[186], [187]} stated that the reduction waves found above 1.0 V vs. RHE are attributed to the reduction of the former formed CoO₂ to a CoOOH phase and that the reduction to a Co²⁺ species happens at lower potentials.

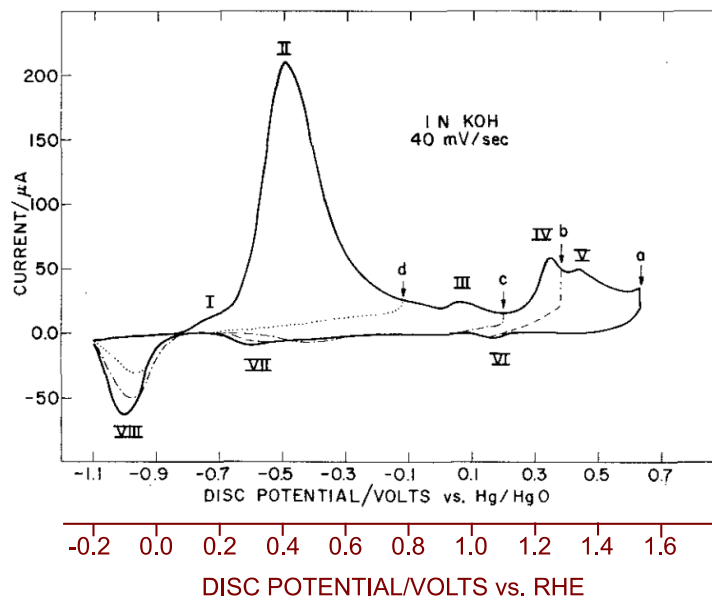
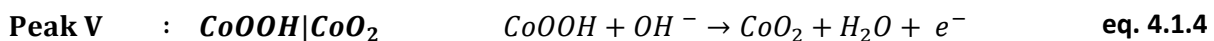
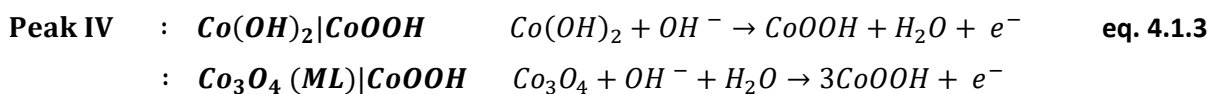
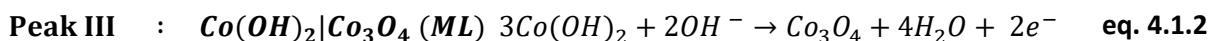
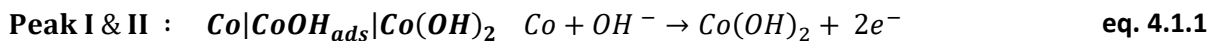


Figure 4.1.3: Cyclic voltammogram of a cobalt electrode in 1 M KOH. Adapted from ^[180] and modified with a second potential scale vs. RHE. The potential scale vs. RHE was calculated with the given reference electrode ($E^0_{\text{Hg}/\text{HgO}}=0.098$ V), using pH=14 for the used electrolyte according to **equation 3.3.1** (cf. **Section 3.3.4**). For more information see text.



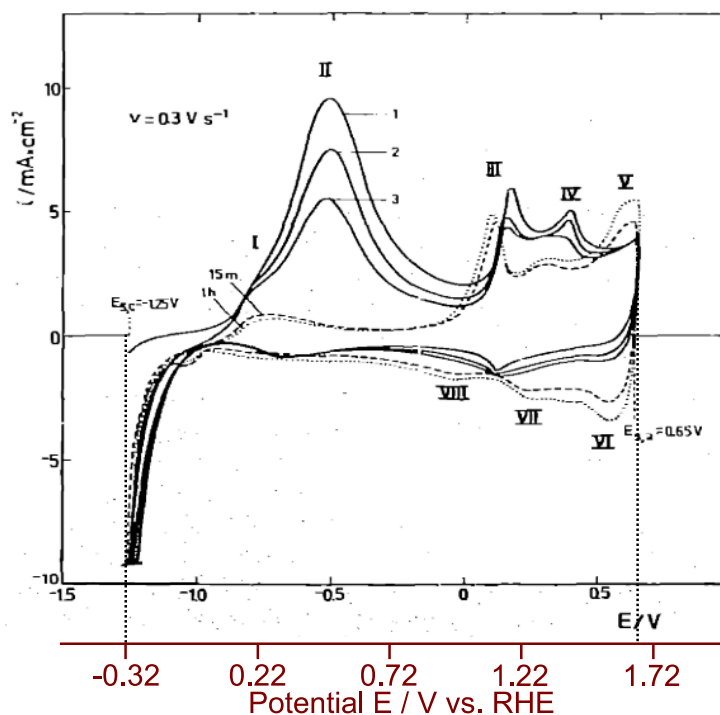


Figure 4.1.4: Cyclic voltammogram of a cobalt electrode in 1 M KOH. Adapted from ^[184] and modified with a second potential scale vs. RHE. The potential scale vs. RHE was calculated with the given reference electrode ($E^0_{\text{Hg}/\text{HgO}}=0.098$ V), using pH=14 for the used electrolyte according to **equation 3.3.1** (cf. **Section 3.3.4**). Meier *et al.*^[184] observed similar oxidation waves as were published by Behl and Toni^[180] (cf. **Figure 4.1.3**). Their findings vary in terms of reduction behavior of the Co^{3+} to Co^{2+} state. For more information see text and ^[184].

Iron electrodes

In literature, mainly two different Pourbaix diagrams for the iron water system are published. Both show a non-stable behavior of iron in an acidic environment and a passivated iron oxide (Fe_2O_3) or hydroxide ($\text{Fe}(\text{OH})_3$ or FeOOH) in alkaline media at positive potentials (cf. **Figure 4.1.5**).^[178] In 2009, Lyons *et al.*^[188] investigated the redox behavior of iron in NaOH, illustrated in **Figure 4.1.6a**. They proposed an oxidation mechanism, which included the iron oxide as a compact inner interlayer with a hydroxide formation at the outer surface. This structured layer formation is developed at peak A3 and A4 (cf. **Figure 4.1.6**) and is located at the interface between the iron electrode and the electrolyte, according to **equation 4.1.5** and **4.1.6** and **Figure 4.1.6b**. This model was introduced by Burke *et al.*^[189] for iridium oxide in alkaline media and has later been adapted by Lyons *et al.*^[188] for the iron-electrolyte interface in NaOH. The anodic peaks A1 and A2 (cf. **Figure 4.1.6**) are attributed to the adsorption of hydroxide and the formation of iron hydroxide ($\text{Fe}(\text{OH})_2$) with an oxidation state of Fe^{+2} (cf. **Equation 4.1.5**). The reduction peak C2 describes the cathodic complement of A3, reducing the Fe^{3+} to a Fe^{2+} species, while peak C1 corresponds to the further reduction to Fe^0 .^{[186]–[188], [190]}

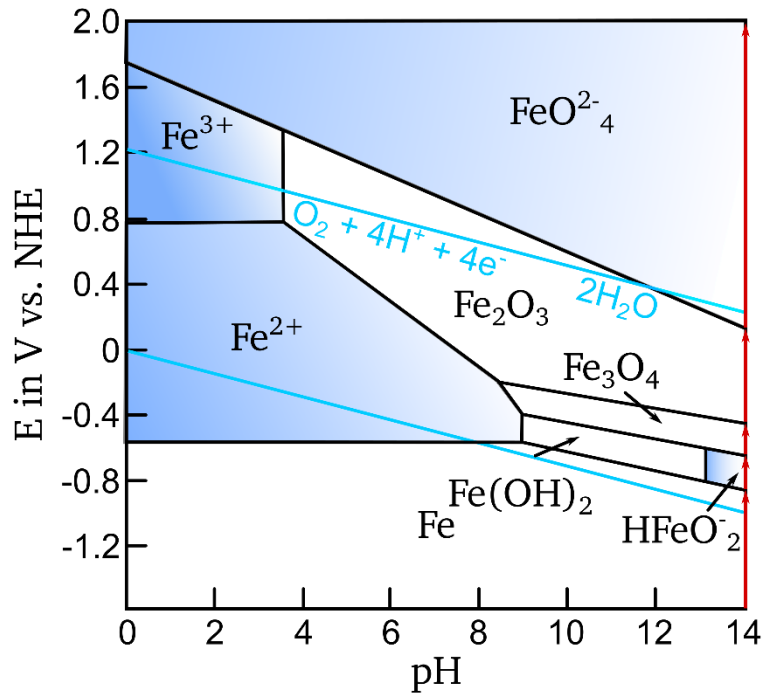


Figure 4.1.5: Pourbaix diagram of iron in water adapted and modified by Pourbaix^[178]. The red arrows show the transition of the iron electrode at the used pH=14. In blue the unstable regime is marked.

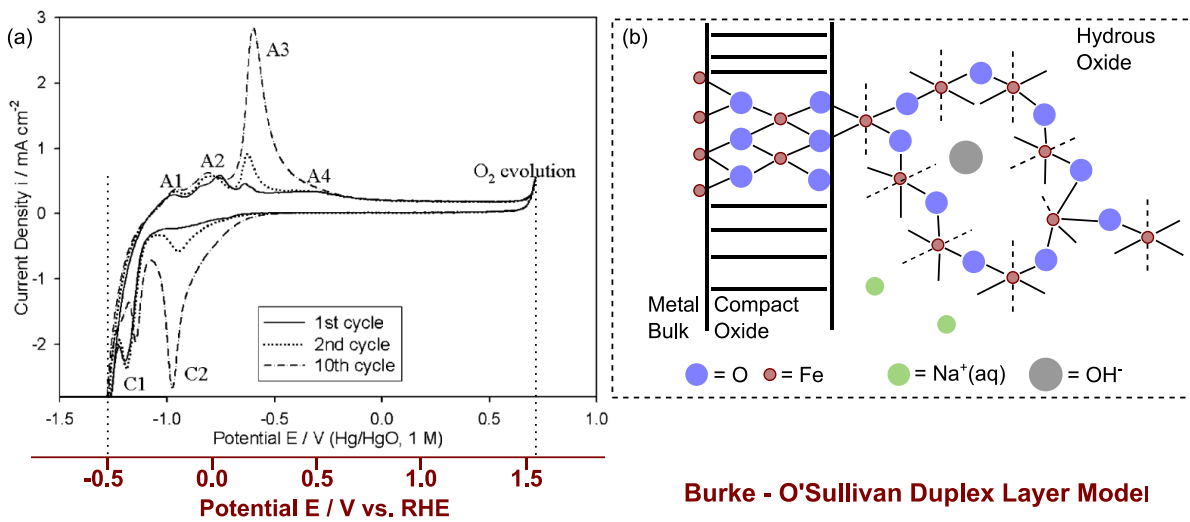
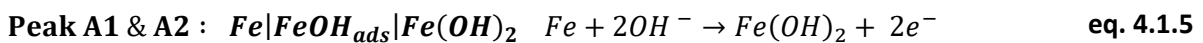


Figure 4.1.6: (a) Cyclic voltammogram of an iron electrode in 1 M NaOH. Adapted from ^[188] and modified with a second potential scale vs. RHE. The potential scale vs. RHE was calculated with the given reference electrode ($E_{Hg/HgO}^0=0.098$ V), using pH=14 for the used electrolyte according to **equation 3.3.1** (cf. **Section 3.3.4**). (b) Schematic picture of the Burke-O'Sullivan Duplex Layer Model^[189] of the metal-electrolyte interface; adapted and modified from ^{[186], [187]}. For more information see text.



Nickel electrodes

In literature, different Pourbaix diagrams for the nickel water system can be found. The proposed phases, which develop in alkaline electrolytes, range from nickel(II)oxide (NiO) to nickel(II)- (Ni(OH)₂), nickel(III)hydroxides (Ni(OH)₃) or nickel(III)oxyhydroxide (NiOOH). Some of these thermodynamically calculated diagrams even show phases of nickel(III)oxide (Ni₂O₃) or nickel(IV)oxide (NiO₂). In **Figure 4.1.7** a respective Pourbaix diagram of the nickel-water system from Huang *et al.*^[191] is depicted, showing the subsequent oxidation of nickel with increased electrode potential.

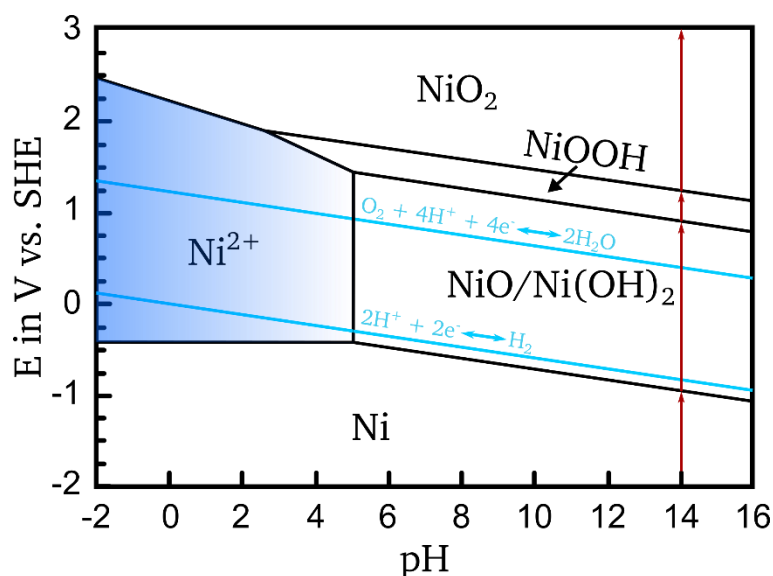


Figure 4.1.7: Pourbaix diagram of nickel in water adapted and modified from ^[191]. The red arrows show the transition of the nickel electrode at the used pH=14. In blue the unstable regime is marked.

From an experimental electrochemical perspective, nickel electrodes spontaneously form a film of a hydrous nickel oxide species α -Ni²⁺(OH)₂ phase when immersed in alkaline media, which can be further transformed reversibly at potentials around 0.5 V vs. Hg/HgO (roughly 1.45 V vs. RHE) to γ -Ni³⁺OOH.^{[190], [192], [193]} In **Figure 4.1.8a** the cyclic voltammograms (adapted from Lyons *et al.*^[193]) of a fresh and an aged nickel electrode after different polarization steps in 1 M NaOH are shown. According to the Bode scheme illustrated in **Figure 4.1.8b**, the hydrous α -Ni²⁺(OH)₂ phase dehydrates and recrystallizes upon aging, forming the less hydrous β -Ni²⁺(OH)₂ phase.^[194] The β -Ni²⁺(OH)₂ transforms reversibly to a β -Ni³⁺OOH phase.^{[193]–[195]} In contrast to the crystalline β -Ni²⁺(OH)₂, both the γ - and β -NiOOH phase are amorphous.^{[193], [196]} Barnard *et al.*^[197] concluded from a series of charging and discharging experiments, that the γ -NiOOH phase has a higher oxidation state (3.3 to 3.67) compared to β -NiOOH (2.7 to 3.0). This difference in oxidation states leads to the higher conductivity of the β -NiOOH compared to the γ -NiOOH phase.

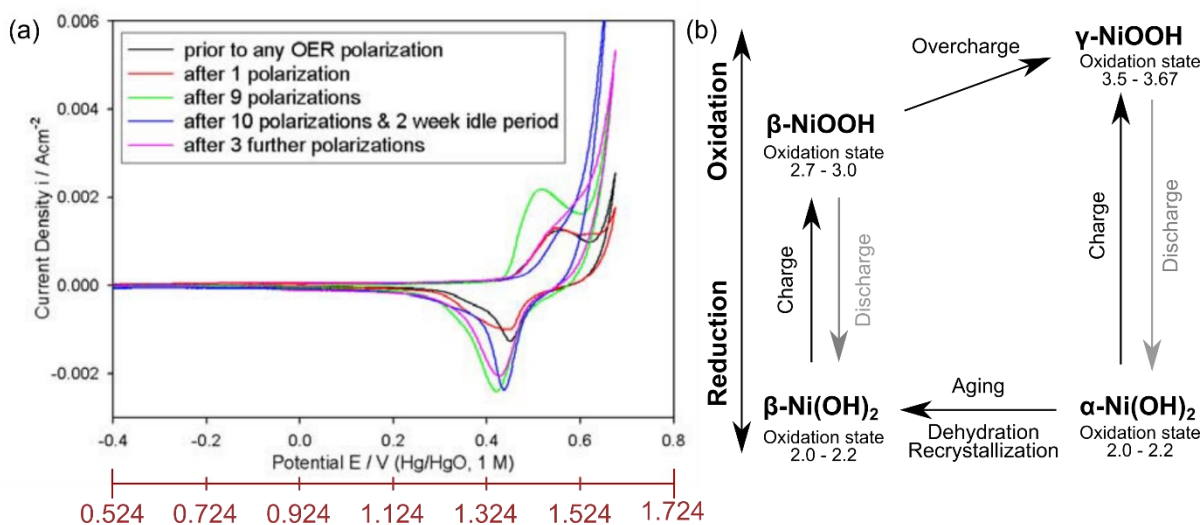


Figure 4.1.8: (a) Cyclic voltammograms of a nickel electrode in 1 M NaOH at 40 mV/s adapted from ^[193] and modified with a second potential scale vs. RHE. The potential scale vs. RHE was calculated with the given reference electrode ($E_{\text{Hg}/\text{HgO}}^0=0.098$ V), using pH=14 for the used electrolyte according to **equation 3.3.1** (cf. **Section 3.3.4**). (b) The Bode scheme for the Ni(OH)₂/NiOOH redox transformation cycle according to ^[194].

As the oxidation states of Ni cannot vary for the stoichiometric compositions the reported variations must be related to defective oxide/hydroxide phases with different contributions of Ni³⁺ and Ni⁴⁺ states and different oxide/hydroxide concentrations. The γ -NiOOH phase contains more Ni⁴⁺, which in turn forms an oxide, leading to a lower overall electronic conductivity of the compound.^{[193], [198], [199]} Barnard *et al.*^{[197], [200]} observed that both the oxidation and reduction peak of the Ni²⁺/Ni³⁺ transition shift to lower potentials for the α - γ transition cycle compared to the β - β cycle. Since Ni(OH)₂ has been investigated for battery applications at the beginning of the second half of the 20th century, the EC redox behavior has been discussed thoroughly in literature.^[195] The Bode phase transition scheme tries to illustrate the complex transformations of nickel hydroxide battery electrodes during the EC investigation (cf. **Figure 4.1.8b**).^[194] Due to a different amount of water intercalation in the α - and β -Ni(OH)₂ phase, not only the unit cell of the material changes during aging but also different transition phases, namely γ - and β -NiOOH, are formed during EC charging. Due to different hydration stages of the Ni(OH)₂ phase, it can also be written as Ni(H₂O)_x(OH)₂. The nickel phases with $0 \leq x \leq 0.1$ are specified as dehydrated β -Ni(OH)₂ and are organized crystalline phases. For $0.1 \leq x \leq 0.4$ the phases are called hydrated β -Ni(OH)₂. Above $x=0.4$ the phases are specified as α -Ni(OH)₂ with a maximum hydration of $x \leq 0.7$.^[195] The less water is intercalated in the system the higher is the degree of crystallization. For more information on this topic the review article by Hall *et al.*^[195] is recommended.

4.1.4 Specifics to X-Ray photoelectron spectroscopy

The investigation of the surface of a catalyst is crucial to understand the changes happening during the water oxidation reaction. With XPS the electronic structure and the oxidation state of the catalyst surface before and after the EC testing can be monitored. Since the main chemical transitions of the catalyst during the OER occur in the reaction layer close to the surface, XPS is, in contrast, to bulk sensitive techniques, beneficial for the investigation of those changes.

In this section, the essential specifics of measuring and analyzing transition metal borides with XPS before and after the EC testing are presented and discussed in detail. The fact, that these metal borides are in powder form makes the XPS analysis demanding.

Cobalt

In contrast to the former investigated Mn-based catalysts (*cf.* **Section 3.1.3**), the oxidation state of Co-based catalyst materials can be distinguished more easily with XPS. Especially cobalt oxides (CoO; Co₃O₄),^{[117], [119], [201]–[204]} hydroxides (Co(OH)₂),^{[117], [201], [203]} and oxyhydroxides (CoOOH)^{[117], [201], [204]} were frequently studied. Additionally, more uncommon Co-based catalysts, like cobalt borides (CoB_i) were studied and can be distinguished well from the above-mentioned cobalt phases.^{[205], [206]} The Co-based compounds relevant for the EC water electrolysis are mainly found with oxidation states of Co⁰(CoP_i; CoB_i), Co^{+II} (CoO; Co(OH)₂; Co₃O₄), and Co^{+III} (CoOOH; Co₃O₄).^[207] The formation of Co^{+IV}O₂ during or rather close to the starting potential of the water oxidation reaction is still under discussion.^{[182], [207], [208]} It is proposed, that CoO₂ should only be visible under reaction conditions and transforms back to its former state at lower potentials.^{[182], [207], [208]} Thus, it cannot be detected by XPS after the EC testing.

Cobalt borides show in the Co 2p photoemission line a peak structure similar to metallic cobalt with a Co 2p_{3/2} main peak located between 778.3 eV^[206] and 777.4 eV^{9 [205]}. The cobalt boride phase can be observed in the B 1s photoemission line around 188.5±0.2 eV.^{[205], [206]} Cobalt oxide (CoO) and cobalt hydroxide (Co(OH)₂) show Co 2p_{3/2} signals around 780.2±0.3 eV^{[117], [201], [202]} and 780.7±0.3 eV,^{[117], [201], [204]} respectively. Both phases show a similar Co 2p photoemission line shape with a satellite peak at an energy difference of 6 eV to the Co 2p_{3/2}. This satellite energy difference is known in literature for cobalt in an oxidation state of Co⁺².^{[117], [201], [202], [204]} Still, both phases can be discriminated by the oxygen photoemission line. While the cobalt oxide shows a feature at 529.6±0.2 eV, representing the lattice oxygen M-(O²⁻),^{[117], [201], [202]} the cobalt hydroxide phase reveals a signal at higher binding energies around 531.2±0.1 eV, which can be attributed to the metal hydroxide bond M-(OH⁻).^{[117], [201], [204]} The

⁹ The differences in the peak position is mainly due to the peak position correction of the C 1s adventitious carbon peak to 284 eV by Mavel *et al.*^[205]

cobalt spinel oxide Co_3O_4 exhibits a similar lattice oxygen signal in the O 1s photoemission line compared to the CoO phase.^{[117], [202], [204]} However, both species illustrate strong deviations in the Co 2p peak positions and line shape. The Co 2p_{3/2} photoemission line of Co_3O_4 shows a double peak structure with the highest signal at 779.7 ± 0.2 eV and a smaller second peak at an energy difference of 1 eV to higher binding energies.^{[117], [202], [204]} In addition to that double structure, Co_3O_4 features the characteristic Co^{2+} satellite (energy difference 6 eV) and a second satellite peak with an energy difference of 10 eV to the Co 2p_{3/2} signal. This satellite energy difference is known in literature for cobalt with an oxidation state of Co^{+3} .^{[117], [201], [202], [204]} Since cobalt possesses both oxidation states Co^{2+} and Co^{3+} in Co_3O_4 , this satellite structure is expected for the cobalt spinel phase. In the cobalt oxyhydroxide (CoOOH) phase cobalt has the oxidation state Co^{III} . Therefore, the Co 2p_{3/2} photoemission line features again the Co^{3+} satellite structure with an energy difference of 10 eV to the main peak, which is located at 780.2 ± 0.2 eV.^{[117], [201], [204]} This phase features a double peak structure, which is less pronounced than the one found for Co_3O_4 . The second smaller signal is located at a distance of around 1.3 eV to higher binding energies.^[204] According to its chemical formula, CoOOH possesses an oxide and a hydroxide component in the ratio 1:1. Thus, the O 1s photoemission line shows two signals, one for the lattice oxygen M-(O²⁻) at binding energies around 529.8 ± 0.1 eV^{[201], [204]} and the metal hydroxide bonding M-(OH) at binding energies around 531.1 ± 0.1 eV,^{[201], [204]} with similar intensities. The XPS results shown in literature for the relevant cobalt species (Co_iB, CoO; Co(OH)₂; Co₃O₄; CoOOH) are summarized in **Table 4.1.2** in terms of oxidation state, peak positions, and satellite structure. Exemplary XP Co 2p detail spectra of different cobalt compounds (*cf.* **Figure A 15**) from literature are shown in the appendix.^[209]

Table 4.1.2: XPS data for the different relevant cobalt phases from literature with oxidation states, peak positions of Co 2p and O 1s photoemission lines, and the difference in satellite structure.^{[117], [165], [201], [202], [204]–[206]}

Cobalt Phase	Oxidation state	E_{Bin} of Co 2p (in eV)			E_{Bin} of O 1s & B 1s (in eV)	
		Co 2p _{3/2}	satellite 6 eV	satellite 10 eV	M-(O ²⁻)/(OH)	M-B
Co _i B	±0	778.3-0.9 ^{1*}	x	x	-	188.0±0.3
CoO	+2	780.2±0.3	✓	x	529.6±0.2	-
Co(OH) ₂	+2	780.7±0.3	✓	x	531.2±0.1	-
Co ₃ O ₄	+2, +3	779.7±0.2	✓	✓	529.7±0.3	-
CoOOH	+3	780.2±0.2	x	✓	529.8±0.1 531.1±0.1	-

^{1*}Mavel *et al.* corrected the adventitious carbon of the C 1s to 284 eV.

Regarding the experiments of this work, it has to be mentioned that the cobalt LMM Auger line located at around 713 eV overlaps with the iron Fe 2p photoemission line, disturbing an unproblematic quantification with XPS of the different phases.^{[47], [69]} A similar effect can be observed for the iron LMM auger line located around 784 eV, which in turn overlaps with the Co 2p photoemission line.^{[47], [69]}

Iron

In nature, a variety of iron compounds in different oxidation states can be found. The iron species relevant for this work include diiron boride (Fe₂B) and all species, which can be obtained by oxidation of the iron boride in an aqueous alkaline solution. Since in literature there is no mutual consent for the exact oxidation species of iron under OER conditions in alkaline media and iron is only used here as a side phase in the ternary metal borides, only the Fe 2p, O 1s, and B 1s XPS photoemission lines of iron boride (Fe₂B), iron(II)oxide (FeO), iron(III)oxide (Fe₂O₃) and iron oxyhydroxide (FeOOH) will be discussed briefly in terms of their peak positions and satellite features. The corresponding literature data for the different iron phases are summarized in **Table 4.1.3**. Exemplary Fe 2p XP detail spectra of different iron compounds (*cf.* **Figure A 16a, b**) from literature are shown in the appendix.^[210] Furthermore, the overlap of the Co LMM auger line with the Fe 2p_{3/2} photoemission signal, which has been already discussed in the cobalt section, additionally hinders the identification of the iron species present.

Table 4.1.3: XPS data for the different relevant iron phases from literature with oxidation states, peak positions of Fe 2p and O 1s photoemission lines, and the differences in satellite structure.^{[210]–[218]}

Iron Phase	Oxidation state	E_{Bin} of Fe 2p (in eV)		E_{Bin} of O 1s & B 1s (in eV)	
		Fe 2p _{3/2}	satellite energy difference	M-(O ²⁻)/(OH)	M-(B)
Fe ₂ B	±0	706.9±0.1	-	-	188.0±0.2
FeO	+2	710.0±0.5	5.9±0.1	529.8±0.1	-
Fe ₂ O ₃	+3	711.0±0.2	8.2±0.4	530.0±0.2	-
FeOOH	+3	711.3±0.5	8.2±0.2	530.1±0.2 531.2±0.2	-

The Fe 2p photoemission lines for different oxidation states of iron can clearly be distinguished from each other. In contrast to the Co 2p spectrum, the chemical shifts in the Fe 2p photoemission line are based on initial state effects and are therefore ordered by their oxidation state. The

Fe 2p_{3/2} signal with oxidation states Fe⁰, Fe²⁺ and Fe³⁺ are located around 706.9 eV, 710.0 eV and 711.0 eV, respectively.^{[210]–[218]} Iron in an oxidation state Fe⁰ exhibits, in contrast to Fe²⁺ and Fe³⁺, no satellite structure. The satellites in the Fe 2p spectrum originate from charge transfer process from the ligand to the iron.^[219] Therefore, the energy difference between the satellite and the main peak is characteristic for the ligand involved and the present oxidation state of iron.^[219] Iron oxide with an oxidation state of Fe²⁺ exhibits a distance to the satellite of around 6 eV,^{[214], [218]} while Fe³⁺ oxide or oxyhydroxide shows an energy difference of around 8 eV.^{[214]–[218]} The O 1s photoemission lines of the iron oxide and hydroxide phases are located at binding energies of roughly 530.0 eV and 531.2 eV, respectively. More peak positions can be found in **Table 4.1.3**.

Nickel

For this work, several nickel species are relevant and, thus, have to be identified with XPS – starting with dinickel boride (Ni₂B) and all species, which can be obtained by oxidation during EC testing in an aqueous alkaline electrolyte solution. These relevant phases were thoroughly discussed in **Section 4.1.3**. Besides the XPS characteristics of Ni₂B, the features of nickel oxide (NiO), nickel hydroxide (Ni(OH)₂), and nickel oxyhydroxide (NiOOH) will be discussed briefly in this section. A summary of the XPS peak positions of the different compounds can be found in **Table 4.1.4**. Exemplary Ni 2p and the corresponding O 1s XP detail spectra of different nickel compounds (*cf.* **Figure A 16****Figure A 17**) from literature are shown in the appendix.^[209]

Nickel borides feature the Ni 2p_{3/2} in the Ni 2p photoemission line at around 852.7±0.7 eV and the corresponding boride feature in the B 1s photoemission line around 187.9±0.0 eV.^{[220], [221]} The oxidation of nickel boride shows features of boron(III) oxide (B₂O₃) and boron(III) hydroxide (H₃BO₃) at around 192.2±0.2 eV. In contrast to nickel boride, nickel oxide (NiO) shows a double peak structure in the Ni 2p_{3/2} signal with the main feature at 842.6±0.6 eV and a shoulder located at higher binding energies. This double peak structure makes it easy to distinguish the Ni²⁺O from other Ni²⁺ phases like Ni(OH)₂.^{[117], [221]–[224]} However, the Ni 2p photoemission line position cannot always be identified that clearly for certain nickel phases. Especially the Ni(OH)₂ and the NiOOH phases are difficult to discriminate from the Ni 2p signal alone. The most pronounced difference is the asymmetric peak shape that is reported for NiOOH, which leads to widely spreading reported peak positions (855.4±0.8 eV), depending on which fitted peak is used.^{[117], [209], [224]} Ni(OH)₂, on the other hand, features a Ni 2p_{3/2} peak at around 855.1±0.3 eV, located in the range of the reported peak positions for NiOOH.^{[117], [209], [224]} In consequence, the O 1s photoemission line must be used additionally to assign the present phase. Ni(OH)₂ features only a hydroxide OH⁻ signal in the O 1s photoemission line, located around

531.0±0.2 eV, while the NiOOH shows a lattice oxygen O²⁻ and a hydroxide OH⁻ signal, located at 529.5±0 eV and 531.2±0 eV, respectively.

The already mentioned α-Ni(OH)₂ phase (cf. **Section 4.1.3**) has water intercalated between two β-Ni(OH)₂ planes, which leads to an increase in the c-parameter of the lattice with trigonal symmetry.^[195] This influence of water onto the XP O 1s detail spectra was investigated by Payne *et al.*^[209], proposing that the intercalated water can be found in the O 1s photoemission line around 531.5 eV. They stated that they excluded this O 1s signal (531.5 eV) from the relative atomic contributions of nickel, because the water is not bound to any Ni²⁺ cations. However, this discrimination between OH⁻ species and the intercalated water is difficult to apply in this work, in which ternary boride systems will be discussed. Therefore, no discrimination between α- and β-Ni(OH)₂ will be included here. Additionally, the fluorine KLL Auger structure overlaps with the Ni 2p photoemission line. This superposition of the two elements arises by mixing the nickel boride catalyst into the NafionTM containing ink. It can be compensated by subtraction of the F KLL Auger intensities from the Ni 2p spectrum (cf. **Section 4.5.3** and **Figure 4.5.13**).

Table 4.1.4: XPS data for the different relevant nickel phases from literature with oxidation states, peak positions of Ni 2p and O 1s photoemission lines, and the difference in satellite structure.^{[117], [209], [220]–[224]}

Nickel Phase	Oxidation state	E_{Bin} in eV		
		Ni 2p _{3/2}	O 1s M-(O ²⁻)/(OH ⁻)	B 1s M-(B)
Ni (metal)	±0	852.8±0.2	-	-
Ni ₂ B	±0	852.7±0.7	-	187.9±0.0
NiO	+2	854.2±0.6* ¹	529.3±0.2	-
Ni(OH) ₂	+2	855.1±0.3	531.0±0.2	-
NiOOH	+3	855.4±0.8* ²	529.5±0 531.2±0	-

*¹ double-peak structure, showing a shoulder

*² asymmetric peak shape, making the positioning of the peak more inaccurate

4.2 Experimental

4.2.1 Synthesis route of the transition metal borides

The synthesis of all TMBs investigated in this work was done in the research group of Professor Barbara Albert (TU Darmstadt, department of chemistry, Eduard-Zintl-institute of inorganic and physical chemistry) and is based on earlier work on this topic.^{[225]–[228]}

Co₂B nanostructures with Ni and Fe

Nanoscale ternary borides with different nickel and iron concentrations ($0 \leq x \leq 0.5$ for (Co_{1-x}Fe_x)₂B and (Co_{1-x}Ni_x)₂B) were synthesized by Dr. Sebastian Klemenz (TU Darmstadt, department of chemistry, Eduard-Zintl-institute of inorganic and physical chemistry).^{[145], [146], [229]} The starting masses of the used materials cobalt(II)-chloride-hexahydrate (CoCl₂ · 6H₂O – 97%, VWR Chemicals), ammonium iron(II)-sulfate-hexahydrate ((NH₄)₂Fe(SO₄)₂ · 6H₂O – 99%, AnalaR NORMAPUR), and nickel(II)-chloride-hexahydrate (NiCl₂ · 6 H₂O – 98%, Riedel-de Haën), were calculated for 1 g of sodium tetrahydridoborate (NaBH₄ – > 97%, Alfa Aesar) to obtain a molar ratio of tetrahydridoborate-to-transition-metal ions of 4:1. The following steps were performed in a glove box under an inert atmosphere. NaBH₄ was dissolved in 100 ml of degassed water and afterward added drop by drop with a dropping funnel to the solution of the metal salts into 150 ml of degassed water. The colored metal salt mixture was stirred at room temperature for one hour. During this time, it loses its color, while generating gas and heat. A black precipitate was afterward separated and washed with 50 ml of degassed water and 100 ml dry acetone. After drying in vacuo, the black precipitate was transferred into a Schlenk tube, in which an additional annealing step at 500 °C in vacuo was performed for two hours.

Co₃B nanoparticles

Tricobalt boride (Co₃B) nanoparticles were synthesized by Dr. Anne-Marie Zieschang^{[144], [230]} (TU Darmstadt, department of chemistry, Eduard-Zintl-institute of inorganic and physical chemistry) using 20 mmol of cobalt(II)-bromide (Sigma Aldrich, 99%) dissolved in 50 ml of tetrahydrofuran (C₄H₈O) and 46 mmol of lithium tetrahydridoborate (Sigma Aldrich, 95%) dissolved in 20 ml of tetrahydrofuran. The solution of lithium tetrahydridoborate (LiBH₄) was added to the solution of cobalt(II)-bromide (CoBr₂) quickly. The solution changed color from blue to black immediately and was stirred for two hours at room temperature. The black precipitate was filtered and washed with 20 ml of tetrahydrofuran. The sample was rinsed with 20 ml of ethanol, added quickly to the precipitate on the frit, which caused it to heat up. The

precipitate was again filtrated and dried in vacuo for eight hours. The black powder was heated to 500 °C within an hour and then treated at 500 °C for two hours in vacuo, yielding Co₃B nanoparticles.

4.2.2 Choice of substrate material

To analyze the synthesized TMB powders in terms of their catalytic activity in an alkaline electrolyte towards the water-splitting reactions, an ink was prepared (*cf.* Section 4.2.4) and drop coated on a substrate. Table 4.2.1 lists certain aspects that must be considered for the choice of a suitable substrate material.

Table 4.2.1: Summary of general requirements for a suitable substrate material for the drop coating process of a catalyst system.

Requirements	
for catalysis	for deposition (drop coating)
<ul style="list-style-type: none"> ❖ good electrical conductivity ❖ chemical inertness in the given electrolyte 	<ul style="list-style-type: none"> ❖ flat; low roughness ❖ wettable

Titanium, ITO, and GC were chosen to fulfill the given requirements (*cf.* Table 4.2.1) and were investigated with different ink compositions in detail in the master thesis of M.Sc. Stefan Hawel.^[231] The best performances were achieved using GC as substrate material. Therefore, in this work, only measurements on GC are presented.

4.2.3 Substrate preparation

The GC was purchased by HTW GmbH in 1x1 cm pieces with a thickness of 2 mm. The GC substrates were first ground by hand for several minutes with 400, 1000, 1500, 2000, and 2500 grit size abrasive paper (Buehler) each. Afterward, the samples were polished to a mirror finish by hand with alumina (Al₂O₃) paste with grain sizes of 1 μm and 0.05 μm (Buehler) on polishing paper (Buehler). Finally, the substrates were rinsed with distilled water, and, to remove the residual dirt and paste, the substrates were cleaned in an ultrasonic bath with acetone and isopropanol.

4.2.4 Catalyst ink preparation and drop coating

An ink for catalytic applications consists of three main components: a binder, a solvent, and the active material. After the coating of the ink on top of the substrate, the solvent evaporates. The binder develops a matrix around the active material, forming a composite. The binder assures the attachment of the catalyst on the substrate. Therefore, the binder material must be chemically stable in the later chosen electrolyte and must possess the charge carrier conductivity for the respective reaction side. For the HER, an electron conductor and for the OER a hole conductor is required. Nafion™ (5 wt% water suspension; Aldrich Chemistry) was used as a hole conducting binder, which was proven to be stable in alkaline electrolytes and is often used as a binder for alkaline media.^{[232], [233]} The ratio between binder and solvent can be varied. Nafion™ contents between 2vol% and 10vol% were tested preliminary in the master thesis of Stefan Hawel.^[231] The best performance was achieved by 2vol%, but the best stability of the powders was reached with 10vol% of Nafion™ in the ink. Therefore, 10vol% of Nafion™ was used to ensure that the stability of the catalyst is independent of the binder itself. As the solvent often a mixture of ethanol and distilled water is used.^[233] Thereby, the more ethanol is used, the faster the ink dries out – and vice versa. In this work, always an ethanol-to-distilled water ratio of 1:1 was used. The last adjustable parameter of the ink preparation is the amount of active catalyst material. If the main catalyst material possesses low intrinsic electrical conductivity or shows insulating behavior, the catalyst material is mixed with carbon powder support to enhance the conductivity of the catalyst. Since metal borides exhibit good electrical conductivity,^{[149], [150]} no carbon powder support had to be used for the preparation of the active catalyst phase. The amount of active material was varied preliminary in the master thesis of Stefan Hawel^[231] and was found to work best with 5 mg catalyst per 1 mL of liquid phase.

To guarantee uniform distribution of the nanoparticles on the substrate, the ink is placed in an ultrasonic bath for 30 minutes and the substrate surface is charged electrostatically. The assembled charges on the substrate lead to the formation of a spherical ink drop when placed on the substrate with an Eppendorf pipette. The volume of the deposited ink was varied preliminary in the master thesis of Stefan Hawel^[231] and was found to work best with 15 μL on an area of around $A_{\text{Drop}} \approx 0.5 \text{ cm}^2$. The resulting catalyst loading of the drop L_{Drop} was determined with

$$L_{\text{Drop}} = \frac{5 \text{ mg mL}^{-1}}{1000} \cdot 15 \text{ }\mu\text{L} = 75 \frac{\mu\text{g}}{0.5\text{cm}^2}, \quad \text{eq. 4.2.1}$$

and the total loading of the catalyst with

$$\Rightarrow L_{\text{total}} = 2 \cdot L_{\text{Drop}} = \underline{150 \mu\text{g cm}^{-2}}. \quad \text{eq. 4.2.2}$$

The complete preparation process of the TMB electrodes is schematically summarized in **Figure 4.2.1**.

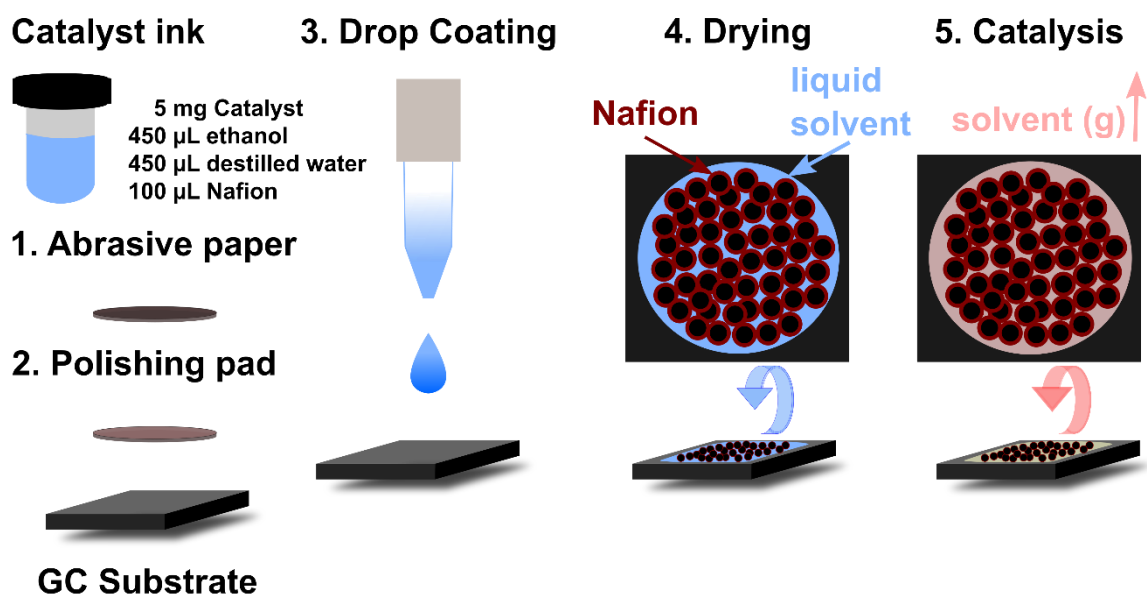


Figure 4.2.1: Schematic picture of the stepwise substrate preparation and the subsequent drop coating process. On the left side, the composition of the ink is shown followed by the grinding and polishing step of the glass-like carbon (GC) substrate. After a cleaning step with distilled water, 15 µL of the ink is drop coated on the substrate. The ink must dry for at least 30 minutes before the electrode can be used. In that time the solvent and the water evaporate.

4.2.5 Electrochemical protocol

The catalytic performance tests were conducted in a three-electrode setup (*cf.* **Section 3.3.4**) in 1 M KOH. The measurement procedure for OCP and EIS measurements were performed equally as described for the manganese-based catalysts (*cf.* **Section 3.3.4**). The electrolyte resistance was corrected with the *IR* correction and the measured potential was referred to the RHE scale according to **Equation 2.3.3** (*cf.* **Section 3.3.4**). The used protocol is summarized in **Figure 4.2.2**. The protocol was extended for the most promising samples with long-term stability measurements, using chronopotentiometry (CP) measurements at 10 mA cm⁻² (Step 7). These measurements were conducted with an extended measurement setup, which contains a peristaltic pump (Hei-LOW Advantage 06 – Heidolph Instruments GmbH & Co. KG) and an electrolyte reservoir. To avoid an oxyhydrogen back reaction, the electrolyte reservoir was bubbled with nitrogen.

1. Open circuit potential (OCP) measurement
2. Electrochemical impedance spectroscopy (EIS) measurement at the OCP at a frequency range from 100 Hz to 100 MHz
3. CV measurement from 1.00 V – 1.90 V vs. RHE for 3 cycles ($\nu = 50 \text{ mV s}^{-1}$)
4. CV conditioning from 1.00 V – 1.55 V vs. RHE for 50 cycles ($\nu = 100 \text{ mV s}^{-1}$)
5. CV measurement from 1.00 V – 1.90 V vs. RHE for 3 cycles ($\nu = 50 \text{ mV s}^{-1}$)
6. CV measurement from 1.00 V – 1.90 V vs. RHE for 2 cycles ($\nu = 10 \text{ mV s}^{-1}$)
7. Chronopotentiometry measurement at 10 mA cm^{-2}

Figure 4.2.2: Description of the electrochemical (EC) measurement protocol used for all transition metal boride catalysts investigated in this work. The abbreviation cyclic voltammogram (CV) stands for cyclic voltammogram and ν defines the scan rate of the CV curve.

4.2.6 Preliminary XPS analysis of Nafion™

The binder material Nafion™ is a modification of tetrafluoroethylene with perfluoro vinyl ether groups ($\text{C}_4\text{O}_2\text{F}_6$ – marked in blue in **Figure 4.2.3**) and sulfonate groups ($\text{O}_2=\text{S}-\text{OH}$ – marked in yellow). The structural formula of Nafion™ with the different existing carbon bonds is illustrated in **Figure 4.2.3**. The carbon bonds can be addressed to certain binding energies in the XP C 1s detail spectrum, which are color-coded. In general, XPS measurements of pure Nafion™ samples are difficult to obtain, since pure Nafion™ tends to degrade under X-Ray radiation.^{[234], [235]} However, the Nafion™ seems to be more stable under X-Ray radiation, if it is mixed with a conductive catalyst and measured as a compound. If the pure material is measured by XPS with longer irradiation times, a shift of the detail spectra due to charging and degradation is visible. In **Figure 4.2.4** the O 1s photoemission lines of Nafion™ are shown for the 1st, 10th, 20th, and 30th scan. The relevant functional groups $\text{O}_2=\text{S}-\text{OH}$ (sulfonate) and $\text{F}_2\text{C}-\text{O}-\text{CF}$ (fluoroether) are marked at binding energies of around 532 eV and 534 eV, respectively. In literature, the assignment of the two different functional groups varies in terms of the respective binding energies. Either the peak at lower binding energies is assigned to the C-O-C group and the peak at higher binding energies to the sulfonated group^{[236]–[239]} or vice versa.^{[234], [235], [240], [241]} However, due to the fluorine connected to the ether groups C-O-C the binding energies of this fluoroether group ($\text{F}_2\text{C}-\text{O}-\text{CF}$) should be shifted to higher binding energies, while the sulfonate group ($\text{O}_2=\text{S}-\text{OH}$) is located at binding energies around 532 eV.^{[236]–[239]} Due to the wetting of the catalyst by Nafion™, XPS measurements before the EC investigation are challenging.

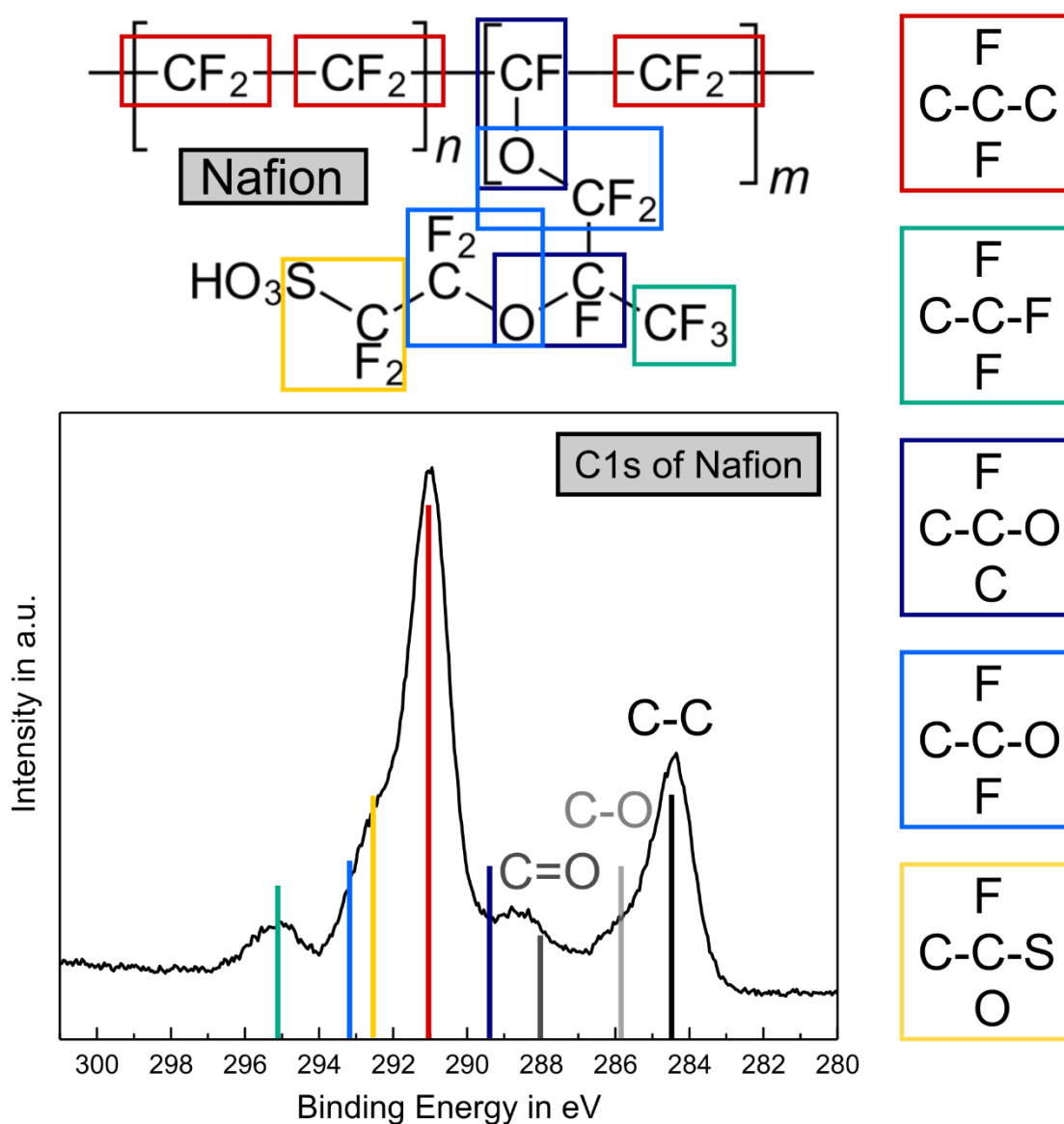


Figure 4.2.3: The structural formula of Nafion™ is color-coded illustrating the variety of carbon bonds in the binder material. On the right side, the isolated color-coded components of the Nafion™ polymer chain are shown. Furthermore, these color-coded components are assigned to specific binding energies in the C1s XP detail spectrum of Nafion™.

The Nafion™ matrix encloses the catalyst particles, leading to either a decrease of the XPS signal of the catalyst photoemission line or even to no signal at all. In XPS, powdered samples already exhibit a decreased intensity compared to thin-film material. Therefore, powdered samples in combination with Nafion™ cannot be used to analyze the catalysts properly. Consequently, the catalyst powders were characterized by XPS embedded in indium foil before EC investigation. Hence, only the XPS measurements after the EC investigation contain a contribution of the Nafion™ binder material.

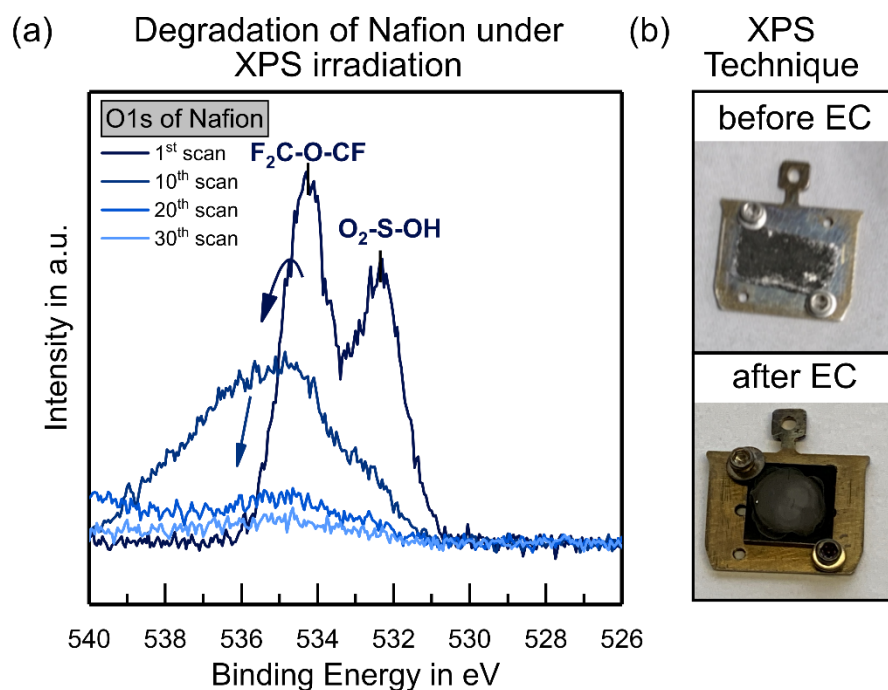


Figure 4.2.4: (a) XP O 1s detail spectra of Nafion™ are shown for the 1st, 10th, 20th, and 30th scan. The higher binding energy feature shows the fluoroether group (F₂C-O-CF) and the lower binding energy feature the sulfonate group (O₂=S-OH). (b) XPS measurement techniques for the catalyst: (top) before electrochemical (EC) investigation the catalyst was embedded in indium foil and (bottom) after EC investigation the catalyst was measured embedded in Nafion™ on the GC substrate.

4.2.7 Electron microscopy

The investigation of the surface morphology of the transition metal powders was performed using scanning (SEM) and transmission electron microscopy (TEM). The SEM images were recorded using a XL30 FEG scanning electron microscope (Philips) with an acceleration voltage of 10 kV. For the TEM analysis, a 200 kV JEOL JEM 2100F (scanning) transmission electron microscope for the (Co_{1-x}Fe_x)₂B catalysts and for the (Co_{1-x}Ni_x)₂B catalysts a (S)TEM with JEOL ARM-200F operated at 200 kV acceleration voltage with a JEOL JED-2300T EDX detector was used.

4.2.8 Atomic absorption spectrometry

The determination of impurities inside the electrolyte was investigated with flame atomic absorption spectrometry (F-AAS). The measurements were conducted with a Perkin Elmer Analyst 300 using hollow-cathode lamps for the respective elements. An acetylene air mixture was used as the working gas.

4.3 Dicobalt boride (Co₂B) and tricobalt boride (Co₃B)

The Co₂B and Co₃B were synthesized by the research group of Professor Barbara Albert by Dr. Sebastian Klemenz and Dr. Anne-Marie Ziechang (TU Darmstadt, department of chemistry, Eduard-Zintl-institute of inorganic and physical chemistry), respectively. In **Section 4.2.1** short summaries of the synthesis routes were given. A more detailed description can be found in the dissertations of Dr. Sebastian Klemenz^[229] and Dr. Anne-Marie Ziechang^[242] or in the common publications.^{[144], [145]} The XRD characterization of the synthesized nano-structured Co₃B and Co₂B powders was also conducted by this group. The obtained data are presented in the appendix (*cf.* **Table A 1**). No evidence of a side phase was found for either the Co₂B or the Co₃B, evidencing phase pureness.

4.3.1 Surface analysis with XPS

The description of the different relevant cobalt phases together with a summary of literature values for the oxidation states, peak positions, and the differences in satellite structure was given in **Section 4.1.4**. The XPS analyses of the transition metal borides before EC were conducted on indium foil, while the analyses after EC were performed on GC. A detailed preparation description is given in **Section 4.1.4**. In a first step of analyzing bimetallic nano-structured Co-based transition metal borides for the OER, the monometallic nano-structured cobalt boride phases, dicobalt (Co₂B), and tricobalt boride (Co₃B) were investigated by XPS. The Co 2p photoemission lines of Co₃B (*cf.* **Figure 4.3.1a**) and Co₂B (*cf.* **Figure 4.3.1b**) are displayed before and after EC investigation.

Co₃B shows in its initial state (before EC) no or only very small amounts of Co⁰, but a high amount of a Co²⁺ phase with a Co 2p_{3/2} signal located at a binding energy of around 781.2 eV.^{[117], [201], [204]} Due to the O 1s photoemission line recorded for Co₃B (*cf.* **Figure 4.3.3a**), this phase can be identified to be mainly Co(OH)₂ with an M-OH peak located at 531.3 eV.^{[117], [201], [204]} The formation of CoO at the surface can be excluded since the lattice oxygen peak M-(O²⁻) of CoO should be visible at 529.6±0.2 eV.^{[117], [201], [202]} In the B 1s photoemission line of Co₃B (*cf.* **Figure 4.3.2a**), boron is only visible in an oxidized B³⁺ state forming possibly B₂O₃ and/or B(OH)₃ or mixtures (BO_xH_y) of those at binding energies between 192 and 194 eV.^{[243], [244]} These observations lead to the assumption, that the surface of the Co₃B phase is strongly oxidized. From XRD measurements of the same powder stored in air at room temperature for two months (conducted in the group of Prof. Albert), Co₃B was found as the main phase, without any oxidative part visible.^[144] Hence, it can be assumed that Co₃B forms a structure with a crystalline Co₃B core and an amorphous Co(OH)₂ surface layer. This oxidative surface layer has

most certainly been formed during the long-time storage in air. Similar structures with an oxidized surface layer were found for transition metal borides before.^[245]

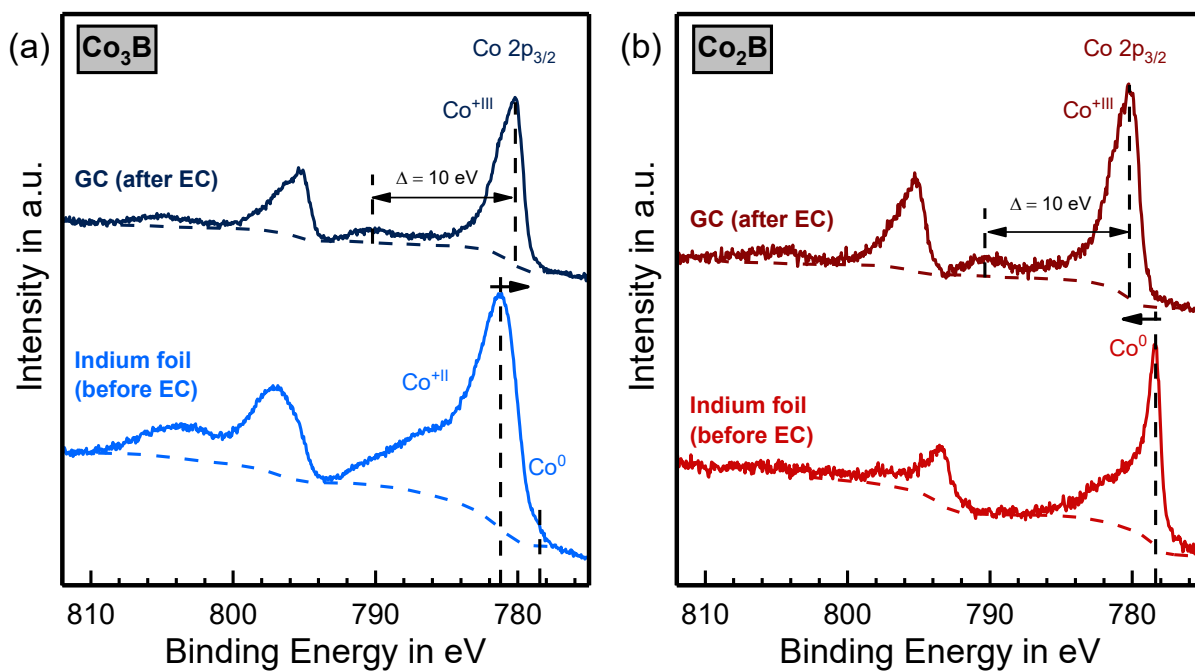


Figure 4.3.1: XP Co 2p detail spectra of (a) Co_3B and (b) Co_2B before and after electrochemical (EC) investigation.

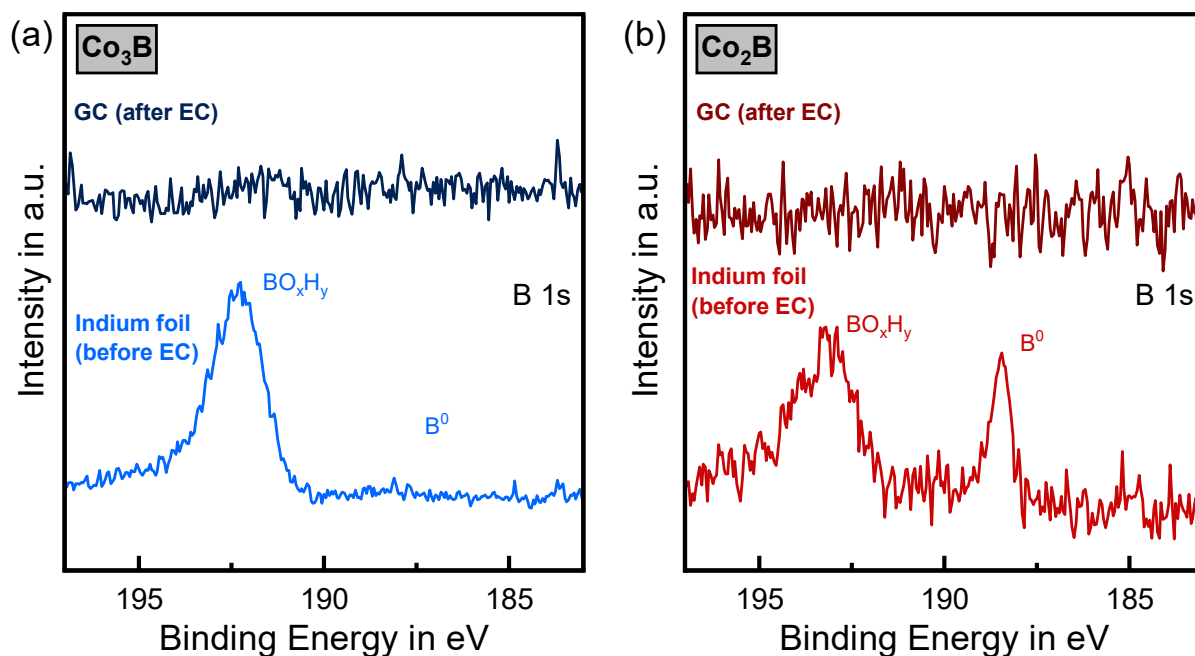


Figure 4.3.2: XP B 1s detail spectra of (a) Co_3B and (b) Co_2B before (bottom) and after electrochemical (EC) investigation (top).

In contrast to the surface oxidation of the Co_3B phase, Co_2B is clearly less oxidized in its initial state (cf. **Figure 4.3.1b**). The main phase located at a binding energy of 778.4 eV is found to be Co^0 with only lower contributions of oxidized parts at higher binding energies. A similar observation can be found in the B 1s photoemission line shown in **Figure 4.3.2b**, in which a distinct B^0 signal, attributed to cobalt boride, was recorded.^{[205], [206]} Here, the oxidative signal of boron BO_xH_y is more clearly visible compared to the one visible in the Co 2p photoemission line.^{[205], [221], [243], [244], [246]–[248]} From quantitative XPS analysis, a cobalt-to-boron ratio of around 1.7 was calculated. This ratio fits quite well to the expected cobalt-to-boron ratio of 2, even though parts of the surface were oxidized. From XRD measurements (conducted in the group of Prof. Albert), it was found that Co_2B was synthesized as a pure phase, with no side phases.^{[145], [229]}

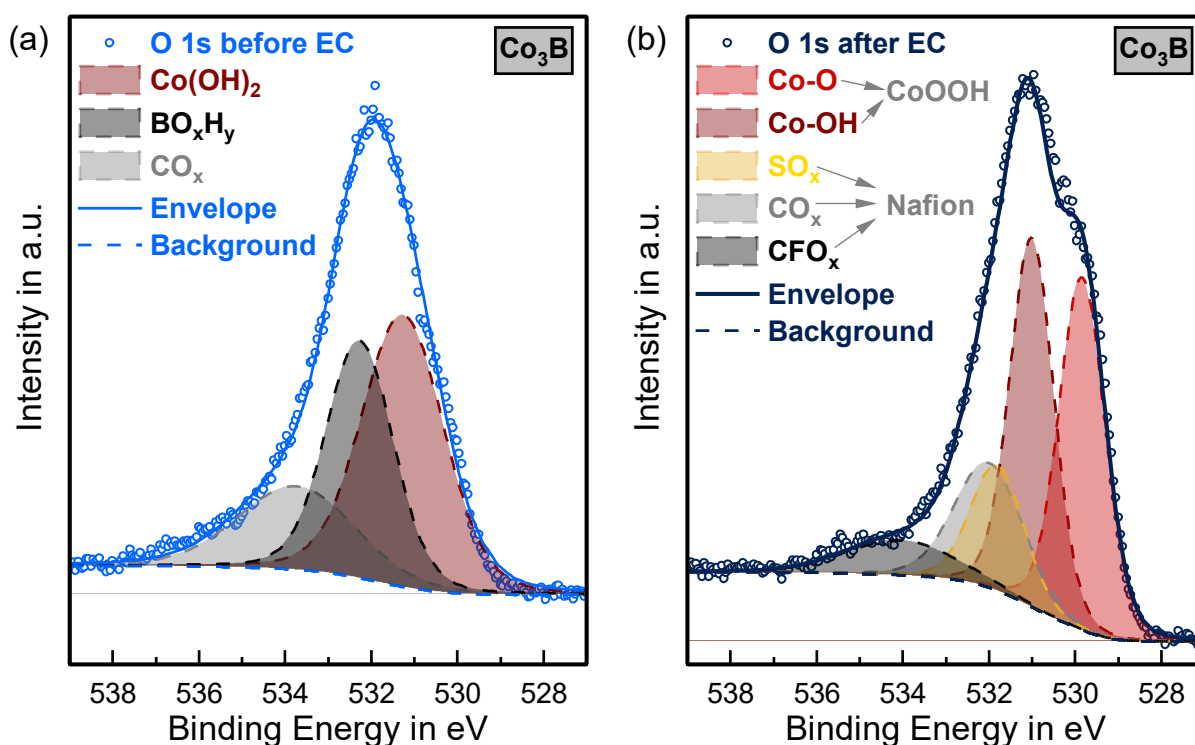


Figure 4.3.3: Exemplarily fitted XP O 1s detail spectra of Co_3B before (a) and after electrochemical (EC) investigation (b) using a Shirley background.^[134]

After the first surface analysis with XPS, the catalyst powders were dispersed in a Nafion™ containing ink. The mixtures were drop coated onto GC substrates, on which they were electrochemically characterized in an alkaline electrolyte (1 M KOH) for the OER (cf. **Section 4.3.2**). Subsequently, a second XPS surface analysis was conducted to monitor changes in the electronic structure, the oxidation states, and the composition of the catalysts. In **Figure 4.3.1** the Co 2p photoemission lines of Co_3B (a) and Co_2B (b) before and after the EC characterization are

shown. Both phases show distinct differences in terms of surface oxidation. After the EC investigation, both samples form a similar phase. **Figure 4.3.4** shows that both phases have a similar peak structure. The satellite signals and energy differences to the Co 2p_{3/2} photoemission line match, indicating that both catalysts form the same surface species during the EC investigation in the alkaline electrolyte. The B 1s photoemission lines of both samples vanish completely (cf. **Figure 4.3.2**), while the Co 2p_{3/2} signal of Co₃B shifts from the binding energy of 781.3 to lower binding energies and the Co 2p_{3/2} signal of Co₂B shifts from 778.4 eV to higher binding energies. For both samples, the binding energy of 780.2 eV was measured for the Co 2p_{3/2} photoemission line, with both showing a distinct satellite at an energy difference of 10.1 eV. Additionally, a side shoulder close to the Co 2p_{3/2} signal is visible at a binding energy of around 781.3 eV. Similar peak structures were found in literature for cobalt in its spinel oxide form (Co₃O₄)^[117],^[202],^[204] and cobalt in an oxyhydroxide form CoOOH^[117],^[135],^[201],^[204].

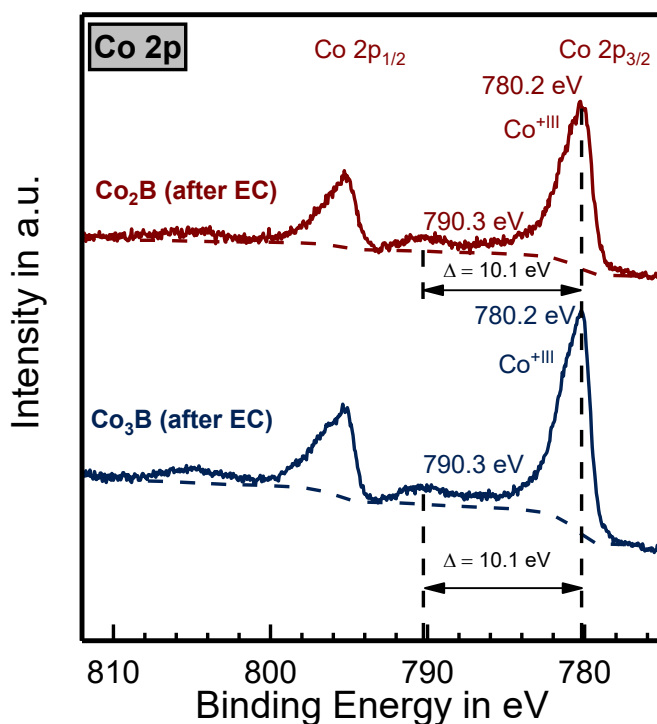


Figure 4.3.4: XP Co 2p detail spectra of Co₃B (blue) and Co₂B (red) after electrochemical (EC) investigation. The respective peaks are marked with the corresponding binding energies and satellite energy differences.

Due to the O 1s photoemission lines of the samples, which are exemplarily depicted in **Figure 4.3.3** for Co₃B, the Co₃O₄ species can be excluded from the phase identification, since a metal hydroxide bonding is visible at binding energies around 531.1 eV. Additionally, a lattice oxygen M-(O²⁻) species can be found around 529.9 eV, which fits the assumption that CoOOH is formed during the EC investigation. Similar results are known for Co-based catalysts.^[47],^[48],^[135],^[145].

[165], [249], [250] To validate the formation of CoOOH, the observed ratio of cobalt hydroxide and cobalt oxide bonding should be 1:1 in the O 1s photoemission line (*cf.* **Figure 4.3.3**). The larger hydroxide amount can be explained by the sulfonyl hydroxide group R-S(=O)₂(OH) of Nafion™ located at a binding energy around 531.8 eV.^{[236]–[239]} The fitted peak positions of the O 1s photoemission lines of Co₃B and Co₂B are summarized in **Table 4.3.1**.

Table 4.3.1: Summary of the O 1s peak positions of the Co₃B and Co₂B phase before and after electrochemical (EC) investigation.

O 1s of Co ₃ B/Co ₂ B	Cobalt		Nafion™		Boron
	Co-O	Co-OH	O=S-OH	F-C-O _x	B-O _x
Co ₃ B before EC	-	531.2	-	-	532.2
Co ₃ B after EC	529.9	531.1	531.8	534.2	-
Co ₂ B before EC	-	-	-	-	532.4
Co ₂ B after EC	529.5	531.0	531.9	534.6	-

4.3.2 Electrochemical investigation

The EC behavior of Co₃B and Co₂B on GC for HER and OER was investigated in 1 M KOH, following the EC protocol described in **Section 4.2.5**. The reaction mechanism of elemental cobalt in alkaline media and the corresponding reaction mechanisms of the subsequently formed oxide/hydroxide species are discussed in **Section 4.1.3**. In **Figure 4.3.5** the CVs before the conditioning step of Co₂B and Co₃B are plotted for the HER and the OER. Since both catalysts show low catalytic activity for HER (*cf.* **Figure 4.3.5a**), only the OER will be further discussed in this section. The CVs illustrated in **Figure 4.3.5** for the HER and OER, represent the catalytic activity before any conditioning step and, therefore, are called “before cond.”. A comparison of the two phases towards the OER reveals major differences in the apparent redox waves (*cf.* **Figure 4.3.5b**). While Co₃B exhibits a large hysteresis behavior with at least two visible oxidation and reduction waves below the onset potential of the OER, the Co₂B phase seems to remain unchanged in this potential region. However, this appearance is deceptive. The inset of **Figure 4.3.5b** magnifies the CV behavior of Co₂B in the potential range between 1.00 and 1.55 V vs. RHE, illustrating a similar redox behavior as observed for the Co₃B phase with two visible oxidation and reduction waves. For simple monometallic systems like platinum or other transition metals, certain redox waves can be referred to as the electrochemically accessible surface area of that system. This is due to the fact, that these waves represent either the adsorption of *e.g.* hydrogen or oxygen onto surface atoms or a transition (oxidation/reduction)

of a surface phase to another one. The integral of these waves results in a specific charge Q , which can then be related to the electrochemically accessible surface sites. A detailed summary of such mechanistic evaluations can be found in the publication of Trasatti *et al.*^[63] from 1991. Here, the size of the redox waves of Co_2B and Co_3B are not causally related to the adsorption of oxygen on the surface but can be attributed to a transition of the present surface species to another one. In this work, no quantitative evaluation of these waves was performed. Only the assumption has been made, that due to the considerably larger redox waves of Co_3B compared to Co_2B (*cf.* **Figure 4.3.6b**) the accessible surface area of Co_3B is higher. A more precise EC method for the determination of the surface area of a catalyst is the ECSA method described in **Section 2.3**. No ECSA measurements were conducted for the Co_3B phase and therefore no comparable quantification of the two phases can be given here.

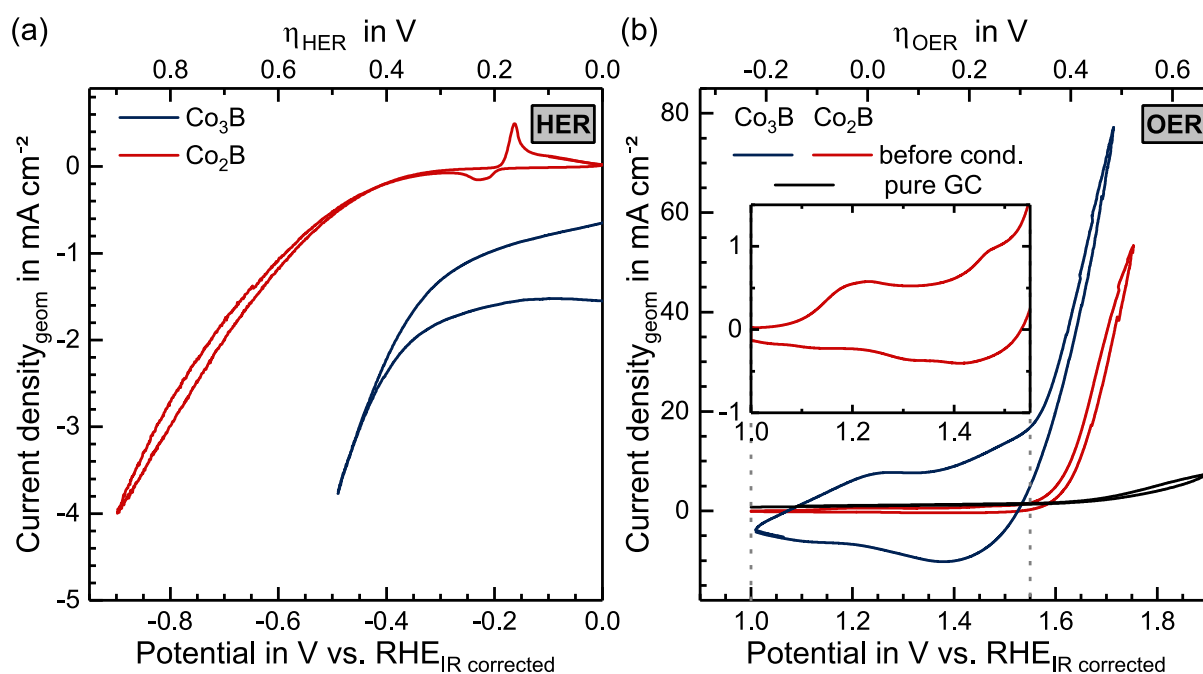


Figure 4.3.5: Cyclic voltammograms (CVs) of Co_2B and Co_3B in 1 M KOH towards the HER (a) and the OER (b) before the conditioning step (before cond.). The inset indicates the oxidation behavior of Co_2B in the potential range of 1.00 to 1.55 V vs. RHE. Both curves are iR compensated (*cf.* **Section 3.3.4**) and measured with a scan rate of 50 mV s^{-1} .

Co_3B shows a lower onset potential for the OER than Co_2B . However, an accurate value is hard to define, due to the large oxidative wave that is close to the onset potential. Therefore, the onset potential of Co_3B can only be assigned to a potential range between 1.54 V and 1.55 V vs. RHE. A slightly higher onset potential with 1.56 V vs. RHE can be estimated for the Co_2B catalyst. The size of the oxidation wave of Co_3B also hinders the determination of the overpotential at 10 mA cm^{-2} (η_{10}), which is often used to compare the activity of water splitting catalyst

systems.^{[18], [19]} Therefore, the overpotential at 20 mA cm⁻² (η_{20}) is estimated for the comparison of Co₃B to other metal boride systems. Already from the CV curves, it is obvious that Co₃B (1.57 V vs. RHE) shows a lower overpotential η_{20} than the Co₂B catalyst (1.66 V vs. RHE). Plotting the conditioning step ($\nu=100$ mV s⁻¹) of only the Co₂B phase and the Co₂B in comparison to the Co₃B highlights the different size of their redox waves as shown in **Figure 4.3.6**. The Co₂B phase exhibits two distinct oxidation waves located between 1.1 and 1.2 V vs. RHE and above 1.4 V vs. RHE, which can be attributed to the transition of Co²⁺ to Co³⁺ and Co³⁺ to Co⁴⁺, respectively.^{[180], [182], [186], [187], [207], [251]} The transition of Co²⁺ to Co³⁺ for Co₃B emerges at around 1.1 V vs. RHE as well, but due to the large active area of the catalyst the current continuously grows until 1.3 V vs. RHE. Then, the current reaches a small plateau until another transition around 1.4 V vs. RHE occurs. This second transition can again be attributed to the oxidation of Co³⁺ to Co⁴⁺. In summary, both catalysts exhibit transitions to Co⁴⁺ before and during the OER; yet the XPS analysis of the catalysts after an EC investigation showed in both cases Co³⁺OOH as the surface species. The occurrence of Co⁴⁺ cannot be proven by the XPS analysis, since Co⁴⁺ is thermodynamically unstable and can only be measured under reaction conditions.^[252]

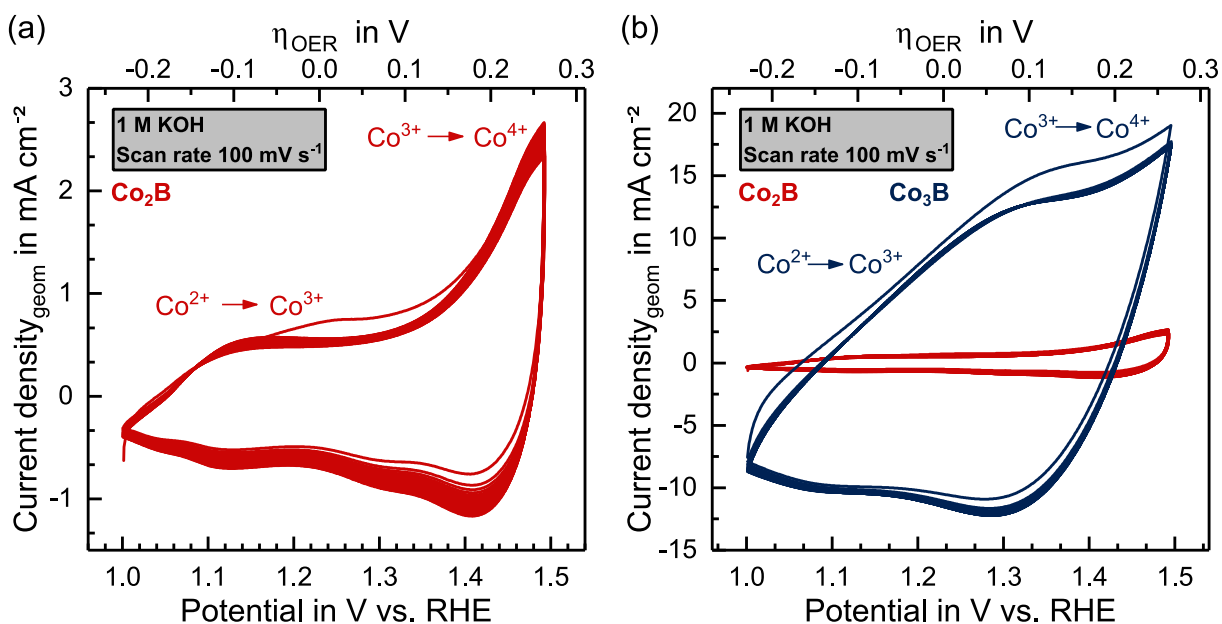


Figure 4.3.6: Conditioning CVs in the potential range between 1 and 1.5 V vs. RHE of (a) Co₂B (red) and (b) Co₂B in comparison to Co₃B (blue) in 1 M KOH. The curves are measured with a scan rate ν of 100 mV s⁻¹ and plotted without iR compensation.

For Co₂B three reduction steps can be observed at 1.4 V, 1.3 V, and 1.1 V vs. RHE, while Co₃B shows one main reduction wave around 1.3 V and a smaller one at 1.1 V vs. RHE. In literature, it is described that the CoO₂ passivation layer is difficult to reduce.^{[183], [185]–[187]} Thus, both

reduction peaks at 1.4 V and 1.3 V vs. RHE are attributed to the reduction of Co^{4+} to Co^{3+} . Doyle *et al.* [186], [187] described the further reduction of a Co^{3+} species to occur at lower potentials at a cathodic peak at 0 V vs. Hg/HgO and between a broader cathodic band approximately -0.4 V and -0.8 V vs. Hg/HgO (in 1 M KOH), transferring to approximated values of 0.9 V and between 0.5 V to 0.1 V vs. RHE, respectively. Accordingly, the reduction of the Co^{3+} species should occur below the lowest potential boundary of the here recorded CV curves, which was limited to 1.0 V vs. RHE and, therefore, the XPS surface analysis after the EC investigation coincides with the expected surface composition of the catalysts. After the activation procedure of 30 cycles ($\nu=100 \text{ mV s}^{-1}$) between 1.0 V and 1.5 V vs. RHE, the activity of the catalyst was re-measured between 1.0 V and 1.9 V vs. RHE. The resulting CV curves are illustrated in **Figure 4.3.7**, in comparison to the CV measurement before the conditioning procedure. While the catalytic performance of Co_2B improves slightly after the conditioning step, the catalytic performance of Co_3B is unaffected by the conditioning procedure.

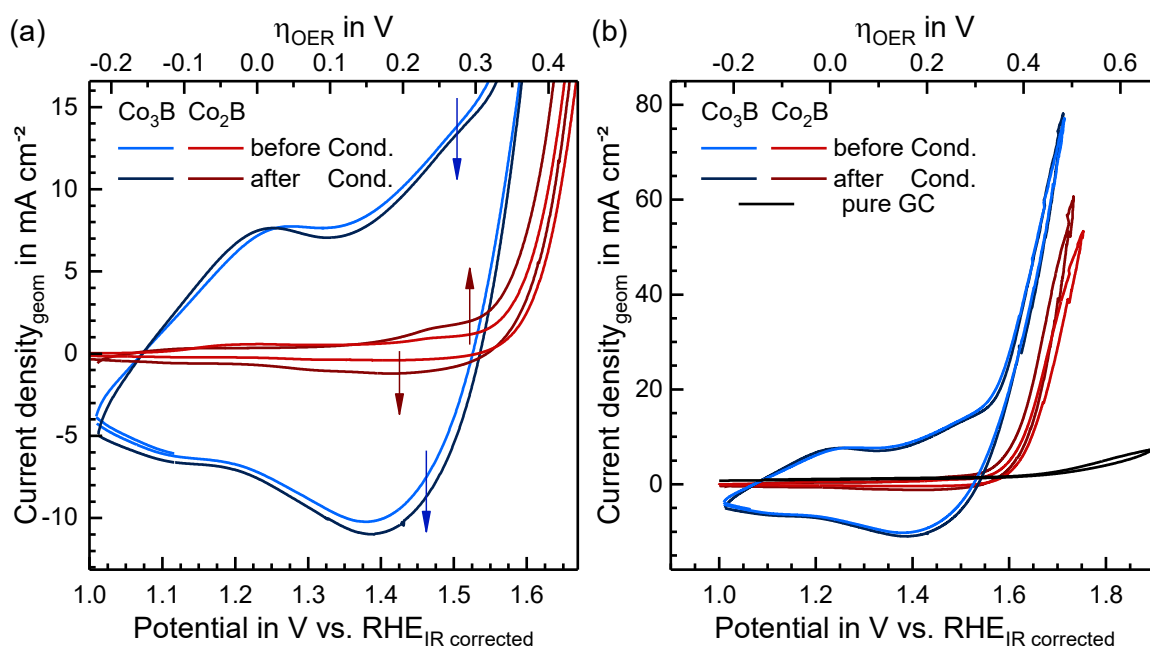


Figure 4.3.7: (a) Cyclic voltammograms (CVs) of Co_3B (blue) and Co_2B (red) emphasizing the redox behavior before and after conditioning. (b) CVs of Co_3B (blue) and Co_2B (red) before and after conditioning emphasizing the activity towards the OER compared to the one of the GC substrate (black). The curves are measured in 1 M KOH and the potentials are *iR* compensated.

Besides the variations in catalytic performance, the shape of the redox waves in Co_2B changes. An increase in the oxidation wave of Co^{3+} to Co^{4+} and the reduction wave of Co^{4+} to Co^{3+} is observed after the conditioning. The distinct increase in the Co^{3+} to Co^{4+} redox wave for the Co_2B catalyst can be attributed to a thickening of the oxide layer during the conditioning

step.^{[185], [251]} Another influence on the redox waves could be the nanostructure of the two catalysts. While Co₃B consists of spherical nanoparticles and shows already before the conditioning step a high accessible surface area, Co₂B forms rather a 2D network in nano dimensions (*cf.* **Figure 4.4.1**).^{[144]–[146], [229], [242]} Hence, the Nafion™ binder material could block certain parts of the network structure of Co₂B, limiting the accessible surface area, which, in turn, limits the intensity of the redox wave. During the cycling of the catalyst, a rising number of blocked parts are set free and the surface area in contact with the electrolyte increases. Additionally, this effect provides a possible explanation for the increased activity of the Co₂B catalyst after the conditioning step.

4.4 Incorporation of iron into dicobalt boride ($\text{Co}_{1-x}\text{Fe}_x$)₂B

The dicobalt boride powders with the incorporation of iron ($\text{Co}_{1-x}\text{Fe}_x$)₂B were synthesized with different iron amounts $0 \leq x \leq 0.5$ in the research group of Professor Barbara Albert by Dr. Sebastian Klemenz (TU Darmstadt, department of chemistry, Eduard-Zintl-institute of inorganic and physical chemistry). The synthesis routes for the ternary borides are presented in **Section 4.2.1**. More detailed information can be found in the dissertation of Dr. Sebastian Klemenz.^[229]

The nano-structured powders were characterized by XRD after synthesis by Sebastian Klemenz to validate the composition of the powders. No evidence of a side phase was found for the samples ($\text{Co}_{1-x}\text{Fe}_x$)₂B with $x \leq 0.2$ (cf. **Figure A11**, **Figure A12**, **Table A 2**, and **Table A 3**). The samples with $x > 0.3$ showed with increasing iron content an increasing amount of an α -Fe side phase. In addition to the expected ratios of cobalt, iron, and boron inside of the catalyst's bulk, the surface ratios of these materials were determined from XPS analysis. All samples were electrochemically investigated for the OER and the HER. However, only a minor activity was measured for the HER and therefore, no further efforts were dedicated towards this catalytic reaction. Before the EC investigation, the surfaces of the different catalyst phases were investigated with XPS. In addition, the best performing catalysts were investigated with XPS a second time after the EC investigation to identify the influence of the EC testing on the surface of the catalyst. Furthermore, scanning and transmission electron microscopy measurements were performed for the most promising catalyst. The SEM measurements were conducted by Kerstin Lakus-Wollny (group of Prof. W. Jaegermann TU Darmstadt, department of material science, surface science department) and the TEM measurements were conducted by Anna Müller (group of Prof. B. Albert, TU Darmstadt, department of chemistry, Eduard-Zintl-institute of inorganic and physical chemistry).

4.4.1 Surface analysis of the catalyst powders

The surface of the ($\text{Co}_{1-x}\text{Fe}_x$)₂B catalyst powders with $0.1 \leq x \leq 0.5$ was investigated with XPS. The idea to measure the catalysts before and after EC investigation to monitor the changes occurring under reaction conditions was limited due to the Nafion™ binder material inside of the catalyst ink. The XPS measurements were performed identically as described in **Section 4.3** for the pure dicobalt. Additionally, the morphology of the Co_2B and ($\text{Co}_{0.7}\text{Fe}_{0.3}$)₂B was exemplarily investigated using SEM and TEM. The SEM images were recorded with a Philips XL30 FEG scanning electron microscope, the TEM measurements were recorded with a 200 kV JEOL JEM 2100F transmission electron microscope. The resulting SEM images are shown in **Figure 4.4.1** with SEM. While the morphology of Co_2B (cf. **Figure 4.4.1a**) reveals an agglomerate structure with short rods and small spheres emerging out of it, the morphology of the

$(\text{Co}_{0.7}\text{Fe}_{0.3})_2\text{B}$ (cf. **Figure 4.4.1b**) shows longer rods forming a network-like structure. Additional TEM images in **Figure 4.4.2** underline the network-like character of the $(\text{Co}_{0.7}\text{Fe}_{0.3})_2\text{B}$ phase. The $(\text{Co}_{0.7}\text{Fe}_{0.3})_2\text{B}$ sample was measured after prolonged storage in air before the EC investigation. The nano- and microstructure of the sponge-like agglomerates are visible. At the same time, the surface of the catalyst is covered by an amorphous oxygen-rich surface layer, which was formed during a long storage time in air. Below that area the ternary boride $(\text{Co}_{0.7}\text{Fe}_{0.3})_2\text{B}$ crystallite phase is visible.

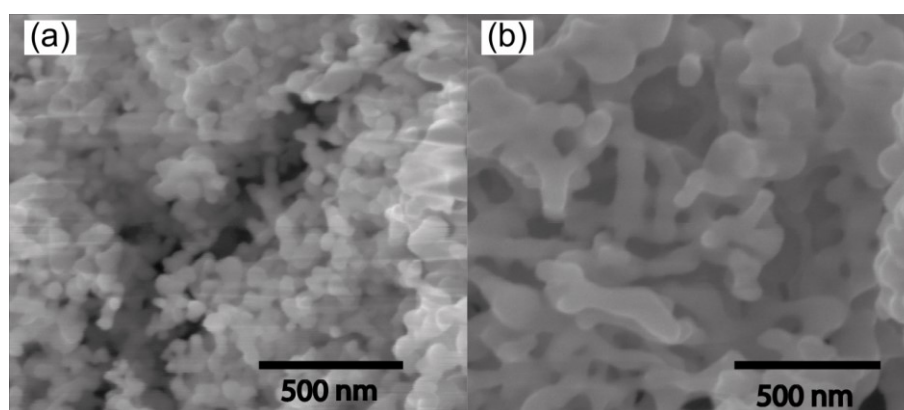


Figure 4.4.1: Scanning electron microscopy (SEM) images of Co_2B (a) and $(\text{Co}_{0.7}\text{Fe}_{0.3})_2\text{B}$ (b) powders measured on a carbon pad. The samples were measured with 10 kV excitation energy and 100000 x magnification.

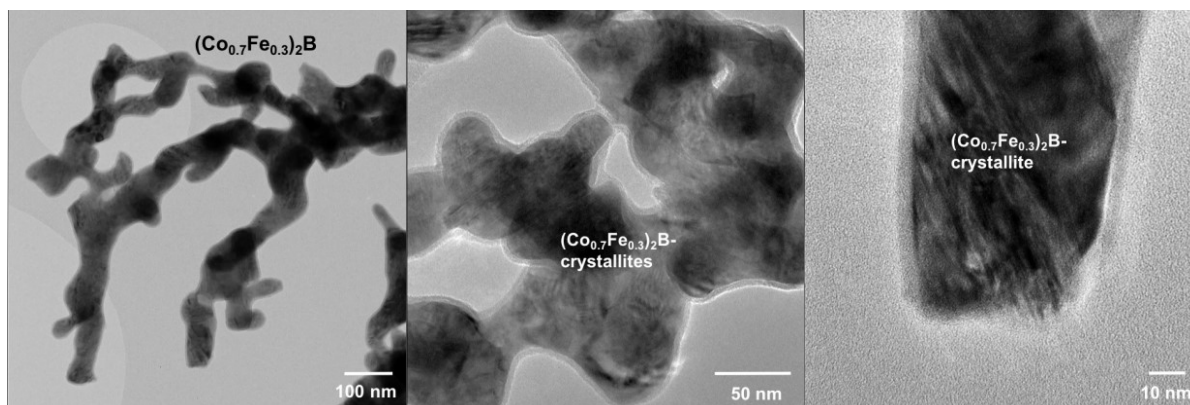


Figure 4.4.2: Bright-field transmission electron microscopy (BF-TEM) images of the $(\text{Co}_{0.7}\text{Fe}_{0.3})_2\text{B}$ catalyst after longer storage in air with different magnifications, showing the nano-structured morphology of the phase.

The surface of the $(\text{Co}_{1-x}\text{Fe}_x)_2\text{B}$ catalyst powders with $0.1 \leq x \leq 0.5$ was investigated with XPS. The measurement of the changes induced by the EC investigation was limited due to the NafionTM binder material inside of the catalyst ink. XPS measurements of NafionTM immersed powders were not feasible due to the detection limits of the method. Therefore, the catalysts before the EC investigation were embedded in indium foil and measured with XPS. The recorded XP

survey spectra embedded in indium foil are shown in **Figure 4.4.3** with the relevant photoemission lines marked. The relevant detailed spectra are shown and discussed in detail later in this chapter. The photoemission lines of the catalyst phase (blue), namely cobalt (Co 2p; Co 3p), iron (Fe 2p; Fe 3p), oxygen (O 1s), and boron (B 1s) are observed. In addition to that, indium (In 3p, In 3d) from the substrate and carbon (C 1s) contamination are found on the surface (grey).

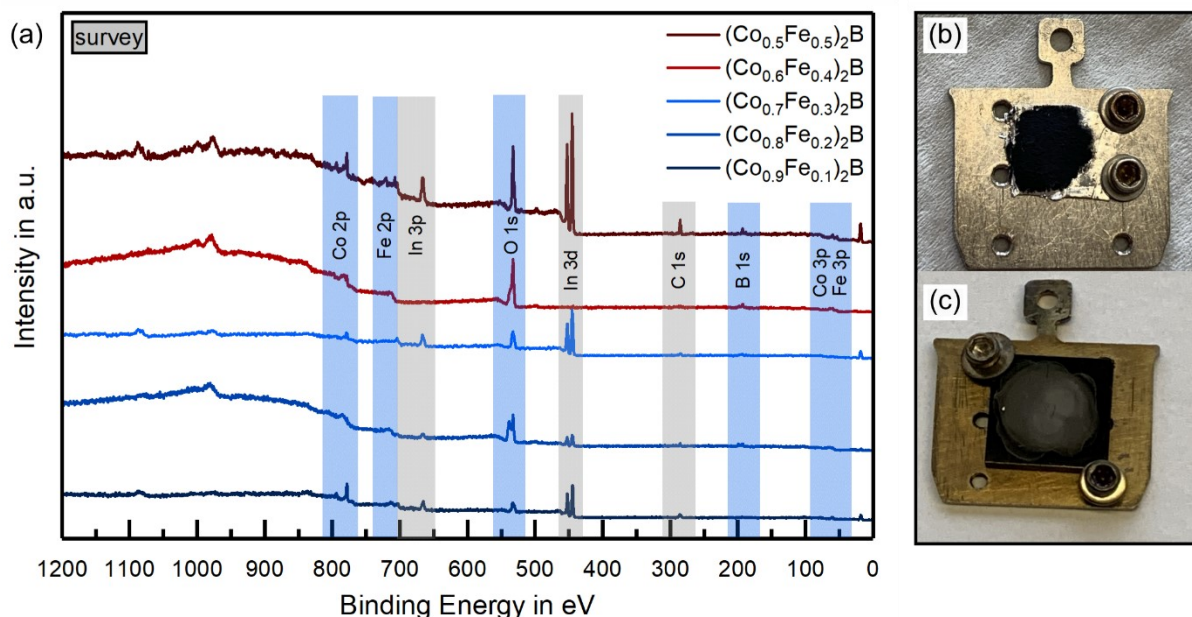


Figure 4.4.3: (a) XP survey spectra of the $(\text{Co}_{1-x}\text{Fe}_x)_2\text{B}$ phases with $0.1 \leq x \leq 0.5$ embedded in indium foil before electrochemical (EC) investigation. The relevant photoemission line positions of cobalt, iron, oxygen, boron, carbon, and indium are marked. (b) Exemplary picture of a sample embedded in indium foil and (c) the sample drop coated from an ink with Nafion™ onto GC substrate.

The surface compositions are determined with XPS for the different catalyst phases in terms of their metal fractions of cobalt and iron and of their overall metal to boron ratios, summarized in **Table 4.4.1**. The percentage of cobalt, iron, and boron at the surface was determined from the XPS data, using tabulated sensitivities for our experimental setup (*cf.* **Table 2.4.1**) in combination with a Shirley background subtraction.^{[72], [134]} From synthesis the iron content was adjusted to yield 10, 20, 30, 40, and 50% iron in the bulk of the catalyst. The metal to boron ratio is expected to be 2:1 for all samples. The assumed errors (*cf.* **Table 4.4.1**) for the different surface compositions are due to measuring inaccuracies, partial surface oxidation, and in terms of the metal fractions due to the overlapping of Auger signals with the corresponding metallic 2p photoemission lines. As an alternative to the 2p photoemission lines of cobalt and iron, the Co 3p and Fe 3p photoemission lines could be used to determine the metallic fractions of the catalysts. However, due to only minor differences in binding energy between these

photoemission lines, the signals overlap slightly. Therefore, the area determination with the corresponding background signal is not precise.

Table 4.4.1: Quantitative surface analysis with XPS of the different $(\text{Co}_{1-x}\text{Fe}_x)_2\text{B}$ catalyst phases embedded in indium foil.

Sample in Indium foil	Surface metal fraction in % ^{*1}		Surface Ratio
	Cobalt	Iron	Metal : Boron ^{*2}
$(\text{Co}_{0.9}\text{Fe}_{0.1})_2\text{B}$	88.9	11.1	1.8
$(\text{Co}_{0.8}\text{Fe}_{0.2})_2\text{B}$	82.9	17.1	2.2
$(\text{Co}_{0.7}\text{Fe}_{0.3})_2\text{B}$	70.6	29.4	2.0
$(\text{Co}_{0.6}\text{Fe}_{0.4})_2\text{B}$	61.7	38.3	3.0
$(\text{Co}_{0.5}\text{Fe}_{0.5})_2\text{B}$	39.3	60.7	1.6

^{*1} The assumed errors for the results are due to measuring inaccuracy and the Auger signals of cobalt and iron overlapping with the photoemission lines as marked in **Figure 4.4.4**. These errors are assumed to be between 1 and 10% in the metallic fraction.

^{*2} The assumed errors for the results are due to measuring inaccuracy and the oxidation of boron as well as of the metallic components as shown in **Figure 4.4.5** and in **Figure 4.4.4**, respectively, and are assumed to be between 0.1 and 0.5.

The respective photoemission lines of Co 2p (*cf.* **Figure 4.4.4a**) and Fe 2p (*cf.* **Figure 4.4.4b**) are shown for the $(\text{Co}_{1-x}\text{Fe}_x)_2\text{B}$ catalysts with $x=0.1$ (dark-colored) as the lower and $x=0.5$ (light-colored) as the upper extreme value of the measured phases. The overlapping Auger signals (Fe LMM and Co LMM) are highlighted to illustrate their influence on the mutual photoemission lines. The Fe LMM Auger signal is located around 783.6 eV (reference value for iron 784 eV^{[47], [69]}), while the Co LMM Auger line can be found around 713.3 eV (reference value for cobalt 713 eV^{[47], [69]}). The metal boride signals can be found for cobalt at around 778.3 eV^{[205], [206]} and for iron at around 706.9 eV.^{[210], [212], [213], [217]} While in the Co 2p photoemission line no or only slight surface oxidation is visible, the Fe 2p photoemission lines show a stronger surface oxidation at a binding energy of around 710.6 eV, which is identified to be mainly Fe^{2+} .^{[210], [214], [218]} These oxidations are of course dependent on the exposure time to ambient conditions. For the $(\text{Co}_{0.9}\text{Fe}_{0.1})_2\text{B}$ and $(\text{Co}_{0.7}\text{Fe}_{0.3})_2\text{B}$ powders an additional XPS study after two weeks of air exposure was conducted. The comparison of the Co 2p and Fe 2p spectra of the two phases is depicted in **Figure 4.4.5**, identifying the changes during this time. For both phases, the signal of the metallic boride (CoB_i and FeB_i) components with the binding energies of 778.4 eV and 706.7 eV decreases under ambient conditions. At the same time, both phases

show a second signal at slightly higher binding energies, which can be identified as a rise in oxidation state for both the cobalt and the iron phase, leading to the conclusion that both boride phases $(\text{Co}_{0.9}\text{Fe}_{0.1})_2\text{B}$ and $(\text{Co}_{0.7}\text{Fe}_{0.3})_2\text{B}$ are not entirely stable under ambient conditions, forming an oxide/hydroxide layer at the surface.

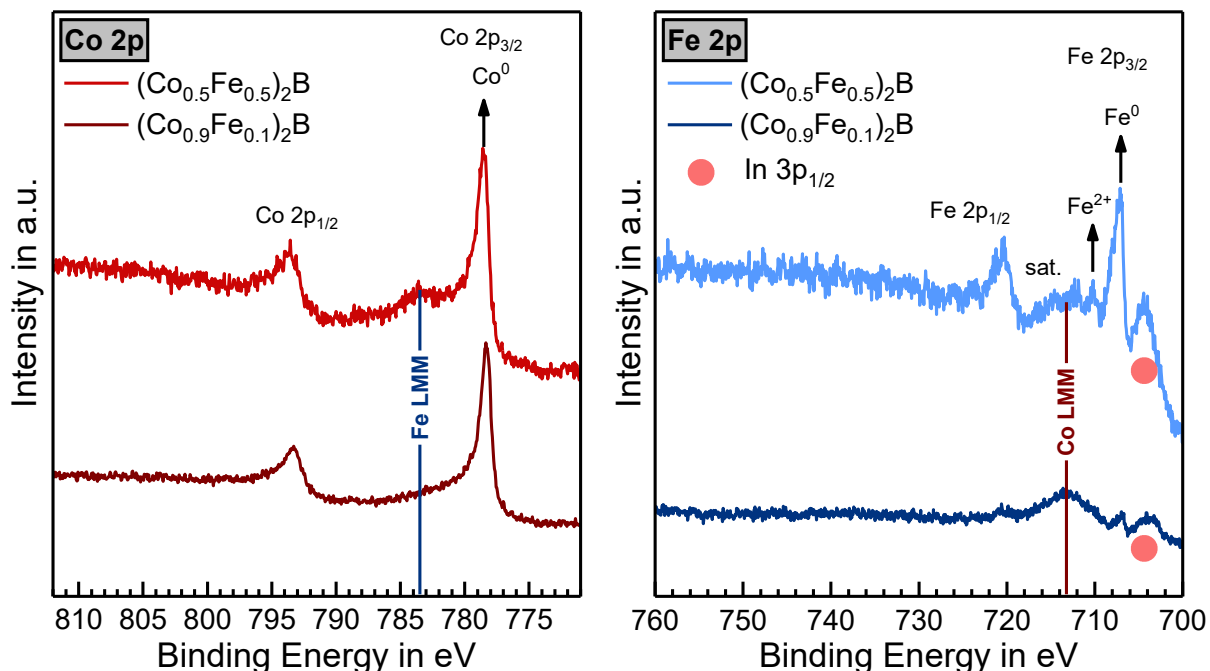


Figure 4.4.4: Comparison of the XP detail spectra of Co 2p ((a) – red) and Fe 2p ((b) – blue) for the $(\text{Co}_{1-x}\text{Fe}_x)_2\text{B}$ catalyst with $x=0.1$ (dark-colored) and $x=0.5$ (light-colored), showing the influence of the overlapping iron and cobalt Auger signals with the respective photoemission lines of cobalt and iron, respectively. With a red dot, the In 3p_{1/2} photoemission line is marked.

This surface oxidation is additionally apparent in the B 1s photoemission line illustrated in **Figure 4.4.6**. Two boron phases are visible in the B 1s detail spectra for the different catalyst phases. Boron with an oxidation state of B^0 at a binding energy of 188.4 eV, representing the metal borides^{[157], [205], [206]} and an oxidized boron phase located at higher binding energies. This boron phase can be most likely identified as boron trioxide B_2O_3 or boron trihydroxide $\text{B}(\text{OH})_3$ with boron in an oxidation state B^{3+} which are located between 192.5 eV and 194.0 eV.^{[157], [212], [221], [243], [244], [246]–[248], [253]} The positions of the oxidized boron phase for the $(\text{Co}_{1-x}\text{Fe}_x)_2\text{B}$ catalysts vary with a changing ratio of cobalt to iron. For $x=0.2$, 0.4, and 0.5 the maximum of the boron oxide peak is located around 192.8 eV, while the maximum for $x=0.1$ and $x=0.3$ is positioned at approximately 193.8 eV. Both positions are in the range of the literature values mentioned earlier.^{[157], [212], [221], [243], [244], [246]–[248], [253]}

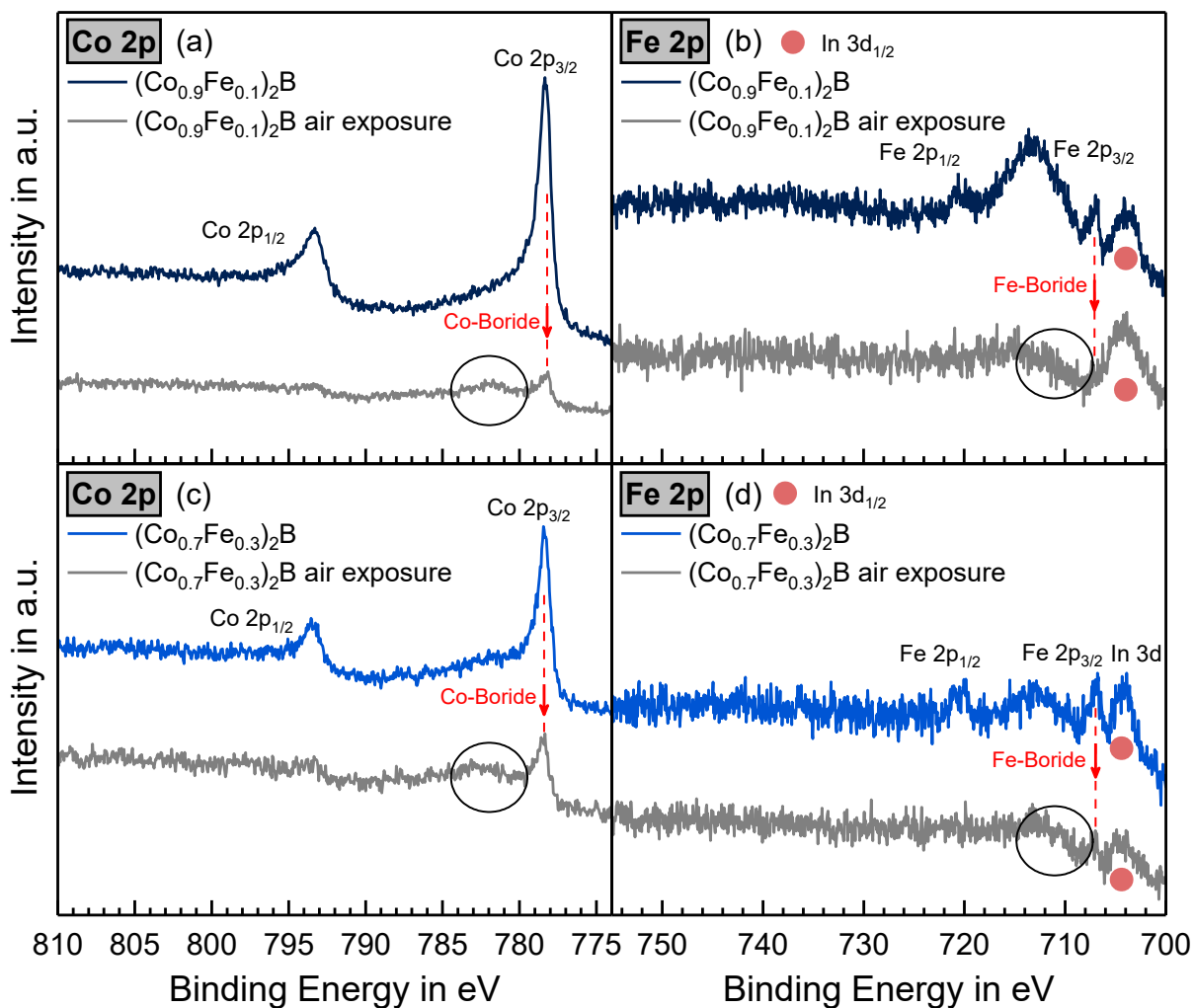


Figure 4.4.5: XP Co 2p (a) & (c) and Fe 2p (b) & (d) detail spectra of $(\text{Co}_{1-x}\text{Fe}_x)_2\text{B}$ with $x=0.1$ (dark blue) and $x=0.3$ (blue), showing the influence of two weeks of air exposure (gray) onto the surface of the catalyst. With a red dot, the In $3p_{1/2}$ photoemission line is marked.

The spin-orbit splitting of the Cl 2p photoemission line for metal chlorides is located around 199 eV for the Cl $2p_{3/2}$ and 201 eV for the Cl $2p_{1/2}$.^[69] While the positioning of the BO_x peaks seems arbitrary, for the samples with the boron oxide at lower binding energies ($x=0.2$, 0.4 , and 0.5) an additional broad peak is apparent at slightly higher binding energies between 198.4 and 201.0 eV. The samples ($x=0.1$ and $x=0.3$) with the higher binding energy position for BO_x show no peak in this binding energy range. To the author's best knowledge, this signal has not been a topic of the scientific discussion for the B 1s photoemission line so far. However, the peak structure fits the chlorine Cl 2p photoemission line, which could arise from residual chlorine from the synthesis route. There cobalt(II)-chloride-hexahydrate was used in the wet chemical preparation procedure of the $(\text{Co}_{1-x}\text{Fe}_x)_2\text{B}$ powders.

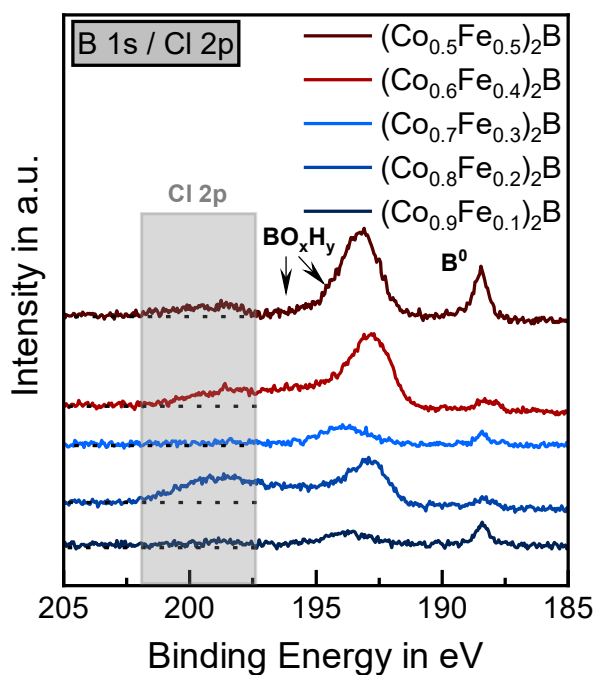


Figure 4.4.6: XP B 1s detail spectra of $(\text{Co}_{1-x}\text{Fe}_x)_2\text{B}$ with $0.1 \leq x \leq 0.5$. At binding energies between 197 eV and 202 eV, the Cl 2p photoemission line is highlighted.

4.4.2 Electrochemical investigation

The EC behavior of the $(\text{Co}_{1-x}\text{Fe}_x)_2\text{B}$ catalysts (with $0.1 \leq x \leq 0.5$) drop coated with ink onto GC was investigated for HER and OER in 1 M KOH. Since these catalysts showed only a poor catalytic performance for HER, the focus for the $(\text{Co}_{1-x}\text{Fe}_x)_2\text{B}$ catalysts was placed on the reactivity for OER.

The same EC measurement protocol as for the pure dicobalt and tricobalt borides is used (*cf.* Section 4.2.5). The conditioning step is again used to activate the cobalt phase (*cf.* Section 4.3.2). A transition from a Co^0 and Fe^0 phase to a more oxidized form is already shown in Section 4.4.1, which was due to the storage of the $(\text{Co}_{1-x}\text{Fe}_x)_2\text{B}$ catalysts under ambient conditions. It is expected that these phases transform further under EC reaction conditions. In Section 4.1.3 the EC redox behavior for pure iron is summarized, featuring no redox waves in the chosen conditioning range. However, for a mixed cobalt iron system, it was shown that the incorporation of iron leads to an anodic shift in the cobalt $\text{Co}^{2+}/\text{Co}^{3+}$ oxidation wave, due to strong electronic interactions of the two elements.^{[44], [47]}

In Figure 4.4.7a the CV curves after the conditioning procedure for the $(\text{Co}_{1-x}\text{Fe}_x)_2\text{B}$ catalysts are depicted with magnifications of the OER regime (*cf.* Figure 4.4.7b) and of the redox waves occurring in the potential interval of 1.00 to 1.55 V vs. RHE (*cf.* Figure 4.4.7c). The redox waves shift with an increasing incorporated amount of iron anodically.^{[44], [47]} While the shift in

the oxidation wave from the $(\text{Co}_{1-x}\text{Fe}_x)_2\text{B}$ with $x=0$ to $x=0.1$ phase is negligible, the shift between the $x=0.1$ and the $x=0.2$ phase is the highest. After that, the anodic shift seems to have a linear behavior for $x=0.2$ to $x=0.5$. The anodically shifted oxidation potentials imply that the oxidation of the catalyst is hindered by the incorporated iron. The more iron is incorporated, the more surplus energy is needed to oxidize the compound. A summary of the values for the onset potential and the maximum of these oxidation waves can be found in **Figure 4.4.8a**.

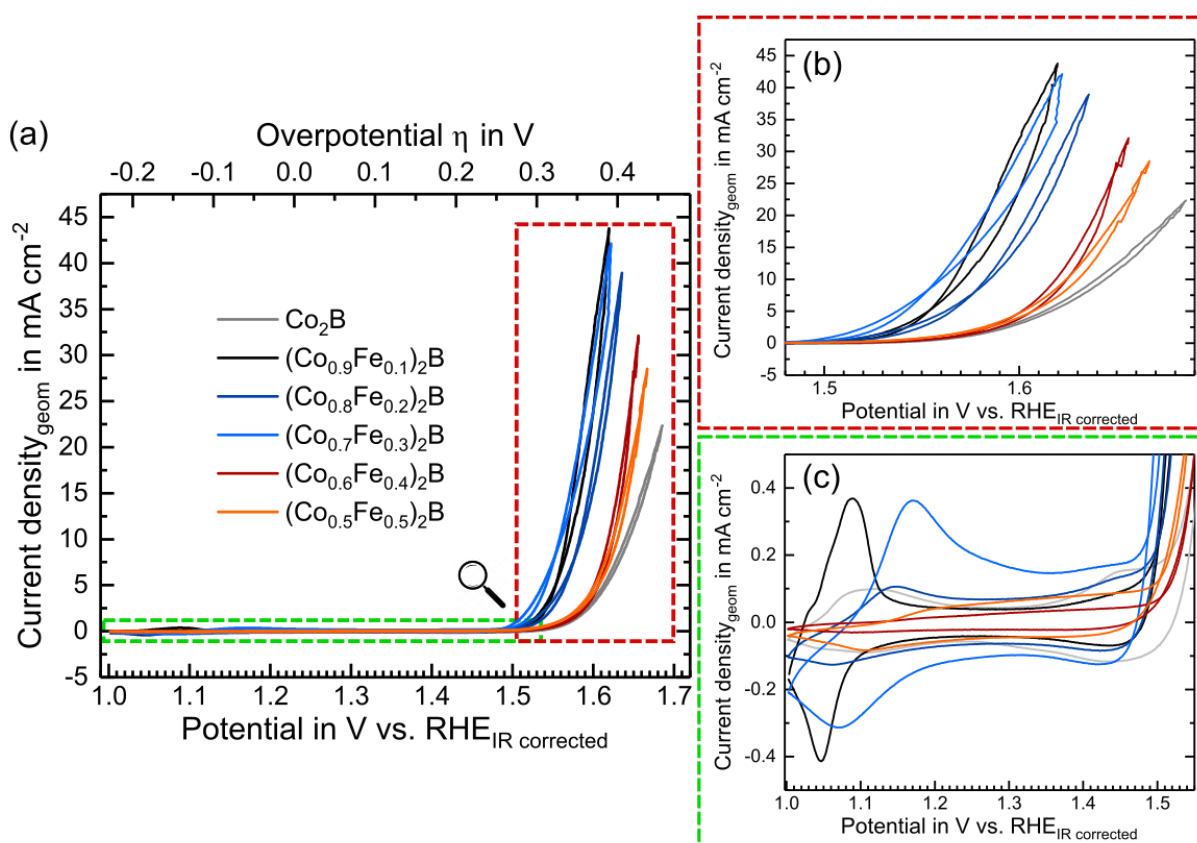


Figure 4.4.7: (a) Cyclic Voltammometry measurements of the $(\text{Co}_{1-x}\text{Fe}_x)_2\text{B}$ catalysts with $0 \leq x \leq 0.5$ after the conditioning procedure and magnifications of the (b) oxygen evolution reaction (OER) and (c) redox waves. All curves were measured with a scan rate of 50 mV s^{-1} according to the electrochemical (EC) protocol (cf. **Section 4.2.5**) in 1 M KOH with an Hg/HgO as a reference electrode and are iR corrected.

As seen in **Figure 4.4.7** a distinct difference in terms of the OER onset potentials is visible. While the $(\text{Co}_{1-x}\text{Fe}_x)_2\text{B}$ catalysts with $0.1 \leq x \leq 0.3$ exhibit an onset potential below 1.5 V vs. RHE, the $(\text{Co}_{1-x}\text{Fe}_x)_2\text{B}$ catalysts with $x > 0.3$ show a comparable OER onset potential ($> 1.5 \text{ V}$ vs. RHE) as the one of Co_2B . The onset potentials for the different catalyst phases are summarized in **Figure 4.4.8b**. The lowest onset potential was obtained by the $(\text{Co}_{0.7}\text{Fe}_{0.3})_2\text{B}$ phase. Similar results are achieved for the overpotential values at a current density of 10 mA cm^{-2} (cf. **Figure 4.4.8c**). The lowest values were again reached for the $(\text{Co}_{1-x}\text{Fe}_x)_2\text{B}$ phase with $x=0.3 < x=0.1 < x=0.2$. The $(\text{Co}_{1-x}\text{Fe}_x)_2\text{B}$ with $x=0.4$ and $x=0.5$ show comparable results to the pure Co_2B phase. A summary of the different values is illustrated in **Figure 4.4.8c**. The same

activity order is found for the determination of the Tafel slopes for the $(\text{Co}_{1-x}\text{Fe}_x)_2\text{B}$ catalysts depicted in **Figure 4.4.9a**. The catalyst phases with $x=0.1$ and $x=0.3$ exhibit a Tafel slope below 50 mV dec^{-1} , followed by $(\text{Co}_{0.8}\text{Fe}_{0.2})_2\text{B}$ with 50 mV dec^{-1} . For the $(\text{Co}_{1-x}\text{Fe}_x)_2\text{B}$ phases with $x=0.4$ and $x=0.5$ Tafel slopes of 52 mV dec^{-1} and 60 mV dec^{-1} were determined. The catalyst phase with the highest Tafel slope and therefore the lowest performance in this regard is the pure Co_2B with 71 mV dec^{-1} . In conclusion, the $(\text{Co}_{1-x}\text{Fe}_x)_2\text{B}$ catalysts with $x=0.1$ and $x=0.3$ exhibit the best performance for the OER in terms of onset potentials ($<1.5 \text{ V vs. RHE}$), overpotentials at 10 mA cm^{-2} ($< 0.35 \text{ V}$) and Tafel slopes ($< 50 \text{ mV dec}^{-1}$) and even exceeds the performance of reported CoFeO_x catalysts ($\eta_{10}=0.37 \text{ V}$).^[19] The overpotential for the best $(\text{Co}_{1-x}\text{Fe}_x)_2\text{B}$ catalysts are only slightly higher as reported values for the noble metal catalyst IrO_2 (cf. **Figure 4.4.8c**).^[19]

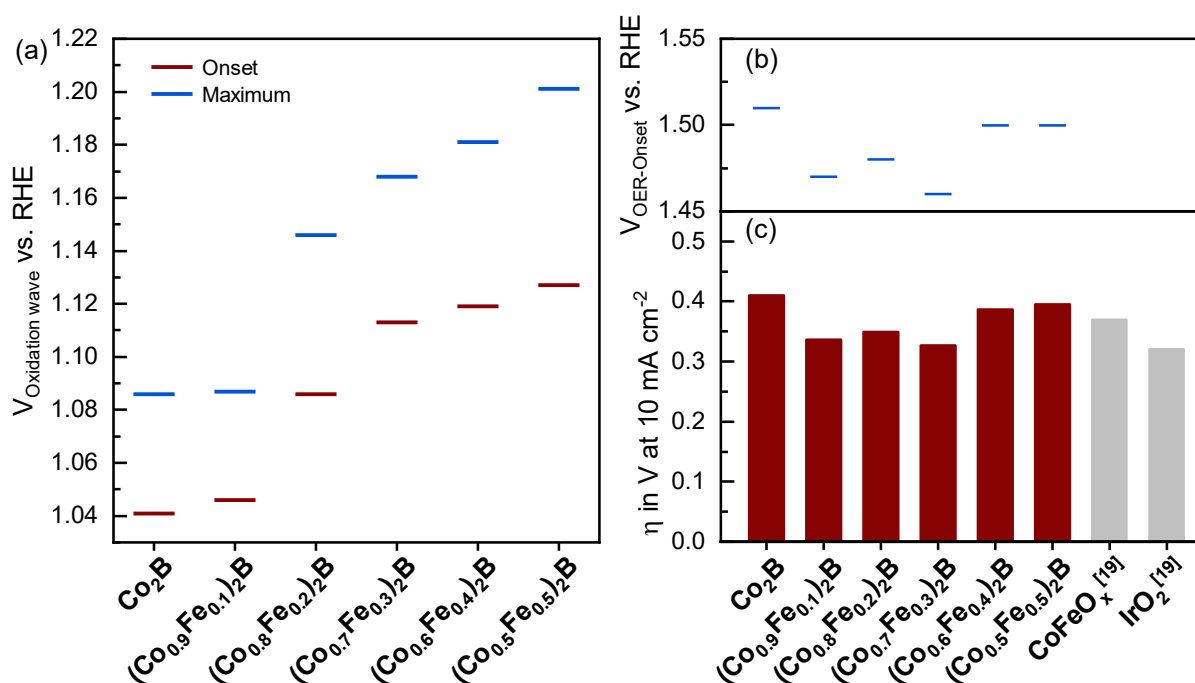


Figure 4.4.8: Summary of the reactivity and activity data from **Figure 4.4.7** of the $(\text{Co}_{1-x}\text{Fe}_x)_2\text{B}$ catalysts with $0 \leq x \leq 0.5$. **(a)** The position of the oxidation waves for the different iron amounts is shown in terms of their onset potential and peak maximum. **(b)** The activity of the different catalyst phases is shown in terms of their onset potential (blue lines) for the OER and **(c)** their overpotential at 10 mA cm^{-2} (η_{10} ; red bars) compared to literature values.^[19]

However, for catalytic processes not only the activity of a certain catalyst is important, but also the stability of this catalyst under reaction conditions. Therefore, the stability of the two best catalysts was investigated over a longer time period at a constant current density of 10 mA cm^{-2} . The chronopotentiometry curves were measured for 30 and 17 hours with a pumping system (Hei-LOW Advantage 06; Heidolph Instruments GmbH) and an electrolyte reservoir

(≈ 200 mL) of around for the $(\text{Co}_{0.9}\text{Fe}_{0.1})_2\text{B}$ and $(\text{Co}_{0.7}\text{Fe}_{0.3})_2\text{B}$ catalyst phase, respectively. During that time, the electrolyte was saturated with nitrogen gas to remove the oxygen and hydrogen gas. The stability curves depicted in **Figure 4.4.9b** show a stable performance for both catalyst systems.

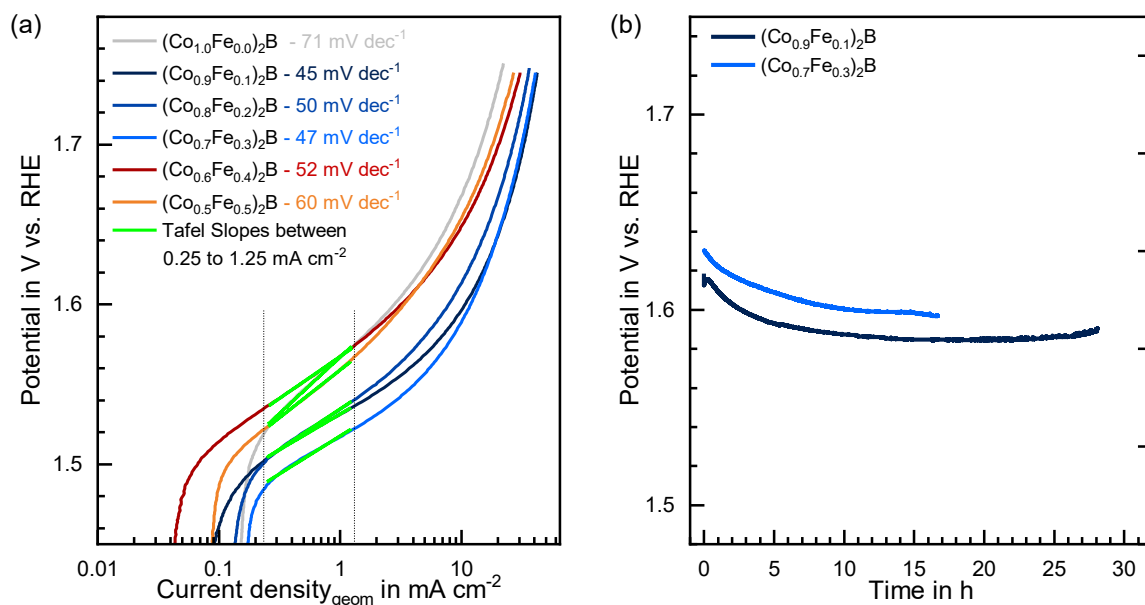


Figure 4.4.9: (a) Tafel slope determination using cyclic voltammogram (CV) with a scan rate of 10 mV s^{-1} for the $(\text{Co}_{1-x}\text{Fe}_x)_2\text{B}$ catalysts with $0 \leq x \leq 0.5$ between 0.25 to 1.25 mA cm^{-2} without iR correction. (b) Long term stability measurements of the two most active phases $(\text{Co}_{0.9}\text{Fe}_{0.1})_2\text{B}$ and $(\text{Co}_{0.7}\text{Fe}_{0.3})_2\text{B}$ at a current density of 10 mA cm^{-2} . All curves were measured according to the electrochemical (EC) protocol (cf. **Section 4.2.5**) in 1 M KOH with an Hg/HgO as a reference electrode.

Over the first five hours of measurement time, the performance of the catalyst improves further. Within the 5th to the 10th measurement hour, only minor further improvements are observable, followed by a constant performance at a potential around 1.58 V and 1.60 V vs. RHE or rather an overpotential $\eta_{10}=350 \text{ V}$ and $\eta_{10}=370 \text{ V}$ for the $(\text{Co}_{0.9}\text{Fe}_{0.1})_2\text{B}$ and $(\text{Co}_{0.7}\text{Fe}_{0.3})_2\text{B}$ catalyst phase, respectively. On the account of this, it can be stated, that $(\text{Co}_{0.9}\text{Fe}_{0.1})_2\text{B}$ and $(\text{Co}_{0.7}\text{Fe}_{0.3})_2\text{B}$ are not only the most active catalysts of this study but are also stable under reaction conditions over a prolonged period of time. Hence, the incorporation of iron into dicobalt boride improved the overall performance of the catalyst system for the OER. An iron incorporation limit to improve the catalytic performance of single metal Co_2B could not be identified. Even the catalyst phase with 50% iron showed an improvement on the OER performance. However, there is a limit in improving the onset potential of the $(\text{Co}_{1-x}\text{Fe}_x)_2\text{B}$ system, which is identified to be between $x=0.3$ and $x=0.4$. Grewe *et al.*^[46] found that 32% of iron incorporation into Co_3O_4 was ideal to optimize the OER performance. A higher ideal incorporation percentage was found by Mendoza-Garcia *et al.*^[254] for dicobalt phosphides, who showed that the most efficient cobalt

iron mixture was 46% of iron. Burke *et al.*^[47] even discussed that iron could be the active site in the material, while cobalt stabilizes the catalyst and at the same time improves the overall conductivity of the compound. They found that cobalt iron oxyhydroxides with more than 50% iron were not stable under reaction conditions, since some parts of the sample lack the stabilizing cobalt.

4.4.3 XPS – oxidation state changes during operating conditions

Besides the functionality of the catalyst system itself (*cf.* **Section 4.4.2**), the changes occurring under reaction conditions are crucial to understand the reaction mechanism of the catalyzing material. To be able to study such changes, XPS analyses before (*cf.* **Section 4.4.1**) and after EC investigation were conducted, for the most active catalyst phases $(\text{Co}_{0.9}\text{Fe}_{0.1})_2\text{B}$ and $(\text{Co}_{0.7}\text{Fe}_{0.3})_2\text{B}$. The Co 2p and Fe 2p XP detail spectra of the two phases before and after EC investigation are depicted in **Figure 4.4.10**.

During the EC investigation, the initial Co_2B peak at 778.4 eV disappears and is replaced by a strong feature at 779.9 eV with an asymmetry at approximately 781.2 eV. The former being assigned to cobalt oxide, the latter to cobalt hydroxide.^{[117], [201], [204]} The peak positions and shape of the photoemission lines corresponding to Co 2p are assigned to CoOOH . In principle they could also be assigned to Co_3O_4 , consisting of cobalt in the two oxidation states Co^{+II} (satellite 785.7 eV) as well as Co^{+III} (satellite at 789.9 eV).^{[117], [119], [204]} However, this assignment can be excluded due to the presence of a strong hydroxide signal in the O 1s photoemission line at a binding energy of 531 eV (*cf.* **Figure 4.4.11**). As already observed for the pure Co_2B and Co_3B catalysts the B 1s photoemission line vanishes completely, leaving no trace of boron at the near-surface of the catalyst (*cf.* **Figure A 18**). Overall, these XPS observations are fully consistent with the formation of a cobalt oxyhydroxide at the surface, which has been observed in cobalt-containing catalysts before.^{[47], [48], [135], [165], [249], [250]} These observations are also in agreement with the occurrence of the redox waves of cobalt-based materials in the investigated potential range (*cf.* **Figure 4.1.4** and **Section 4.1.3**). The detail O 1s spectrum of CoOOH features two signals (oxide: 529.3 eV and hydroxide: 530.9 eV) with similar intensities, according to the stoichiometric ratio.^{[119], [135], [201], [204]} In our case the hydroxide species shows a slightly higher intensity. This is because the $(\text{Co}_{1-x}\text{Fe}_x)_2\text{B}$ catalysts were drop coated with a NafionTM containing ink. The structural formula and the XPS specifics of NafionTM are summarized in **Section 4.2.6**. NafionTM contains sulfonyl hydroxide ($\text{R-S(=O)}_2(\text{OH})$), oxocarbon (CO_x), and oxocarbon with fluorine (OCF), which account for the signals around 531.7 to 535 eV.^{[234], [239], [255]}

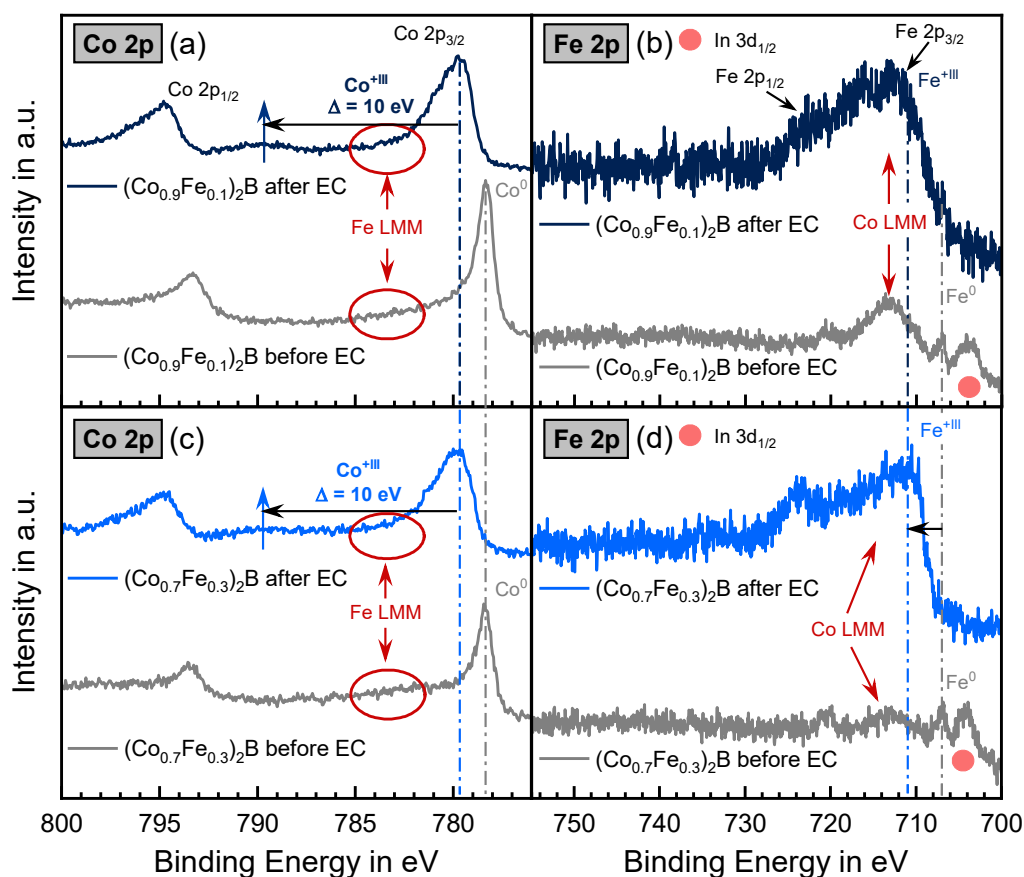


Figure 4.4.10: XP Co 2p (a) & (c) and Fe 2p (b) & (d) detail spectra of $(\text{Co}_{1-x}\text{Fe}_x)_2\text{B}$ with $x=0.1$ (dark blue) and $x=0.3$ (light blue) before (gray) and after (blue) electrochemical (EC) investigation, indicating the changes in composition occurring during the EC testing of the samples. With a red dot, the In $3d_{1/2}$ photoemission line is marked.

Especially, the sulfonyl hydroxide peak of the NafionTM overlaps with the hydroxide component of the CoOOH , increasing the hydroxide component in the O 1s signal. The influence of NafionTM on the O 1s photoemission line is further clarified in **Figure 4.4.11**. Here, different NafionTM amounts are observed for the $(\text{Co}_{0.9}\text{Fe}_{0.1})_2\text{B}$ and $(\text{Co}_{0.7}\text{Fe}_{0.3})_2\text{B}$ catalysts, leading to a change in the sulfonyl hydroxide signal and further to a change in the overall shape of the O 1s photoemission line. The different apparent NafionTM amounts in the XP spectra are simply because of the randomized arrangement of the catalyst powders on the surface of the substrate and not because of the different NafionTM amounts inside the drop coated ink. The Fe 2p photoemission line is hard to interpret in detail due to the overlap with the Co LMM Auger line located at around 713.3 eV. However, the oxidation state can be assigned to a Fe^{3+} , which fits to the oxidation state expected from electrochemistry. In the O 1s photoemission line mainly a Fe_2O_3 phase is visible, but due to the many components assigned in the O 1s also a mixed iron oxide/hydroxide/oxyhydroxide $\text{Fe}^{3+}\text{O}_x\text{H}_y$ phase cannot be excluded as stated in the Burke O'Sullivan Duplex Layer Model by Lyons et al.^[187] (cf. **Figure 4.1.6**).

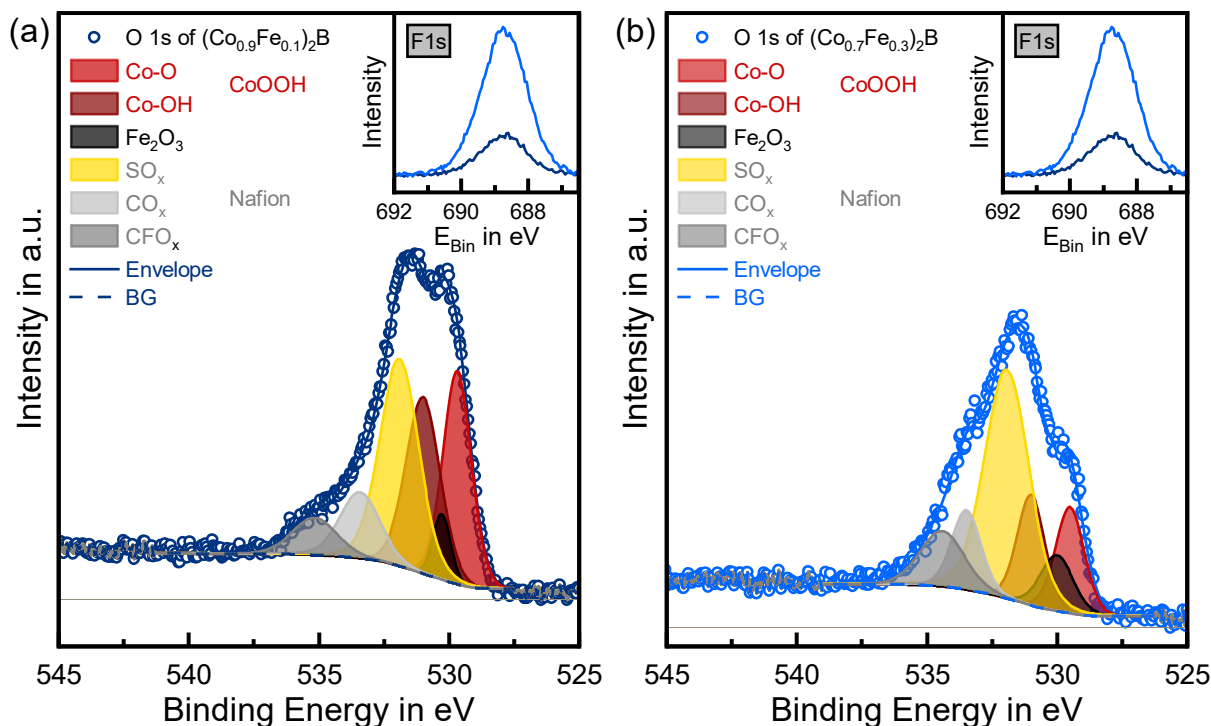


Figure 4.4.11: XP O 1s detail spectra of $(\text{Co}_{1-x}\text{Fe}_x)_2\text{B}$ with $x=0.1$ ((a) – dark blue) and $x=0.3$ ((b) – light blue) after electrochemical (EC) investigation. The corresponding F 1s photoemission lines are shown as an inset in the upper right corner to compare the Nafion™ amount measured with XPS. The yellow and grey fit illustrating the influence of Nafion™ within the O 1s photoemission line. SO_x displays the sulfonyl hydroxide part, while CO_x and CFO_x display the oxocarbon and oxocarbon with fluorine parts of Nafion™.

The chemical composition of the catalysts after the EC investigation was again calculated by XPS, using the Fe 2p and Co 2p photoemission lines. The used parameters are given in **Table 2.4.1**. In **Table 4.4.2** the calculated values for iron on the surface of the $(\text{Co}_{0.9}\text{Fe}_{0.1})_2\text{B}$ and $(\text{Co}_{0.7}\text{Fe}_{0.3})_2\text{B}$ catalysts before and after the EC investigation are summarized.

Table 4.4.2: Chemical composition of the surface of the two most active catalysts $(\text{Co}_{0.9}\text{Fe}_{0.1})_2\text{B}$ and $(\text{Co}_{0.7}\text{Fe}_{0.3})_2\text{B}$ determined with XPS before and after the electrochemical (EC) investigation.

Sample	Iron content x at the surface in % *		
	Expected	Before EC	After EC
$(\text{Co}_{0.9}\text{Fe}_{0.1})_2\text{B}$	10	11.1	8.7
$(\text{Co}_{0.7}\text{Fe}_{0.3})_2\text{B}$	30	29.4	27.8

*1 The assumed errors for the results are due to measuring inaccuracy and the Auger signals of cobalt and iron overlapping with the photoemission lines as marked in **Figure 4.4.4**. These errors are assumed to be between 1 and 10% in metallic fraction.

Only slight changes in the iron amount for both catalysts after the EC investigation are visible. These changes are within the assumed measurement error (cf. **Table 4.4.2**), which is relatively high due to the overlap of the photoemission lines (Co 2p & Fe 2p) with the Auger lines (Fe LMM & Co LMM) (cf. **Figure 4.4.4**). However, for both phases, a lower amount of iron after the EC investigation is calculated. Therefore, it cannot be definitely excluded that iron dissolves under reaction conditions.

4.4.4 Conclusion of the proposed mechanism

In this chapter, an attempt to assemble the corresponding mechanism explaining the good EC performance for the OER of the $(\text{Co}_{1-x}\text{Fe}_x)_2\text{B}$ catalysts in an alkaline electrolyte will be given. First, it should be stated that the ternary metal boride powders are not stable under ambient conditions (cf. **Section 4.4.1**). During the EC investigation, the surface of the ternary metal boride oxidizes further and forms a cobalt oxyhydroxide (CoOOH) and a Fe^{3+} phase, which is mainly assigned to iron oxide (Fe_2O_3) with possible contributions of mixed oxide/hydroxide FeO_xH_y phase as stated by Lyons et al.^[187]. This is in agreement with earlier EC studies developed for cobalt and iron electrodes (cf. **Section 4.1.3**).^{[183]–[188], [190]} The oxidation and reduction waves of the $\text{Co}^{2+/3+}$ transition both shift anodically with increasing iron content, which leads to the assumption that strong electronic coupling between cobalt and iron is present. These findings are supported by literature results for other cobalt-iron-based catalyst systems.^{[44], [47]} From our XPS-data before and after the EC investigation, it is proposed that the structure of the $(\text{Co}_{1-x}\text{Fe}_x)_2\text{B}$ catalyst changes from a nano-structured network with a thin oxide layer (after air storage) to one with a thick oxide or rather oxyhydroxide layer. This oxidation process of the ternary metal boride catalyst is schematically illustrated in **Figure 4.4.12**. The three different stages of the powder “as is” (**d**), “air stored” (**e**), and “after electrochemistry” (**f**) are presented schematically and with the corresponding Co 2p ((**a**), (**b**), and (**c**)) and Fe 2p XP detail spectra ((**g**), (**h**), and (**i**)). The outer oxidation surface layer forms with the remaining metal boride core a suitable catalyst system. In 1994, Shveikin^[245] specified the combination of the oxidized surface layer with the metal boride core as a core-shell structure. From 2016 to 2019, several studies on the formation of core-shell structures of transition metal borides during the OER were published, which was due to a rising scientific interest in transition metal borides for the water-splitting reaction.^{[165], [171], [172], [174]–[176], [256]} In this work, the term core-shell structure is avoided, since it cannot be proven that the boride core acts as a catalyst itself. However, it is beneficial for the catalytic process in terms of the overall conductivity of the catalytic system. Metal borides show in contrast to metal oxides/hydroxides an increased electrical conductivity.^{[149], [150], [245]} Carenco *et al.*^[149] and Wang *et al.*^[150] stated in their publications that transition

metal borides are often even more conductive than the parent metal. As it has been shown, the incorporation of up to 50% iron into the $(\text{Co}_{1-x}\text{Fe}_x)_2\text{B}$ ($0.1 \leq x \leq 0.5$) catalyst is beneficial for the catalytic performance of the OER catalyst. However, an improved OER onset potential was only obtained with an incorporation of $x \leq 0.3$. This could be due to the formation of an α -Fe side phase during the synthesis of the $(\text{Co}_{1-x}\text{Fe}_x)_2\text{B}$ catalysts with $x > 0.3$ observed by XRD (cf. Table A 3).

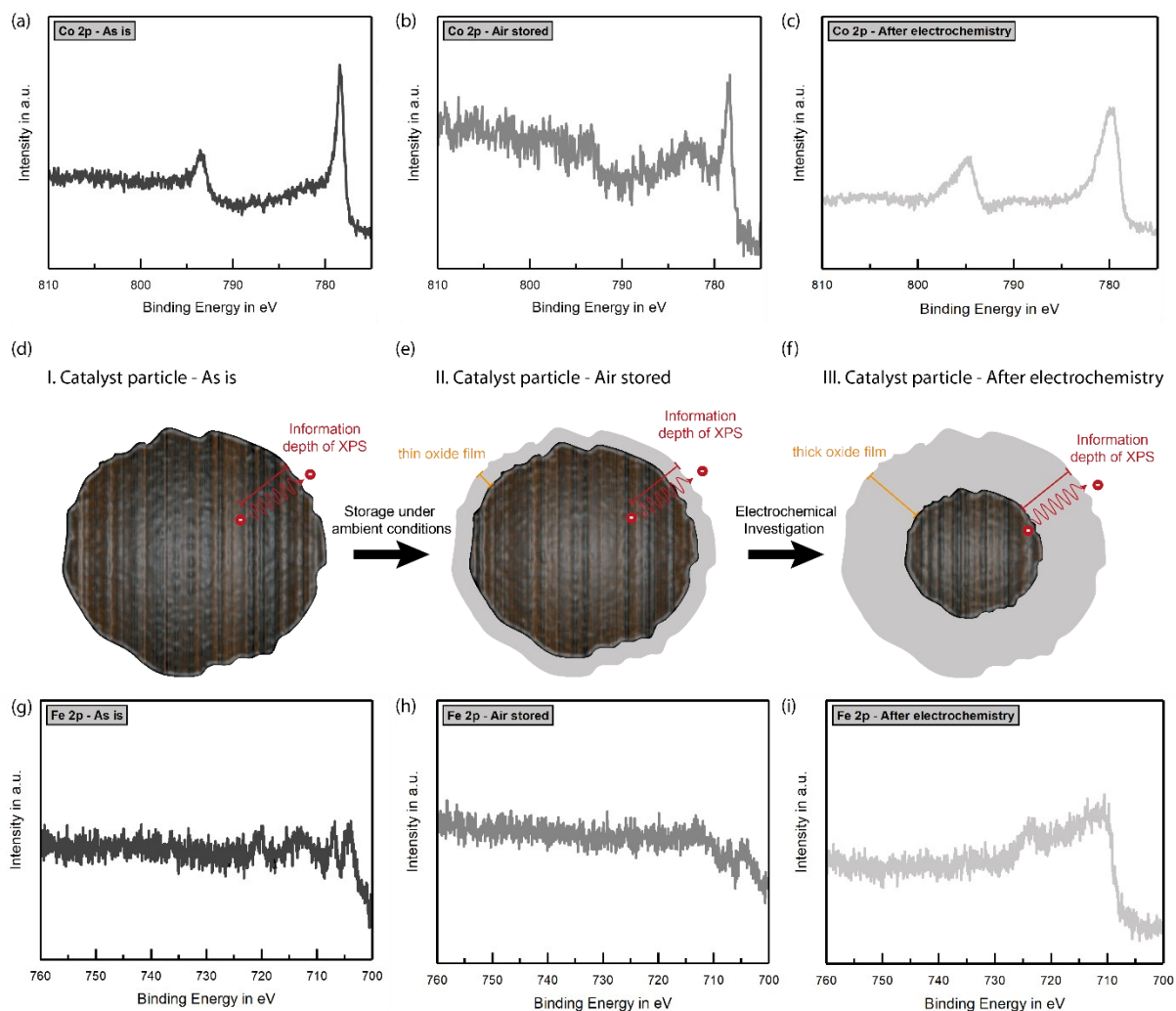


Figure 4.4.12: XP Co 2p (a), (b), (c) and Fe 2p (g), (h), (i) detail spectra of the $(\text{Co}_{0.7}\text{Fe}_{0.3})_2\text{B}$, respectively, in three different stages. Schematic picture of the assumed cross section of the nanostructure of the catalyst (cf. Figure 4.4.2) in these measurement stages: (d) I. As is; (e) II. Air stored; and (f) III. After electrochemistry, representing the correlation of the surface of the catalyst powder to the measured XP spectra. The information depth of the XPS is illustrated in red.

Additionally, it is discussed by Burke *et al.*^[47] that unlike to iron in Ni-Fe based oxyhydroxides, iron does not increase the effective electrical conductivity of Co-Fe based oxyhydroxides. They state that the pure FeOOH phase shows even dramatically lower conductivity than those phases containing cobalt.^[47] The lower conductivity of the FeOOH could have a local negatively effect on the conductivity of the $(\text{Co}_{1-x}\text{Fe}_x)_2\text{B}$ catalysts with $x > 0.3$, which form an α -Fe side phase during synthesis. The conductivity of the powdered electrodes is difficult to access and is even more challenging to measure it locally for the mixed phases. Consequently, conductivity measurements were not investigated in this work.

The discussed transition from Co^{3+}OOH to Co^{4+}O_2 under reaction conditions could neither be proved nor disproved. In contrast to the pure Co_2B , no isolated oxidation wave close to the OER was found for the ternary $(\text{Co}_{1-x}\text{Fe}_x)_2\text{B}$ catalyst system. Therefore, it is assumed that CoOOH is the active catalyst phase, while a certain amount of iron is beneficial for the performance of the catalyst system. However, the question of how iron improves the activity for the OER in the mixed system could not be clarified finally.

4.5 Incorporation of nickel into dicobalt boride ($\text{Co}_{1-x}\text{Ni}_x$)₂B

In this chapter, an intermixing of nickel into the dicobalt boride phase is presented. These ($\text{Co}_{1-x}\text{Ni}_x$)₂B powders were synthesized with different nickel amounts $0 \leq x \leq 0.5$ by Dr. Sebastian Klemenz (TU Darmstadt, department of chemistry, Eduard-Zintl-institute of inorganic and physical chemistry). The synthesis routes for the ternary borides are presented in **Section 4.2.1**. More detailed information can be found in the dissertation of Dr. Sebastian Klemenz^[229] or in the corporate publication.^[146]

The nano-structured powders were characterized after synthesis by XRD by Dr. Sebastian Klemenz to validate the composition of the powders. The XRD images and the corresponding refined data are presented in the appendix (*cf.* **Figure A 14** and **Table A 4**). No evidence of a side phase was found for the samples ($\text{Co}_{1-x}\text{Ni}_x$)₂B with $x \leq 0.2$. The samples with $x > 0.3$ showed an increasing amount of M_3B side phase with increasing nickel content, which led to a slightly increased unit cell compared to pure Ni_2B .^[151]

In addition to cobalt, nickel, and boron bulk ratios expected from synthesis, the surface ratios of these materials were determined by XPS. All samples were electrochemically investigated for the OER and the HER. However, only a minor activity was measured for the HER and therefore, no further efforts were dedicated towards this catalytic reaction. The surfaces of the different catalyst phases were investigated before electrochemistry with XPS. In addition, the best performing catalysts were investigated with XPS a second time after the EC activation and a third time after the complete EC investigation to identify the influence of the EC testing on the surface of the catalyst. Furthermore, differential capacitance measurements were performed to determine the ECSA. The SEM measurements were conducted by Kerstin Lakus-Wollny (group of Prof. W. Jaegermann, TU Darmstadt, department of material science, surface science department). The electrolyte was investigated before and after EC investigation to identify any dissolution of the catalyst phases using flame atomic adsorption spectroscopy (F-AAS – *cf.* **Section 4.2.7**). These measurements were performed with the help of Stephanie Dolique (group of Prof. B. Albert, TU Darmstadt, department of chemistry, Eduard-Zintl-institute of inorganic and physical chemistry).

4.5.1 Surface analysis of the catalyst powders

The surface of the ($\text{Co}_{1-x}\text{Ni}_x$)₂B catalyst powders with $0.1 \leq x \leq 0.5$ was investigated with XPS. The idea to measure the catalysts before and after EC investigation to monitor the changes occurring under reaction conditions was limited due to the Nafion™ binder material inside of the catalyst ink. The XPS measurements were performed identically as described in **Section 4.3**

for the pure dicobalt and tricobalt borides and the ternary $(\text{Co}_{1-x}\text{Fe}_x)_2\text{B}$ (cf. **Section 4.4**) catalysts. Additionally, the morphology of the $(\text{Co}_{1-x}\text{Ni}_x)_2\text{B}$ catalyst powders with $0.1 \leq x \leq 0.5$ was investigated by SEM (cf. **Figure 4.5.1**). The $(\text{Co}_{1-x}\text{Ni}_x)_2\text{B}$ catalyst powders show a porous morphology formed from rod-like structures with dimensions in the nanometer range. The detailed structure of the different phases exhibits visible differences. While the morphology of the Co_2B shows a high-level of agglomerated phase with a particle-structure, the morphology of the metal borides containing nickel reveals a more network-like structure of small rods. The samples containing 10, 20, and 50% nickel show higher porosity with large pores, while the sample with 30% nickel shows less porosity. The morphology of the $(\text{Co}_{0.6}\text{Ni}_{0.4})_2\text{B}$ exhibits in parts particle-like and porous rod-like structure with average-sized porosity.

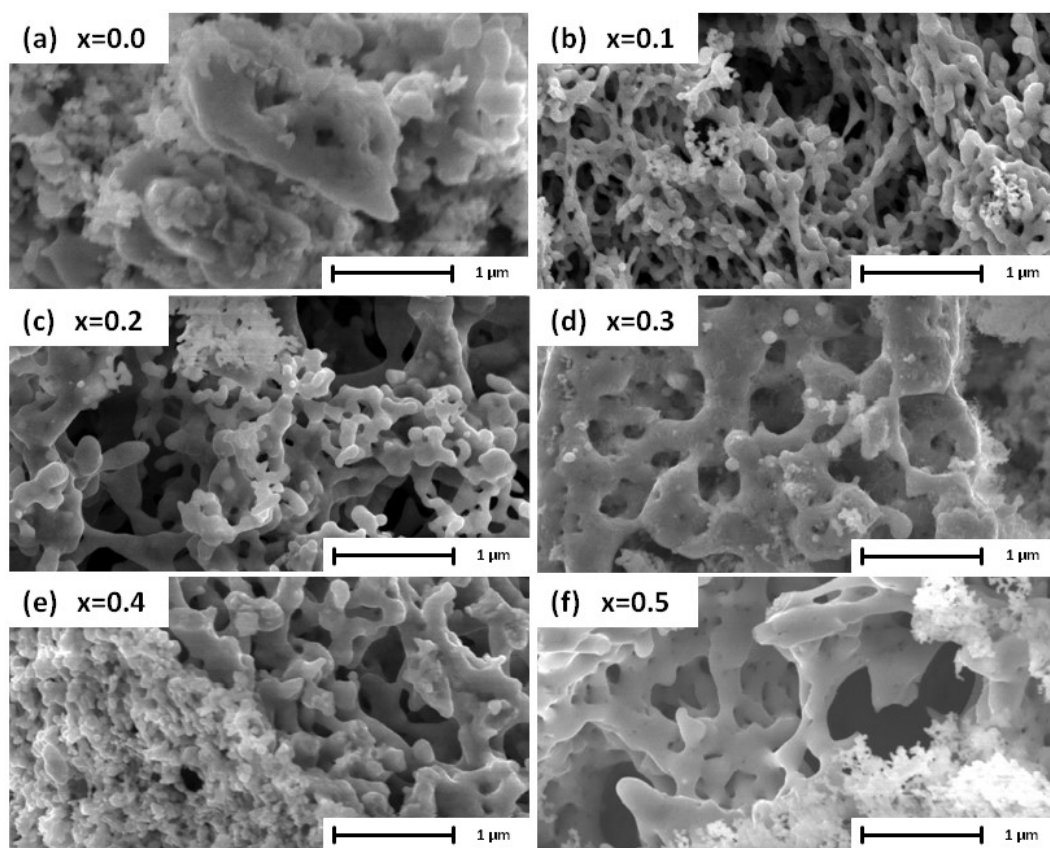


Figure 4.5.1: SEM images of the $(\text{Co}_{1-x}\text{Ni}_x)_2\text{B}$ catalysts for (a) $x=0.0$, (b) $x=0.1$, (c) $x=0.2$, (d) $x=0.3$ (e) $x=0.4$, and (f) $x=0.5$ measured with an excitation voltage of 10 kV and a magnification of 25000.

The recorded XP survey spectra of the $(\text{Co}_{1-x}\text{Ni}_x)_2\text{B}$ catalysts embedded in indium foil are shown in **Figure 4.5.2** with the relevant photoemission lines marked. The relevant detailed spectra are shown and discussed in detail later in this chapter. The photoemission lines of the catalyst phase (blue) namely cobalt (Co 2p; Co 3p), nickel (Ni 2p; Ni 3p), oxygen (O 1s), and boron (B 1s) can

be observed. In addition to that, indium (In 3p; In 3d) from the substrate and carbon (C 1s) contamination can be found on the surface (grey).

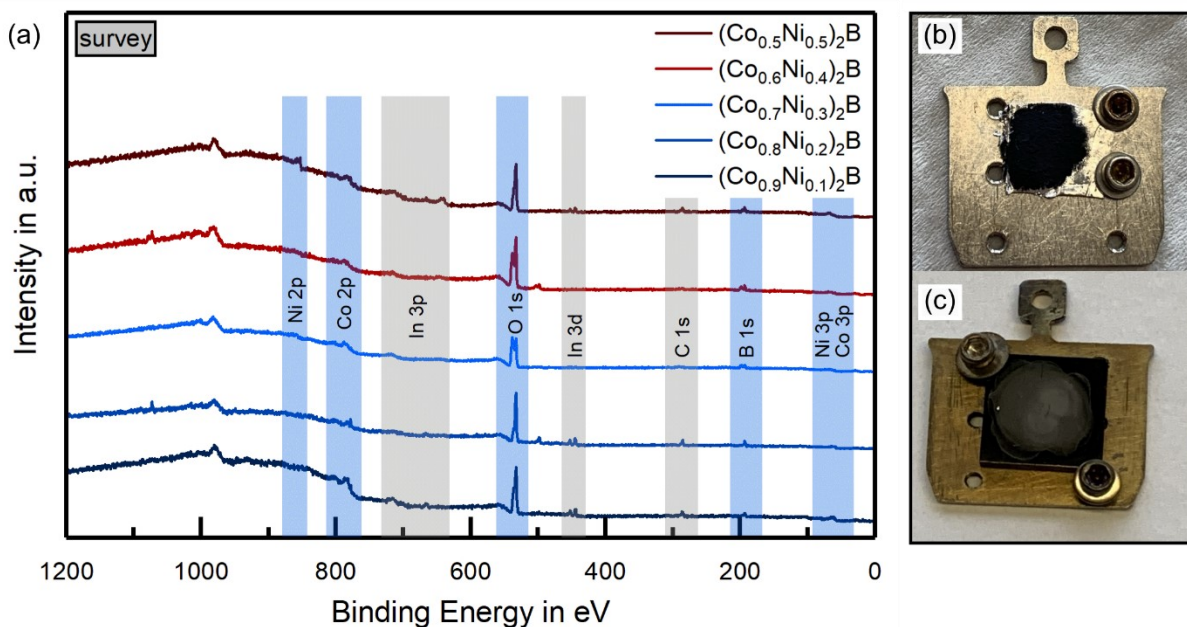


Figure 4.5.2: (a) XP survey spectra of the $(\text{Co}_{1-x}\text{Ni}_x)_2\text{B}$ phases with $0.1 \leq x \leq 0.5$ embedded in indium foil before electrochemical (EC) investigation. The relevant photoemission line positions of cobalt, nickel, oxygen, boron, carbon, and indium are marked. (b) Exemplary picture of a sample embedded in indium foil and (c) the sample drop coated from an ink with Nafion™ onto GC substrate.

The surface compositions are determined from XPS for the different catalyst phases in terms of their metal fractions of cobalt and nickel and of their overall metal to boron ratios, summarized in **Table 4.5.1**. The percentage of cobalt, nickel, and boron at the surface was determined from the XPS data using tabulated sensitivities for the experimental setup in combination with a Shirley background subtraction.^{[72], [134]} From the synthesis the nickel content was adjusted to yield 10, 20, 30, 40, and 50% nickel in the bulk of the catalyst. The metal to boron ratio is expected to be 2:1 for all samples. The assumed errors for the elemental surface compositions are due to measuring inaccuracies, partial oxidation of the surface, and carbon contaminations. The calculated values for the elemental composition fit well with the expected ratios. However, the $(\text{Co}_{0.6}\text{Ni}_{0.4})_2\text{B}$ sample shows the strongest deviation from the assumed composition.

In **Figure 4.5.3** the respective photoemission lines of Co 2p (a) and Ni 2p (b) for $(\text{Co}_{1-x}\text{Ni}_x)_2\text{B}$ with $x=0.1$ (dark-colored) as the lower and $x=0.5$ (light-colored) as the upper extreme value of the measured phases are shown. In contrast to the $(\text{Co}_{1-x}\text{Fe}_x)_2\text{B}$ catalysts, the $(\text{Co}_{1-x}\text{Ni}_x)_2\text{B}$ phases show a larger amount of oxide under ambient conditions.

Table 4.5.1: Quantitative surface analysis with XPS of the different catalyst phases embedded in indium foil. Tabulated sensitivity factors are used from [72] with a Shirley background. [134]

Sample in Indium foil	Surface metal fraction in %* ¹		Surface Ratio Metal : Boron* ²
	Cobalt	Nickel	
(Co _{0.9} Ni _{0.1}) ₂ B	89.1	10.9	2.0
(Co _{0.8} Ni _{0.2}) ₂ B	79.1	20.9	2.1
(Co _{0.7} Ni _{0.3}) ₂ B	72.1	27.9	2.0
(Co _{0.6} Ni _{0.4}) ₂ B	66.9	33.1	2.3
(Co _{0.5} Ni _{0.5}) ₂ B	49.9	50.1	2.1

*¹ The assumed errors for the results are due to measuring inaccuracy. These errors are assumed to be between 1 and 5% in metallic fraction.

*² The assumed errors for the results are due to measuring inaccuracy and the oxidation of boron as well as of the metallic components as shown in **Figure 4.5.4** and **Figure 4.5.3**, respectively, and are assumed to be between 0.1 and 0.5.

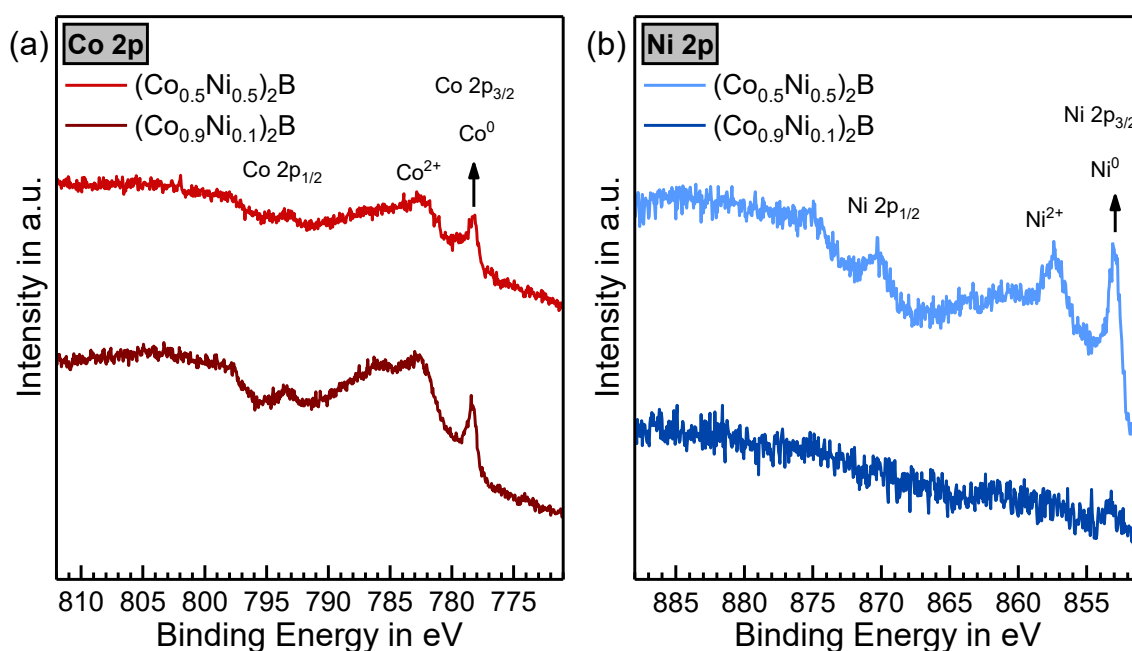


Figure 4.5.3: Comparison of the XP detail spectra of Co 2p ((a) – red) and Ni 2p ((b) – blue) for the (Co_{1-x}Ni_x)₂B catalyst with x=0.1 (dark-colored) and x=0.5 (light-colored), showing the intense oxidation of the catalyst under ambient conditions.

Measurement data of the pure (Co_{1-x}Ni_x)₂B catalysts always included a metal oxide signal visible in the Co 2p and Ni 2p detail spectra at binding energies of 781.8 eV to 785 eV and 856.8 eV to 858.3 eV, respectively. These signals can be attributed to an oxidation/hydroxylation forming

CoO/Co(OH)₂ and NiO/Ni(OH)₂ at the surface of the metal boride powders.^{[117], [202], [204]} The metal boride signals themselves are also observable and can be found for cobalt (Co⁰) at approximately 778.3 eV and for nickel (Ni⁰) at approximately 853.1 eV.^{[205], [206], [220], [221]}

The oxidation of the surface is also apparent in the B 1s photoemission line illustrated in **Figure 4.5.4**. Two boron phases are visible in the B 1s detail spectra for the different catalyst phases. Boron with an oxidation state of B⁰ at a binding energy of 188.4 eV, representing the metal borides^{[157], [205], [206]} and an oxidized boron phase located at higher binding energies, which is split into one sharp peak at binding energies around 193 eV and a second broader signal at slightly higher binding energies. This boron phase can be attributed to boron trioxide B₂O₃ or boron trihydroxide B(OH)₃ with boron in an oxidation state B³⁺, which are located between 192.5 eV and 198.0 eV.^{[157], [212], [221], [243], [244], [246]–[248], [253]} In contrast to the observed variations in the sharp BO_x signals of the (Co_{1-x}Fe_x)₂B catalysts (*cf.* **Figure 4.4.6**), the (Co_{1-x}Ni_x)₂B phases exhibit no change in the BO_x peak positions with varying nickel content. However, a residual chlorine signal, as already observed for the (Co_{1-x}Fe_x)₂B phases, can be found for the (Co_{1-x}Ni_x)₂B catalysts with x=0.2, 0.3, and 0.4. The signals are attributed to residual cobalt and nickel chloride hexahydrate from the wet chemical synthesis route.^[69]

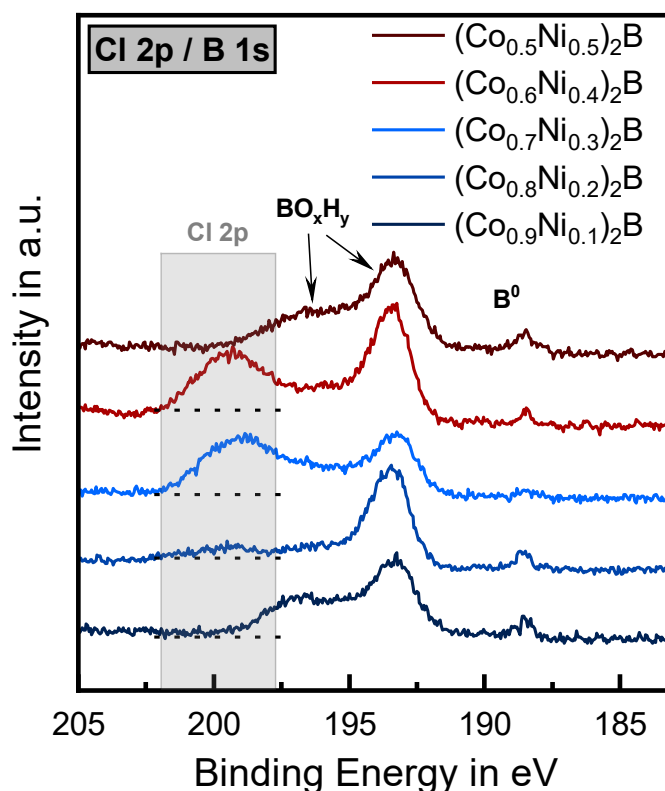


Figure 4.5.4: XP B 1s detail spectra of (Co_{1-x}Ni_x)₂B with 0.1 ≤ x ≤ 0.5. On the left side, the Cl 2p photoemission line is marked.

In addition to XPS and SEM images, the $(\text{Co}_{0.9}\text{Ni}_{0.1})_2\text{B}$ catalyst was exemplarily investigated with TEM and scanning TEM (STEM). The resulting (S)TEM images of the $(\text{Co}_{0.9}\text{Ni}_{0.1})_2\text{B}$ catalyst (cf. **Figure 4.5.5**) show a layer of low contrast material encasing the crystalline core of the material. With STEM the chemical composition of the catalyst was analyzed in the marked region (cf. **Figure 4.5.5d**) using energy dispersive X-ray spectroscopy (EDX) (cf. **Figure 4.5.5e**). The particles mainly consist of cobalt, nickel, and oxygen with small impurities of carbon. Due to instrumental limitation, the detection of the element boron was not possible. The elemental mapping with EDX depicts the outer low contrast layer to be oxygen-rich, confirming the XPS data conducted for the catalyst. An additional EDX line scan was conducted across the line shown in **Figure 4.5.5e** the resulting profile is illustrated in **Figure 4.5.5f** with normalized intensities of cobalt, nickel, and oxygen, supporting the assumption of an oxygen-rich surface layer. The XPS data provides evidence for a boron oxide/hydroxide layer covering the surface (cf. **Figure 4.5.4**), which explains the absent signals from cobalt and nickel at the particles surface.

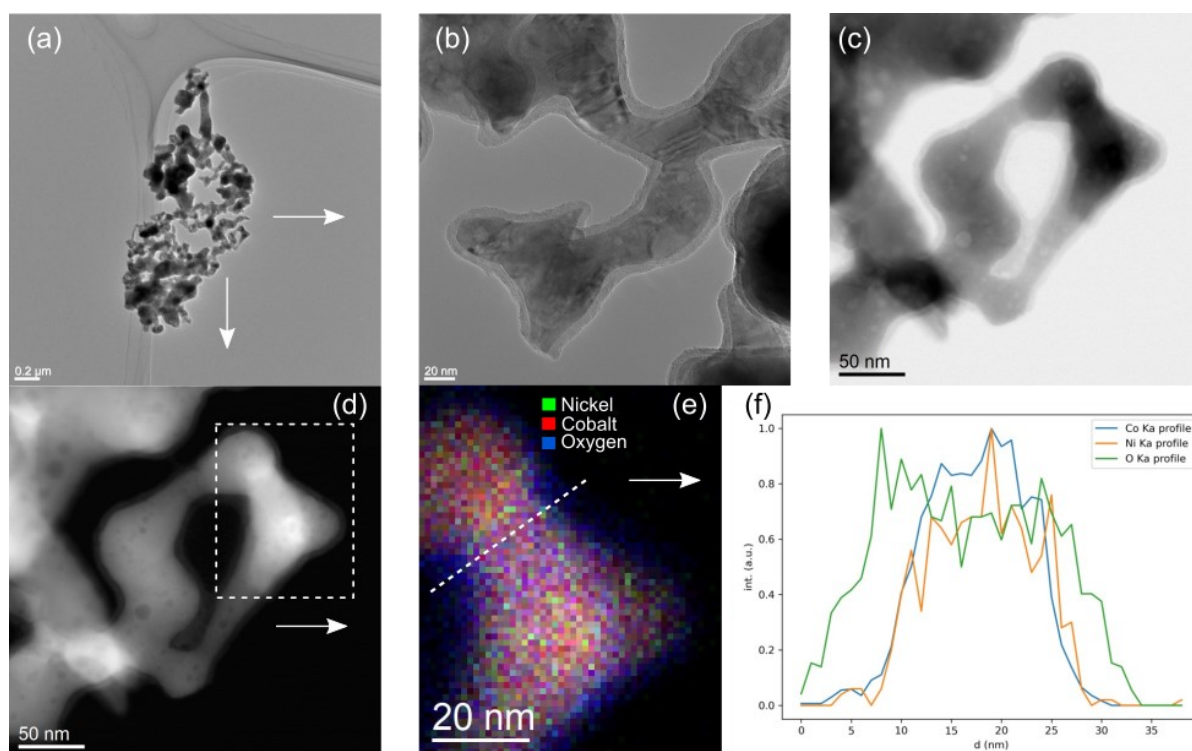


Figure 4.5.5: (a), (b) Transmission electron microscopy (TEM) images of the $(\text{Co}_{0.9}\text{Ni}_{0.1})_2\text{B}$ catalyst before electrochemical investigation with different magnification. In (c) and (d) scanning TEM images with bright-field (BF) and high-angle annular dark-field (HAADF) are shown of the same region. In (e) the same region is shown again with energy dispersive X-ray spectroscopy (EDX) map of the catalyst showing normalized intensities of nickel (green), cobalt (red), and oxygen (blue) over the marked area of (d). In (f) normalized K_{α} line profiles of the EDX data across the line in (e) are shown for cobalt (blue), nickel (orange), and oxygen (green).

4.5.2 Electrochemical investigation

The EC behavior of the $(\text{Co}_{1-x}\text{Ni}_x)_2\text{B}$ catalysts (with $0.1 \leq x \leq 0.5$) drop coated with ink onto GC was investigated for the HER and the OER in 1 M KOH. Since these catalysts showed only a poor catalytic performance for the HER, the focus for the $(\text{Co}_{1-x}\text{Ni}_x)_2\text{B}$ catalysts was placed on the reactivity for the OER.

For the $(\text{Co}_{1-x}\text{Ni}_x)_2\text{B}$ catalysts the standard EC measurement protocol (*cf.* **Section 4.2.5**) was used. A transition from a Co^0 and Ni^0 phase to a more oxidized form was already visible during the storage under ambient conditions (*cf.* **Section 4.5.1**). It is expected that these phases transform further under EC reaction conditions in alkaline media since cobalt and nickel both feature an oxidation and reduction behavior in the chosen conditioning range. In **Figure 4.5.6a** the CV curves after the conditioning procedure for the $(\text{Co}_{1-x}\text{Ni}_x)_2\text{B}$ catalysts ($0 \leq x \leq 0.5$) are shown with an additional magnification (*cf.* **Figure 4.5.6b**) of the redox waves occurring in the potential interval of 1.00 to 1.65 V vs. RHE.

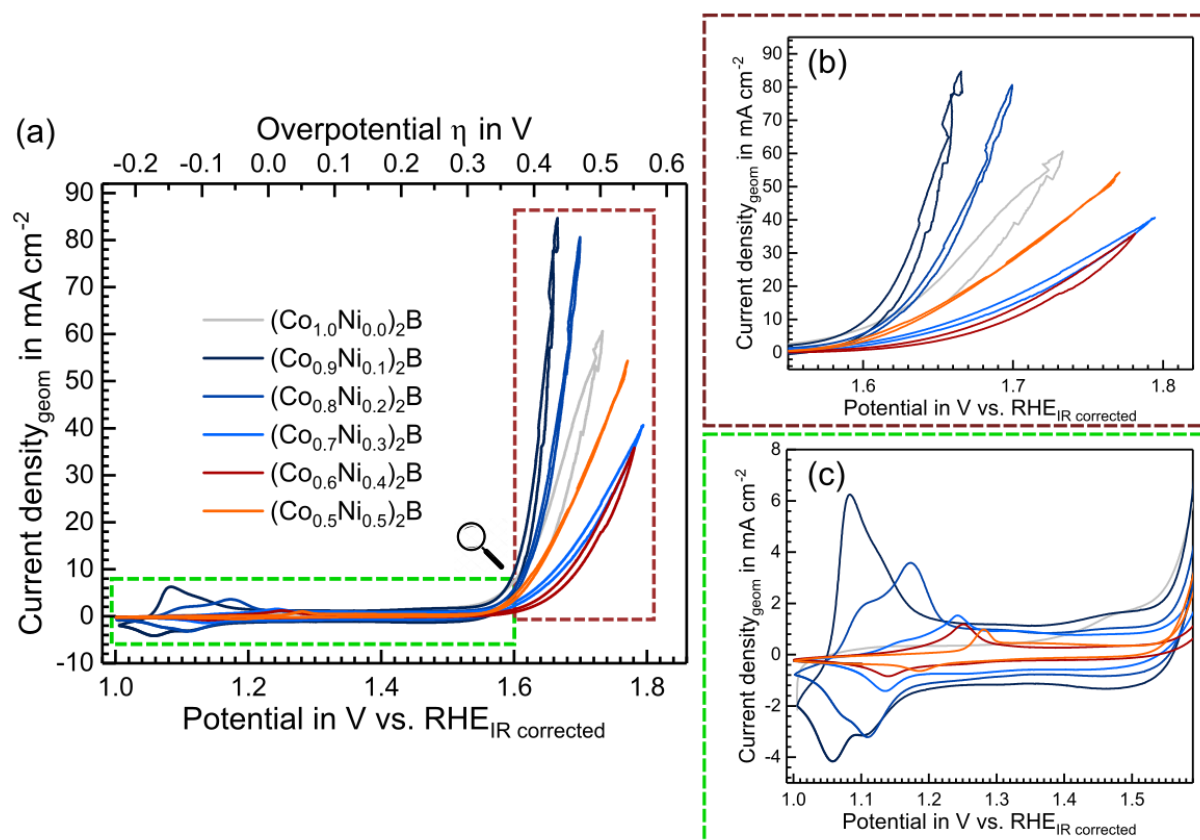


Figure 4.5.6: (a) Cyclic Voltammetry measurements of the $(\text{Co}_{1-x}\text{Ni}_x)_2\text{B}$ catalysts with $0 \leq x \leq 0.5$ after the conditioning procedure and magnifications of the (b) oxygen evolution reaction (OER) and (c) redox waves. All curves were measured with a scan rate of 50 mV s^{-1} according to the electrochemical (EC) protocol (*cf.* **Section 4.2.5**) in 1 M KOH with Hg/HgO as a reference electrode and are iR corrected.

The oxidation wave for the $\text{Co}^{2+}/\text{Co}^{3+}$ transition (according to $\text{Co}(\text{OH})_2 + \text{OH}^- \rightleftharpoons \text{CoOOH} + \text{H}_2\text{O} + e^-$)^[186] of pure Co_2B can be found at potentials around 1.00 to 1.15 V vs. RHE. This oxidation wave shifts with an increasing amount of nickel anodically. Similar results were observed for the incorporation of iron into dicobalt boride (cf. **Section 4.4.2**). In contrast to the oxidation waves discussed for the $(\text{Co}_{1-x}\text{Fe}_x)_2\text{B}$ catalysts (cf. **Section 4.4.2**), the $(\text{Co}_{1-x}\text{Ni}_x)_2\text{B}$ catalysts with $x=0.1, 0.2,$ and 0.3 show a highly asymmetric peak shape, which seems to consist of two separated peaks each, which is in agreement with earlier findings of asymmetric redox wave shapes for NiCo-based catalysts.^{[54], [257]–[259]} However, the anodic shift induced by the incorporation of nickel into the cobalt-based catalyst or the observed double oxidation waves were not explained. The anodic redox wave shift induced by the incorporation of iron into Co-based catalysts is assigned to strong electronic interactions between the cobalt and the iron inside of the catalyst phase.^{[44], [47]} There, only single oxidation signals were reported for the Co-Fe system, which could be due to the fact that iron exhibits no redox behavior in the discussed potential range (cf. **Section 4.1.3** and **Figure 4.1.6**). In contrast to that, the nickel system possesses an oxidation and reduction wave in this potential range (cf. $\text{Ni}(\text{OH})_2 + \text{OH}^- \rightleftharpoons \text{NiOOH} + \text{H}_2\text{O} + e^-$).^{[186], [187]} Consequently, it is assumed that on the one hand the incorporation of nickel into the Co-based catalyst increases the energy needed to perform the $\text{Co}^{2+}/\text{Co}^{3+}$ transition and on the other hand the $\text{Ni}^{2+}/\text{Ni}^{3+}$ transition is facilitated by the cobalt inside the catalyst phase, leading to the double wave structure. A summary of the determined values for the onset potential and the maximum of these oxidation waves can be found in **Figure 4.5.7a**. Additionally, the potential of the double oxidation peak is given.

In **Section 4.4**, it is shown that a defined amount of iron incorporated into the dicobalt boride decreases the OER onset potential by up to 50 mV. This improvement of the onset potential towards the OER cannot be observed for the incorporation of nickel into the dicobalt boride phase. In **Figure 4.5.6** the CV curves after the conditioning procedure are shown. All probed samples show comparable OER onset potentials slightly above 1.50 V vs. RHE. The highest onset potential can be found for $(\text{Co}_{0.6}\text{Ni}_{0.4})_2\text{B}$ with 1.55 V vs. RHE and the lowest for pure Co_2B with 1.51 V vs. RHE. The incorporation of a defined amount of nickel ($x \leq 0.2$) improves the overall activity of the $(\text{Co}_{1-x}\text{Ni}_x)_2\text{B}$ catalyst, leading with $\eta_{10}=371$ mV for $(\text{Co}_{0.9}\text{Ni}_{0.1})_2\text{B}$ and $\eta_{10}=384$ mV for $(\text{Co}_{0.8}\text{Ni}_{0.2})_2\text{B}$ to a reduction in the overpotential at 10 mA cm^{-2} compared to the Co_2B phase ($\eta_{10}=410$ mV). A higher amount of nickel ($0.3 \leq x \leq 0.5$) reduces the electrocatalytic performance compared to the pure Co_2B catalyst. In **Figure 4.5.7b** a summary of the OER onset potentials and overpotentials of the $(\text{Co}_{1-x}\text{Ni}_x)_2\text{B}$ is illustrated. The $(\text{Co}_{1-x}\text{Ni}_x)_2\text{B}$ catalyst system with $0.1 \leq x \leq 0.4$ shows a trend in terms of OER overpotential at 10 mA cm^{-2} . The lowest overpotential (η_{10}) is achieved by the $(\text{Co}_{1-x}\text{Ni}_x)_2\text{B}$ with $\eta_{10} (x=0.1) < \eta_{10} (x=0.2) < \eta_{10} (x=0.3) < \eta_{10} (x=0.4)$. The only phase not fitting the trend in decreasing activity is $(\text{Co}_{0.5}\text{Ni}_{0.5})_2\text{B}$, which shows a better performance as $(\text{Co}_{0.7}\text{Ni}_{0.3})_2\text{B}$ and $(\text{Co}_{0.6}\text{Ni}_{0.4})_2\text{B}$. However, it could also possible

that the minimum in activity is reached with $(\text{Co}_{0.6}\text{Ni}_{0.4})_2\text{B}$ and a further increase in nickel content improves the catalytic performance again. However, to confirm this assumption $(\text{Co}_{1-x}\text{Ni}_x)_2\text{B}$ with a higher amount of nickel must be investigated. The overpotential of the $(\text{Co}_{0.9}\text{Ni}_{0.1})_2\text{B}$ catalyst extends the performance of reported CoNiO_x catalysts ($\eta_{10}=0.38\text{ V}$), but shows higher overpotentials compared to reported values for the noble metal catalyst IrO_2 (cf. **Figure 4.5.7c**).^[19]

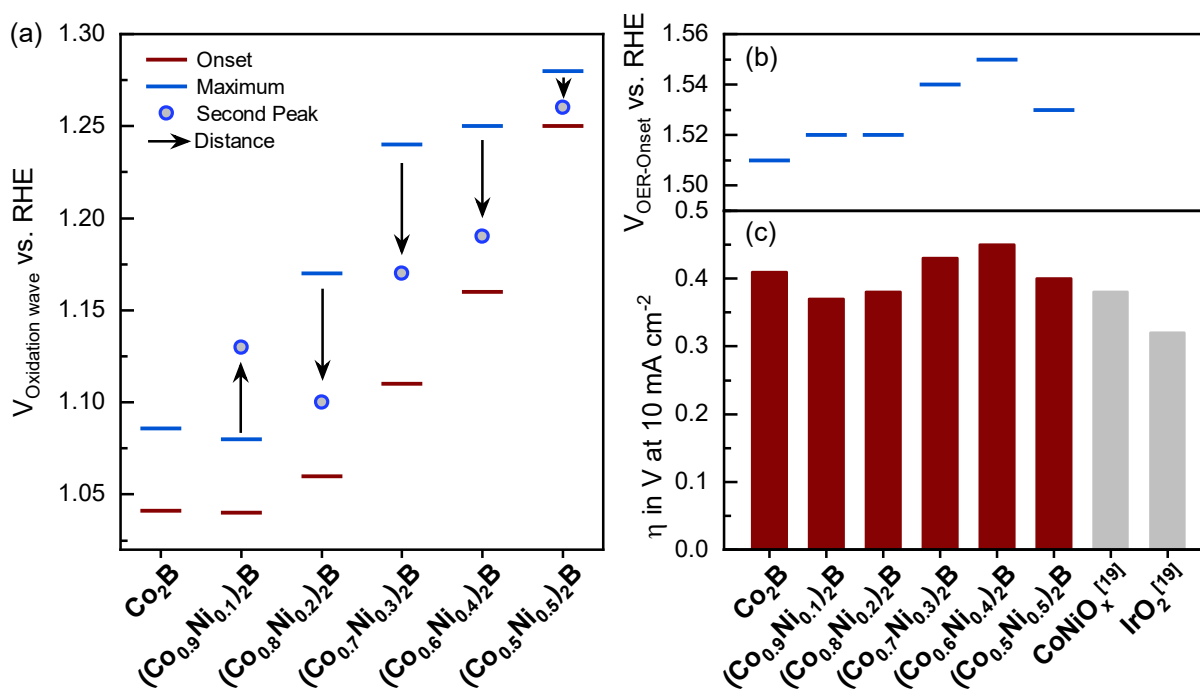


Figure 4.5.7: Summary of the reactivity and activity of the $(\text{Co}_{1-x}\text{Ni}_x)_2\text{B}$ catalysts with $0 \leq x \leq 0.5$. **(a)** The position of the oxidation waves for the different iron amounts is shown in terms of their onset potential and peak maximum. **(b)** The activity of the different catalyst phases is shown in terms of their onset potential (blue lines) for the OER and **(c)** their overpotential at 10 mA cm^{-2} (η_{10} ; red bars) compared to literature values.^[19]

The Tafel plots shown in **Figure 4.5.8a** manifest the performance trend as observed from the CV measurements. The lowest Tafel slopes can be found for the $(\text{Co}_{1-x}\text{Ni}_x)_2\text{B}$ catalyst with $0 \leq x \leq 0.2$. The slopes of Co_2B and $(\text{Co}_{0.9}\text{Ni}_{0.1})_2\text{B}$ are around $60\text{--}80\text{ mV dec}^{-1}$, while the two lowest slopes can be found for $(\text{Co}_{0.8}\text{Ni}_{0.2})_2\text{B}$ and for $(\text{Co}_{0.5}\text{Ni}_{0.5})_2\text{B}$, which showed an average performance in the CV curve activity. A reason for this result could be a difference in the accessible surface areas for the different catalyst phases. Therefore, the Helmholtz double-layer capacitance (C_{DL}) is determined by potential differential capacitance measurements conducted with scan rates of 10, 20, 30, 40, and 50 mV s^{-1} around a certain potential for the different catalyst phases (cf. **Figure A 19**). The C_{DL} is a quantitative indicator of the catalyst's surface area accessible to the electrolyte.^{[19], [61], [63]} A more detailed description of this measurement method and different techniques of activity normalizations can be found in **Section 2.3**. In **Figure 4.5.9a**

the resulting current densities plotted versus the scan rates are shown. From the slope of the regression line, the Helmholtz double-layer capacitance C_{DL} can be determined for the $(\text{Co}_{1-x}\text{Ni}_x)_2\text{B}$ catalysts. $(\text{Co}_{0.8}\text{Ni}_{0.2})_2\text{B}$ and $(\text{Co}_{0.5}\text{Ni}_{0.5})_2\text{B}$ possess the highest capacitance values and show the lowest Tafel slopes. The same holds for Co_2B and $(\text{Co}_{0.9}\text{Ni}_{0.1})_2\text{B}$, which feature moderate Tafel slopes and moderate capacitance values in the ECSA measurement. Finally, $(\text{Co}_{0.7}\text{Ni}_{0.3})_2\text{B}$ and $(\text{Co}_{0.6}\text{Ni}_{0.4})_2\text{B}$ exhibit the highest Tafel slopes, while showing the lowest C_{DL} values. In **Figure 4.5.8b** the correlation of the Tafel slope with the Helmholtz capacitance is illustrated (as measured by ECSA – cf. **Figure 4.5.9a**). The trend of the different Tafel slopes indeed matches the trend of the accessible surface areas of the catalysts. However, for the low Tafel slope of $(\text{Co}_{0.5}\text{Ni}_{0.5})_2\text{B}$ a change in the OER mechanism due to the high amount of nickel inside the catalyst phase cannot be excluded.

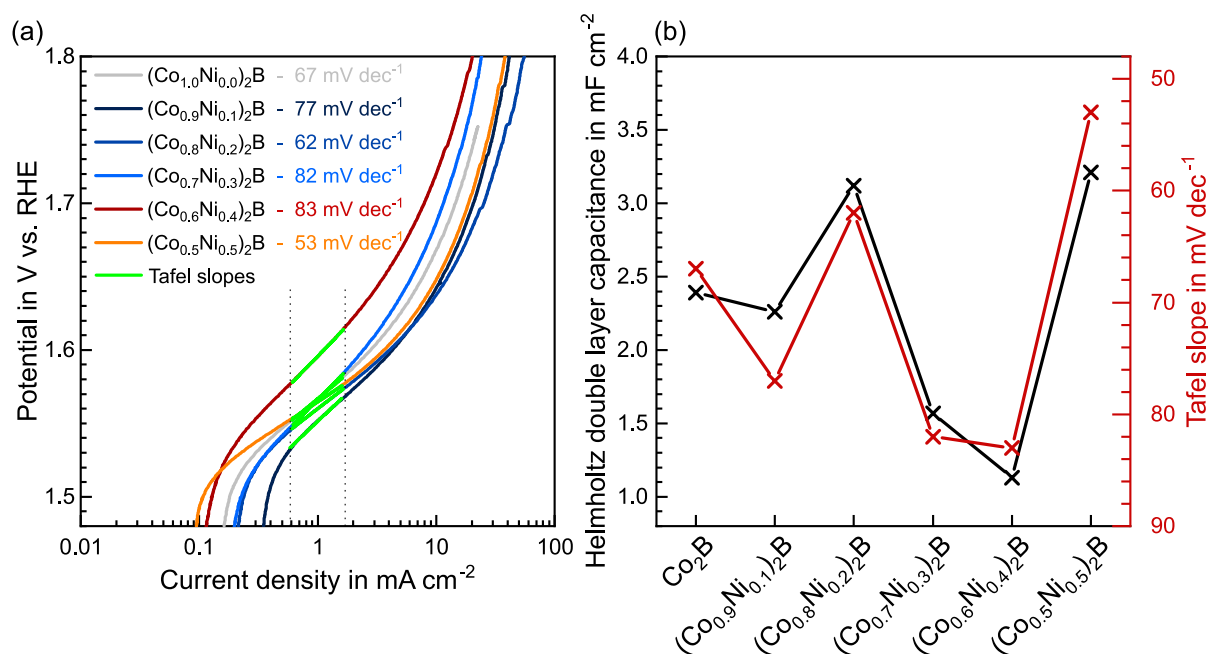


Figure 4.5.8: (a) Tafel slope determination from a CV with a scan rate of 10 mV s^{-1} for the $(\text{Co}_{1-x}\text{Ni}_x)_2\text{B}$ catalysts with $0 \leq x \leq 0.5$. The CV curves are not iR corrected (b) Illustration of the influence of the Helmholtz double-layer capacitances (C_{DL}) with the Tafel slopes of the $(\text{Co}_{1-x}\text{Ni}_x)_2\text{B}$ catalysts with $0 \leq x \leq 0.5$. All curves were measured in 1 M KOH with an Hg/HgO as a reference electrode.

To decrease the influence of the accessible surface areas, the determined Helmholtz capacitances can additionally be included in the CV behavior of the different $(\text{Co}_{1-x}\text{Ni}_x)_2\text{B}$ catalysts. The $(\text{Co}_{0.5}\text{Ni}_{0.5})_2\text{B}$ and the $(\text{Co}_{0.7}\text{Ni}_{0.3})_2\text{B}$ catalysts show the highest C_{DL} with 3.21 and 3.12 mF cm^{-2} . The C_{DL} of $(\text{Co}_{0.6}\text{Ni}_{0.4})_2\text{B}$, however, is three times lower with 1.13 mF cm^{-2} . Helmholtz double-layer capacitance values for flat metal oxide surfaces are reported to be around $22 \mu\text{F cm}^{-2}$ to $130 \mu\text{F cm}^{-2}$.^{[19], [63]} Due to the large differences in reported C_{DL} values for different catalyst phases and the fact that in this work powdered materials were used, the C_{DL} was not

normalized with values from literature. However, since the Helmholtz double-layer capacitance C_{DL} values of the $(\text{Co}_{1-x}\text{Ni}_x)_2\text{B}$ catalysts vary by a factor of up to ≈ 3 , a normalization of the different C_{DL} values to the lowest one ($C_{DL}=1.13 \text{ mF cm}^{-2}$) of the $(\text{Co}_{0.6}\text{Ni}_{0.4})_2\text{B}$ catalyst phase was performed (cf. **Figure 4.5.9a**). Accordingly, the current densities of the CV curves of **Figure 4.5.6** were normalized by normalization factors, which are their C_{DL} values divided by the lowest capacitance of $(\text{Co}_{0.6}\text{Ni}_{0.4})_2\text{B}$. The normalization procedure is illustrated in **Figure 4.5.9a** and the resulting CV curves are shown in **Figure 4.5.9b**. The catalyst with the best catalytic performance $(\text{Co}_{0.9}\text{Ni}_{0.1})_2\text{B}$ remains the most active one. Consequently, it can be stated that a certain small amount of nickel incorporated into the dicobalt boride phase decreases the overpotential for the OER independent of the different surface areas. The surface normalization influences the performance of the $(\text{Co}_{0.5}\text{Ni}_{0.5})_2\text{B}$ catalyst in such a way that it blends well with the trend in overpotential at 10 mA cm^{-2} with $x=0.1 < x=0.2 < x=0.3 \cong x=0.4 < x=0.5$. In conclusion, the $(\text{Co}_{0.9}\text{Ni}_{0.1})_2\text{B}$ exhibits the best performance for the OER in terms of the overpotentials at 10 mA cm^{-2} ($\eta_{10} < 350 \text{ mV}$) and the maximum current density reached in the investigated potential range (1.0 to 1.9 V vs. RHE). The onset potential could not be improved by an incorporation of nickel. Furthermore, the Tafel slopes were strongly influenced by the corresponding accessible surface area of the catalysts, showing an otherwise trendless behavior.

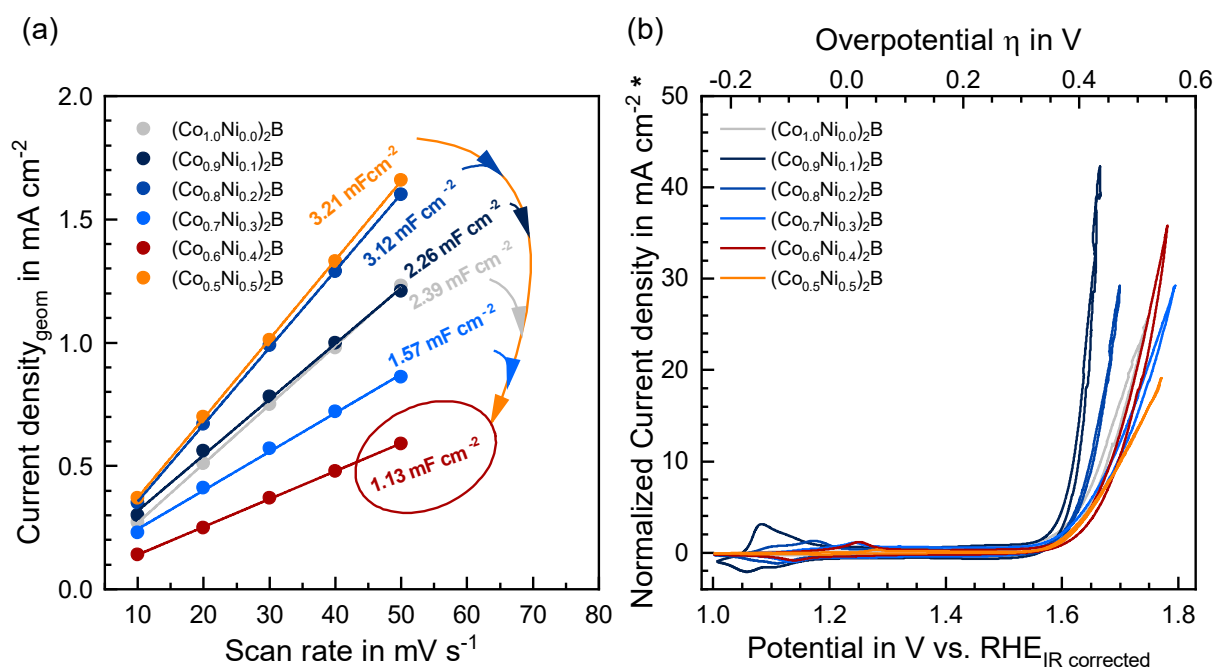


Figure 4.5.9: (a) Determination of the Helmholtz double-layer capacities of the $(\text{Co}_{1-x}\text{Ni}_x)_2\text{B}$ catalysts (with $0 \leq x \leq 0.5$). (b) *Normalized current densities of the $(\text{Co}_{1-x}\text{Ni}_x)_2\text{B}$ catalysts onto the catalyst with the lowest double layer capacitance – $(\text{Co}_{0.6}\text{Ni}_{0.4})_2\text{B}$. All curves were measured in 1 M KOH with an Hg/HgO as a reference electrode.

Besides the activity of the catalyst, the stability plays a crucial role in EC catalysis. The stability of the best catalyst $(\text{Co}_{0.9}\text{Ni}_{0.1})_2\text{B}$ was investigated over a longer time period at a constant current density of 10 mA cm^{-2} . The chronopotentiometry measurement was measured for 8 hours with a pumping system (Hei-LOW Advantage 06; Heidolph Instruments GmbH) combined with an electrolyte reservoir ($\approx 200 \text{ mL}$). During that time, the electrolyte was bubbled with nitrogen gas to remove the oxygen and hydrogen gas. The stability curves shown in **Figure 4.5.10** show a stable performance of the OER catalyst. Over the first four hours of measurement time, the performance of the catalyst slightly decreases. Then from the 4th until the 8th hour of measurement time, the performance of the catalyst increases again. In summary, the catalyst starts with an overpotential of $\eta_{10}=350 \text{ mV}$, which increases to $\eta_{10}=360 \text{ mV}$ at around four hours of measurement time and decreases until the end of the measurement, reaching again an overpotential of $\eta_{10}=350 \text{ mV}$. Thus, it can be stated, that $(\text{Co}_{0.9}\text{Ni}_{0.1})_2\text{B}$ is not only the most active catalysts of the $(\text{Co}_{1-x}\text{Ni}_x)_2\text{B}$ compounds but is also stable under reaction conditions over a longer time period. A CV curve measured after the long-term stability test of the catalyst shows even improved EC performance. The slope of the CV curve is steeper in contrast to the slope determined after the conditioning of the catalyst phase.

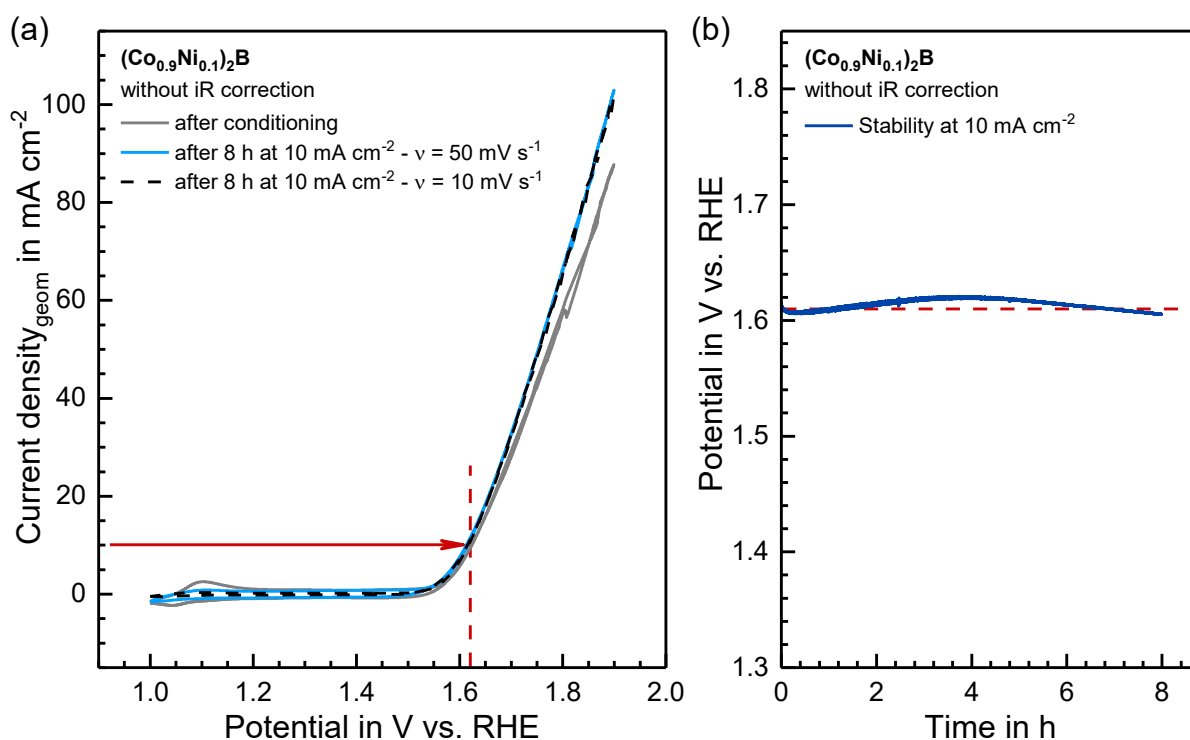


Figure 4.5.10: (a) Comparison of the cyclic voltammograms (CVs) of the most active $(\text{Co}_{0.9}\text{Ni}_{0.1})_2\text{B}$ catalyst after the electrochemical (EC) conditioning and after a chronopotentiometry (at $j=10 \text{ mA cm}^{-2}$) stability test for 8 h. (b) The long-term chronopotentiometry stability measurement of the most active $(\text{Co}_{0.9}\text{Ni}_{0.1})_2\text{B}$ catalyst (at $j=10 \text{ mA cm}^{-2}$). In red, the potential to drive a current density of 10 mA cm^{-2} is marked. Both curves are shown without iR correction. All curves were measured according to the EC protocol (*cf.* **Section 4.2.5**) in 1 M KOH with an Hg/HgO as a reference electrode.

Additionally, the overpotential of $(\text{Co}_{0.9}\text{Ni}_{0.1})_2\text{B}$ decreases after the stability measurement from $\eta_{10}=371$ mV to $\eta_{10}=355$ mV vs. RHE. Such a change in the catalytic performance can arise due to *e.g.* roughening and/or reorganization of the surface and (re)intercalation of impurities from the electrolyte. To address and investigate those changes in the catalytic performance, detailed XPS measurements of the catalyst after different EC measurement stages were conducted.

4.5.3 XPS – oxidation state changes during operation

Besides the functionality of the catalyst system itself (*cf.* **Section 4.5.2**), the changes occurring under reaction conditions are crucial to understand the reaction mechanism of the catalyzing material. To be able to study such changes, XPS analyses before (*cf.* **Section 4.5.1**) and after different EC investigations steps were conducted.

These changes are presented, analyzed, and compared in this section, using as example the most active catalyst phase $(\text{Co}_{0.9}\text{Ni}_{0.1})_2\text{B}$. The Co 2p and Ni 2p XP detail spectra of $(\text{Co}_{0.9}\text{Ni}_{0.1})_2\text{B}$ before EC, after the EC activation, and after the complete EC testing are depicted in **Figure 4.5.11a** and **Figure 4.5.11b**. Similar to the reactions occurring for the $(\text{Co}_{1-x}\text{Fe}_x)_2\text{B}$ catalyst phase during the EC investigation (*cf.* **Section 4.4.3**), the former Co-B peak of the Co $2p_{3/2}$ photoemission line at 778.4 eV of the $(\text{Co}_{0.9}\text{Ni}_{0.1})_2\text{B}$ catalyst disappears during the EC activation and is replaced by a strong feature at 779.7 eV with a shoulder signal around 781.0 eV. These peaks are shifted to lower binding energies, in contrast to the ones observed for the Co $2p_{3/2}$ photoemission lines of $(\text{Co}_{0.9}\text{Fe}_{0.1})_2\text{B}$ and $(\text{Co}_{0.7}\text{Fe}_{0.3})_2\text{B}$ catalyst. The binding energy shift adds up to 0.2 eV for the whole spectrum. This is caused by charging effects shown by a shift of the C 1s photoemission line by the same amount. At the same time, the B 1s photoemission line vanishes completely during the EC activation process, leaving no trace of boron at the near-surface of the catalyst. Thus, the surface of the catalyst gets more oxidized during the activation process. The two visible features in the Co $2p_{3/2}$ photoemission line can be assigned to cobalt oxide and cobalt hydroxide, respectively.^{[117], [201], [204]} Due to a satellite structure with an energy difference of 10 eV to the Co $2p_{3/2}$ main signal the formation of Co_3O_4 at the surface can be excluded. The Co_3O_4 generally exhibits two satellite features, one with an energy difference of 6 eV and another one with an energy difference of 10 eV, which arise due to cobalt in an oxidation state of Co^{+II} and Co^{+III} , respectively.^{[117], [201], [204]} An intense and broad hydroxide signal is visible in the O 1s photoemission line at binding energies around 531 eV (*cf.* **Figure 4.5.11d**). This observation combined with cobalt in an oxidation state of Co^{+III} is fully consistent with the formation of a cobalt oxyhydroxide at the surface, which has been observed in cobalt-containing catalysts before.^{[47], [48], [135], [145], [165], [249], [250]} This is also in agreement with the occurrence of the irreversible oxidation wave of cobalt-based materials in the investigated potential range (*cf.*

Figure 4.1.4 and Section 4.1.3).^{[186], [187]} The XP detail O 1s spectrum of CoOOH features two signals (oxide: 529.3 eV and hydroxide: 530.9 eV) with similar intensities, according to the bonding ratio.^{[119], [135], [201], [204]} In the O 1s spectrum after the EC activation the hydroxide component has a higher intensity than the oxide one located at binding energies around 529.2 eV. However, for the $(\text{Co}_{0.9}\text{Ni}_{0.1})_2\text{B}$ catalyst the formation of an additional nickel hydroxide component has to be considered since the Ni $2p_{3/2}$ photoemission line after EC activation (cf. Figure 4.5.11c) shows a signal at 855.4 eV with a corresponding shake-up peak at 861.7 eV, which can be attributed to the formation of $\text{Ni}(\text{OH})_2$.^{[209], [260]}

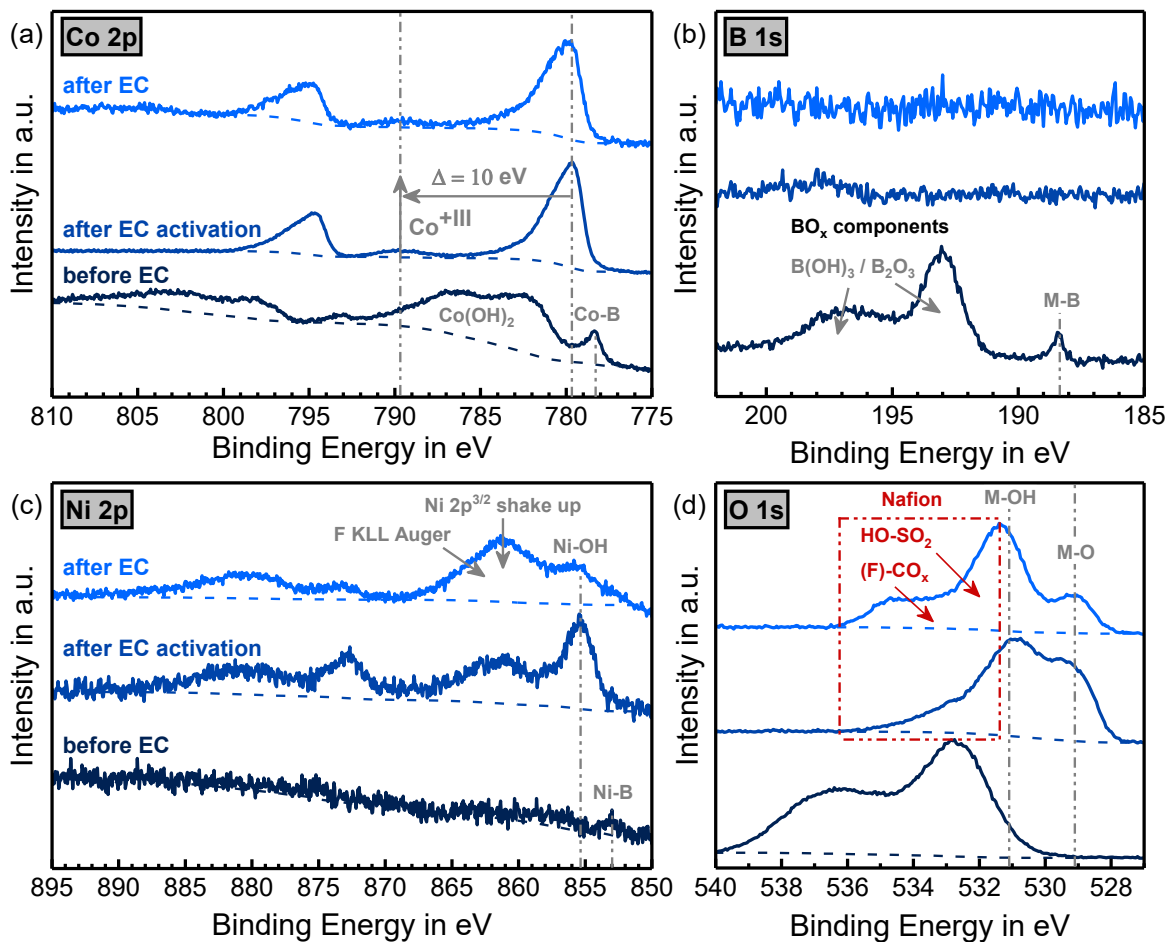


Figure 4.5.11: XP Co 2p (a) and Ni 2p (c) detail spectra and XP B 1s (b) and O 1s (d) detail spectra of $(\text{Co}_{0.9}\text{Ni}_{0.1})_2\text{B}$ before (dark blue), after electrochemical (EC) activation (blue), and after (light blue) EC investigation, indicating the changes in composition occurring during the EC testing of the samples.

The former Ni-B peak of the Ni $2p_{3/2}$ photoemission at 852.9 eV vanishes during the EC activation. The formation of $\text{Ni}(\text{OH})_2$ is in agreement with the reversible redox behavior of nickel

hydroxide to nickel oxyhydroxide and vice versa in the investigated potential range.^{[190], [192], [193]} Additionally, the Nafion™ binder features several signals in the O 1s spectrum. The structural formula and the XPS specifics of Nafion™ are summarized in **Section 4.1.4**. Nafion™ contains sulfonyl hydroxide (R-S(=O)₂(OH)), oxocarbon (CO_x), and oxocarbon with fluorine (OCF), which account for the signals at approximately 531.7 to 535 eV.^{[234], [239], [255]} Especially, the sulfonyl hydroxide peak of the Nafion™ overlays with the hydroxide component of the CoOOH and Ni(OH)₂, broadening the hydroxide component in the O 1s photoemission line towards higher binding energies. The structure and shape of the Co 2p photoemission line do not alter during the complete EC investigation. Therefore, it can be stated that during the EC activation process the cobalt phase is already fully oxidized to Co³⁺OOH. Similar behavior can be observed for the Ni 2p photoemission line since the positioning of the peaks does not change after the complete EC investigation. Hence, the cobalt, as well as the nickel phase, shows no further transformation after the EC activation process. However, the intensity ratio between the Ni 2p_{3/2} signal and the corresponding shake-up peak changes strongly. The shake-up peak even exceeds the Ni 2p_{3/2} signal. This phenomenon cannot be clarified by the Ni 2p photoemission line itself. In **Figure 4.5.12** the XP survey spectra of the (Co_{0.9}Ni_{0.1})₂B catalyst after the EC activation and after the complete EC testing are plotted and compared to a survey spectrum of pure Nafion™. The XPS measurement of the catalyst after the EC investigation exhibits a higher fluorine signal compared to the catalyst after the EC activation. This phenomenon is caused by unequal XPS measurement spots used for the investigation of the sample. Since the powdered catalyst is not completely homogeneously distributed, variations in the Nafion™ catalyst distribution can lead to differences in the XP spectra. The higher fluorine content is an equivalent of a higher Auger F KLL peak and thus, to a higher F KLL peak structure, which is shown in the inset in **Figure 4.5.12**. The marked “Auger structure I” overlaps with the Ni 2p_{3/2} shake-up peak, while the “Auger structure II” overlaps with the satellite structure of the Ni 2p_{1/2} signal. For the determination of the surface composition after the EC investigation (*cf.* **Table 4.5.2**), this Auger structure must be subtracted from the measured Ni 2p signal. The exemplification of this subtraction is shown in **Figure 4.5.13**. The used parameters for the quantitative analysis are summarized in **Table 2.4.1**. The peak shape and position of the remaining Ni 2p signal confirms the assumption that nickel remained in its Ni²⁺ oxidation state as in Ni(OH)₂ after the EC investigation.^{[209], [260]}

Table 4.5.2: Chemical composition of the surface of the most active catalyst $(\text{Co}_{0.9}\text{Ni}_{0.1})_2\text{B}$ with XPS before (before EC), after the electrochemical activation procedure (after EC activation), and after the EC testing (after EC). Additionally, the metal fraction expected from synthesis is given (as expected).

Metal “x”	Metal fraction x at the surface in % *			
	as expected	before EC	after EC activation* ¹	after EC* ¹
Cobalt	90	86.4	78.8	72.4
Nickel	10	13.6	21.2	27.6

*¹ The assumed errors for the results are due to overlaps of the F KLL Auger signal of Nafion™ with the Ni 2p photoemission line as shown in **Figure 4.5.12**. These errors are assumed to be between 1 and 10% in metallic fraction.

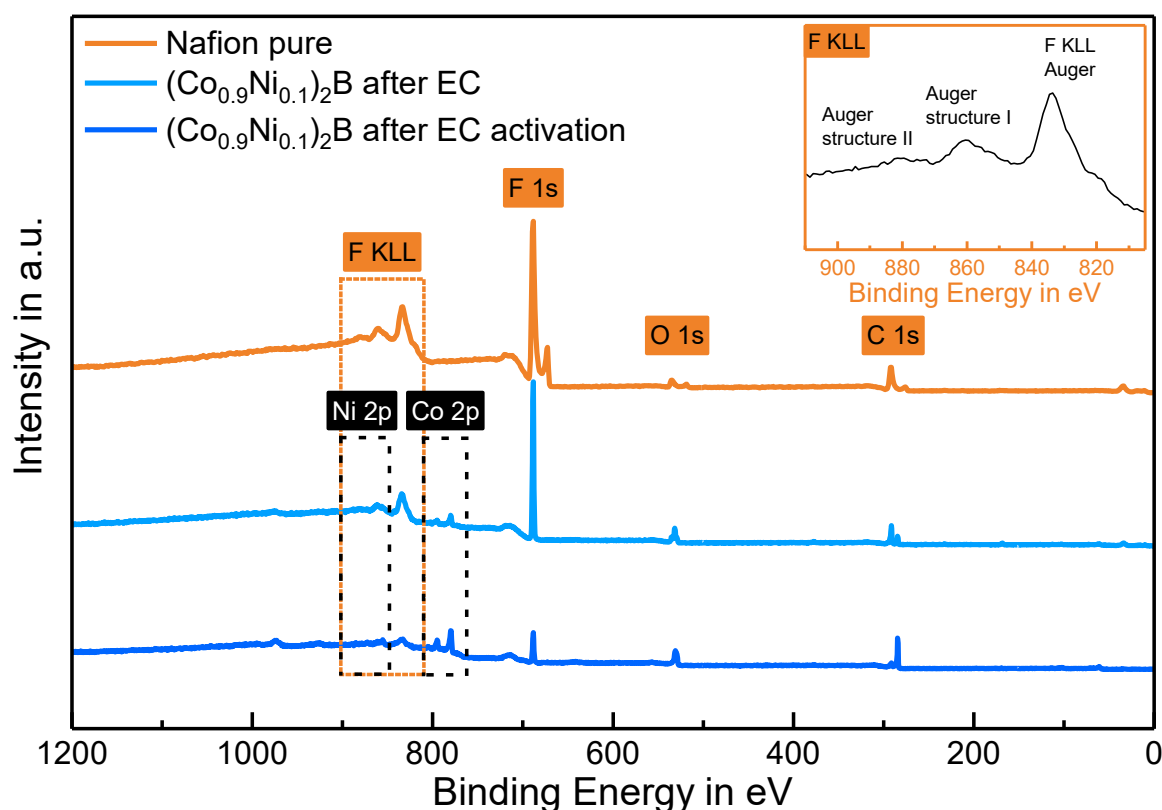


Figure 4.5.12: XP survey spectra of $(\text{Co}_{0.9}\text{Ni}_{0.1})_2\text{B}$ after electrochemical (EC) activation (blue), and after the complete EC investigation (light blue) compared to the survey spectrum of pure Nafion™ (orange), indicating the overlap of the fluorine Auger structure with the Ni 2p photoemission line.

The Nafion™ content additionally leads to a discrepancy in other XP detail spectra. The hydroxide signal in the O 1s photoemission line of the $(\text{Co}_{0.9}\text{Ni}_{0.1})_2\text{B}$ after the EC investigation (*cf.* **Figure 4.5.11d**) shifts slightly to higher binding energies compared to the one after the EC activation, due to the enlarged sulfonyl hydroxide ($\text{R-S(=O)}_2(\text{OH})$) component, which is located at higher binding energies compared to the metal hydroxide signals of cobalt and

nickel.^{[119], [135], [201], [204], [209], [236]–[239], [260]} Additionally, the shoulder signals at binding energies of 532.8 eV to 535 eV increase, which is due to oxocarbon (CO_x) and oxocarbon with fluorine (OCF) components.^{[236]–[239]} From quantitative analyses of the discussed XP detail spectra (*cf.* **Table 4.5.2**) of the different investigation stages (before EC, after EC activation, and after EC), it was found that the nickel content of the complete metallic fraction changes compared to the cobalt amount. The nickel amount at the surface increases with consecutive EC testing.

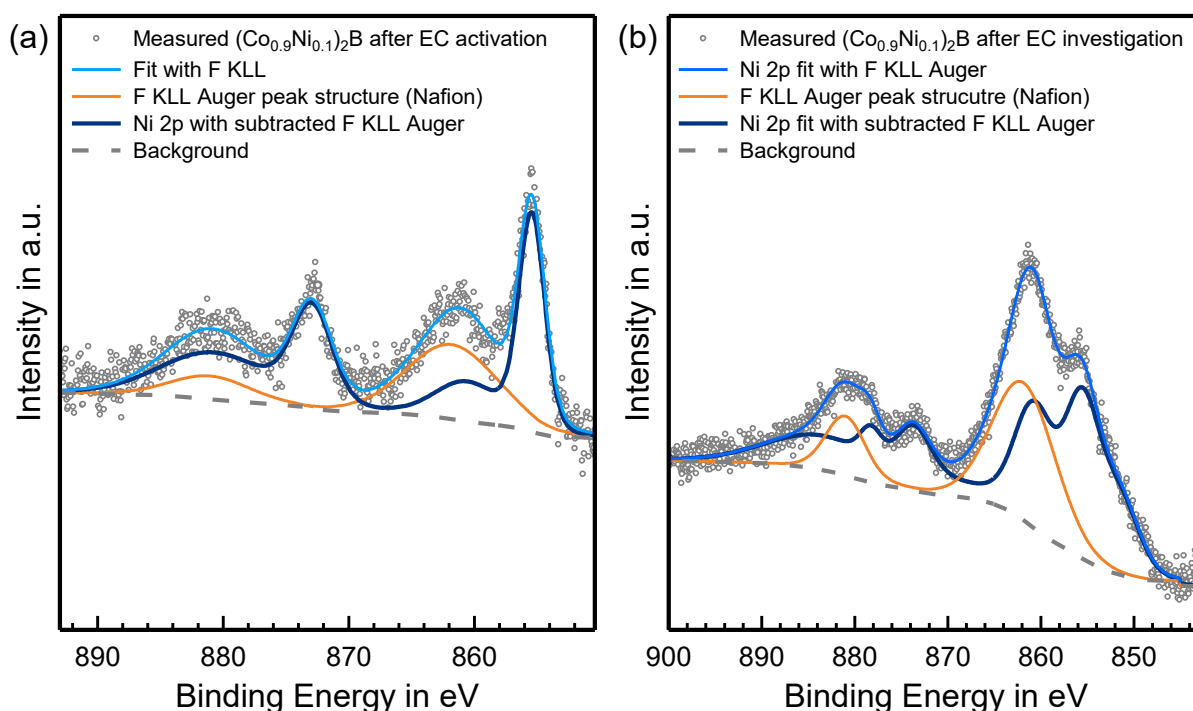


Figure 4.5.13: XP Ni 2p detail spectra of (Co_{0.9}Ni_{0.1})₂B after electrochemical (EC) activation **(a)** and after the complete EC investigation **(b)**. Two difference spectra are formed by subtraction of the measured Ni 2p photoemission line (grey dots & light blue line) with the KLL Auger structure (orange), leading to Ni 2p spectra independent of fluorine (dark blue line).

The nickel content before EC testing was found to be 13.6%. After the EC activation, the content increases to 21.2% and after the complete EC testing, a nickel content of 27.6% was calculated from the XP spectra. These surface calculations could either be due to a degradation of the cobalt phase inside the alkaline electrolyte or due to a rearrangement of the surface phase during the EC testing. To conclude on these explanation, F-AAS measurements of the used alkaline electrolyte were performed. Consequently, the electrolyte is investigated at three different measurement stages: before EC, after EC activation, and after EC investigation. From the F-AAS the quantitative cobalt and nickel contents inside the electrolyte can be monitored (*cf.* **Figure 4.5.14**).

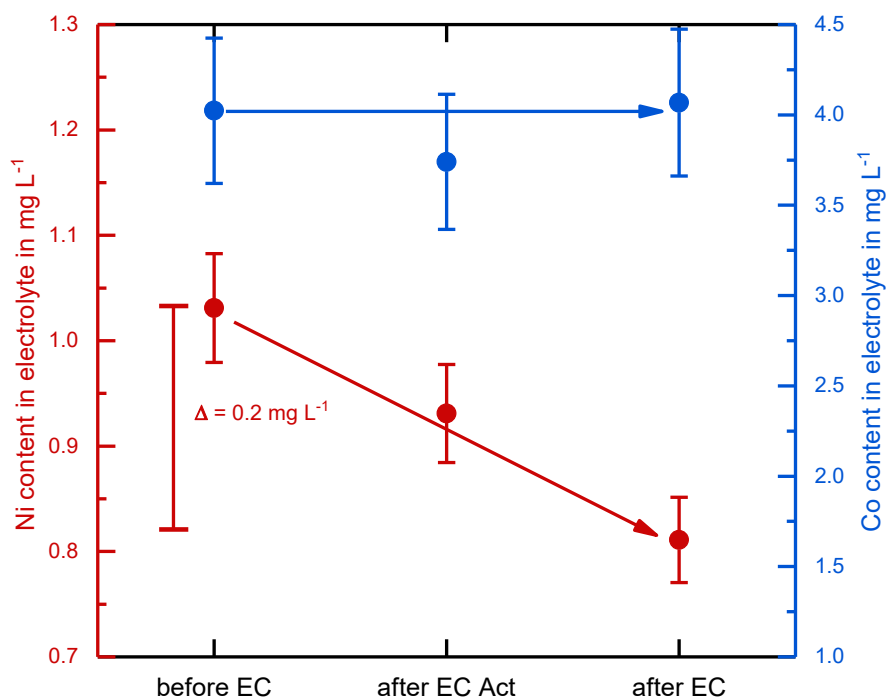


Figure 4.5.14: F-AAS measurements of the 1 M KOH electrolyte as purchased by Carl Roth (before EC), after electrochemical activation (after EC act.), and after EC investigation (after EC) of the $(\text{Co}_{0.9}\text{Ni}_{0.1})_2\text{B}$ catalyst.

The cobalt content (blue) shows no change during the EC investigations, which leads to the conclusion that no cobalt is dissolved from the catalyst into the electrolyte during the EC investigation. But a change in the nickel content (red) of the electrolyte is found during the EC measurement procedure. The nickel content decreases already after the EC activation procedure, revealing a total nickel mass loss in the electrolyte after the complete EC investigation of 0.2 mg L^{-1} . Considering that the complete mass loss of nickel in the electrolyte is absorbed onto the surface of the catalyst, an increased amount of the total catalyst composition can be calculated.

The volume of the electrolyte inside the EC cell (Zahner cell) is limited to 7.2 mL. The investigated surface of the catalyst is defined by an O-ring with a radius of 0.25 cm. Consequently, the size of the investigated area of the catalyst is calculated to be 0.2 cm^2 ($\text{Area}_{\text{circle}} = \pi r^2$). Due to the total loading calculated in **Section 4.2.4** of $150 \mu\text{g cm}^{-2}$, the loading of the EC investigated area is estimated to be $30 \mu\text{g}$. The adsorbed nickel mass from the electrolyte onto the surface of the catalyst can further be calculated with **Equation 4.5.1**, considering homogenous adsorption.

$$\Delta Ni_{mass\ adsorbed} = \frac{0.2\ mg\ L^{-1}}{1000} \cdot 7.2\ mL \quad \text{eq. 4.5.1}$$

$$\Rightarrow \Delta Ni_{mass\ adsorbed} = 1.44\ \mu g$$

The calculated nickel mass equals an increase in the metallic mass of the whole catalyst loading (bulk) of 5%. The total percentage change is even higher if only the surface of the catalysts is considered. Therefore, it can be stated that the change in nickel content found by XPS after the EC testing is caused by nickel (re)adsorption from the electrolyte onto the surface of the catalyst layer during the EC investigation. Consequently, this could explain the slightly improved performance of the catalyst after the long-term stability testing. Also, an enhanced electrical conductivity at the near surface of the catalyst due to the nickel atoms could be possible. A similar observation concerning iron impurities found after the EC investigation of transition metal-based catalyst systems in alkaline electrolytes have been reported.^[261] It is assumed that the iron (re)adsorption from the alkaline electrolyte is responsible for an enhancement in the catalytic performance of Ni-based catalysts.^{[52], [250], [261], [262]} A similar adsorption of iron from the alkaline electrolyte into the catalyst phase is not likely but cannot be completely excluded. However, the nickel amount found by XPS is significantly (*cf.* **Table 4.5.2**) increased after the EC testing, while on the surface of the catalysts no iron can be found with XPS. The active surface species, which forms during the EC testing is identified to be $Co^{3+}OOH$ and $Ni^{2+}(OH)_2$. It is assumed that the bulk of the powdered $(Co_{1-x}Ni_x)_2B$ catalysts remains in its initial metal boride state. A comparable structure has been proposed before for metal boride particles by Shveikin^[245] and was found in metal boride and metal phosphide catalysts tested for OER.^{[145], [165], [254], [263], [264]}

4.5.4 Conclusion of the proposed mechanism

In this chapter, an explanation for the observed improvement of the EC performance for the OER of the $(\text{Co}_{1-x}\text{Ni}_x)_2\text{B}$ catalysts in an alkaline electrolyte is proposed.

First, it should be stated that the ternary metal boride powders are not stable under ambient conditions. The $(\text{Co}_{1-x}\text{Ni}_x)_2\text{B}$ powders oxidize even faster than the $(\text{Co}_{1-x}\text{Fe}_x)_2\text{B}$ catalysts as presented in **Section 4.5.1**. During the EC activation, the surface of the ternary metal boride oxidizes further and forms a cobalt oxyhydroxide (Co^{3+}OOH) and nickel hydroxide ($\text{Ni}^{2+}(\text{OH})_2$). These active phases for cobalt and nickel are expected due to EC studies that have been developed for cobalt and nickel electrodes in the tested potential range in the past.^{[183]–[187], [190], [192], [193]} The oxidation and reduction waves of the $\text{Co}^{2+/3+}$ transition both shift anodically with increasing nickel content, leading to the assumption that strong electronic coupling between cobalt and nickel is present, as it is reported for other cobalt-nickel-based catalyst systems.^{[257]–[259]} A further EC investigation of the samples does not change the present surface phases. However, a change in the metallic fractions in the near-surface region can be observed. The nickel-to-cobalt ratio increased. F-AAS measurements showed that the cobalt does not dissolve under reaction conditions but some nickel impurities, which were found in the original electrolyte (1 M KOH – Carl Roth), (re)adsorb onto the surface of the catalyst. A (re)absorption of iron^{[52], [250], [261], [262]} could not be found from XPS measurements after the EC investigation and are therefore not assumed to be responsible for the improved EC activity of the catalyst after the long-term stability measurement. However, the influence of this phenomenon cannot entirely be excluded. Further measurements are required to clarify this phenomenon. From the XPS-data before and after the EC investigation, it is proposed that the structure of the $(\text{Co}_{1-x}\text{Ni}_x)_2\text{B}$ catalyst changes from a nano-structured network with a thin oxide layer (after air storage) to one with a thicker hydroxide (Ni) and oxyhydroxide layer (Co). With subsequent EC investigation, the nickel amount at the surface of the catalyst increases in comparison to the cobalt phase. It is assumed that the nickel is (re)adsorbed from the electrolyte onto the surface of the catalyst. The oxidation process of the ternary metal boride catalyst and the (re)adsorption of the nickel is schematically illustrated in **Figure 4.5.15**. The three different stages of the powder “air stored” (cf. **Figure 4.5.15d**), “after EC activation” (cf. **Figure 4.5.15e**), and “after EC investigation” (cf. **Figure 4.5.15f**) are presented schematically and with the corresponding Co 2p (cf. **Figure 4.5.15a, b, c**) and Ni 2p (cf. **Figure 4.5.15g, h, i**) XP detail spectra. The outer oxidation surface layer forms (grey) with the remaining metal boride core (black) a similar structure as already seen for the $(\text{Co}_{1-x}\text{Fe}_x)_2\text{B}$ catalyst system (cf. **Section 4.4.4**). The intact metal boride core is especially beneficial for the catalytic process in terms of the overall conductivity of the catalytic system. In contrast to metal oxides/hydroxides, di-metal borides (M_2B) show an increased electrical conductivity.^{[149], [150], [245]}

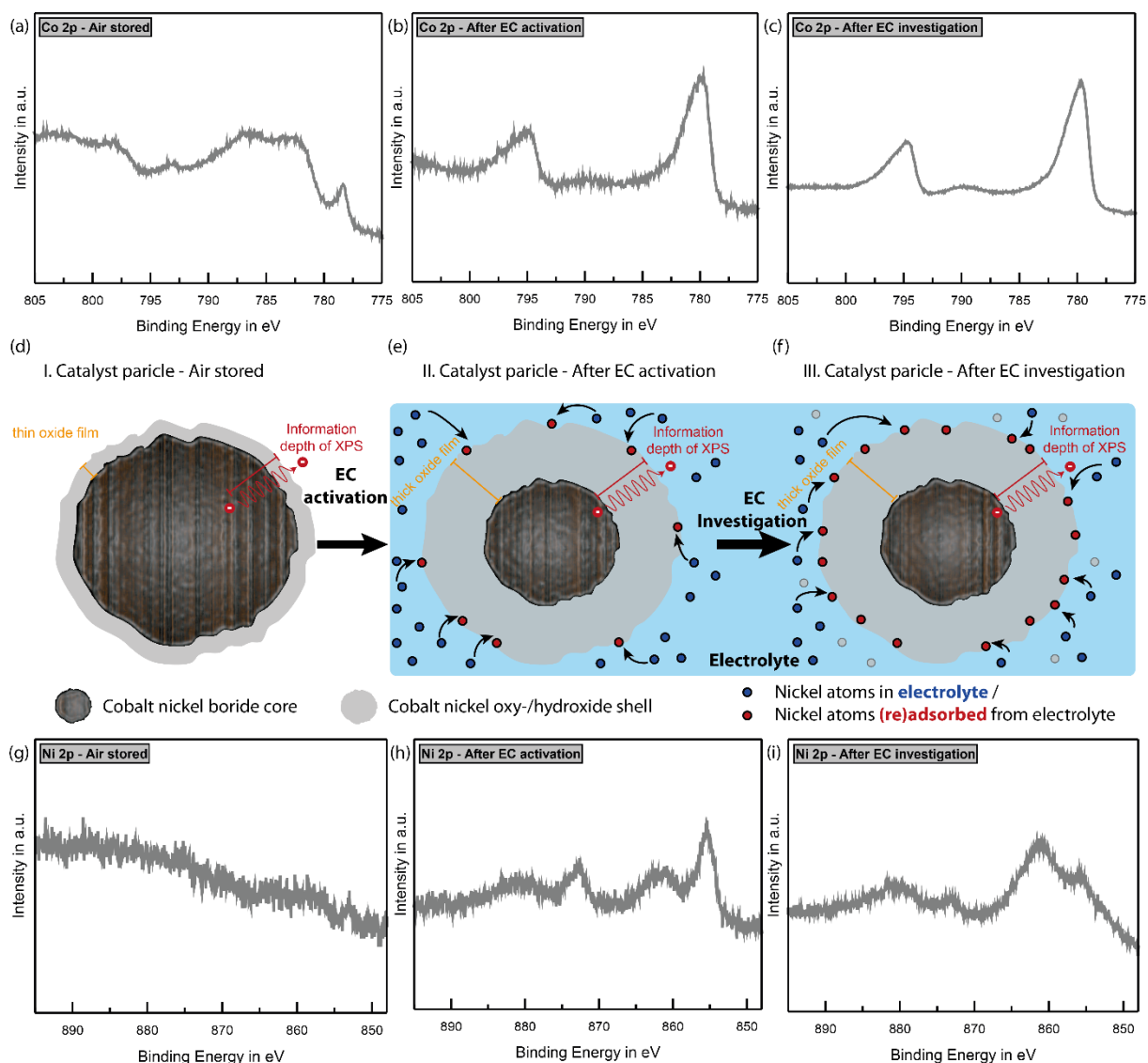


Figure 4.5.15: XP Co 2p (a), (b), (c) and Ni 2p (g), (h), (i) detail spectra of the $(\text{Co}_{0.9}\text{Ni}_{0.1})_2\text{B}$, respectively, in three different measurement stages. Schematic picture of the assumed cross section of the nanostructure of the catalyst (cf. Figure 4.5.5) from the measured XPS data in these measurement stages: (e) I. Air stored; (f) II. After electrochemical (EC) activation*¹ and (g) III. After EC investigation*¹. The blue dots represent the nickel inside of the electrolyte; the red dots illustrate the adsorption onto the surface of the catalyst. During the adsorption, the amount of nickel inside the electrolyte is reduced (grey dots).

*¹Here the raw data of the Ni 2p detail spectra are shown without the subtraction of the F KLL Auger peaks (cf. Figure 4.5.13).

5 Conclusions and Perspectives

In the broad context of the development of efficient materials for the catalytic process of water electrolysis, this work covers at first the catalytic perspectives of manganese-based oxides for the OER in the context of the MANGAN BMBF project (03EK3552), focusing mainly on the influence of the substrate material on the catalytic activity of these manganese catalysts in alkaline media. As a second main topic in cooperation with the Eduard-Zintl-institute of inorganic and physical chemistry, transition metal borides were investigated for their applicability as catalysts for OER and HER in alkaline media, focusing on cobalt-based materials with systematic incorporation of nickel and iron into the lattice, synthesized in a one-step solution process with a subsequent calcination step published in ^{[144]–[146]}.

In the MANGAN project, manganese oxide thin film catalysts were successfully deposited via a PE-CVD process on several different substrate materials, using dimanganese decacarbonyl ($\text{Mn}_2(\text{CO})_{10}$) as a precursor. According to XPS results, Mn_2O_3 and a mixture of MnO and Mn_2O_3 could be produced by varying the substrate temperature of the PE-CVD process. The variation of the oxygen content in the reactive gas showed no influence on the film composition. The identification of the PE-CVD parameters to receive different manganese oxide thin films was carried out on freshly cleaned titanium substrates and was afterward adapted to the deposition on a variety of other substrates, showing reproducible results in terms of thin-film composition for nearly all used substrates. It was shown that the produced MnO_x catalysts exhibit unstable behavior in high concentrated alkaline electrolytes (1 M KOH), at which the catalyst degraded under OER potentials. Consequently, an electrolyte with a lower ionic concentration (0.1 M KOH) was used for the subsequent experiments, leading to distinctly better stability of both MnO_x phases. A manganese oxidation state between Mn^{3+} and Mn^{4+} was identified on the surface of all MnO_x catalysts after the EC testing. Similar compositions have been reported for MnO_x catalysts before. ^{[118]–[120], [123], [125]} The EC investigation of the Ti/ MnO_x systems showed only minor catalytic activity towards the OER for both MnO_x phases. The low achieved current densities of 0.5 mA cm^{-2} and 0.18 mA cm^{-2} at potentials of 1.8 V vs. RHE for Ti/ Mn_2O_3 and Ti/ Mn_2O_3 & MnO , respectively, were attributed to a native TiO_2 layer in between the Ti substrate and the catalyst layer, exhibiting poor electrical conductivity. Consequently, the MnO_x catalysts were deposited on various other substrates that do not form nonconductive native oxide layers, namely GC, HOPG, ITO/Au, and stainless steel. The carbon-based supports were chosen to investigate manganese oxide catalysts on substrates that can be prepared easily and show only a small number of core level lines, not interfering with manganese and oxygen. The ITO/Au system was chosen due to the often stated synergy effect between Au and MnO_x , ^{[55], [56]} whereas the cheap SS support was used as a possible support for an industrial approach. For all catalyst/support systems, the Mn_2O_3 showed superior catalytic performance compared to the

mixed MnO/Mn₂O₃ phase. The increased activity is attributed to a better intrinsic conductivity of the thin films in the absence of MnO,^{[140], [141]} and a better transition capability of the Mn₂O₃ to the electrochemically active Mn₂O₃/MnO₂ phase during the EC investigation.^{[87], [90], [93], [100], [106]} In contrast to previously reported results, no increase in activity was found for the Au/MnO_x systems. The MnO_x catalysts on the ITO/Au support showed the second-lowest activity besides the Ti/TiO₂/MnO_x system. The highest catalytic performance was reached with carbon-based supports either with the mixed MnO/Mn₂O₃ on GC or with the pure Mn₂O₃ phase in combination with HOPG. Interface experiments are necessary, to better understand the processes and properties of the support/catalyst interface. However, since the deposition reactor is not connected to the UHV system of the DAISY-FUN all produced MnO_x catalysts are *ex situ* samples unsuitable for performing interface experiments. Still, this work shows that a simple investigation of the properties of the catalysts alone is insufficient to identify suitable working catalysts. The catalyst has to be investigated in a broader context, including the interactions with the support material and the electrolyte. Altogether, binary MnO_x bulk catalysts yield only poor electrocatalysts for the OER in alkaline media and cannot reach the expectations established by the chemical isolated Mn₄CaO₅ clusters of the PS II, at which a current density of 12 mA cm⁻² can be reached in neutral pH with an estimated overpotential of only 60 mV.^[26] One possible explanation is the poor electrical bulk conductivity of the MnO_x phases. This obstacle should have been avoided by depositing MnO_x thin-films, which lead to losses at the contact between the support and the catalyst layer. These efficiency losses emerging at the support/catalyst interface interfere strongly with the overall performance of the catalyst and are so far rarely discussed in the literature. To further address these losses, additional EC measurements are suggested using a four-electrode setup, at which the 4th electrode is situated directly at the surface of the catalyst allowing to quantify the losses throughout the support catalyst system. This measurement setup is not limited to manganese-based catalysts only and could help – in combination with interface experiments – to understand the complete EC system. The main obstacles of MnO_x catalysts for their applicability in the OER are the poor electrical bulk conductivity and the poor electrochemical stability in highly concentrated alkaline electrolytes. However, nature shows us that manganese can work as a catalyst in a tailor-made environment. A comparable system in this regard is iron oxide, which shows as a binary system poor stability towards the OER in alkaline media,^{[47], [48]} but can improve the performance significantly when used as an additive in *e.g.* cobalt or nickel-based catalyst systems. One promising ternary transition metal system was investigated in the second part of this work with the systematic incorporation of iron and nickel into Co₂B nanostructures. Consequently, a further research approach for manganese oxides could lead to mixtures with other transition metals to form ternary catalyst systems.

The second part of this work is motivated by the search for new catalyst systems for the OER. Cobalt-based transition metal borides were synthesized in a one-step solution process with a subsequent calcination step with systematic incorporation of iron and nickel into binary Co_2B forming $(\text{Co}_{1-x}\text{Fe}_x)_2\text{B}$ and $(\text{Co}_{1-x}\text{Ni}_x)_2\text{B}$ with incorporation limits of $0 \leq x \leq 0.5$. The powdered catalysts are amorphous before the annealing step at $500\text{ }^\circ\text{C}$ and show crystallinity afterward. The resulting borides exhibit nano-structured network morphologies. With TEM, an amorphous oxygen-rich surface layer on top of the crystalline transition metal boride support was detected. Partial oxidation of the transition metal borides during a longer storage time in air was confirmed via XPS. The powdered catalysts were drop-coated with a spot of ink onto mirror-finished GC substrates and were successfully investigated with EC methods for HER and OER in 1 M KOH . For all samples, only a minor activity for the HER was observed and, thus, the HER was not investigated further in this work. For the OER, distinctly higher activity was observed.

In the $(\text{Co}_{1-x}\text{Fe}_x)_2\text{B}$ system, $\text{Co}^{\text{III}}\text{OOH}$ and mainly Fe_2O_3 (with possible small amounts of $\text{Fe}^{\text{III}}\text{O}_x\text{H}_y$) were identified on the surface of the catalysts after the EC investigation with XPS. With increasing iron content, an anodic shift in the redox waves for the $\text{Co}^{2+}/\text{Co}^{3+}$ transition is observed in the CV curves, highlighting the strong electronic coupling between the Co and the Fe, as it has been reported for other cobalt-iron-based catalyst systems. [183]–[188], [190] Thus, the iron incorporation makes it more difficult for the cobalt to oxidize. All prepared $(\text{Co}_{1-x}\text{Fe}_x)_2\text{B}$ catalyst systems (with $0 \leq x \leq 0.5$) show an improved catalytic activity compared to the binary Co_2B . But the best EC performance is reached with $(\text{Co}_{1-x}\text{Fe}_x)_2\text{B}$ catalyst with $0.1 \leq x \leq 0.3$. These phases show a distinct improvement in the onset potential for the OER. In contrast to that, the onset potential of the $(\text{Co}_{1-x}\text{Fe}_x)_2\text{B}$ catalyst with $x=0.4$ and $x=0.5$ show a comparable onset potential as it is observed for the binary Co_2B . Consequently, an incorporation limit of iron inside the Co_2B phase was found to be between $x=0.3$ and $x=0.4$ to be beneficial for the OER. Additional investigations in this regard could be helpful to further quantify the maximum iron content which exhibits a beneficial effect on the onset potential in the $(\text{Co}_{1-x}\text{Fe}_x)_2\text{B}$ phase. The often-discussed formation of Co^{IV} during the OER could neither be proven nor disproven and, thus, $\text{Co}^{\text{III}}\text{OOH}$ and a Fe^{3+} phase, which is mainly assigned to iron oxide (Fe_2O_3) with possible contributions of mixed oxide/hydroxide FeO_xH_y phase as stated by Lyons et al. [187] are identified as the active phases under reaction conditions. The role of iron inside the material could not definitively be pinned down. The most active catalyst phases $(\text{Co}_{0.9}\text{Fe}_{0.1})_2\text{B}$ and $(\text{Co}_{0.7}\text{Fe}_{0.3})_2\text{B}$ showed a stable catalytic performance over 30 and 17 hours at 10 mA cm^{-2} without a sign of dissolution or delamination, respectively. However, the question of how iron improves the activity for the OER in the mixed system could not be clarified finally.

In the $(\text{Co}_{1-x}\text{Ni}_x)_2\text{B}$ system, $\text{Co}^{\text{III}}\text{OOH}$ and $\text{Ni}^{\text{II}}(\text{OH})_2$ were identified on the surface of the catalysts after the EC investigation with XPS. The oxidation and reduction waves of the $\text{Co}^{2+}/\text{Co}^{3+}$ transition both shift anodically with increasing nickel content, leading to the assumption that

strong electronic coupling between cobalt and nickel is also present, as it has been reported for other cobalt-nickel-based catalyst systems.^{[257]–[259]} Thus, the nickel incorporation also leads to a positive shift of the cobalt oxidation waves. In contrast to $(\text{Co}_{1-x}\text{Fe}_x)_2\text{B}$, the incorporation of nickel shows no effect on the onset potential for the OER inside the investigated concentrations. But a nickel content of $x=0.1$ and $x=0.2$ shows a beneficial effect on the slope of the CV curves for the OER regime, leading to a lowering of the overpotential at 10 mA cm^{-2} of 40 mV and 30 mV, respectively. It was shown that during the EC investigations nickel was (re)absorbed from the electrolyte onto the surface of the catalyst, which was even measurable by XPS. However, the often-discussed influence of iron adsorption onto the surface of the catalysts from the electrolyte was not observed in XPS but cannot be ruled out completely. The $(\text{Co}_{0.9}\text{Fe}_{0.1})_2\text{B}$ showed a stable catalytic performance at 10 mA cm^{-2} for over 8 hours and showed an even improved CV behavior after the stability measurement. This phenomenon could not be clarified in detail. But it is assumed that the (re)adsorbed nickel from the electrolyte shows a local improvement of the electrical conductivity at the nearest surface, leading to an increase in the slope of the CV curve.

In the prospect of future measurements, the determination of the resistance (van-der-Pauw method) of the different $(\text{Co}_{1-x}\text{Fe}_x)_2\text{B}$ and $(\text{Co}_{1-x}\text{Ni}_x)_2\text{B}$ catalyst phases would be of interest. This could be investigated by pressing pellets from the different powders and investigate these pellets by four-terminal sensing. The use of a flat electrode (e.g. pellets or thin-film deposition) could additionally help to reduce the influence of different electrochemical active surface areas and allows to investigate the depth of oxidation during or rather after the EC investigation with TEM. With this approach the here proposed remaining metal-boride core could be verified irrevocably. *In operando* measurements (e.g. XPS, Raman, etc.) could help to identify the oxidation states of cobalt and iron at the active potential range during the OER.

List of references

- [1] Bundesministerium für Umwelt Naturschutz und nukleare Sicherheit, *Klimaschutz in Zahlen - Fakten, Trends und Impulse deutscher Klimapolitik*. 2018.
- [2] H. Dau, P. Kurz, and M.-D. Weitze, *Künstliche Photosynthese*. Berlin, Heidelberg: Springer Berlin Heidelberg, 2019.
- [3] M. Roser, H. Ritchie, and E. Ortiz-Ospina, “World Population Growth,” *Ourworldindata.org*, 2013. <https://ourworldindata.org/world-population-growth> (accessed Feb. 22, 2021).
- [4] H. Ritchie, “Global energy consumption still rising,” *Ourworldindata.org*, 2014. <https://ourworldindata.org/energy> (accessed Feb. 22, 2021).
- [5] M. Höök and X. Tang, “Depletion of fossil fuels and anthropogenic climate change—A review,” *Energy Policy*, vol. 52, pp. 797–809, Jan. 2013, doi: 10.1016/j.enpol.2012.10.046.
- [6] S. Shafiee and E. Topal, “When will fossil fuel reserves be diminished?,” *Energy Policy*, vol. 37, no. 1, pp. 181–189, 2009, doi: 10.1016/j.enpol.2008.08.016.
- [7] C. McGlade and P. Ekins, “The geographical distribution of fossil fuels unused when limiting global warming to 2°C,” *Nature*, vol. 517, no. 7533, pp. 187–190, 2015, doi: 10.1038/nature14016.
- [8] U. Neupert, T. Euting, T. Kretschmer, and C. Notthoff, *Energiespeicher: Technische Grundlagen und energiewirtschaftliches Potenzial*. Euskirchen: Fraunhofer Institut Naturwissenschaftlich-Technische Trenanalysen, 2009.
- [9] P. Rundel, B. Meyer, M. Meiller, I. Meyer, R. Daschner, M. Jakuttis, M. Franke, *et al.*, *Speicher für die Energiewende*. Sulzbach-Rosenberg: Fraunhofer-Institut für Umwelt-, Sicherheits- und Energietechnik, 2013.
- [10] G. Fuchs, B. Lunz, M. Leuthold, and D. U. Sauer, “Technology Overview on Electricity Storage,” Aachen, 2012. [Online]. Available: http://www.sefep.eu/activities/projects-studies/120628_Technology_Overview_Electricity_Storage_SEFEP_ISEA.pdf.
- [11] Wissenschaftliche Dienste, “Ausarbeitung Vor- und Nachteile verschiedener Energiespeichersysteme,” 2015. [Online]. Available: <https://www.bundestag.de/blob/412904/ca2dd030254284687a1763059f1f4c0c/wd-8-032-14-pdf-data.pdf>.
- [12] European Commission, “Energy storage – the role of electricity,” Brussels, 2017. [Online]. Available: https://ec.europa.eu/energy/sites/ener/files/documents/swd2017_61_document_travail_service_part1_v6.pdf.
- [13] J. Moore and B. Shabani, “A critical study of stationary energy storage policies in Australia in an international context: The role of hydrogen and battery technologies,” *Energies*, vol. 9, no. 9, 2016, doi: 10.3390/en9090674.
- [14] M. Sterner and I. Stadler, *Energiespeicher - Bedarf, Technologien, Integration*, 1st ed. Berlin, Heidelberg: Springer Berlin Heidelberg, 2014.
- [15] A. Y. Khodakov, W. Chu, and P. Fongarland, “Advances in the development of novel cobalt Fischer-Tropsch catalysts for synthesis of long-chain hydrocarbons and clean fuels,” *Chem. Rev.*, vol. 107, no. 5, pp. 1692–1744, 2007, doi: 10.1021/cr050972v.
- [16] P. C. K. Vesborg and T. F. Jaramillo, “Addressing the terawatt challenge: Scalability in the supply of chemical elements for renewable energy,” *RSC Adv.*, vol. 2, no. 21, pp. 7933–7947, 2012, doi: 10.1039/c2ra20839c.
- [17] A. Moysiadou and X. Hu, “Stability profiles of transition metal oxides in the oxygen evolution reaction in alkaline medium,” *J. Mater. Chem. A*, vol. 7, no. 45, pp. 25865–25877, 2019, doi: 10.1039/c9ta10308b.
- [18] C. C. L. McCrory, S. Jung, I. M. Ferrer, S. M. Chatman, J. C. Peters, and T. F. Jaramillo, “Benchmarking Hydrogen Evolving Reaction and Oxygen Evolving Reaction

- Electrocatalysts for Solar Water Splitting Devices,” *J. Am. Chem. Soc.*, vol. 137, no. 13, pp. 4347–4357, 2015, doi: 10.1021/ja510442p.
- [19] C. C. L. McCrory, S. Jung, J. C. Peters, and T. F. Jaramillo, “Benchmarking Heterogeneous Electrocatalysts for the Oxygen Evolution Reaction,” *J. Am. Chem. Soc.*, vol. 135, no. 45, pp. 16977–16987, 2013, doi: 10.1021/ja407115p.
- [20] P. H. Stauffer and J. W. Hendley II, “Rare Earth Elements—Critical Resources for High Technology,” 2002. [Online]. Available: <https://pubs.usgs.gov/fs/2002/fs087-02/>.
- [21] J. Barber and M. D. Archer, “P680, the primary electron donor of photosystem II,” *J. Photochem. Photobiol. A Chem.*, vol. 142, no. 2–3, pp. 97–106, 2001, doi: 10.1016/S1010-6030(01)00503-2.
- [22] V. Krewald, M. Retegan, N. Cox, J. Messinger, W. Lubitz, S. DeBeer, F. Neese, *et al.*, “Metal oxidation states in biological water splitting,” *Chem. Sci.*, vol. 6, no. 3, pp. 1676–1695, 2015, doi: 10.1039/c4sc03720k.
- [23] M. M. Najafpour, M. Z. Ghobadi, B. Haghighi, J. J. Eaton-Rye, T. Tomo, J. R. Shen, and S. I. Allakhverdiev, “Nano-sized manganese-calcium cluster in photosystem II,” *Biochem. (Moscow)*, vol. 79, no. 4, pp. 324–336, Apr. 2014, doi: 10.1134/S0006297914040026.
- [24] M. M. Najafpour, M. Z. Ghobadi, B. Haghighi, T. Tomo, R. Carpentier, J.-R. Shen, and S. I. Allakhverdiev, “A nano-sized manganese oxide in a protein matrix as a natural water-oxidizing site,” *Plant Physiol. Biochem.*, vol. 81, pp. 3–15, Aug. 2014, doi: 10.1016/j.plaphy.2014.01.020.
- [25] W. Lubitz, M. Chrysina, and N. Cox, “Water oxidation in photosystem II,” *Photosynth. Res.*, vol. 142, no. 1, pp. 105–125, Oct. 2019, doi: 10.1007/s11120-019-00648-3.
- [26] S. D. Tilley, S. Lany, and R. van de Krol, *Advances in Photoelectrochemical Water Splitting*. Cambridge: Royal Society of Chemistry, 2018.
- [27] M. Zeng and Y. Li, “Recent advances in heterogeneous electrocatalysts for the hydrogen evolution reaction,” *J. Mater. Chem. A*, vol. 3, no. 29, pp. 14942–14962, 2015, doi: 10.1039/c5ta02974k.
- [28] F. Wang, T. A. Shifa, X. Zhan, Y. Huang, K. Liu, Z. Cheng, C. Jiang, *et al.*, “Recent advances in transition-metal dichalcogenide based nanomaterials for water splitting,” *Nanoscale*, vol. 7, no. 47, pp. 19764–19788, 2015, doi: 10.1039/c5nr06718a.
- [29] P. Yu, F. Wang, T. A. Shifa, X. Zhan, X. Lou, F. Xia, and J. He, “Earth abundant materials beyond transition metal dichalcogenides: A focus on electrocatalyzing hydrogen evolution reaction,” *Nano Energy*, vol. 58, no. January, pp. 244–276, 2019, doi: 10.1016/j.nanoen.2019.01.017.
- [30] K. Xu, P. Chen, X. Li, Y. Tong, H. Ding, X. Wu, W. Chu, *et al.*, “Metallic Nickel Nitride Nanosheets Realizing Enhanced Electrochemical Water Oxidation,” *J. Am. Chem. Soc.*, vol. 137, no. 12, pp. 4119–4125, Apr. 2015, doi: 10.1021/ja5119495.
- [31] C. Walter, P. W. Menezes, S. Orthmann, J. Schuch, P. Connor, B. Kaiser, M. Lerch, *et al.*, “A Molecular Approach to Manganese Nitride Acting as a High Performance Electrocatalyst in the Oxygen Evolution Reaction,” *Angew. Chemie - Int. Ed.*, vol. 57, no. 3, pp. 698–702, 2018, doi: 10.1002/anie.201710460.
- [32] S. Gupta, M. K. Patel, A. Miotello, and N. Patel, “Metal Boride-Based Catalysts for Electrochemical Water-Splitting: A Review,” *Adv. Funct. Mater.*, vol. 30, no. 1, 2020, doi: 10.1002/adfm.201906481.
- [33] C. H. Hamann, A. Hamnett, and W. Vielstich, *Electrochemistry*, 2nd ed. Weinheim: Wiley-VCH Verlag GmbH & Co. KGaA, 2007.
- [34] C. H. Hamann and W. Vielstich, *Elektrochemie*, 4th ed. Weinheim: Wiley-VCH Verlag GmbH & Co. KGaA, 2005.
- [35] J. H. Montoya, L. C. Seitz, P. Chakthranont, A. Vojvodic, T. F. Jaramillo, and J. K. Nørskov, “Materials for solar fuels and chemicals,” *Nat. Mater.*, vol. 16, no. 1, pp. 70–81, 2016, doi: 10.1038/nmat4778.

- [36] J. Rossmeisl, Z. W. Qu, H. Zhu, G. J. Kroes, and J. K. Nørskov, "Electrolysis of water on oxide surfaces," *J. Electroanal. Chem.*, vol. 607, no. 1–2, pp. 83–89, 2007, doi: 10.1016/j.jelechem.2006.11.008.
- [37] I. C. Man, H. Y. Su, F. Calle-Vallejo, H. A. Hansen, J. I. Martinez, N. G. Inoglu, J. Kitchin, *et al.*, "Universality in Oxygen Evolution Electrocatalysis on Oxide Surfaces," *ChemCatChem*, vol. 3, no. 7, pp. 1159–1165, 2011, doi: 10.1002/cctc.201000397.
- [38] N. B. Halck, V. Petrykin, P. Krtil, and J. Rossmeisl, "Beyond the volcano limitations in electrocatalysis-oxygen evolution reaction," *Phys. Chem. Chem. Phys.*, vol. 16, no. 27, pp. 13682–13688, 2014, doi: 10.1039/c4cp00571f.
- [39] S. Giménez and J. Bisquert, *Photoelectrochemical solar fuel production: From basic principles to advanced devices*. 2016.
- [40] A. Valdés, J. Brilllet, M. Grätzel, H. Gudmundsdóttir, H. A. Hansen, H. Jónsson, P. Klüpfel, *et al.*, "Solar hydrogen production with semiconductor metal oxides: New directions in experiment and theory," *Phys. Chem. Chem. Phys.*, vol. 14, no. 1, pp. 49–70, 2012, doi: 10.1039/c1cp23212f.
- [41] H. Dau, C. Limberg, T. Reier, M. Risch, S. Roggan, and P. Strasser, "The Mechanism of Water Oxidation: From Electrolysis via Homogeneous to Biological Catalysis," *ChemCatChem*, vol. 2, no. 7, pp. 724–761, 2010, doi: 10.1002/cctc.201000126.
- [42] Z. Xu, J. Rossmeisl, and J. R. Kitchin, "A linear response DFT+U study of trends in the oxygen evolution activity of transition metal rutile dioxides," *J. Phys. Chem. C*, vol. 119, no. 9, pp. 4827–4833, 2015, doi: 10.1021/jp511426q.
- [43] J. Rossmeisl, A. Logadottir, and J. K. Nørskov, "Electrolysis of water on (oxidized) metal surfaces," *Chem. Phys.*, vol. 319, no. 1–3, pp. 178–184, 2005, doi: 10.1016/j.chemphys.2005.05.038.
- [44] R. D. L. Smith, M. S. Prévot, R. D. Fagan, S. Trudel, and C. P. Berlinguette, "Water oxidation catalysis: Electrocatalytic response to metal stoichiometry in amorphous metal oxide films containing iron, cobalt, and nickel," *J. Am. Chem. Soc.*, vol. 135, no. 31, pp. 11580–11586, Aug. 2013, doi: 10.1021/ja403102j.
- [45] L. Trotochaud, S. L. Young, J. K. Ranney, and S. W. Boettcher, "Nickel-Iron oxyhydroxide oxygen-evolution electrocatalysts: The role of intentional and incidental iron incorporation," *J. Am. Chem. Soc.*, vol. 136, no. 18, pp. 6744–6753, 2014, doi: 10.1021/ja502379c.
- [46] T. Grewe, X. Deng, and H. Tüysüz, "Influence of Fe doping on structure and water oxidation activity of nanocast Co₃O₄," *Chem. Mater.*, vol. 26, no. 10, pp. 3162–3168, 2014, doi: 10.1021/cm5005888.
- [47] M. S. Burke, M. G. Kast, L. Trotochaud, A. M. Smith, and S. W. Boettcher, "Cobalt-Iron (Oxy)hydroxide Oxygen Evolution Electrocatalysts: The Role of Structure and Composition on Activity, Stability, and Mechanism," *J. Am. Chem. Soc.*, vol. 137, no. 10, pp. 3638–3648, 2015, doi: 10.1021/jacs.5b00281.
- [48] M. S. Burke, S. Zou, L. J. Enman, J. E. Kellon, C. A. Gabor, E. Pledger, and S. W. Boettcher, "Revised Oxygen Evolution Reaction Activity Trends for First-Row Transition-Metal (Oxy)hydroxides in Alkaline Media," *J. Phys. Chem. Lett.*, vol. 6, no. 18, pp. 3737–3742, 2015, doi: 10.1021/acs.jpcclett.5b01650.
- [49] D. Friebel, M. W. Louie, M. Bajdich, K. E. Sanwald, Y. Cai, A. M. Wise, M. J. Cheng, *et al.*, "Identification of highly active Fe sites in (Ni,Fe)OOH for electrocatalytic water splitting," *J. Am. Chem. Soc.*, vol. 137, no. 3, pp. 1305–1313, 2015, doi: 10.1021/ja511559d.
- [50] L. J. Enman, M. S. Burke, A. S. Batchellor, and S. W. Boettcher, "Effects of Intentionally Incorporated Metal Cations on the Oxygen Evolution Electrocatalytic Activity of Nickel (Oxy)hydroxide in Alkaline Media," *ACS Catal.*, vol. 6, no. 4, pp. 2416–2423, 2016, doi: 10.1021/acscatal.5b02924.
- [51] A. M. Smith, L. Trotochaud, M. S. Burke, and S. W. Boettcher, "Contributions to activity

- enhancement via Fe incorporation in Ni-(oxy) hydroxide/borate catalysts for near-neutral pH oxygen evolution,” *Chem. Commun.*, vol. 51, no. 25, pp. 5261–5263, 2015, doi: 10.1039/c4cc08670h.
- [52] L. Trotochaud, J. K. Ranney, K. N. Williams, and S. W. Boettcher, “Solution-Cast Metal Oxide Thin Film Electrocatalysts for Oxygen Evolution,” *J. Am. Chem. Soc.*, vol. 134, no. 41, pp. 17253–17261, 2012, doi: 10.1021/ja307507a.
- [53] J. R. Swierk, S. Klaus, L. Trotochaud, A. T. Bell, and T. D. Tilley, “Electrochemical Study of the Energetics of the Oxygen Evolution Reaction at Nickel Iron (Oxy)Hydroxide Catalysts,” *J. Phys. Chem. C*, vol. 119, no. 33, pp. 19022–19029, 2015, doi: 10.1021/acs.jpcc.5b05861.
- [54] C. Zhu, D. Wen, S. Leubner, M. Oschatz, W. Liu, M. Holzschuh, F. Simon, *et al.*, “Nickel cobalt oxide hollow nanosponges as advanced electrocatalysts for the oxygen evolution reaction,” *Chem. Commun.*, vol. 51, no. 37, pp. 7851–7854, 2015, doi: 10.1039/c5cc01558h.
- [55] Y. Gorlin, C. J. Chung, J. D. Benck, D. Nordlund, L. Seitz, T. C. Weng, D. Sokaras, *et al.*, “Understanding interactions between manganese oxide and gold that lead to enhanced activity for electrocatalytic water oxidation,” *J. Am. Chem. Soc.*, vol. 136, no. 13, pp. 4920–4926, 2014, doi: 10.1021/ja407581w.
- [56] M. S. El-Deab, M. I. Awad, A. M. Mohammad, and T. Ohsaka, “Enhanced water electrolysis: Electrocatalytic generation of oxygen gas at manganese oxide nanorods modified electrodes,” 2007. doi: 10.1016/j.elecom.2007.06.011.
- [57] A. M. Mohammad, M. I. Awad, M. S. El-Deab, T. Okajima, and T. Ohsaka, “Electrocatalysis by nanoparticles: Optimization of the loading level and operating pH for the oxygen evolution at crystallographically oriented manganese oxide nanorods modified electrodes,” *Electrochim. Acta*, vol. 53, no. 13, pp. 4351–4358, May 2008, doi: 10.1016/j.electacta.2008.01.081.
- [58] M. Busch, E. Ahlberg, and I. Panas, “Hydroxide oxidation and peroxide formation at embedded binuclear transition metal sites; TM = Cr, Mn, Fe, Co,” *Phys. Chem. Chem. Phys.*, vol. 13, no. 33, pp. 15062–15068, 2011, doi: 10.1039/c1cp20487d.
- [59] J. O. M. Bockris and T. Otagawa, “Mechanism of oxygen evolution on perovskites,” *J. Phys. Chem.*, vol. 87, no. 15, pp. 2960–2971, 1983, doi: 10.1021/j100238a048.
- [60] J. O. Bockris, “The Electrocatalysis of Oxygen Evolution on Perovskites,” *J. Electrochem. Soc.*, vol. 131, no. 2, p. 290, 1984, doi: 10.1149/1.2115565.
- [61] C. Wei, S. Sun, D. Mandler, X. Wang, S. Z. Qiao, and Z. J. Xu, “Approaches for measuring the surface areas of metal oxide electrocatalysts for determining their intrinsic electrocatalytic activity,” *Chem. Soc. Rev.*, vol. 48, no. 9, pp. 2518–2534, 2019, doi: 10.1039/c8cs00848e.
- [62] P. Connor, J. Schuch, B. Kaiser, and W. Jaegermann, “The Determination of Electrochemical Active Surface Area and Specific Capacity Revisited for the System MnOx as an Oxygen Evolution Catalyst,” *Zeitschrift für Phys. Chemie*, vol. 0, no. 0, pp. 1–16, 2020, doi: 10.1515/zpch-2019-1514.
- [63] S. Trasatti and O. A. Petrii, “Real surface area measurements in electrochemistry,” *Pure Appl. Chem.*, vol. 63, no. 5, pp. 711–734, 1991, doi: 10.1351/pac199163050711.
- [64] A. J. Bard, H. D. Abruña, C. E. Chidsey, L. R. Faulkner, S. W. Feldberg, K. Itaya, M. Majda, *et al.*, “The electrode/electrolyte interface - A status report,” *J. Phys. Chem.*, vol. 97, no. 28, pp. 7147–7173, 1993, doi: 10.1021/j100130a007.
- [65] V. S. Bagotsky, *Fundamentals of Electrochemistry*, Second Edi. Pennington: 2006 John Wiley & Sons, Inc., 2005.
- [66] J. C. Vickerman and I. S. Gilmore, *Surface Analysis - The Principal Techniques: Second Edition*, 2nd ed. Wiley, 2009.
- [67] A. Klein, T. Mayer, A. Thissen, and W. Jaegermann, “Photoelectron Spectroscopy in

-
- Materials Science and Physical Chemistry: Analysis of Composition, Chemical Bonding, and Electronic Structure of Surfaces and Interfaces,” in *Methods in Physical Chemistry*, R. Schäfer and P. C. Schmidt, Eds. Wiley-VCH Verlag GmbH & Co. KGaA, 2012, pp. 477–512.
- [68] S. Hofmann, *Auger- and X-Ray Photoelectron Spectroscopy in Materials Science*, vol. 49. Berlin, Heidelberg: Springer Berlin Heidelberg, 2013.
- [69] J. F. Moulder, W. F. Stickle, P. E. Sobol, and K. D. Bomben, *Handbook of X-ray Photoelectron Spectroscopy*. Physical Electronics Inc., 1995.
- [70] D. Briggs, D. M. Brewis, R. H. Dahm, and I. W. Fletcher, “Analysis of the surface chemistry of oxidized polyethylene: Comparison of XPS and ToF-SIMS,” *Surf. Interface Anal.*, vol. 35, no. 2, pp. 156–167, 2003, doi: 10.1002/sia.1515.
- [71] N. Fairley and A. Carrick, *The Casa cookbook: Recipes for XPS data processing*. Acolyte Science, 2005.
- [72] J. H. Scofield, “Hartree-Slater Subshell Photoionization Cross-Sections at 1254 and 1487 eV,” *J. Electron Spectros. Relat. Phenomena*, vol. 8, pp. 129–137, 1976.
- [73] Beer, “Bestimmung der Absorption des rothen Lichts in farbigen Flüssigkeiten,” *Ann. der Phys. und Chemie*, vol. 162, no. 5, pp. 78–88, 1852, doi: 10.1002/andp.18521620505.
- [74] M.P.Seah and W.A.Dench, “Quantitative Electron Spectroscopy of Surface,” *Surf. Interface Anal.*, vol. 1, no. 1, p. 2, 1979.
- [75] W. Jaegermann, “The Semiconductor/Electrolyte Interface: A surface Science Approach,” *Mod. Asp. Electrochem.*, vol. 30, no. 13, pp. 1–186, 1996.
- [76] W. H. Gries, “A Universal Predictive Equation for the Inelastic Mean Free Pathlengths of X-ray Photoelectrons and Auger Electrons,” *Surf. Interface Anal.*, vol. 24, no. 1, pp. 38–50, Jan. 1996, doi: 10.1002/(SICI)1096-9918(199601)24:1<38::AID-SIA84>3.0.CO;2-H.
- [77] K. Sauer, “A role for manganese in oxygen evolution in photosynthesis,” *Acc. Chem. Res.*, vol. 13, no. 8, pp. 249–256, Aug. 1980, doi: 10.1021/ar50152a001.
- [78] J. E. Post, “Manganese oxide minerals: Crystal structures and economic and environmental significance,” *Proc. Natl. Acad. Sci.*, vol. 96, no. 7, pp. 3447–3454, Mar. 1999, doi: 10.1073/pnas.96.7.3447.
- [79] S. Namgung, C.-M. Chon, and G. Lee, “Formation of diverse Mn oxides: a review of bio/geochemical processes of Mn oxidation,” *Geosci. J.*, vol. 22, no. 2, pp. 373–381, Apr. 2018, doi: 10.1007/s12303-018-0002-7.
- [80] C. P. Yi and S. R. Majid, “The Electrochemical Performance of Deposited Manganese Oxide-Based Film as Electrode Material for Electrochemical Capacitor,” in *Semiconductors - Growth and Characterization*, R. Inguanta and C. Sunseri, Eds. Rijeka: Croatia InTech, 2018.
- [81] H. Dau and M. Haumann, “The manganese complex of photosystem II in its reaction cycle-Basic framework and possible realization at the atomic level,” *Coord. Chem. Rev.*, vol. 252, no. 3–4, pp. 273–295, 2008, doi: 10.1016/j.ccr.2007.09.001.
- [82] M. Askerka, G. W. Brudvig, and V. S. Batista, “The O₂-Evolving complex of photosystem II: Recent insights from quantum mechanics/molecular mechanics (QM/MM), extended X-ray absorption fine structure (EXAFS), and femtosecond X-ray crystallography data,” *Acc. Chem. Res.*, vol. 50, no. 1, pp. 41–48, 2017, doi: 10.1021/acs.accounts.6b00405.
- [83] J. Kern, R. Chatterjee, I. D. Young, F. D. Fuller, L. Lassalle, M. Ibrahim, S. Gul, *et al.*, “Structures of the intermediates of Kok’s photosynthetic water oxidation clock,” *Nature*, vol. 563, no. 7731, pp. 421–425, 2018, doi: 10.1038/s41586-018-0681-2.
- [84] L. Pohlmann and H. Tributsch, “A model for Co-operative electron transfer,” *J. Theor. Biol.*, vol. 156, no. 1, pp. 63–72, 1992, doi: 10.1016/S0022-5193(05)80656-3.
- [85] H. Tributsch and L. Pohlmann, “Electron transfer: Classical approaches and new frontiers,” *Science (80-.)*, vol. 279, no. 5358, pp. 1891–1895, 1998, doi: 10.1126/science.279.5358.1891.

- [86] D. M. Proserpio, R. Hoffmann, and G. C. Dismukes, "Molecular Mechanism of Photosynthetic Oxygen Evolution. A Theoretical Approach," *J. Am. Chem. Soc.*, vol. 114, no. 11, pp. 4374–4382, 1992, doi: 10.1021/ja00037a052.
- [87] S. Trasatti, "Electrocatalysis by oxides - Attempt at a unifying approach," *J. Electroanal. Chem.*, vol. 111, no. 1, pp. 125–131, 1980, doi: 10.1016/S0022-0728(80)80084-2.
- [88] M. Morita, C. Iwakura, and H. Tamura, "The anodic characteristics of manganese dioxide electrodes prepared by thermal decomposition of manganese nitrate," *Electrochim. Acta*, vol. 22, no. 4, pp. 325–328, 1977, doi: 10.1016/0013-4686(77)85081-0.
- [89] M. Morita, C. Iwakura, and H. Tamura, "The anodic characteristics of modified Mn oxide electrode: Ti/RuOx/MnOx," *Electrochim. Acta*, vol. 23, no. 4, pp. 331–335, 1978, doi: 10.1016/0013-4686(78)80070-X.
- [90] M. Morita, C. Iwakura, and H. Tamura, "The anodic characteristics of massive manganese oxide electrode," *Electrochim. Acta*, vol. 24, no. 4, pp. 357–362, 1979, doi: 10.1016/0013-4686(79)87019-X.
- [91] R. Naumann, C. Hirche, and G. Wolf, "Untersuchungen zur Chlor- und Sauerstoffabscheidung an β -Braunstein unter halbleiterelektrochemischen Aspekten," *Zeitschrift für Phys. Chemie*, vol. 2570, no. 1, pp. 697–704, 1976, doi: <https://doi.org/10.1515/zpch-1976-25778>.
- [92] Y. Matsumoto and E. Sato, "Electrocatalytic properties of transition metal oxides for oxygen evolution reaction," *Mater. Chem. Phys.*, vol. 14, no. 5, pp. 397–426, May 1986, doi: 10.1016/0254-0584(86)90045-3.
- [93] A. Indra, P. W. Menezes, and M. Driess, "Uncovering structure-activity relationships in manganese-oxide-based heterogeneous catalysts for efficient water oxidation," *ChemSusChem*, vol. 8, no. 5, pp. 776–785, 2015, doi: 10.1002/cssc.201402812.
- [94] J. Melder, S. Mebs, P. A. Heizmann, R. Lang, H. Dau, and P. Kurz, "Carbon fibre paper coated by a layered manganese oxide: A nano-structured electrocatalyst for water-oxidation with high activity over a very wide pH range," *J. Mater. Chem. A*, vol. 7, no. 44, pp. 25333–25346, 2019, doi: 10.1039/c9ta08804k.
- [95] M. Huynh, D. K. Bediako, and D. G. Nocera, "A Functionally Stable Manganese Oxide Oxygen Evolution Catalyst in Acid," *J. Am. Chem. Soc.*, vol. 136, no. 16, pp. 6002–6010, 2014, [Online]. Available: <http://dx.doi.org/10.1021/ja413147e>.
- [96] M. M. Najafpour, M. Abasi, M. Hołyńska, and B. Pashaei, "Manganese oxides as water-oxidizing catalysts for artificial photosynthetic systems: The effect of support," *Int. J. Hydrogen Energy*, vol. 41, no. 12, pp. 5475–5483, Apr. 2016, doi: 10.1016/j.ijhydene.2016.02.031.
- [97] M. Mahdi Najafpour, D. Jafarian Sedigh, S. Maedeh Hosseini, and I. Zaharieva, "Treated Nanolayered Mn Oxide by Oxidizable Compounds: A Strategy to Improve the Catalytic Activity toward Water Oxidation," *Inorg. Chem.*, vol. 55, no. 17, pp. 8827–8832, 2016, doi: 10.1021/acs.inorgchem.6b01334.
- [98] T. Hayashi, N. Bonnet-Mercier, A. Yamaguchi, K. Suetsugu, and R. Nakamura, "Electrochemical characterization of manganese oxides as a water oxidation catalyst in proton exchange membrane electrolyzers," *R. Soc. Open Sci.*, vol. 6, no. 5, 2019, doi: 10.1098/rsos.190122.
- [99] C. E. Frey, F. Kwok, D. González-Flores, J. Ohms, K. A. Cooley, H. Dau, I. Zaharieva, *et al.*, "Evaporated manganese films as a starting point for the preparation of thin-layer MnO: X water-oxidation anodes," *Sustain. Energy Fuels*, vol. 1, no. 5, pp. 1162–1170, 2017, doi: 10.1039/c7se00172j.
- [100] A. Ramírez, P. Hillebrand, D. Stellmach, M. M. May, P. Bogdanoff, and S. Fiechter, "Evaluation of MnOx, Mn2O3, and Mn 3O4 electrodeposited films for the oxygen evolution reaction of water," *J. Phys. Chem. C*, vol. 118, no. 26, pp. 14073–14081, 2014, doi: 10.1021/jp500939d.

-
- [101] P. W. Menezes, A. Indra, O. Levy, K. Kailasam, V. Gutkin, J. Pfrommer, and M. Driess, "Using nickel manganese oxide catalysts for efficient water oxidation (ESI)," *Chem. Commun.*, vol. 51, no. 24, pp. 5005–5008, 2015, doi: 10.1039/C4CC09671A.
- [102] L. C. Seitz, T. J. P. Hersbach, D. Nordlund, and T. F. Jaramillo, "Enhancement Effect of Noble Metals on Manganese Oxide for the Oxygen Evolution Reaction," *J. Phys. Chem. Lett.*, vol. 6, no. 20, pp. 4178–4183, 2015, doi: 10.1021/acs.jpcclett.5b01928.
- [103] F. D. Speck, P. G. Santori, F. Jaouen, and S. Cherevko, "Mechanisms of Manganese Oxide Electrocatalysts Degradation during Oxygen Reduction and Oxygen Evolution Reactions," *J. Phys. Chem. C*, vol. 123, no. 41, pp. 25267–25277, 2019, doi: 10.1021/acs.jpcc.9b07751.
- [104] M. Rabe, C. Toparli, Y. H. Chen, O. Kasian, K. J. J. Mayrhofer, and A. Erbe, "Alkaline manganese electrochemistry studied by: In situ and operando spectroscopic methods-metal dissolution, oxide formation and oxygen evolution," *Phys. Chem. Chem. Phys.*, vol. 21, no. 20, pp. 10457–10469, 2019, doi: 10.1039/c9cp00911f.
- [105] S. W. Donne, "General Principles of Electrochemistry," in *Supercapacitors: Materials, Systems, and Applications*, 2013, pp. 1–68.
- [106] Z. M. Chan, D. A. Kitchaev, J. N. Weker, C. Schnedermann, K. Lim, G. Ceder, W. Tumas, *et al.*, "Electrochemical trapping of metastable Mn³⁺ ions for activation of MnO₂ oxygen evolution catalysts," *Proc. Natl. Acad. Sci. U. S. A.*, vol. 115, no. 23, pp. E5261–E5268, 2018, doi: 10.1073/pnas.1722235115.
- [107] C. E. Frey and P. Kurz, "Water Oxidation Catalysis by Synthetic Manganese Oxides with Different Structural Motifs: A Comparative Study," *Chem. - A Eur. J.*, vol. 21, no. 42, pp. 14958–14968, 2015, doi: 10.1002/chem.201501367.
- [108] S. Bernardini, F. Bellatreccia, A. Casanova Municchia, G. Della Ventura, and A. Sodo, "Raman spectra of natural manganese oxides," *J. Raman Spectrosc.*, vol. 50, no. 6, pp. 873–888, 2019, doi: 10.1002/jrs.5583.
- [109] M. Wiechen, I. Zaharieva, H. Dau, and P. Kurz, "Layered manganese oxides for water-oxidation: Alkaline earth cations influence catalytic activity in a photosystem II-like fashion," *Chem. Sci.*, vol. 3, no. 7, pp. 2330–2339, 2012, doi: 10.1039/c2sc20226c.
- [110] H. Simchi, K. A. Cooley, J. Ohms, L. Huang, P. Kurz, and S. E. Mohney, "Cospattered Calcium Manganese Oxide Electrodes for Water Oxidation," *Inorg. Chem.*, vol. 57, no. 2, pp. 785–792, 2018, doi: 10.1021/acs.inorgchem.7b02717.
- [111] A. Yamaguchi, R. Inuzuka, T. Takashima, T. Hayashi, K. Hashimoto, and R. Nakamura, "Regulating proton-coupled electron transfer for efficient water splitting by manganese oxides at neutral pH," *Nat. Commun.*, vol. 5, no. May, pp. 1–6, 2014, doi: 10.1038/ncomms5256.
- [112] S. Kosasang, N. Ma, P. Wuamprakhon, N. Phattharasupakun, T. Maihom, J. Limtrakul, and M. Sawangphruk, "Insight into the effect of intercalated alkaline cations of layered manganese oxides on the oxygen reduction reaction and oxygen evolution reaction," *Chem. Commun.*, vol. 54, no. 62, pp. 8575–8578, 2018, doi: 10.1039/c8cc03775b.
- [113] D. M. Robinson, Y. B. Go, M. Mui, G. Gardner, Z. Zhang, D. Mastrogiovanni, E. Garfunkel, *et al.*, "Photochemical water oxidation by crystalline polymorphs of manganese oxides: Structural requirements for catalysis," *J. Am. Chem. Soc.*, vol. 135, no. 9, pp. 3494–3501, 2013, doi: 10.1021/ja310286h.
- [114] R. P. Gupta and S. K. Sen, "Calculation of multiplet structure of core p -vacancy levels," *Phys. Rev. B*, vol. 10, no. 1, pp. 71–77, Jul. 1974, doi: 10.1103/PhysRevB.10.71.
- [115] R. P. Gupta and S. K. Sen, "Calculation of multiplet structure of core p-vacancy levels. II," *Phys. Rev. B*, vol. 12, no. 1, pp. 15–19, 1975, doi: 10.1103/PhysRevB.12.15.
- [116] H. W. Nesbitt and D. Banerjee, "Interpretation of XPS Mn(2p) spectra of Mn oxyhydroxides and constraints on the mechanism of MnO₂ precipitation," *Am. Mineral.*, vol. 83, no. 3–4, pp. 305–315, 1998, doi: 10.2138/am-1998-3-414.
- [117] M. C. Biesinger, B. P. Payne, A. P. Grosvenor, L. W. M. Lau, A. R. Gerson, and R. S. C.

- Smart, "Resolving surface chemical states in XPS analysis of first row transition metals, oxides and hydroxides: Cr, Mn, Fe, Co and Ni," *Appl. Surf. Sci.*, vol. 257, no. 7, pp. 2717–2730, Jan. 2011, doi: 10.1016/j.apsusc.2010.10.051.
- [118] M. Oku, K. Hirokawa, and S. Ikeda, "X-ray photoelectron spectroscopy of manganese-oxygen systems," *J. Electron Spectros. Relat. Phenomena*, vol. 7, no. 5, pp. 465–473, 1975, doi: 10.1016/0368-2048(75)85010-9.
- [119] M. Oku and K. Hirokawa, "X-ray photoelectron spectroscopy of Co₃O₄, Fe₃O₄, Mn₃O₄, and related compounds," *J. Electron Spectros. Relat. Phenomena*, vol. 8, no. 5, pp. 475–481, 1976, doi: 10.1016/0368-2048(76)80034-5.
- [120] Y. Gorlin and T. F. Jaramillo, "A Bifunctional Nonprecious Metal Catalyst for Oxygen Reduction and Water Oxidation," *J. Am. Chem. Soc.*, vol. 132, no. 39, pp. 13612–13614, Oct. 2010, doi: 10.1021/ja104587v.
- [121] C. S. Fadley, D. A. Shirley, A. J. Freeman, P. S. Bagus, and J. V. Mallow, "Multiplet splitting of core-electron binding energies in transition-metal ions," *Phys. Rev. Lett.*, vol. 23, no. 24, pp. 1397–1401, 1969, doi: 10.1103/PhysRevLett.23.1397.
- [122] M. Chigane and M. Ishikawa, "Manganese Oxide Thin Film Preparation by Potentiostatic Electrolyses and Electrochromism," *J. Electrochem. Soc.*, vol. 147, no. 6, pp. 2246–2251, 2000, doi: 10.1149/1.1393515.
- [123] A. A. Audi and P. M. A. Sherwood, "Valence-band x-ray photoelectron spectroscopic studies of manganese and its oxides interpreted by cluster and band structure calculations," *Surf. Interface Anal.*, vol. 33, no. 3, pp. 274–282, Mar. 2002, doi: 10.1002/sia.1211.
- [124] M. Toupin, T. Brousse, and D. Bélanger, "Influence of microstructure on the charge storage properties of chemically synthesized manganese dioxide," *Chem. Mater.*, vol. 14, no. 9, pp. 3946–3952, 2002, doi: 10.1021/cm020408q.
- [125] E. S. Ilton, J. E. Post, P. J. Heaney, F. T. Ling, and S. N. Kerisit, "XPS determination of Mn oxidation states in Mn (hydr)oxides," *Appl. Surf. Sci.*, vol. 366, pp. 475–485, 2016, doi: 10.1016/j.apsusc.2015.12.159.
- [126] H. A. Le, S. Chin, E. Park, L. T. Linh, G. N. Bae, and J. Jurng, "Chemical vapor synthesis and characterization of manganese oxides," *Chem. Vap. Depos.*, vol. 17, no. 7–9, pp. 228–234, Sep. 2011, doi: 10.1002/cvde.201106914.
- [127] M. Ritala, J. Niinisto, S. Krumdieck, P. Chalker, H. Aspinall, M. E. Pemble, W. L. Gladfelter, *et al.*, *Chemical Vapour Deposition*. The Royal Society of Chemistry, 2009.
- [128] J.-O. Carlsson and P. M. Martin, "Chemical Vapor Deposition," in *Handbook of Deposition Technologies for Films and Coatings*, 3rd ed., Elsevier, 2010, pp. 314–363.
- [129] Y. Xu and X.-T. Yan, *Chemical Vapor Deposition - An Integrated Engineering Design for Advanced Materials*. Springer, 2010.
- [130] M. Konuma, *Film Deposition by Plasma Techniques*. Heidelberg: Springer Berlin Heidelberg, 1992.
- [131] L. M. Fillman and S. C. Tang, "Thermal decomposition of metal carbonyls: A thermogravimetry-mass spectrometry study," *Thermochim. Acta*, vol. 75, no. 1–2, pp. 71–84, 1984, doi: 10.1016/0040-6031(84)85008-X.
- [132] V. Di Castro and G. Polzonetti, "A photoemission study of the Cu/MnO interface," *Chem. Phys. Lett.*, vol. 139, no. 2, pp. 215–218, 1987, doi: 10.1016/0009-2614(87)80181-1.
- [133] V. Di Castro and G. Polzonetti, "XPS study of MnO oxidation," *J. Electron Spectros. Relat. Phenomena*, vol. 48, no. 1, pp. 117–123, Jan. 1989, doi: 10.1016/0368-2048(89)80009-X.
- [134] D. A. Shirley, "High-Resolution X-Ray Photoemission Spectrum of the Valence Bands of Gold," *Phys. Rev. B*, vol. 5, no. 12, pp. 4709–4714, 1972, doi: 10.1103/PhysRevB.5.4709.
- [135] N. Weidler, S. Paulus, J. Schuch, J. Klett, S. Hoch, P. Stenner, A. Maljusch, *et al.*, "CoOx thin film deposited by CVD as efficient water oxidation catalyst: Change of oxidation

- state in XPS and its correlation to electrochemical activity,” *Phys. Chem. Chem. Phys.*, vol. 18, no. 16, pp. 10708–10718, 2016, doi: 10.1039/c5cp05691h.
- [136] N. Weidler, J. Schuch, F. Knaus, P. Stenner, S. Hoch, A. Maljusch, R. Schäfer, *et al.*, “X-ray Photoelectron Spectroscopic Investigation of Plasma-Enhanced Chemical Vapor Deposited NiOx, NiOx(OH)y, and CoNiOx(OH)y: Influence of the Chemical Composition on the Catalytic Activity for the Oxygen Evolution Reaction,” *J. Phys. Chem. C*, vol. 121, no. 12, pp. 6455–6463, 2017, doi: 10.1021/acs.jpcc.6b12652.
- [137] H. E. Zittel and F. J. Miller, “A Glassy-Carbon Electrode for Voltammetry,” *Anal. Chem.*, vol. 37, no. 2, pp. 200–203, 1965, doi: 10.1021/ac60221a006.
- [138] W. E. Van der Linden and J. W. Dieker, “Glassy carbon as electrode material in electroanalytical chemistry,” *Anal. Chim. Acta*, vol. 119, no. 1, pp. 1–24, 1980, doi: 10.1016/S0003-2670(00)00025-8.
- [139] J. D. Benck, B. A. Pinaud, Y. Gorlin, and T. F. Jaramillo, “Substrate Selection for Fundamental Studies of Electrocatalysts and Photoelectrodes: Inert Potential Windows in Acidic, Neutral, and Basic Electrolyte,” *PLoS One*, vol. 9, no. 10, p. e107942, Oct. 2014, doi: 10.1371/journal.pone.0107942.
- [140] V. G. Bhide and R. H. Dani, “Electrical conductivity in oxides of manganese and related compounds,” *Physica*, vol. 27, no. 9, pp. 821–826, Sep. 1961, doi: 10.1016/0031-8914(61)90079-9.
- [141] F. Hong, B. Yue, N. Hirao, Z. Liu, and B. Chen, “Significant improvement in Mn2O3 transition metal oxide electrical conductivity via high pressure,” *Sci. Rep.*, vol. 7, no. March, pp. 1–7, 2017, doi: 10.1038/srep44078.
- [142] P. Connor, “Manganoxide als Katalysatoren für die alkalische Sauerstoffentwicklungsreaktion,” Technische Universität Darmstadt, 2020.
- [143] D. Schmeißer, O. Böhme, A. Yfantis, T. Heller, D. R. Batchelor, I. Lundstrom, and A. L. Spetz, “Dipole moment of nanoparticles at interfaces,” *Phys. Rev. Lett.*, vol. 83, no. 2, pp. 380–383, 1999, doi: 10.1103/PhysRevLett.83.380.
- [144] A. M. Zieschang, J. D. Bocarsly, J. Schuch, C. V. Reichel, B. Kaiser, W. Jaegermann, R. Seshadri, *et al.*, “Magnetic and Electrocatalytic Properties of Nanoscale Cobalt Boride, Co3B,” *Inorg. Chem.*, vol. 58, no. 24, pp. 16609–16617, 2019, doi: 10.1021/acs.inorgchem.9b02617.
- [145] S. Klemenz, J. Schuch, S. Hawel, A. M. Zieschang, B. Kaiser, W. Jaegermann, and B. Albert, “Synthesis of a Highly Efficient Oxygen-Evolution Electrocatalyst by Incorporation of Iron into Nanoscale Cobalt Borides,” *ChemSusChem*, vol. 11, no. 18, pp. 3150–3156, 2018, doi: 10.1002/cssc.201801547.
- [146] J. Schuch, S. Klemenz, P. Schuldt, A.-M. Zieschang, S. Dolique, P. Connor, B. Kaiser, *et al.*, “Efficient Oxygen Evolution Electrocatalyst by Incorporation of Nickel into Nanoscale Dicobalt Boride,” *ChemCatChem*, vol. n/a, no. n/a, Feb. 2021, doi: <https://doi.org/10.1002/cctc.202002030>.
- [147] N. Weidler, “Plasma-enhanced chemical vapor deposition of cobalt-based catalysts for the oxygen evolution reaction,” Technische Universität, Darmstadt, 2017.
- [148] G. Akopov, M. T. Yeung, and R. B. Kaner, “Rediscovering the Crystal Chemistry of Borides,” *Adv. Mater.*, vol. 29, no. 21, p. 1604506, 2017, doi: 10.1002/adma.201604506.
- [149] S. Carenco, D. Portehault, C. Boissière, N. Mézailles, and C. Sanchez, “Nanoscaled metal borides and phosphides: Recent developments and perspectives,” *Chem. Rev.*, vol. 113, no. 10, pp. 7981–8065, Oct. 2013, doi: 10.1021/cr400020d.
- [150] C. C. Wang, S. A. Akbar, W. Chen, and V. D. Patton, “Electrical properties of high-temperature oxides, borides, carbides, and nitrides,” *J. Mater. Sci.*, vol. 30, no. 7, pp. 1627–1641, 1995, doi: 10.1007/BF00351591.
- [151] S. Rundqvist, “Crystal Structure of Ni3B and Co3B,” *Acta Chem. Scand.*, vol. 12, pp. 658–662, 1958, doi: 10.3891/acta.chem.scand.12-0658.
- [152] E. E. Havinga, H. Damsma, and P. Hokkeling, “Compounds and pseudo-binary alloys

- with the CuAl₂(C16)-type structure I. Preparation and X-ray results,” *J. Less-Common Met.*, vol. 27, no. 2, pp. 169–186, 1972, doi: 10.1016/0022-5088(72)90028-8.
- [153] S. Klemenz, “Nanoskalige 3d-Übergangsmetallboride: Synthese und Charakterisierung,” Technische Universität, Darmstadt, 2017.
- [154] C. Kapfenberger, B. Albert, R. Pöttgen, and H. Huppertz, “Structure refinements of iron borides Fe₂B and FeB,” *Zeitschrift für Krist.*, vol. 221, no. 5–7, pp. 477–481, Jan. 2006, doi: 10.1524/zkri.2006.221.5-7.477.
- [155] A. Iga, “Magnetocrystalline Anisotropy in (Fe_{1-x}Co_x)₂B System,” *Jpn. J. Appl. Phys.*, vol. 9, no. 4, pp. 415–416, Apr. 1970, doi: 10.1143/JJAP.9.415.
- [156] T. Osaka, H. Ishibashi, T. Endo, and T. Yoshida, “Oxygen Evolution Reaction on Transition Metal Borides,” *Electrochim. Acta*, vol. 26, pp. 339–343, 1980.
- [157] T. Osaka, Y. Iwase, H. Kitayama, and T. Ichino, “Oxygen Evolution Reaction on Composite Cobalt Borides,” *Chem. Soc. Japan*, vol. 56, no. 7, pp. 2106–2111, 1983.
- [158] I. E. L. Stephens, A. S. Bondarenko, F. J. Perez-Alonso, F. Calle-Vallejo, L. Bech, T. P. Johansson, A. K. Jepsen, *et al.*, “Tuning the activity of Pt(111) for oxygen electroreduction by subsurface alloying,” *J. Am. Chem. Soc.*, vol. 133, no. 14, pp. 5485–5491, 2011, doi: 10.1021/ja111690g.
- [159] M. W. Kanan and D. G. Nocera, “In situ formation of an oxygen-evolving catalyst in neutral water containing phosphate and Co²⁺,” *Science (80-)*, vol. 321, no. 5892, pp. 1072–1075, 2008, doi: 10.1126/science.1162018.
- [160] L. A. Stern, L. Feng, F. Song, and X. Hu, “Ni₂P as a Janus catalyst for water splitting: The oxygen evolution activity of Ni₂P nanoparticles,” *Energy Environ. Sci.*, vol. 8, no. 8, pp. 2347–2351, 2015, doi: 10.1039/c5ee01155h.
- [161] E. J. Popczun, J. R. McKone, C. G. Read, A. J. Baciocchi, A. M. Wiltrout, N. S. Lewis, and R. E. Schaak, “Nanostructured nickel phosphide as an electrocatalyst for the hydrogen evolution reaction,” *J. Am. Chem. Soc.*, vol. 135, no. 25, pp. 9267–9270, 2013, doi: 10.1021/ja403440e.
- [162] J. Tian, Q. Liu, A. M. Asiri, and X. Sun, “Self-supported nanoporous cobalt phosphide nanowire arrays: An efficient 3D hydrogen-evolving cathode over the wide range of pH 0–14,” *J. Am. Chem. Soc.*, vol. 136, no. 21, pp. 7587–7590, 2014, doi: 10.1021/ja503372r.
- [163] M. Dincă, Y. Surendranath, and D. G. Nocera, “Nickel-borate oxygen-evolving catalyst that functions under benign conditions,” *Proc. Natl. Acad. Sci. U. S. A.*, vol. 107, no. 23, pp. 10337–10341, 2010, doi: 10.1073/pnas.1001859107.
- [164] Y. Surendranath, M. Dincă, and D. G. Nocera, “Electrolyte-dependent electrosynthesis and activity of cobalt-based water oxidation catalysts,” *J. Am. Chem. Soc.*, vol. 131, no. 7, pp. 2615–2620, 2009, doi: 10.1021/ja807769r.
- [165] J. Masa, P. Weide, D. Peeters, I. Sinev, W. Xia, Z. Sun, C. Somsen, *et al.*, “Amorphous Cobalt Boride (Co₂B) as a Highly Efficient Nonprecious Catalyst for Electrochemical Water Splitting: Oxygen and Hydrogen Evolution,” *Adv. Energy Mater.*, vol. 6, no. 12, pp. 1–10, 2016, doi: 10.1002/aenm.201600980.
- [166] X. Ma, J. Wen, S. Zhang, H. Yuan, K. Li, F. Yan, X. Zhang, *et al.*, “Crystal CoxB (x = 1–3) Synthesized by a Ball-Milling Method as High-Performance Electrocatalysts for the Oxygen Evolution Reaction,” *ACS Sustain. Chem. Eng.*, vol. 5, no. 11, pp. 10266–10274, 2017, doi: 10.1021/acssuschemeng.7b02281.
- [167] P. Zhang, M. Wang, Y. Yang, T. Yao, H. Han, and L. Sun, “Electroless plated Ni-B_x films as highly active electrocatalysts for hydrogen production from water over a wide pH range,” *Nano Energy*, vol. 19, pp. 98–107, 2016, doi: 10.1016/j.nanoen.2015.11.020.
- [168] M. Zeng, H. Wang, C. Zhao, J. Wei, K. Qi, W. Wang, and X. Bai, “Nanostructured Amorphous Nickel Boride for High-Efficiency Electrocatalytic Hydrogen Evolution over a Broad pH Range,” *ChemCatChem*, vol. 8, no. 4, pp. 708–712, 2016, doi:

- 10.1002/cctc.201501221.
- [169] H. Li, P. Wen, Q. Li, C. Dun, J. Xing, C. Lu, S. Adhikari, *et al.*, “Earth-Abundant Iron Diboride (FeB₂) Nanoparticles as Highly Active Bifunctional Electrocatalysts for Overall Water Splitting,” *Adv. Energy Mater.*, vol. 7, no. 17, pp. 1–12, 2017, doi: 10.1002/aenm.201700513.
- [170] S. Gupta, N. Patel, R. Fernandes, R. Kadrekar, A. Dashora, A. K. Yadav, D. Bhattacharyya, *et al.*, “Co-Ni-B nanocatalyst for efficient hydrogen evolution reaction in wide pH range,” *Appl. Catal. B Environ.*, vol. 192, pp. 126–133, 2016, doi: 10.1016/j.apcatb.2016.03.032.
- [171] H. Chen, S. Ouyang, M. Zhao, Y. Li, and J. Ye, “Synergistic Activity of Co and Fe in Amorphous Cox-Fe-B Catalyst for Efficient Oxygen Evolution Reaction,” *ACS Appl. Mater. Interfaces*, vol. 9, no. 46, pp. 40333–40343, Nov. 2017, doi: 10.1021/acsami.7b13939.
- [172] J. M. V. Nsanzimana, Y. Peng, Y. Y. Xu, L. Thia, C. Wang, B. Y. Xia, and X. Wang, “An Efficient and Earth-Abundant Oxygen-Evolving Electrocatalyst Based on Amorphous Metal Borides,” *Adv. Energy Mater.*, vol. 8, no. 1, pp. 1–7, 2018, doi: 10.1002/aenm.201701475.
- [173] Y. Li, B. Huang, Y. Sun, M. Luo, Y. Yang, Y. Qin, L. Wang, *et al.*, “Multimetal Borides Nanochains as Efficient Electrocatalysts for Overall Water Splitting,” *Small*, vol. 15, no. 1, pp. 1–8, 2019, doi: 10.1002/sml.201804212.
- [174] J. M. V. Nsanzimana, L. Gong, R. Dangol, V. Reddu, V. Jose, B. Y. Xia, Q. Yan, *et al.*, “Tailoring of Metal Boride Morphology via Anion for Efficient Water Oxidation,” *Adv. Energy Mater.*, vol. 9, pp. 1–6, 2019, doi: 10.1002/aenm.201901503.
- [175] J. M. V. Nsanzimana, R. Dangol, V. Reddu, S. Duo, Y. Peng, K. N. Dinh, Z. Huang, *et al.*, “Facile Synthesis of Amorphous Ternary Metal Borides-Reduced Graphene Oxide Hybrid with Superior Oxygen Evolution Activity,” *ACS Appl. Mater. Interfaces*, vol. 11, no. 1, pp. 846–855, 2019, doi: 10.1021/acsami.8b17836.
- [176] N. Xu, G. Cao, Z. Chen, Q. Kang, H. Dai, and P. Wang, “Cobalt nickel boride as an active electrocatalyst for water splitting,” *J. Mater. Chem. A*, vol. 5, no. 24, pp. 12379–12384, 2017, doi: 10.1039/c7ta02644g.
- [177] H. S. Han, Y. R. Hong, J. Woo, S. Mhin, K. M. Kim, J. Kwon, H. Choi, *et al.*, “Electronically Double-Layered Metal Boride Hollow Nanoprism as an Excellent and Robust Water Oxidation Electrocatalysts,” *Adv. Energy Mater.*, vol. 9, no. 13, pp. 1–11, 2019, doi: 10.1002/aenm.201803799.
- [178] M. Pourbaix, *Atlas of electrochemical equilibria in aqueous solutions*, 2nd ed. Brussels: NACE International, 1974.
- [179] E. Peek, T. Akre, and E. Asselin, “Technical and business considerations of cobalt hydrometallurgy,” *Jom*, vol. 61, no. 10, pp. 43–53, 2009, doi: 10.1007/s11837-009-0151-2.
- [180] W. K. Behl and J. E. Toni, “Anodic oxidation of cobalt in potassium hydroxide electrolytes,” *J. Electroanal. Chem.*, vol. 31, no. 1, pp. 63–75, 1971, doi: 10.1016/S0022-0728(71)80043-8.
- [181] P. Benson, G. W. D. Briggs, and W. F. K. Wynne-Jones, “The cobalt hydroxide electrode-I. Structure and phase transitions of the hydroxides,” *Electrochim. Acta*, vol. 9, no. 3, pp. 275–280, 1964, doi: 10.1016/0013-4686(64)80016-5.
- [182] M. Hamdani, R. N. Singh, and P. Chartier, “Co₃O₄ and co-based spinel oxides bifunctional oxygen electrodes,” *Int. J. Electrochem. Sci.*, vol. 5, no. 4, pp. 556–577, 2010.
- [183] L. D. Burke, M. E. Lyons, and O. J. Murphy, “Formation of hydrous oxide films on cobalt under potential cycling conditions,” *J. Electroanal. Chem.*, vol. 132, no. C, pp. 247–261, 1982, doi: 10.1016/0022-0728(82)85022-5.
- [184] H. G. Meier, J. R. Vilche, and A. J. Arvía, “The electrochemical behaviour of cobalt in alkaline solutions part II. The potentiodynamic response of Co(OH)₂ electrodes,” *J. Electroanal. Chem.*, vol. 138, no. 2, pp. 367–379, 1982, doi: 10.1016/0022-0728(82)85088-2.

- [185] T. C. Liu, W. G. Pell, and B. E. Conway, "Stages in the development of thick cobalt oxide films exhibiting reversible redox behavior and pseudocapacitance," *Electrochim. Acta*, vol. 44, no. 17, pp. 2829–2842, 1999, doi: 10.1016/S0013-4686(99)00002-X.
- [186] R. L. Doyle, I. J. Godwin, M. P. Brandon, and M. E. G. G. Lyons, "Redox and electrochemical water splitting catalytic properties of hydrated metal oxide modified electrodes," *Phys. Chem. Chem. Phys.*, vol. 15, no. 33, pp. 13737–13783, 2013, doi: 10.1039/c3cp51213d.
- [187] R. L. Doyle and M. E. G. Lyons, "An electrochemical impedance study of the oxygen evolution reaction at hydrous iron oxide in base," *Phys. Chem. Chem. Phys.*, vol. 15, no. 14, pp. 5224–5237, 2013, doi: 10.1039/c3cp43464h.
- [188] M. E. G. Lyons and M. P. Brandon, "Redox switching and oxygen evolution electrocatalysis in polymeric iron oxyhydroxide films," *Phys. Chem. Chem. Phys.*, vol. 11, no. 13, pp. 2203–2217, 2009, doi: 10.1039/b815338h.
- [189] L. D. Burke, J. K. Mulcahy, and D. P. Whelan, "Preparation of an oxidized iridium electrode and the variation of its potential with pH," *J. Electroanal. Chem. Interfacial Electrochem.*, vol. 163, no. 1, pp. 117–128, 1984, doi: [https://doi.org/10.1016/S0022-0728\(84\)80045-5](https://doi.org/10.1016/S0022-0728(84)80045-5).
- [190] M. E. G. G. Lyons and M. P. Brandon, "A comparative study of the oxygen evolution reaction on oxidised nickel, cobalt and iron electrodes in base," *J. Electroanal. Chem.*, vol. 641, no. 1–2, pp. 119–130, Mar. 2010, doi: 10.1016/j.jelechem.2009.11.024.
- [191] L. F. Huang, M. J. Hutchison, R. J. Santucci, J. R. Scully, and J. M. Rondinelli, "Improved Electrochemical Phase Diagrams from Theory and Experiment: The Ni-Water System and Its Complex Compounds," *J. Phys. Chem. C*, vol. 121, no. 18, pp. 9782–9789, 2017, doi: 10.1021/acs.jpcc.7b02771.
- [192] A. Seghioeur, J. Chevalet, A. Barhoun, and F. Lantelme, "Electrochemical oxidation of nickel in alkaline solutions: A voltammetric study and modelling," *J. Electroanal. Chem.*, vol. 442, no. 1–2, pp. 113–123, 1998, doi: 10.1016/S0022-0728(97)00498-1.
- [193] M. E. G. Lyons and M. P. Brandon, "The Oxygen Evolution Reaction on Passive Oxide Covered Transition Metal Electrodes in Aqueous Alkaline Solution. Part 1-Nickel," *Int. J. Electrochem. Sci.*, vol. 3, no. 12, pp. 1386–1424, 2008.
- [194] H. Bode, K. Dehmelt, and J. Witte, "Zur Kenntnis der Nickelhydroxidelektrode - I. Ueber das Nickel (II)-Hydroxidehydrat," *Electrochim. Acta*, vol. 11, no. September 1965, p. 1079, 1966.
- [195] D. S. Hall, D. J. Lockwood, C. Bock, and B. R. MacDougall, "Nickel hydroxides and related materials: A review of their structures, synthesis and properties," *Proc. R. Soc. A Math. Phys. Eng. Sci.*, vol. 471, no. 2174, 2015, doi: 10.1098/rspa.2014.0792.
- [196] J. McBreen, *Handbook of Battery Materials*, Ed. Weinheim: Wiley-VCH, 1999.
- [197] R. Barnard, C. F. Randell, and F. L. Tye, "Studies concerning charged nickel hydroxide electrodes I. Measurement of reversible potentials," *J. Appl. Electrochem.*, vol. 10, no. 1, pp. 109–125, 1980, doi: 10.1007/BF00937345.
- [198] P. W. T. Lu and S. Srinivasan, "Electrochemical-Ellipsometric Studies of Oxide Film Formed on Nickel during Oxygen Evolution," *J. Electrochem. Soc.*, vol. 125, no. 9, pp. 1416–1422, 1978, doi: 10.1149/1.2131689.
- [199] Kinoshita K., "Chapter 2," in *Electrochemical Oxygen Technology*, New York: Wiley-Interscience, 1992, pp. 78–99.
- [200] R. Barnard, C. F. Randell, and F. L. Tye, "Studies concerning charged nickel hydroxide electrodes: Part III. Reversible potentials at low states of charge," *J. Electroanal. Chem. Interfacial Electrochem.*, vol. 119, no. 1, pp. 17–24, 1981, doi: [https://doi.org/10.1016/S0022-0728\(81\)80120-9](https://doi.org/10.1016/S0022-0728(81)80120-9).
- [201] N. S. McIntyre and M. G. Cook, "X-Ray Photoelectron Studies on Some Oxides and Hydroxides of Cobalt, Nickel, and Copper," *Anal. Chem.*, vol. 47, no. 13, pp. 2208–2213,

- 1975, doi: 10.1021/ac60363a034.
- [202] T. J. Chuang, C. R. Brundle, and D. W. Rice, "Interpretation of the x-ray photoemission spectra of cobalt oxides and cobalt oxide surfaces," *Surf. Sci.*, vol. 59, no. 2, pp. 413–429, 1976, doi: 10.1016/0039-6028(76)90026-1.
- [203] S. C. Petitto, E. M. Marsh, G. A. Carson, and M. A. Langell, "Cobalt oxide surface chemistry: The interaction of CoO(1 0 0), Co₃O₄(1 1 0) and Co₃O₄(1 1 1) with oxygen and water," *J. Mol. Catal. A Chem.*, vol. 281, no. 1–2, pp. 49–58, 2008, doi: 10.1016/j.molcata.2007.08.023.
- [204] J. Yang, H. Liu, W. N. Martens, and R. L. Frost, "Synthesis and characterization of Cobalt hydroxide, cobalt oxyhydroxide, and cobalt oxide nanodiscs," *J. Phys. Chem. C*, vol. 114, no. 1, pp. 111–119, 2010, doi: 10.1021/jp908548f.
- [205] G. Mavel, J. Escard, P. Costa, and J. Castaing, "ESCA surface study of metal borides," *Surf. Sci.*, vol. 35, no. C, pp. 109–116, 1973, doi: 10.1016/0039-6028(73)90207-0.
- [206] P. Krishnan, K. L. Hsueh, and S. D. Yim, "Catalysts for the hydrolysis of aqueous borohydride solutions to produce hydrogen for PEM fuel cells," *Appl. Catal. B Environ.*, vol. 77, no. 1–2, pp. 206–214, 2007, doi: 10.1016/j.apcatb.2007.07.024.
- [207] X. Deng and H. Tüysüz, "Cobalt-oxide-based materials as water oxidation catalyst: Recent progress and challenges," *ACS Catal.*, vol. 4, no. 10, pp. 3701–3714, 2014, doi: 10.1021/cs500713d.
- [208] M. A. M. Cartaxo, T. A. S. Ferreira, M. R. Nunes, M. H. Mendonça, M. I. da Silva Pereira, and F. M. Costa, "Studies on Fe-Co spinel electrodes," *Solid State Sci.*, vol. 9, no. 8, pp. 744–749, 2007, doi: 10.1016/j.solidstatesciences.2007.05.001.
- [209] B. P. Payne, M. C. Biesinger, and N. S. McIntyre, "Use of oxygen/nickel ratios in the XPS characterisation of oxide phases on nickel metal and nickel alloy surfaces," *J. Electron Spectros. Relat. Phenomena*, vol. 185, no. 5–7, pp. 159–166, 2012, doi: <http://dx.doi.org/10.1016/j.elspec.2012.06.008>.
- [210] W. Temesghen and P. M. Sherwood, "Analytical utility of valence band X-ray photoelectron spectroscopy of iron and its oxides, with spectral interpretation by cluster and band structure calculations," *Anal Bioanal Chem*, vol. 373, no. 7, pp. 601–608, 2002, doi: 10.1007/s00216-002-1362-3.
- [211] D. Brion, "Etude par spectroscopie de photoelectrons de la degradation superficielle de FeS₂, CuFeS₂, ZnS et PbS a l'air et dans l'eau," *Appl. Surf. Sci.*, vol. 5, no. 2, pp. 133–152, 1980, doi: 10.1016/0378-5963(80)90148-8.
- [212] D. J. Joyner, O. Johnson, and D. M. Hercules, "A Study of the Iron Borides. 1. Electron Spectroscopy," *J. Am. Chem. Soc.*, vol. 102, no. 6, pp. 1910–1917, 1980, doi: 10.1021/ja00526a025.
- [213] P. C. J. Graat and M. A. J. Somers, "Simultaneous determination of composition and thickness of thin iron-oxide films from XPS Fe 2p spectra," *Appl. Surf. Sci.*, vol. 100, pp. 36–40, 1996, doi: 10.1016/0169-4332(96)00252-8.
- [214] A. P. Grosvenor, B. A. Kobe, M. C. Biesinger, and N. S. McIntyre, "Investigation of multiplet splitting of Fe 2p XPS spectra and bonding in iron compounds," *Surf. Interface Anal.*, vol. 36, no. 12, pp. 1564–1574, 2004, doi: 10.1002/sia.1984.
- [215] S. A. Chambers, Y. J. Kim, and Y. Gao, "Fe 2 p Core-Level Spectra for Pure, Epitaxial α -Fe₂O₃ (0001), γ -Fe₂O₃ (001), and Fe₃O₄ (001) ," *Surf. Sci. Spectra*, vol. 5, no. 3, pp. 219–228, 1998, doi: 10.1116/1.1247873.
- [216] L. Martinez, D. Leinen, F. Martín, M. Gabas, J. R. Ramos-Barrado, E. Quagliata, and E. A. Dalchiele, "Electrochemical growth of diverse iron oxide (Fe₃O₄, α -FeOOH, and γ -FeOOH) thin films by electrodeposition potential tuning," *J. Electrochem. Soc.*, vol. 154, no. 3, pp. 126–133, 2007, doi: 10.1149/1.2424416.
- [217] N. S. McIntyre and D. G. Zetaruk, "X-ray Photoelectron Spectroscopic Studies of Iron Oxides," *Anal. Chem.*, vol. 49, no. 11, pp. 1521–1529, 1977, doi: 10.1021/ac50019a016.
- [218] T. Yamashita and P. Hayes, "Analysis of XPS spectra of Fe²⁺ and Fe³⁺ ions in oxide

- materials,” *Appl. Surf. Sci.*, vol. 254, no. 8, pp. 2441–2449, 2008, doi: 10.1016/j.apsusc.2007.09.063.
- [219] S. Hüfner, *Photoelectron Spectroscopy*, vol. 33. Berlin, Heidelberg: Springer Berlin Heidelberg, 2003.
- [220] J. A. Schreifels, P. C. Maybury, and W. E. Swartz, “X-Ray photoelectron spectroscopy of nickel boride catalysts: Correlation of surface states with reaction products in the hydrogenation of acrylonitrile,” *J. Catal.*, vol. 65, no. 1, pp. 195–206, 1980, doi: [https://doi.org/10.1016/0021-9517\(80\)90294-8](https://doi.org/10.1016/0021-9517(80)90294-8).
- [221] J. Legrand, A. Taleb, S. Gota, M. J. Guittet, and C. Petit, “Synthesis and XPS characterization of nickel boride nanoparticles,” *Langmuir*, vol. 18, no. 10, pp. 4131–4137, 2002, doi: 10.1021/la0117247.
- [222] J. Matienzo, L. I. Yin, S. O. Grim, and W. E. Swartz, “X-ray photoelectron spectroscopy of nickel compounds,” *Inorg. Chem.*, vol. 12, no. 12, pp. 2762–2769, 1973, doi: 10.1021/ic50130a005.
- [223] G. C. Allen, S. J. Harris, J. A. Jutson, and J. M. Dyke, “A study of a number of mixed transition metal oxide spinels using X-ray photoelectron spectroscopy,” *Appl. Surf. Sci.*, vol. 37, no. 1, pp. 111–134, 1989, doi: 10.1016/0169-4332(89)90977-X.
- [224] M. C. Biesinger, B. P. Payne, L. W. M. Lau, A. Gerson, and R. S. C. Smart, “X-ray photoelectron spectroscopic chemical state Quantification of mixed nickel metal, oxide and hydroxide systems,” *Surf. Interface Anal.*, vol. 41, no. 4, pp. 324–332, 2009, doi: 10.1002/sia.3026.
- [225] G. N. Glavee, K. J. Klabunde, C. M. Sorensen, and G. C. Hadjapanayis, “Borohydride Reductions of Metal Ions. A New Understanding of the Chemistry Leading to Nanoscale Particles of Metals, Borides, and Metal Borates,” *Langmuir*, vol. 8, no. 3, pp. 771–773, 1992, doi: 10.1021/la00039a008.
- [226] G. N. Glavee, K. J. Klabunde, C. M. Sorensen, and G. C. Hadjipanayis, “Borohydride Reduction of Cobalt Ions in Water. Chemistry Leading to Nanoscale Metal, Boride, or Borate Particles,” *Langmuir*, vol. 9, no. 1, pp. 162–169, 1993, doi: 10.1021/la00025a034.
- [227] G. N. Glavee, K. J. Klabunde, C. M. Sorensen, and G. C. Hadjipanayis, “Chemistry of Borohydride Reduction of Iron(II) and Iron(III) Ions in Aqueous and Nonaqueous Media. Formation of Nanoscale Fe, FeB, and Fe₂B Powders,” *Inorg. Chem.*, vol. 34, no. 1, pp. 28–35, Jan. 1995, doi: 10.1021/ic00105a009.
- [228] C. Kapfenberger, K. Hofmann, and B. Albert, “Room-temperature synthesis of metal borides,” *Solid State Sci.*, vol. 5, no. 6, pp. 925–930, 2003, doi: 10.1016/S1293-2558(03)00117-1.
- [229] S. Klemenz, “Nanoskalige 3d-Übergangsmetallboride: Synthese und Charakterisierung,” Technische Universität, Darmstadt, 2017.
- [230] A.-M. C. Zieschang, “Nanopartikuläre 3d-Übergangsmetallnitride aus flüssigem Ammoniak,” Technische Universität, Darmstadt, 2019.
- [231] S. Hawel, “Investigation of Cobalt Boride (Co₂B) as Catalyst for Electrochemical Water Splitting (unpublished),” Technische Universität, Darmstadt, 2017.
- [232] H. L. S. Salerno, F. L. Beyer, and Y. A. Elabd, “Anion exchange membranes derived from nafion precursor for the alkaline fuel cell,” *J. Polym. Sci. Part B Polym. Phys.*, vol. 50, no. 8, pp. 552–562, 2012, doi: 10.1002/polb.23033.
- [233] K. A. Mauritz and R. B. Moore, “State of understanding of Nafion,” *Chem. Rev.*, vol. 104, no. 10, pp. 4535–4585, 2004, doi: 10.1021/cr0207123.
- [234] C. Chen, G. Levitin, D. W. Hess, and T. F. Fuller, “XPS investigation of Nafion® membrane degradation,” *J. Power Sources*, vol. 169, no. 2, pp. 288–295, 2007, doi: 10.1016/j.jpowsour.2007.03.037.
- [235] C. Chen and T. F. Fuller, “XPS analysis of polymer membrane degradation in PEMFCs,” *J. Electrochem. Soc.*, vol. 156, no. 10, pp. 1218–1224, 2009, doi: 10.1149/1.3187731.

- [236] M. Schulze, M. Lorenz, N. Wagner, and E. Gülzow, "XPS analysis of the degradation of Nafion," *Fresenius. J. Anal. Chem.*, vol. 365, no. 1–3, pp. 106–113, 1999, doi: 10.1007/s002160051454.
- [237] J. Huslage, T. Rager, B. Schnyder, and A. Tsukada, "Radiation-grafted membrane/electrode assemblies with improved interface," *Electrochim. Acta*, vol. 48, no. 3, pp. 247–254, 2002, doi: 10.1016/S0013-4686(02)00621-7.
- [238] M. del Valle Martínez de Yuso, A. Arango-Díaz, S. Bijani, V. Romero, J. Benavente, and E. Rodríguez-Castellón, "Chemical Surface, Thermal and Electrical Characterization of Nafion Membranes Doped with IL-Cations," *Appl. Sci.*, vol. 4, no. 2, pp. 195–206, 2014, doi: 10.3390/app4020195.
- [239] A. K. Friedman, W. Shi, Y. Losovyj, A. R. Siedle, and L. A. Baker, "Mapping Microscale Chemical Heterogeneity in Nafion Membranes with X-ray Photoelectron Spectroscopy," *J. Electrochem. Soc.*, vol. 165, no. 11, pp. H733–H741, 2018, doi: 10.1149/2.0771811jes.
- [240] V. Parry, G. Berthomé, J. C. Joud, O. Lemaire, and A. A. Franco, "XPS investigations of the proton exchange membrane fuel cell active layers aging: Characterization of the mitigating role of an anodic CO contamination on cathode degradation," *J. Power Sources*, vol. 196, no. 5, pp. 2530–2538, 2011, doi: 10.1016/j.jpowsour.2010.11.027.
- [241] W. Qiu, R. Müller, E. Voroshazi, B. Conings, R. Carleer, H. G. Boyen, M. Turbiez, *et al.*, "Nafion-modified MoO_x as effective room-temperature hole injection layer for stable, high-performance inverted organic solar cells," *ACS Appl. Mater. Interfaces*, vol. 7, no. 6, pp. 3581–3589, 2015, doi: 10.1021/am507459t.
- [242] A.-M. C. Zieschang, "Nanopartikeläre 3d-Übergangsmetallnitride aus flüssigem Ammoniak," Technische Universität, Darmstadt, 2019.
- [243] Y. Wang, J. Fan, and M. Trenary, "Surface Chemistry of Boron Oxidation. 1. Reactions of Oxygen and Water with Boron Films Grown on Ta(110)," *Chem. Mater.*, vol. 5, no. 2, pp. 192–198, 1993, doi: 10.1021/cm00026a007.
- [244] Y. Wang and M. Trenary, "Surface chemistry of boron oxidation. 2. The reactions of boron oxides B₂O₂ and B₂O₃ with boron films grown on tantalum(110)," *Chem. Mater.*, vol. 5, no. 2, pp. 199–205, 1993, doi: 10.1021/cm00026a008.
- [245] G. P. Shveikin and A. L. Ivanovskii, "The chemical bonding and electronic properties of metal borides," *Russ. Chem. Rev.*, vol. 63, no. 9, pp. 711–734, 1994, doi: 10.1070/RC1994v063n09ABEH000114.
- [246] C. W. Ong, H. Huang, B. Zheng, R. W. M. Kwok, Y. Y. Hui, and W. M. Lau, "X-ray photoemission spectroscopy of nonmetallic materials: Electronic structures of boron and B_xO_y," *J. Appl. Phys.*, vol. 95, no. 7, pp. 3527–3534, 2004, doi: 10.1063/1.1651321.
- [247] O. M. Moon, B. C. Kang, S. B. Lee, and J. H. Boo, "Temperature effect on structural properties of boron oxide thin films deposited by MOCVD method," *Thin Solid Films*, vol. 464–465, pp. 164–169, 2004, doi: 10.1016/j.tsf.2004.05.107.
- [248] A. Pilli, J. Jones, V. Lee, N. Chugh, J. Kelber, F. Pasquale, and A. LaVoie, "In situ XPS study of low temperature atomic layer deposition of B₂O₃ films on Si using BCl₃ and H₂O precursors," *J. Vac. Sci. Technol. A*, vol. 36, no. 6, p. 061503, 2018, doi: 10.1116/1.5044396.
- [249] R. Subbaraman, D. Tripkovic, K. C. Chang, D. Strmcnik, A. P. Paulikas, P. Hirunsit, M. Chan, *et al.*, "Trends in activity for the water electrolyser reactions on 3d M(Ni,Co,Fe,Mn) hydr(oxy)oxide catalysts," *Nat. Mater.*, vol. 11, no. 6, pp. 550–557, 2012, doi: 10.1038/nmat3313.
- [250] L. Trotochaud and S. W. Boettcher, "Precise oxygen evolution catalysts: Status and opportunities," *Scr. Mater.*, vol. 74, pp. 25–32, 2014, doi: 10.1016/j.scriptamat.2013.07.019.
- [251] R. P. Šimpraga, "Reversibility and irreversibility in the formation and reduction of oxide film states on Co at ambient and low temperatures," *J. Electroanal. Chem.*, vol. 355, no. 1–2, pp. 79–96, 1993, doi: 10.1016/0022-0728(93)80355-L.

- [252] G. W. Simmons, A. Vertes, M. L. Varsanyi, and H. Leidheiser, "Emission Moessbauer Studies of Anodically Formed CoO₂," *J. Electrochem. Soc.*, vol. 126, no. 2, pp. 187–189, 1979, doi: 10.1149/1.2129003.
- [253] Wei Cho Foo, J. S. Ozcomert, and M. Trenary, "The reaction of B₂O₃ with the β -rhombohedral boron (111) surface," *Surf. Sci.*, vol. 262, no. 1–2, pp. 88–96, 1992, doi: 10.1016/0039-6028(92)90462-F.
- [254] A. Mendoza-Garcia, D. Su, and S. Sun, "Sea urchin-like cobalt-iron phosphide as an active catalyst for oxygen evolution reaction," *Nanoscale*, vol. 8, no. 6, pp. 3244–3247, 2016, doi: 10.1039/c5nr08763e.
- [255] E. McCafferty, J. P. Wightman, E. Mcca, and J. P. Wightman, "Determination of the concentration of surface hydroxyl groups on metal oxide films by a quantitative XPS method," *Surf. Interface Anal.*, vol. 26, no. 8, pp. 549–564, 1998, doi: 10.1002/(SICI)1096-9918(199807)26:8<549::AID-SIA396>3.3.CO;2-H.
- [256] S. Gupta, N. Patel, R. Fernandes, S. Hanchate, A. Miotello, and D. C. Kothari, "Co-Mo-B Nanoparticles as a non-precious and efficient Bifunctional Electrocatalyst for Hydrogen and Oxygen Evolution," *Electrochim. Acta*, vol. 232, pp. 64–71, 2017, doi: 10.1016/j.electacta.2017.02.100.
- [257] S. Yoon, J. Y. Yun, J. H. Lim, and B. Yoo, "Enhanced electrocatalytic properties of electrodeposited amorphous cobalt-nickel hydroxide nanosheets on nickel foam by the formation of nickel nanocones for the oxygen evolution reaction," *J. Alloys Compd.*, vol. 693, pp. 964–969, 2017, doi: 10.1016/j.jallcom.2016.09.247.
- [258] S. Wang, P. He, Z. Xie, L. Jia, M. He, X. Zhang, F. Dong, *et al.*, "Tunable nanocotton-like amorphous ternary Ni-Co-B: A highly efficient catalyst for enhanced oxygen evolution reaction," *Electrochim. Acta*, vol. 296, pp. 644–652, 2019, doi: 10.1016/j.electacta.2018.11.099.
- [259] J. Zhang, X. Li, Y. Liu, Z. Zeng, X. Cheng, Y. Wang, W. Tu, *et al.*, "Bi-metallic boride electrocatalysts with enhanced activity for the oxygen evolution reaction," *Nanoscale*, vol. 10, no. 25, pp. 11997–12002, 2018, doi: 10.1039/c8nr02198h.
- [260] R. S. C. Smart, A. P. Grosvenor, M. C. Biesinger, and N. S. McIntyre, "New interpretations of XPS spectra of nickel metal and oxides," *Surf. Sci.*, vol. 600, no. 9, pp. 1771–1779, 2006, doi: 10.1016/j.susc.2006.01.041.
- [261] D. A. Corrigan, "The Catalysis of the Oxygen Evolution Reaction by Iron Impurities in Thin Film Nickel Oxide Electrodes," *J. Electrochem. Soc.*, vol. 134, no. 2, p. 377, 1987, doi: 10.1149/1.2100463.
- [262] S. Klaus, Y. Cai, M. W. Louie, L. Trotochaud, and A. T. Bell, "Effects of Fe Electrolyte Impurities on Ni(OH)₂/NiOOH Structure and Oxygen Evolution Activity," *J. Phys. Chem. C*, vol. 119, no. 13, pp. 7243–7254, 2015, doi: 10.1021/acs.jpcc.5b00105.
- [263] N. Xu, G. Cao, Z. Chen, Q. Kang, H. Dai, and P. Wang, "Cobalt nickel boride as an active electrocatalyst for water splitting," *J. Mater. Chem. A*, vol. 5, no. 24, pp. 12379–12384, 2017, doi: 10.1039/c7ta02644g.
- [264] J. Masa, C. Andronesco, H. Antoni, I. Sinev, S. Seisel, K. Elumeeva, S. Barwe, *et al.*, "Role of Boron and Phosphorus in Enhanced Electrocatalytic Oxygen Evolution by Nickel Borides and Nickel Phosphides," *ChemElectroChem*, vol. 6, no. 1, pp. 235–240, 2019, doi: 10.1002/celec.201800669.

Part A – Manganese Oxide

XPS reference spectra of manganese compounds

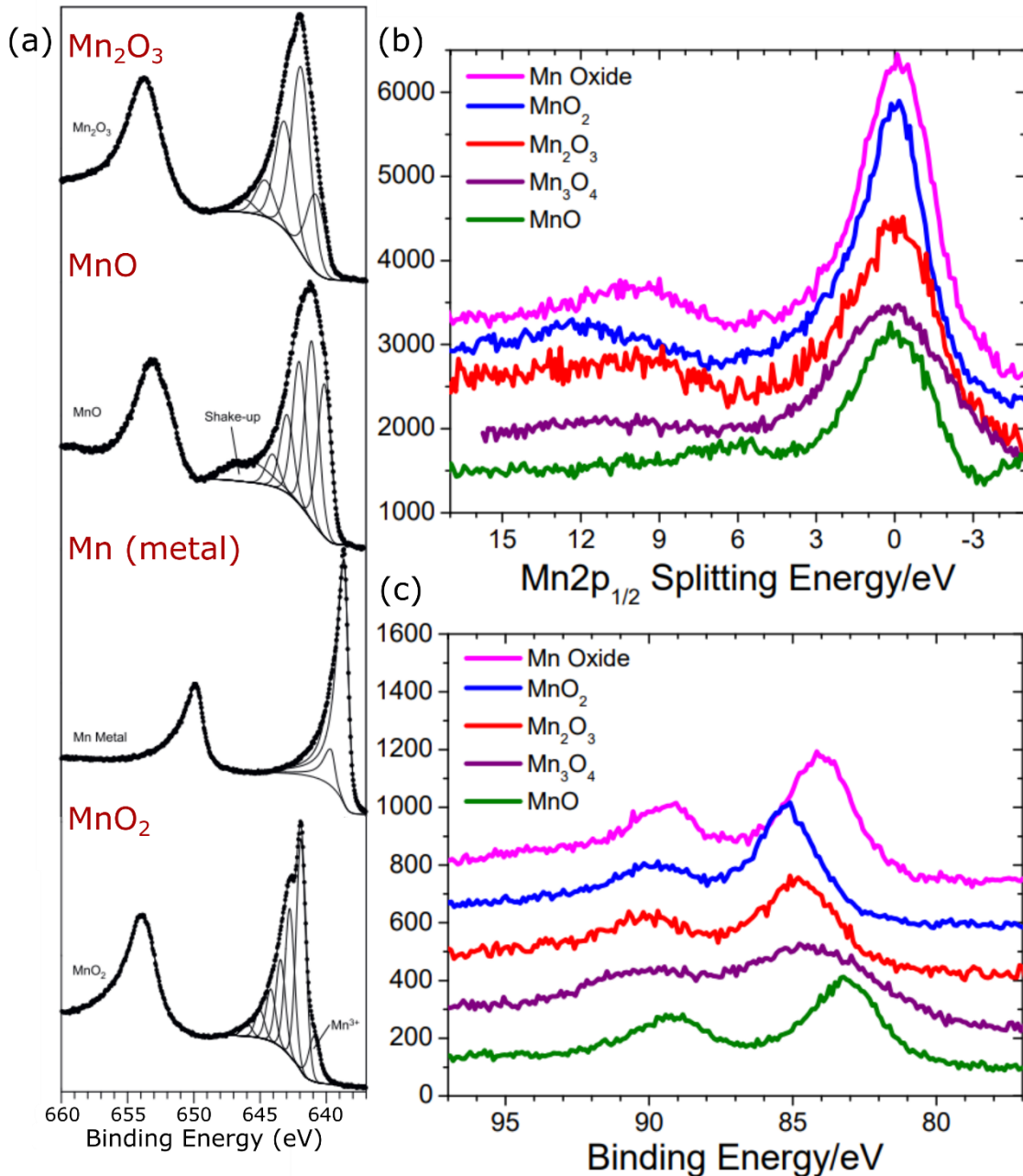


Figure A 1: XP detail spectra of different manganese compounds. In (a) the XP Mn 2p detail spectra are shown adapted and modified with permission from ^[117]. Copyright 2011 Elsevier. In (b) and (c) the Mn 2p_{1/2} and Mn 3s detail spectra for different manganese oxides are shown adapted with permission from ^[120]. Copyright 2010 American Chemical Society.

XPS of substrate preparation steps

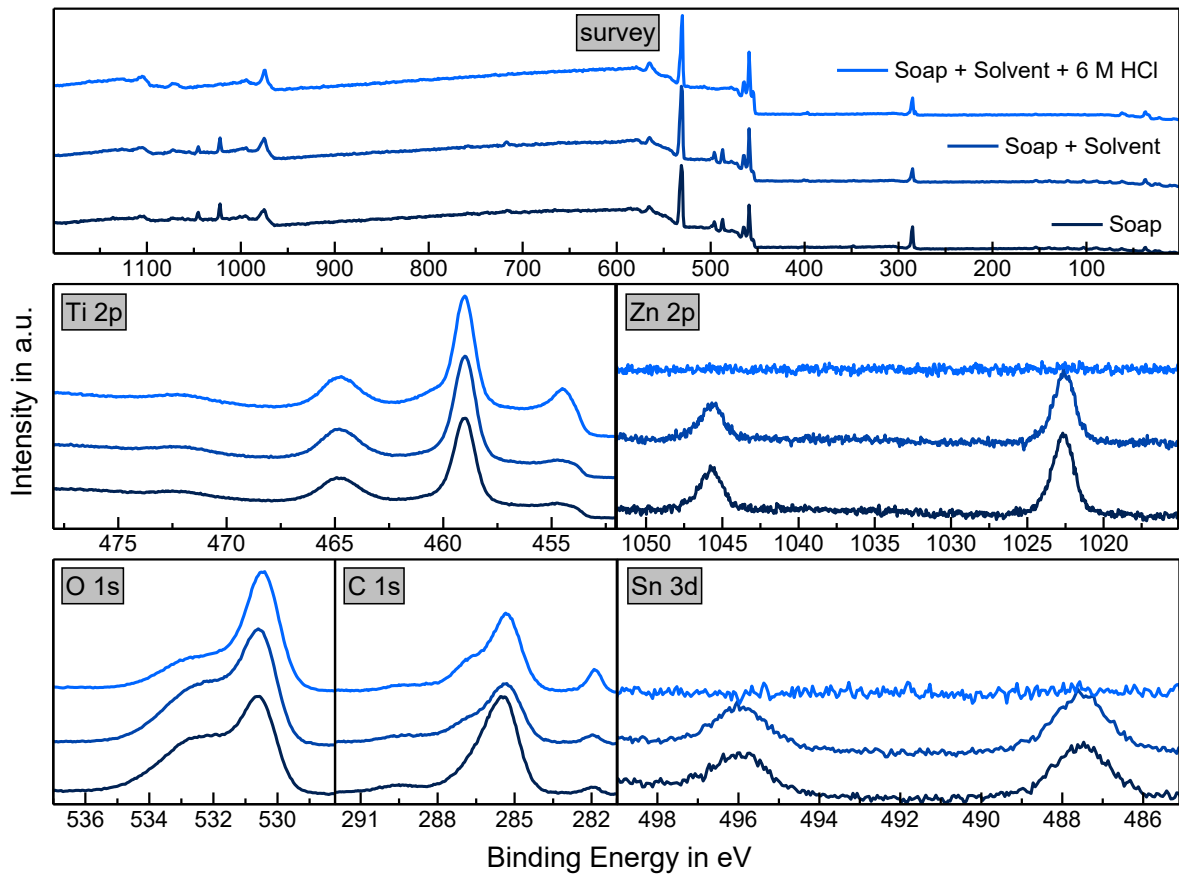


Figure A 2: Substrate preparation of a titanium substrate after different cleaning steps: ① soap, ② soap and solvent, and ③ soap, solvent, and 6 M HCl etching.

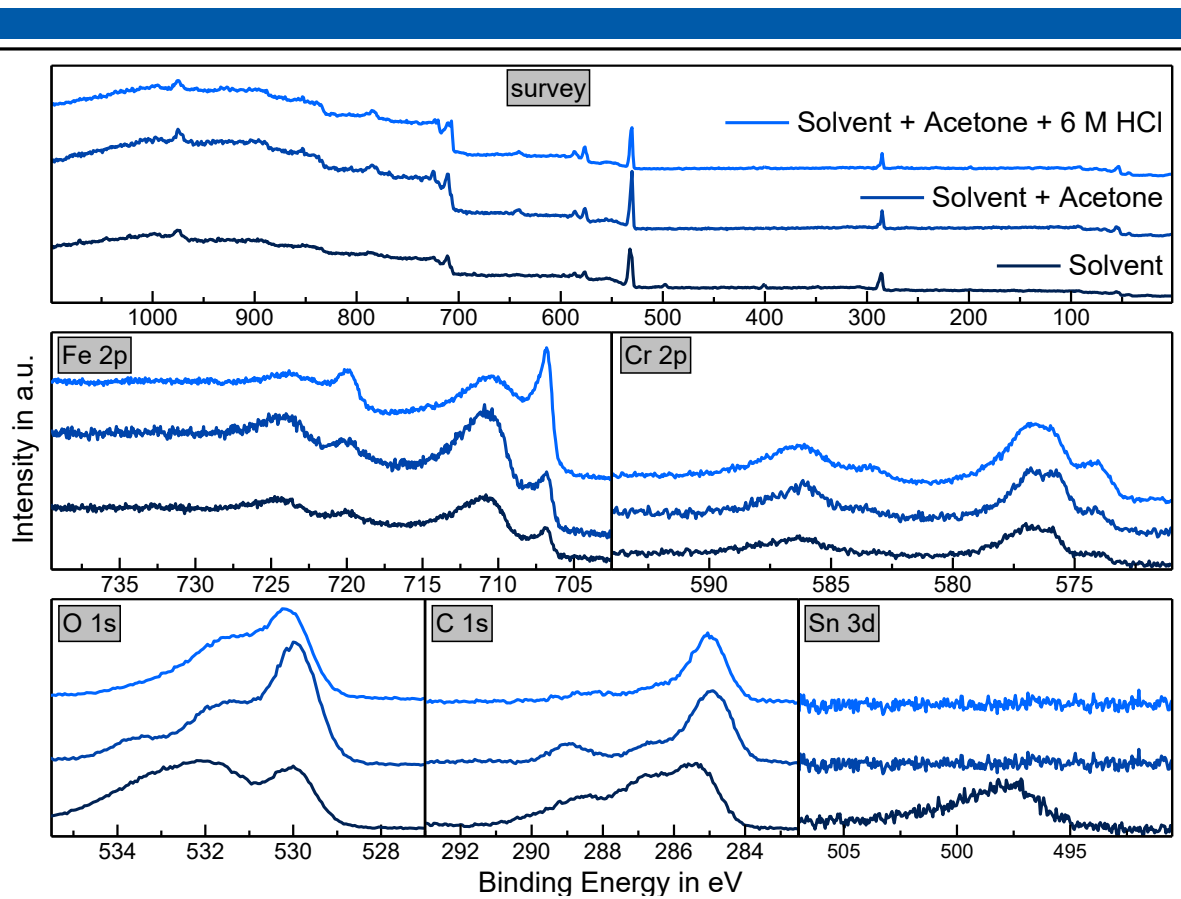


Figure A 3: Substrate preparation of a stainless-steel substrate after different cleaning steps: ① solvent cleaning, ② solvent and additional acetone cleaning, and ③ solvent plus acetone and 6 M HCl etching.

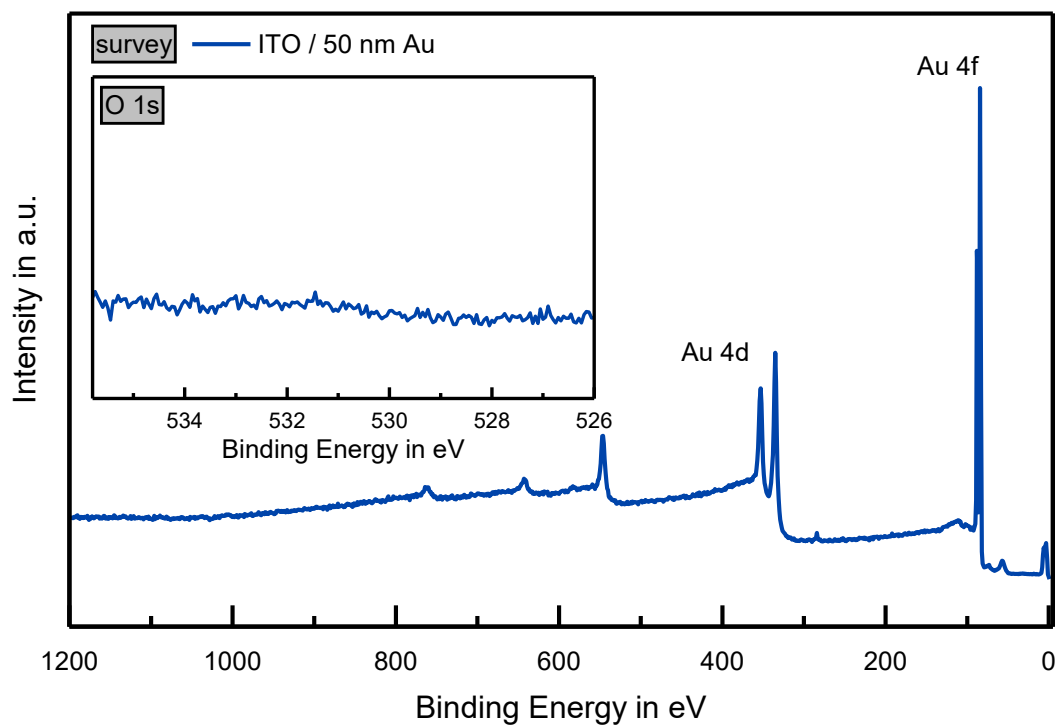


Figure A 4: XP survey spectrum of an indium tin oxide (ITO) sample with an over layer of 50 nm sputtered gold (Au). The O 1s photoemission line is shown in the inset.

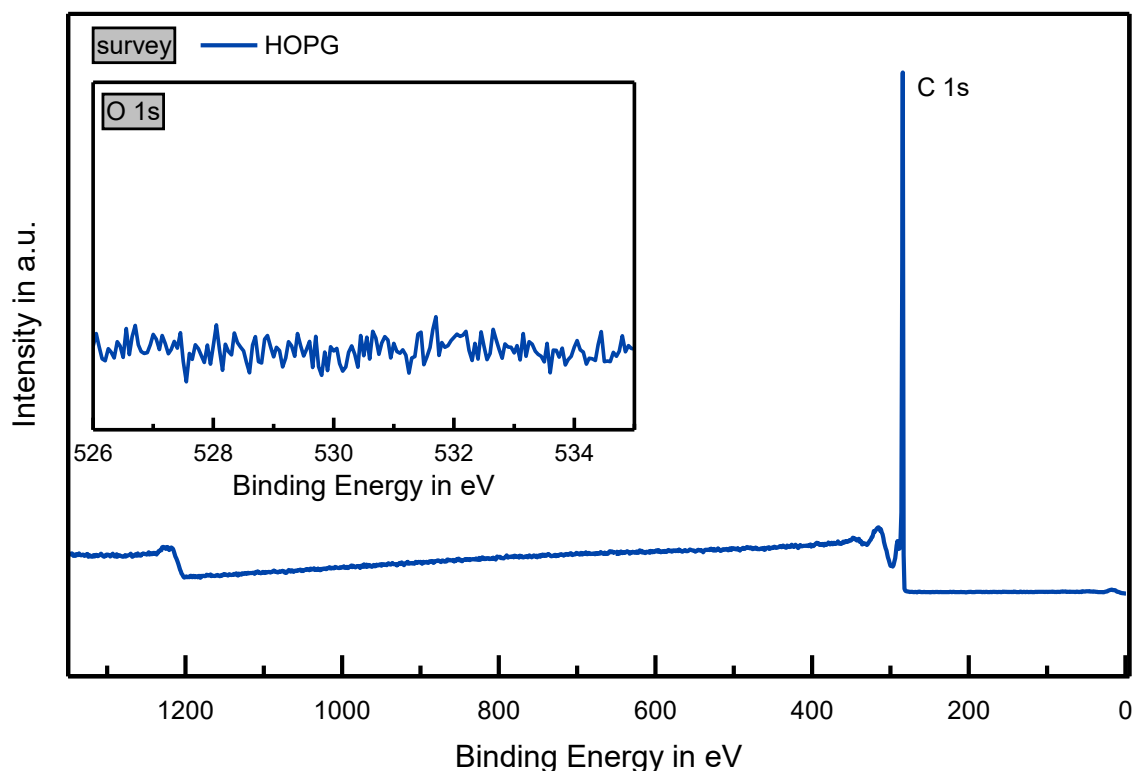


Figure A 5: XP survey spectrum of a highly oriented pyrolytic graphite (HOPG) substrate after detaching one layer with scotch tape (*cf.* Section 3.3.1).

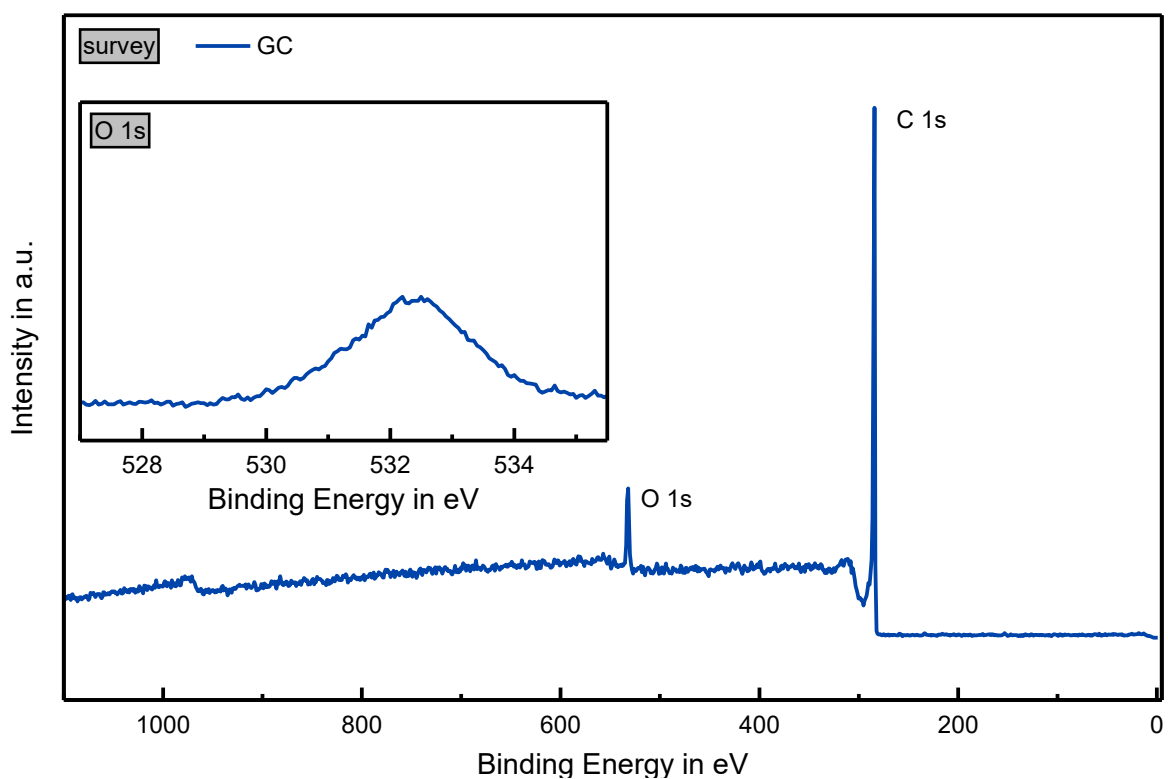


Figure A 6: XP survey spectrum of a glass-like carbon (GC) substrate after the grinding, polishing, and cleaning steps (*cf.* Section 3.3.1).

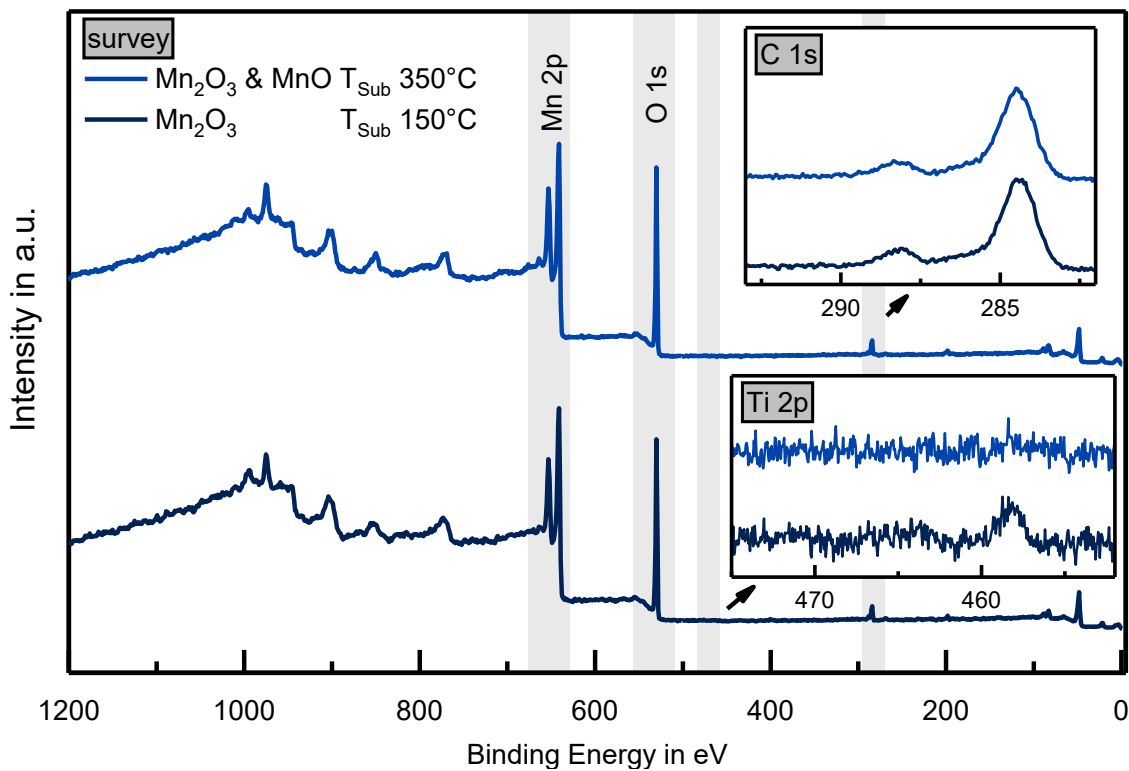


Figure A 7: XPS survey spectra of two manganese oxide phases deposited at a substrate temperature of 150 °C and 350 °C. The XPS C 1s and Ti 2p detail spectra are shown as insets.

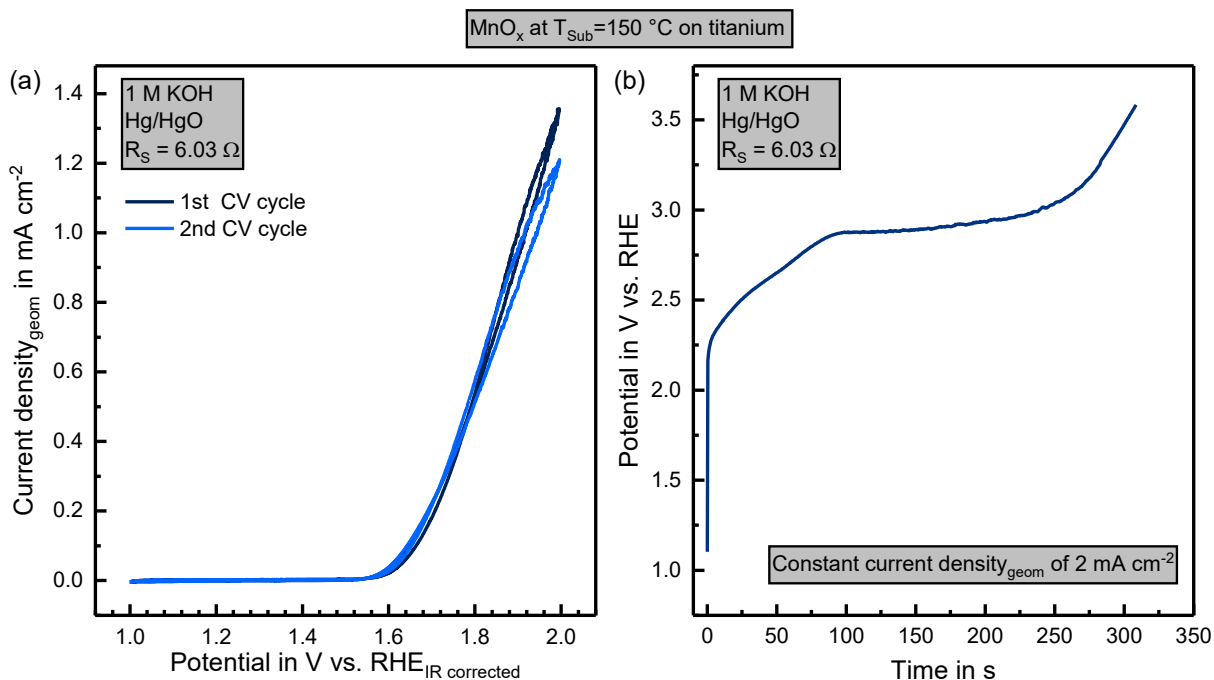


Figure A 8: Electrochemical (EC) investigation of the manganese oxide thin films in 1 M KOH. (a) Cyclic-voltammograms (CV) at a scan rate of 50 mVs⁻¹ after the conditioning step, showing reduced EC performance after the first CV cycle. (b) EC stability measurement of the same sample at a constant geometric current density of 2 mA cm⁻², showing a continuous decrease in performance in the first minute of measurement time.

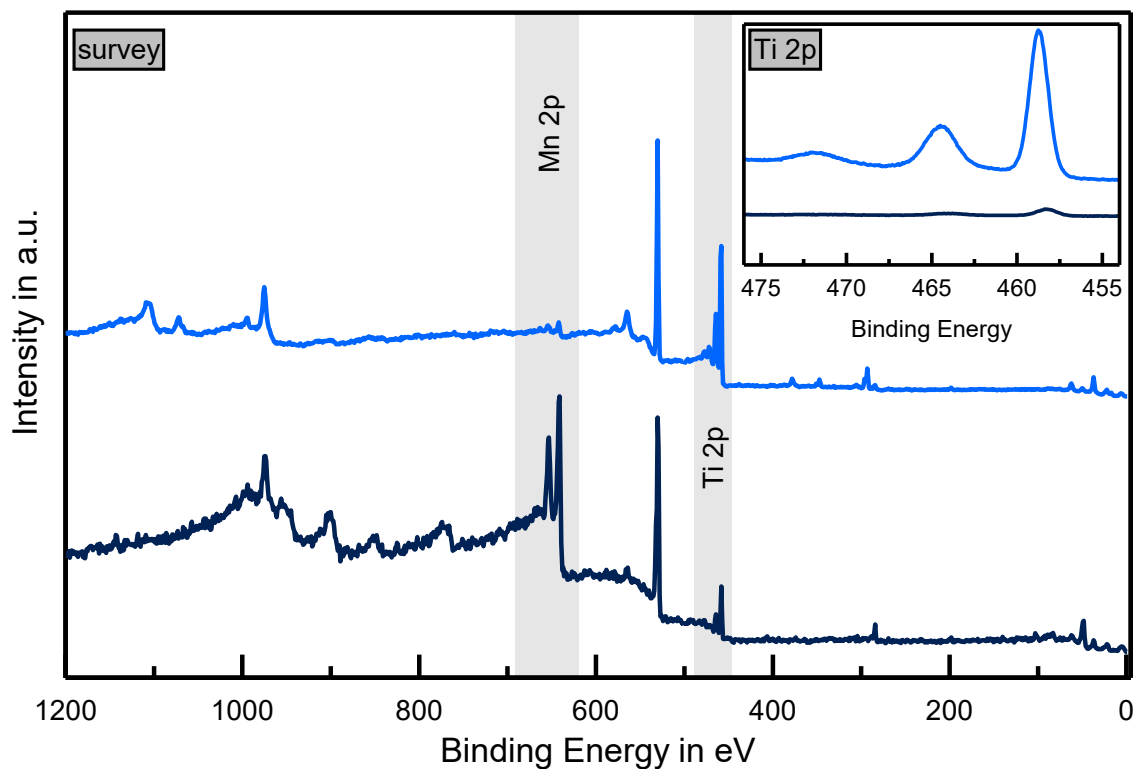


Figure A 9: XP survey spectra of the in **Figure A 8** investigated manganese oxide sample before and after electrochemical (EC) investigation. The Ti 2p detail spectra for both measurement stages are shown as inset. It can be observed that the Mn 2p photoemission line decreases drastically during the EC investigation, while the Ti 2p signal is strongly increased, showing that the manganese oxide phase is not stable in 1 M KOH.

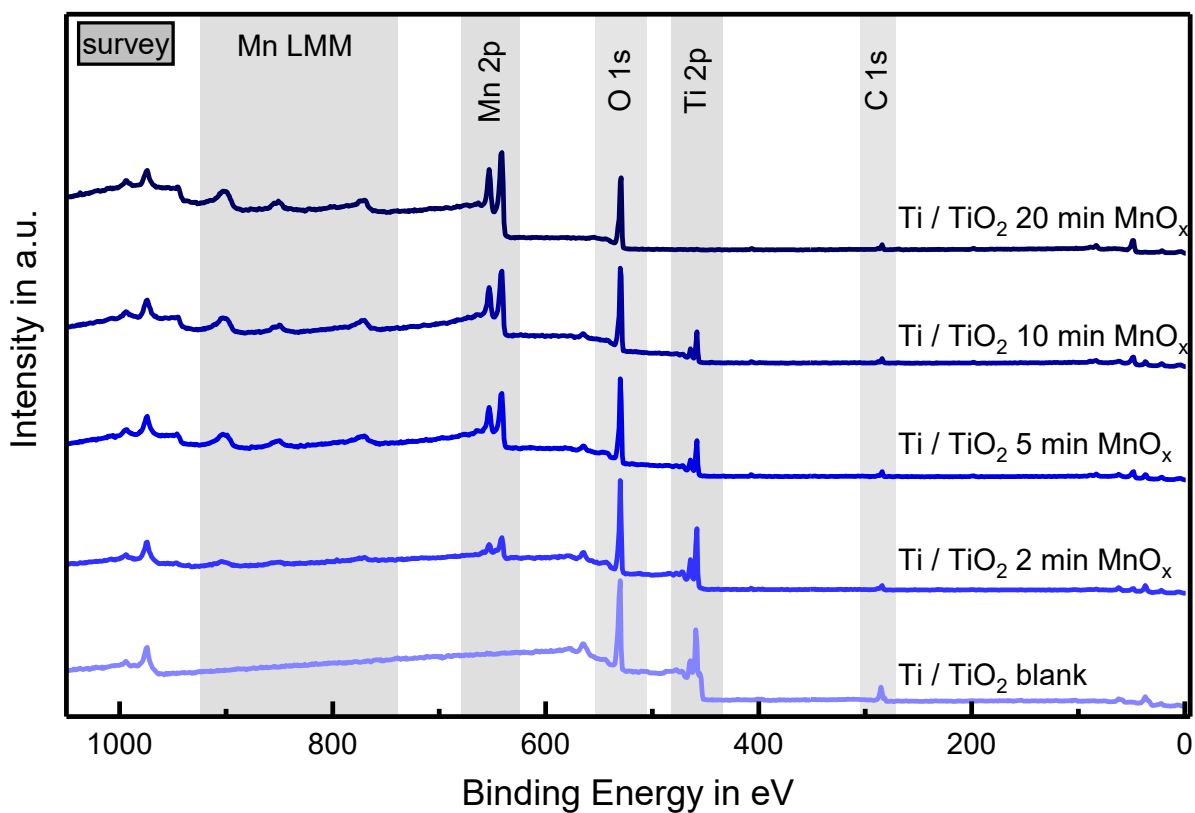


Figure A 10: XP survey spectra of the blank Ti / TiO₂ substrate and the Mn₂O₃ phase deposited at substrate temperatures of 150 °C after different deposition times (2 min, 5 min, 10 min, 20 min). The relevant photoemission lines are marked.

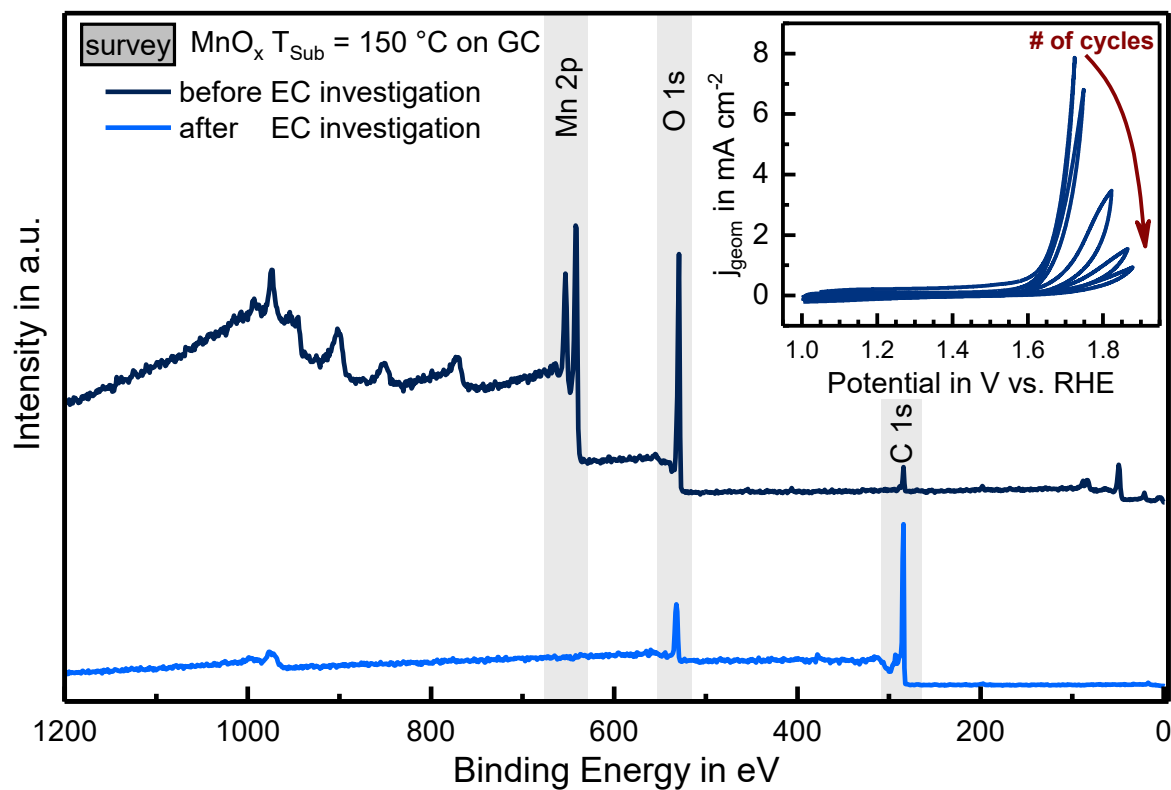


Figure A 11: XP survey spectra of the MnO_x deposited at a T_{sub} of 150°C on GC before and after the electrochemical investigation. The inset shows the degradation of the catalyst with increasing cycle number. The survey spectrum after the EC investigation shows no Mn on the surface.

Part B – Transition metal borides

XRD pictures and refinement data

Table A 1: Rietveld refinement data of Co_3B and Co_2B . Published in ^{[144], [145]}.

	Co_3B	Co_2B
Temperature in K	295	293
Space group	Pnma	I4/mcm
a in Å	5.2132(2)	5.0133(3)
b in Å	6.6375(2)	-
c in Å	4.4113(1)	4.2084(4)
V in Å ³	152.640(5)	105.77(2)
Average crystallite size in nm	12(10)	20.1(2)
Phase contribution	100%	100%

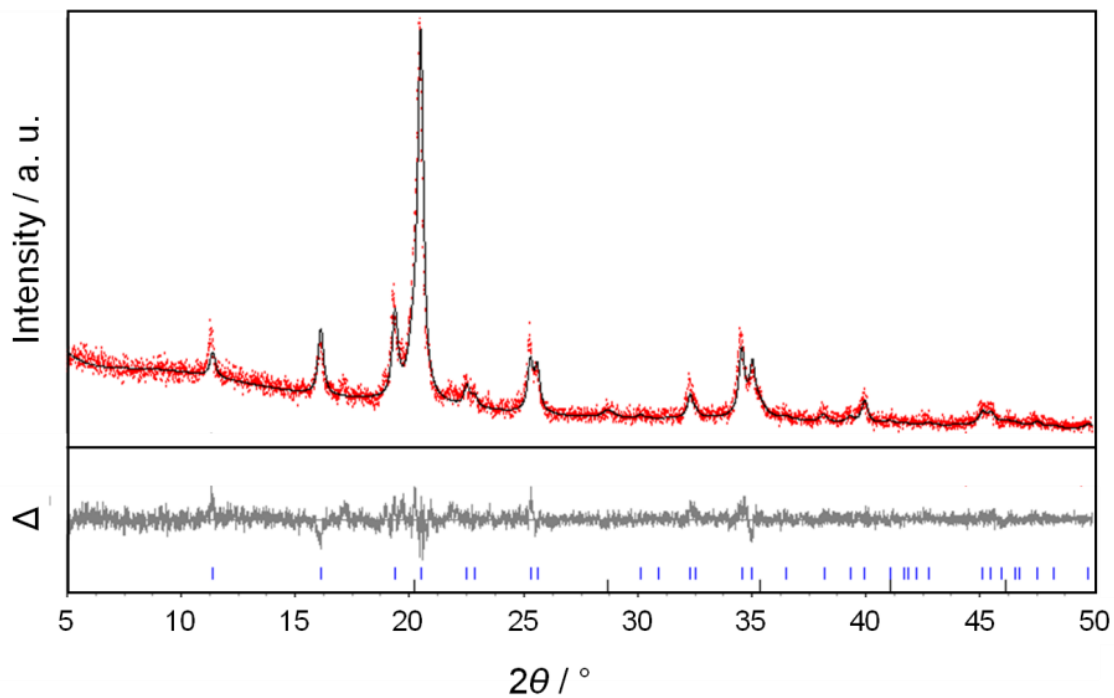


Figure A 12: XRD pattern of the $(\text{Co}_{0.7}\text{Fe}_{0.3})_2\text{B}$ phase. The measured pattern (red), Rietveld fit profile (black) and difference curve (gray) are illustrated. Adapted from our publication. ^[145]

Table A 2: Rietveld refinement data for $(\text{Co}_{0.7}\text{Fe}_{0.3})_2\text{B}$ published in ^[145]. Adapted and modified from our publication.^[145]

Formula	$(\text{Co}_{0.7}\text{Fe}_{0.3})_2\text{B}$	Fe/Co
Space group	$I 4/mcm$	$Im\bar{3}m$
Lattice parameters in pm	$a = 505.94(5)$ $c = 421.54(6)$	$a = 286.0(2)$
Unit cell volume	$107.91(3) \text{ \AA}^3$	$23.40(3) \text{ \AA}^3$
Z	4	2
Crystallite size (Lorentzian)	18(2) nm	7(9) nm
Linear absorption coefficient	$327.90(8) \text{ cm}^{-1}$	$329.0(5) \text{ cm}^{-1}$
Phase contribution	83.7(5) %	16.3(5) %
R_{Bragg}	2.917	1.737
Temperature		293(2) K
Zero point error / 2θ		-0.000(2) °
Wavelength		0.70930 Å
Range / 2θ		5-50 °
R_{wp}		10.23
R_{p}		7.98
GOF		1.07
R_{exp}		9.56

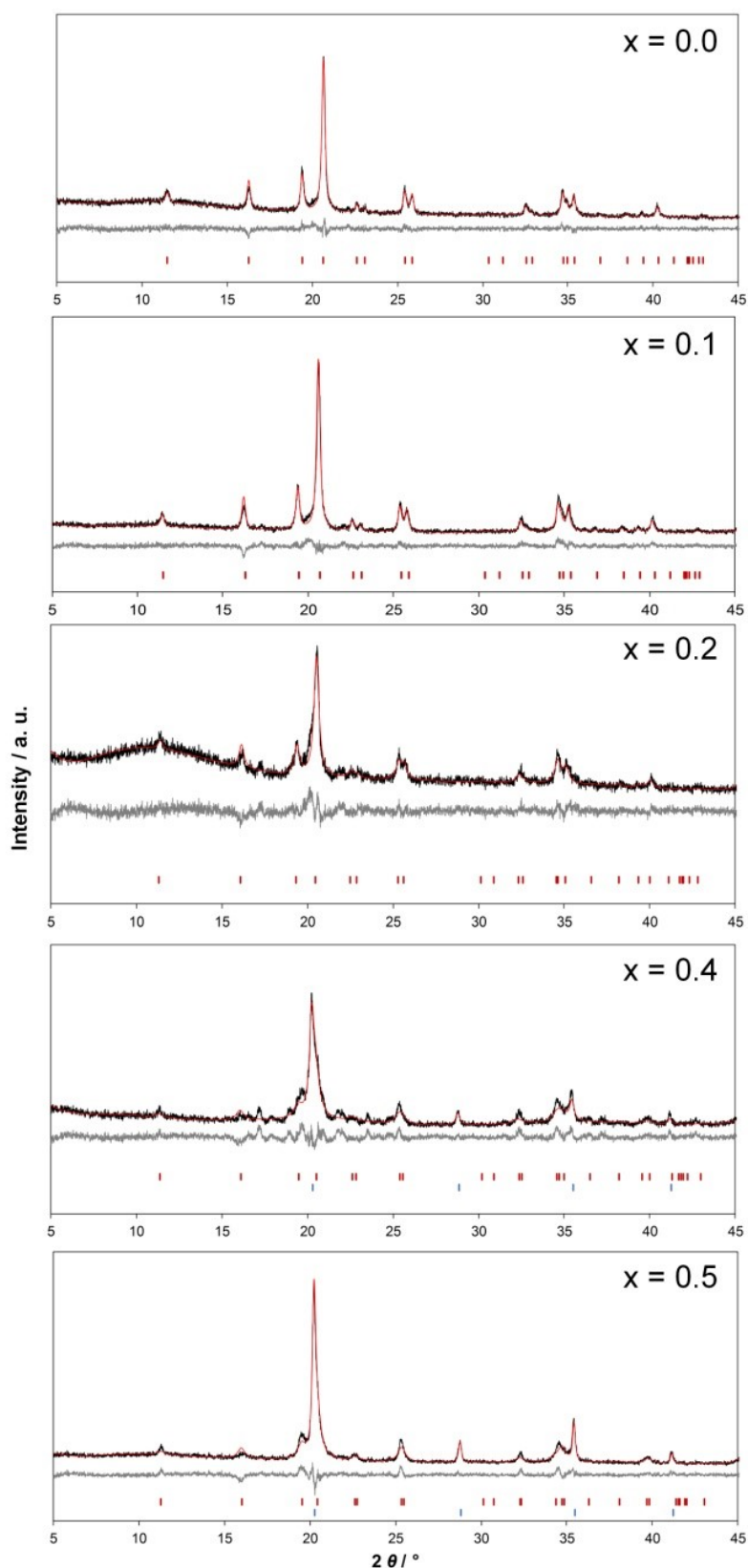


Figure A 13: XRD pattern of the $(\text{Co}_{1-x}\text{Fe}_x)_2\text{B}$ phases with $0 \leq x \leq 0.5$. The $(\text{Co}_{0.7}\text{Fe}_{0.3})_2\text{B}$ phase is shown in the previous diffractogram. The measured pattern (red), Rietveld fit profile (black) and difference curve (gray) are illustrated. Adapted from our publication.^[145]

Table A 3: Rietveld refinement data for $(\text{Co}_{1-x}\text{Fe}_x)_2\text{B}$ phases with $0 \leq x \leq 0.5$. The $(\text{Co}_{0.7}\text{Fe}_{0.3})_2\text{B}$ phase is shown in the previous table. Adapted and modified from our publication.^[145]

	x = 0.0	x = 0.1	x = 0.2	x = 0.4	x = 0.5
Space group	$(\text{Co}_{1-x}\text{Fe}_x)_2\text{B}$ $I 4/mcm$; $Z = 4$				
Lattice parameters in pm	$a =$ 501.33(3)	$a =$ 503.00(3)	$a =$ 505.03(7)	$a =$ 507.9(2)	$a =$ 509.79(9)
	$c =$ 420.84(4)	$c =$ 421.43(4)	$c =$ 421.3(2)	$c =$ 418.5(3)	$c =$ 419.2(2)
Unit cell volume	105.77(2) \AA^3	106.63(2) \AA^3	107.43(4) \AA^3	107.9(1) \AA^3	108.94(6) \AA^3
Crystallite size (Lorentzian)	20.1(2) nm	20.6(9) nm	13.9(4) nm	8.0(2) nm	8.7(1) nm
Linear absorption coefficient	334.52(4) cm^{-1}	334.52(4) cm^{-1}	329.4(2) cm^{-1}	327.7(3) cm^{-1}	324.8(2) cm^{-1}
Phase contribution	100 %	100 %	100 %	67.0(6) %	62.9(3) %
R_{Bragg}	2.491	2.977	2.597	3.686	3.318
Space group	Fe $Im\bar{3}m$; $Z = 2$				
	x = 0.0	x = 0.1	x = 0.2	x = 0.4	x = 0.5
Lattice parameters in pm	-	-	-	$a =$ 285.32(3)	$a =$ 285.602(9)
Unit cell volume in \AA^3	-	-	-	23.226(8)	23.296(3)
Crystallite size (Lorentzian)	-	-	-	15(3) nm	26.4(5) nm
Linear absorption coefficient in cm^{-1}	-	-	-	331.5(1)	330.46(3)
Phase contribution	-	-	-	33.0(6) %	37.1(3) %
R_{Bragg}	-	-	-	2.607	3.015
Temperature	293(2) K	293(2) K	293(2) K	293(2) K	293(2) K
Zero-point error / 2θ	0.0000(7) °	-0.0016(7) °	-0.007(2) °	-0.013(3) °	-0.0086(8) °
Wavelength in \AA	0.70930 \AA	0.70930 \AA	0.70930 \AA	0.70930 \AA	0.70930 \AA
Range / 2θ	5-50 °	5-50 °	5-50 °	5-50 °	5-50 °
R_{wp}	7.56	7.94	8.88	12.90	8.19
R_{p}	5.97	6.19	6.96	10.06	6.28
GOF	1.03	1.16	1.14	1.30	1.25
R_{exp}	7.36	6.82	7.78	9.94	6.55

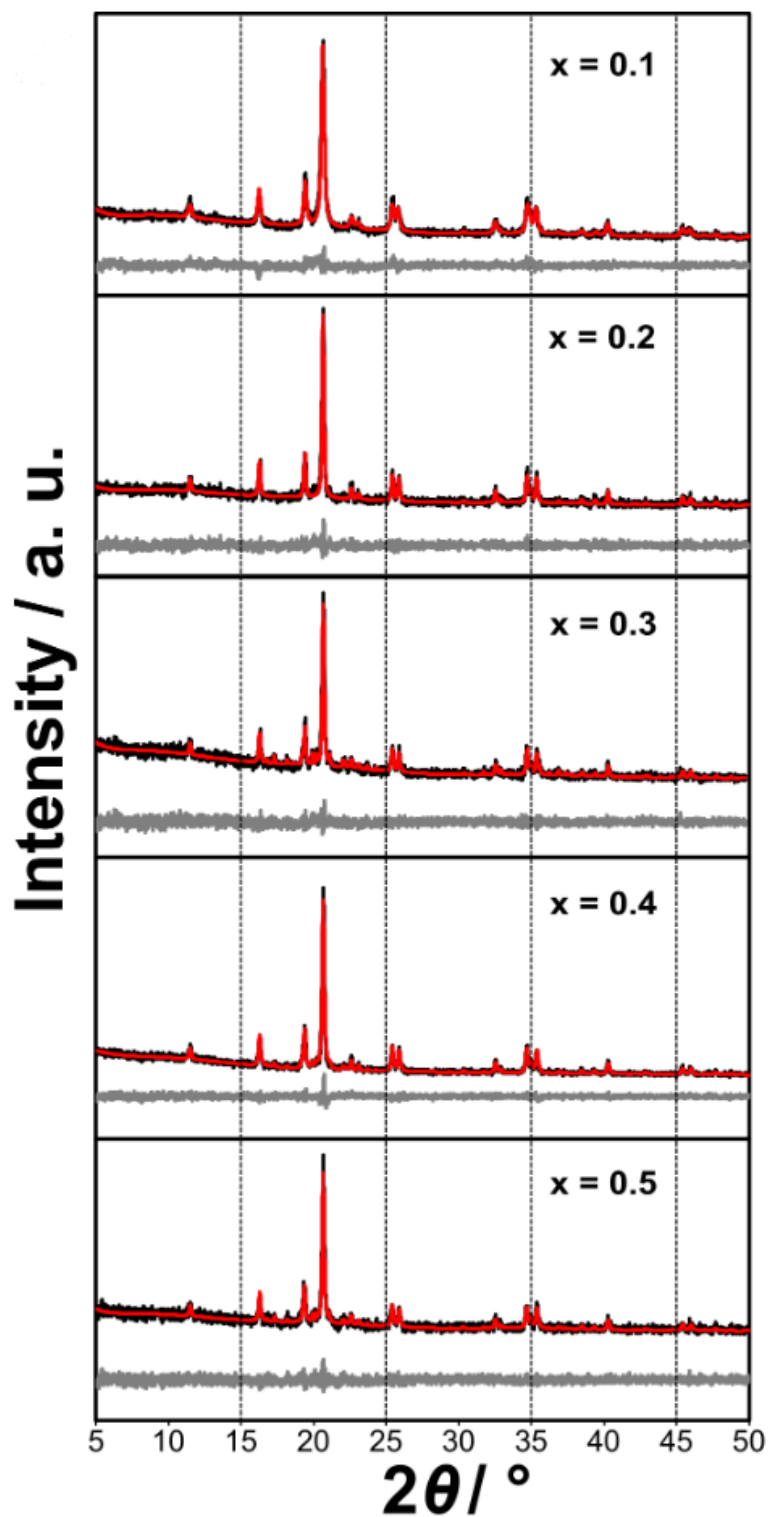


Figure A 14: XRD pattern of the $(\text{Co}_{1-x}\text{Ni}_x)_2\text{B}$ phases with $0 \leq x \leq 0.5$. The measured pattern (red), Rietveld fit profile (black) and difference curve (gray) are illustrated. Adapted and modified from our publication.

Table A 4: Rietveld refinement data for $(\text{Co}_{1-x}\text{Ni}_x)_2\text{B}$ phases with $0 \leq x \leq 0.5$. Adapted and modified from our publication.

	x = 0.0	x = 0.1	x = 0.2	x = 0.3	x = 0.4	x = 0.5
$(\text{Co}_{1-x}\text{Ni}_x)_2\text{B}$ <i>I4/mcm</i>; <i>Z</i> = 4						
Lattice parameters in pm	a = 501.33(3)	a = 501.76(3)	a = 501.06(3)	a = 500.84(3)	a = 500.71(2)	a = 500.60(4)
	c = 420.84(4)	c = 420.33(4)	c = 420.91(4)	c = 420.91(4)	c = 421.34(3)	c = 421.56(5)
Unit cell volume in \AA^3	105.77(2)	105.82(2)	105.67(2)	105.58(2)	105.63(1)	105.64(2)
Crystallite size (Lorentzian) in nm	20.1(2)	19.8(2)	36.7(7)	53(2)	38.9(5)	28.6(6)
Linear absorption coefficient in cm^{-1}	334.52(4)	334.34(5)	334.81(4)	335.11(5)	334.94(4)	334.91(6)
Phase contribution	100%	100%	100%	79.6(6) %	90.6(4) %	85.4(7) %
R_{Bragg}	2.491	2.306	1.968	2.537	1.555	1.896
Space group	Ni_3B <i>Pbnm</i>; <i>Z</i> = 4					
	x = 0.0	x = 0.1	x = 0.2	x = 0.3	x = 0.4	x = 0.5
Lattice parameters in pm	-	-	-	a = 439.48(7)	a = 439.0(3)	a = 439.2(1)
	-	-	-	b = 522.39(9)	b = 522.9(4)	b = 522.3(2)
	-	-	-	c = 661.7(2)	c = 662.6(5)	c = 662.6(3)
Unit cell volume in \AA^3	-	-	-	151.91(5)	152.1(2)	151.75(8)
Crystallite size (Lorentzian)	-	-	-	44(4) nm	45(6) nm	34(4) nm
Linear absorption coefficient in cm^{-1}	-	-	-	397.9(2)	397.4(5)	398.3(3)
Phase contribution	-	-	-	20.4(6) %	9.4(4) %	14.7(7) %
R_{Bragg}	-	-	-	2.849	2.111	2.129
Temperature	293(2) K	293(2) K	293(2) K	293(2) K	293(2) K	293(2) K
Zero point error / 2θ	0.0000(7) °	0.015(3) °	0.0000(8) °	0.0015(8)	0.0012(6) °	0.0001(9) °
Wavelength in \AA	0.70930	0.70930	0.70930	0.70930	0.70930	0.70930
Range / 2θ	5-50 °	5-50 °	5-50 °	5-50 °	5-50 °	5-50 °
R_{wp}	7.56	7.75	12.75	12.13	8.83	13.83
R_{p}	5.97	6.05	9.91	9.28	6.95	10.63
GOF	1.03	1.01	0.95	0.94	0.95	0.91
R_{exp}	7.36	7.68	13.37	12.95	9.25	15.12

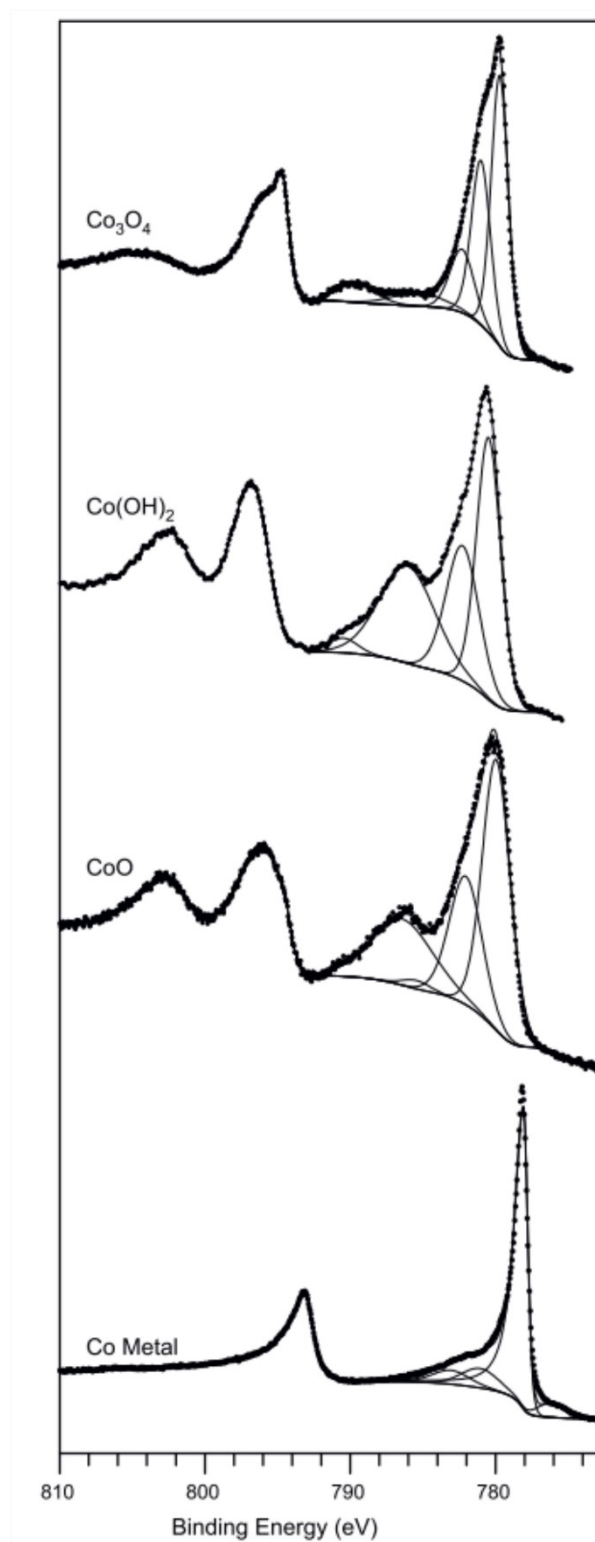


Figure A 15: XP Co 2p detail spectra of different cobalt compounds. Reprinted and modified with permission from ^[209]. Copyright 2012 Elsevier.

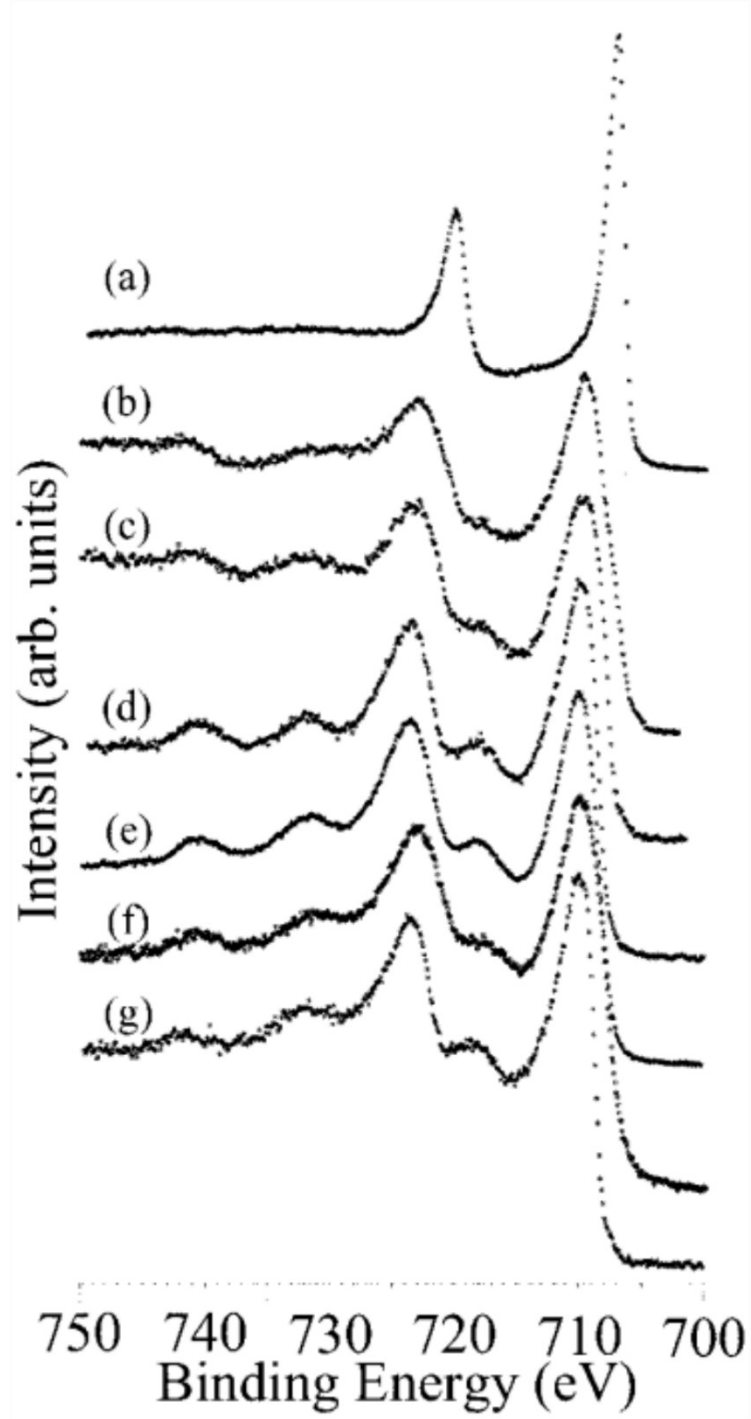


Figure A 16: XP Fe 2p detail spectra of different iron compounds, namely (a) metallic iron, (b) FeO, (c) Fe₃O₄, (d) α -FeOOH, (e) γ -FeOOH, (f) α -Fe₂O₃, and (g) γ -Fe₂O₃, adapted and modified with permission from ^[210]. Copyright 2002 Springer-Verlag.

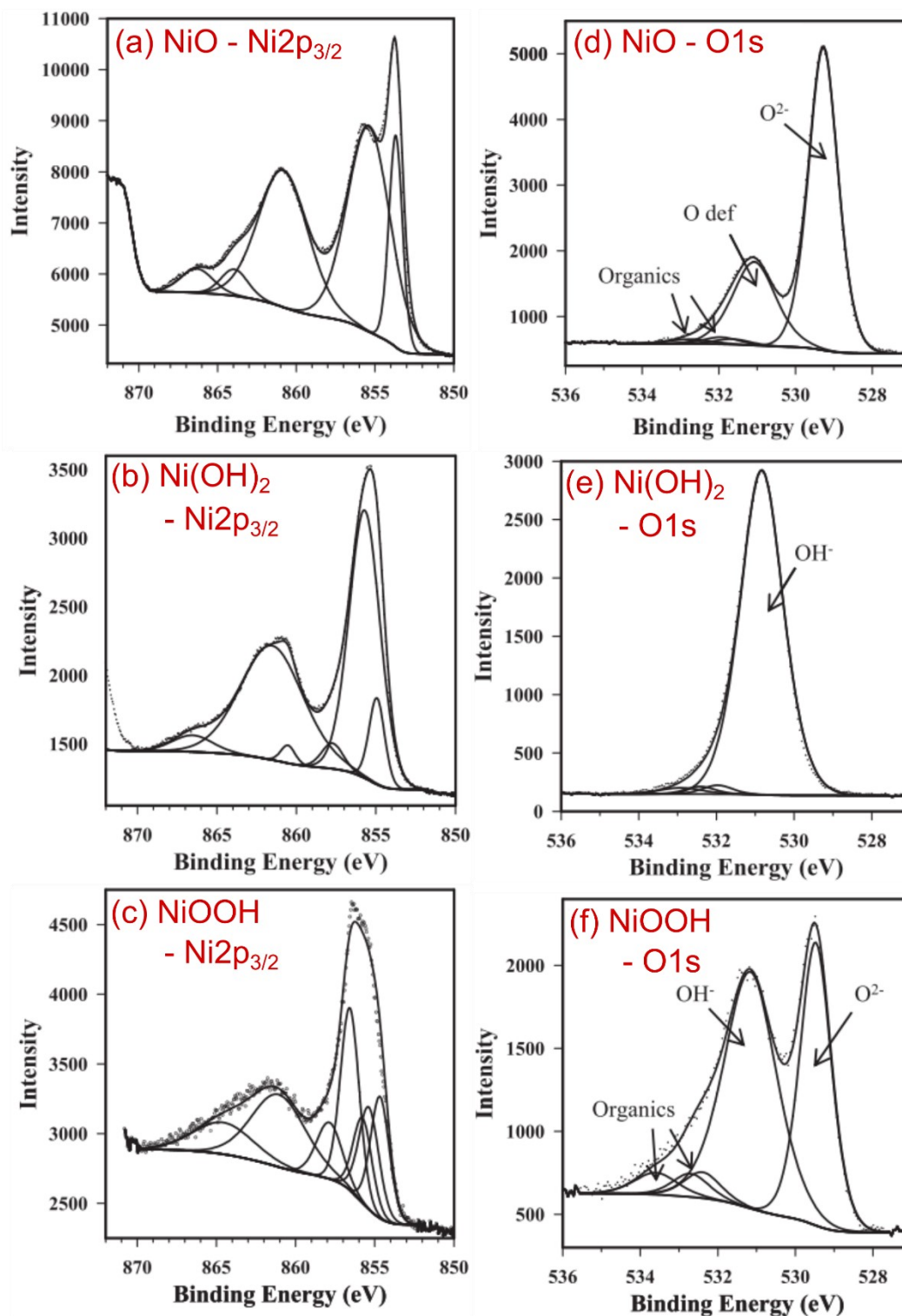


Figure A 17: XPS Ni $2p_{3/2}$ detail spectra of different nickel compounds, namely **(a)** NiO, **(b)** Ni(OH)₂, and **(c)** NiOOH with their corresponding O 1s detail spectra **(d)** NiO, **(e)** Ni(OH)₂, and **(f)** NiOOH, reprinted and modified with permission from ^[209]. Copyright 2012 Elsevier.

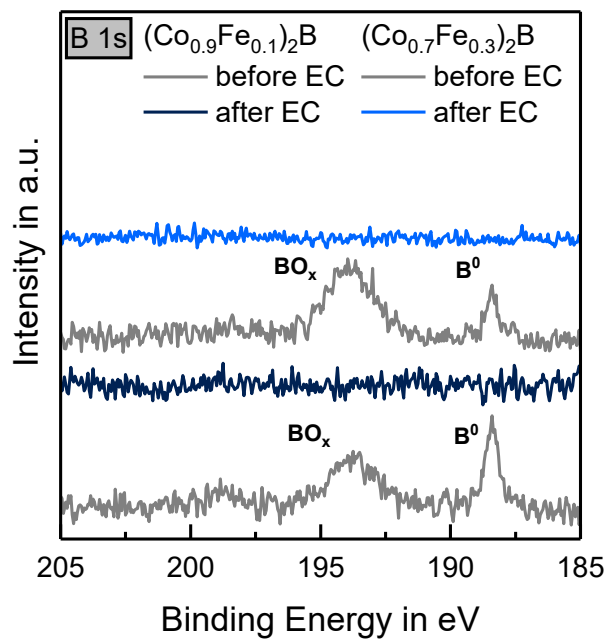


Figure A 18: XP B 1s detail spectra of $(\text{Co}_{0.9}\text{Fe}_{0.1})_2\text{B}$ and $(\text{Co}_{0.7}\text{Fe}_{0.3})_2\text{B}$ before (grey) and after electrochemical (EC) investigation (blue).

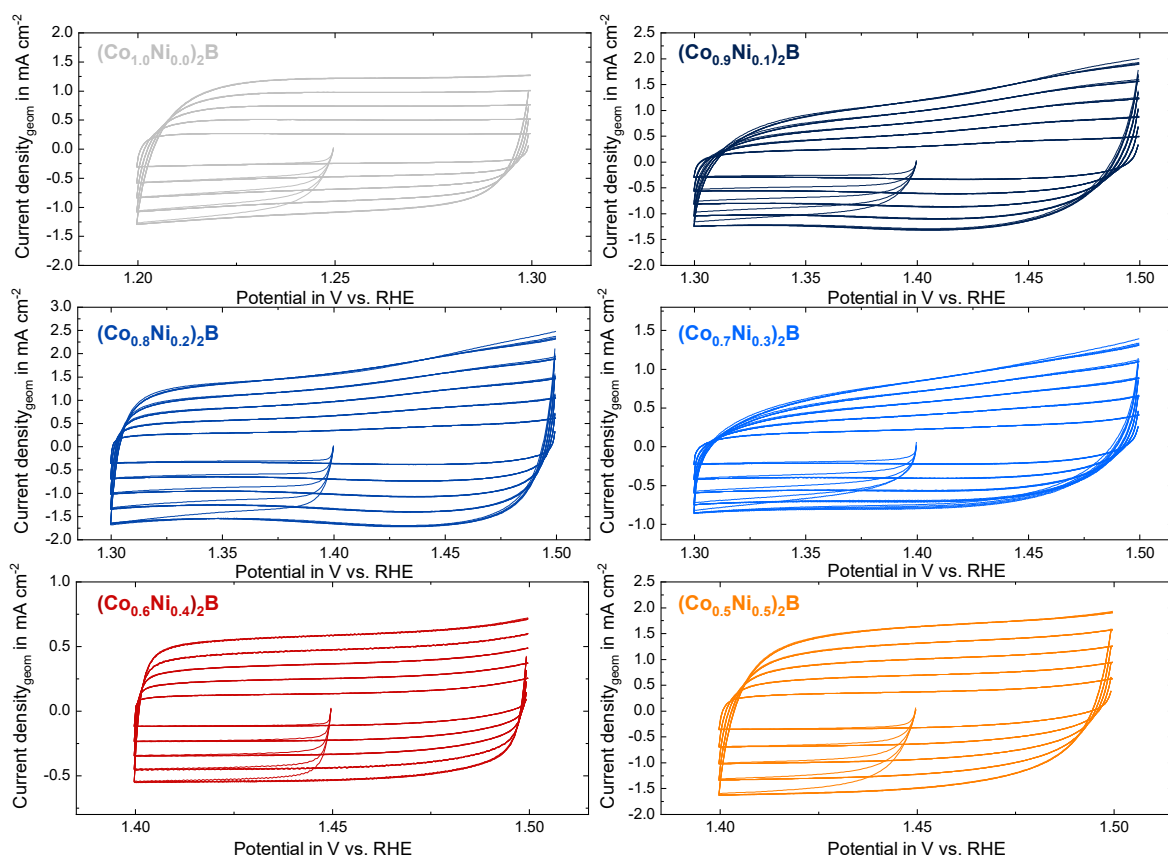


Figure A 19: Sweep potential curves of $(\text{Co}_{1-x}\text{Ni}_x)_2\text{B}$ catalyst with $0 \leq x \leq 0.5$ for the determination of the electrochemical surface area.

Danksagung

An dieser Stelle möchte ich mir die Zeit nehmen mich bei allen Menschen zu bedanken, die mich während meiner Promotionszeit an der TU Darmstadt unterstützt und zur Entstehung dieser Arbeit beigetragen haben.

Als erstes möchte ich mich bei Herrn Prof. Dr. Wolfram Jaegermann für die Betreuung meiner Arbeit und die Möglichkeit bedanken, diese Arbeit auf einem so zukunftsnahe Forschungsgebiet anfertigen zu können. Zudem wurde mir stets die Möglichkeit gegeben eigene Ideen und Ansätze zu verfolgen und diese mit in die Diskussionen einzubringen. PD Dr. Bernhard Kaiser danke ich für die Betreuung und Korrektur meiner Arbeit und das entgegengebrachte Vertrauen meine Forschung selbstständig gestalten zu können.

Prof. Dr. Wolfgang Ensinger danke ich herzlich für die freundliche Übernahme des Zweitgutachtens. Prof. Dr. Oliver Gutfleisch und Prof. Dr. Barbara Albert danke ich für die Bereitschaft ein Teil der Prüfungskommission für dieser Arbeit zu werden.

Dr. Marcus Schulze danke ich für die schnelle und fachkundige Korrektur der ersten Version meiner Arbeit.

Dr. Sebastian Klemenz und Dr. Anne-Marie Zieschang danke ich für die Herstellung der Übergangsmetall-Boride, aber darüber hinaus auch für die gute kooperative Zusammenarbeit und anregenden Diskussionen in vielen Bereichen. Stephanie Dolique danke ich für die Hilfe bei den F-AAS Messungen der Elektrolyten und Claudia Fasel für die thermische Analyse der Precursoren. Ich möchte auch meinen Studenten Stefan Hawel (M.Sc.) und Patrick Schuldt (B.Sc. und HiWi) danken, die mit ihren (Vor)Arbeiten im Bereich der Übergangsmetall-Boride einen beachtlichen Anteil am Gelingen dieser Arbeit hatten.

Des Weiteren möchte ich mich bei der gesamten OF-Gruppe für das angenehme Arbeitsklima bedanken. Die gemeinsamen Kaffee-, Kuchen- und Zopfunden mit wissenschaftlichen als auch nicht-wissenschaftlichen Themen waren mir immer eine große Freude. Bei Kerstin Lakus-Wollny möchte ich mich für die niemals langweilige Zeit am REM bedanken. Ein besonderer Dank geht auch an die Wasserspalter und Quasi-Wasserspalter für die gute Zusammenarbeit, den Zusammenhalt und die gemeinsame Wartung der Vakuumanlagen. Es war selten einfach, aber gemeinsam (und mit DAISY-FUNK) konnten wir stets alle Probleme meistern. Mein Dank gilt aber nicht nur den jetzigen Angehörigen der OF-Gruppe, sondern auch den ehemaligen Kollegen, die mich herzlich in ihrem Kreis aufgenommen und mir viele Dinge beigebracht haben.

Bei meinen Freunden und meiner Familie möchte ich mich für all die liebevolle Unterstützung bedanken, ohne die ich heute nicht hier wäre.

